Department of Electrical and Computer Engineering

A Study of Visible Light Communication Channels for High Speed Roadways

Samir Abdullah Al-Busaidi

This thesis is presented for the Degree of

Doctor of Philosophy

of

Curtin University

September 2015

Declaration

To the best of my knowledge and belief this thesis contains no material previously published by any other person except where due acknowledgement has been made.

This thesis contains no material which has been accepted for the award of any other degree or diploma in any university.

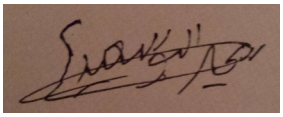

Signature: …….

Date: 25 September 2015

Acknowledgment

I would foremost like to endlessly thank my wonderful parents for their infinite support, deep concern and continuous followup in each phase of my study. I would like to thank my wife and daughter for their great patients and kind and loving support. Moreover, I thank them deeply for enduring by my side all the hardships that I faced during the course of my study. I would also like to thank my sister for her concern and followup to the success of this study.

I would also like to sincerely thank my supervisors Dr. Yee-Hong Leung, Head of Department of Electrical and Computer Engineering, Curtin University, and Associate Prof. Ba Tuong Vo, Department of Electrical and Computer Engineering, Curtin University, for seeing me through my study, and their valuable insight, dedicated time, and patience. Moreover, I thank you both for providing a friendly environment along with your a high level of professional supervision at a time of great strain and frustration.

My special thanks to my PhD committee chair person, Professor Syed Islam, John Curtin Distinguished Professor, Curtin University, Australia, who always stood up very strong at my side especially at the toughest of times during my studies at Curtin University, and who believed that there is always a possible outcome even when all indicators point otherwise.

I would also like to thank HE Dr. Rawya Al-Busaidi, Minster of Higher Education, Oman, Dr. Ali Al-Bimani, Vice Chancellor of Sultan Qaboos University, Oman, Prof. Kate Wright, Associate DVC, Research Training, Curtin University, Australia, for all their support in seeing me through the course of my study.

My special thanks, too, to Mr. Shuaib Edwards and his family, whom all have kindly accommodated me as part of their family, and for making my stay as

comfortable as possible at a time when my family could not be at my side. And I thank to Mr. Othman Maghdoof and his family who were kind to initially stand beside me.

I would also like to thank Eng. Mohammed Ibrahim from Egypt for both his valuable time and effort that he had dedicated towards providing all the necessary electrical design details of roadway streetlights.

Abstract

Digital data transmission using visible light communication (VLC) is beginning to emerge as an attractive alternative to wireless transmission. Due to the drop in price of light emitting diode (LED) light bulbs and the switching capability inherently associated within LEDs, VLC is perceived as a highly desirable asset for high speed digital communications. One such application that has been envisaged within this study, is to integrate VLC onto high speed roadways for information delivery. Of the possible types of information, one type could be related to leveraging intelligent transport system (ITS) services that are life critical. Vehicle occupants in accidents on high speed roadways are more prone to greater injury, if not death. This fact is due to the high speed of the traveling vehicles involved in crashes, as compared to their slower moving counterparts. By adopting an accident reporting scheme built within an ITS framework, it is possible to instantaneously dispatch the required aid to the injured, while simultaneously transmitting advance warnings of hazardous road conditions to other vehicles within the vicinity.

For VLC to be applicable along high speed roadways it is necessary to adopt streetlight luminaires as transmitters. This solution is an efficient and cost effective way to broadcast information to mobile road users. The air medium, which is effectively the VLC channel, must therefore be closely inspected to determine the plausible bit rates that can be achieved. Equally important, is to form an understanding on the underlying physical perturbation effects that could probably disrupt the communications link under clear sky night time conditions.

The initial step towards forming an all round VLC channel understanding requires a reference framework on which the physical road parameters and LED geometry should be included within the model. Furthermore, the model must also take into account the light intensity distribution of the streetlight luminaire. By fulfilling these two requirements an accurate DC channel response can be obtained.

To obtain the exact DC channel response over a stretch of road, it is necessary to determine the summed effect of individual LEDs over all points on the road surface. The process is time consuming and computationally expensive. To reduce the complexity, two methods were investigated, primarily based upon the idea that it is possible to obtain the DC channel response from a single reference LED. The first method investigated using a single reference LED DC channel response in conjunction with the differential DC channel responses of all remaining LEDs. The DC channel responses, however, comprises multiple variables, which upon differentiation, yields a computationally intensive evaluation of the DC channel responses attributed to each LED. The second method investigated is based upon the fact that an LED array can be accurately modeled by an equivalent single LED placed in the center of the luminaire. This analytical approximation can provide insights into the dominant factors affecting the system and facilitate analysis of both channel root mean square (RMS) delay spread and channel capacity. This single LED equivalency method proved to be sufficiently accurate over the luminaire illumination zone, while simultaneously drastically reducing the computational complexity.

The effect of any physical perturbations can be grouped into either rotation or translation perturbations. This includes all possible relative motion associated with the slender streetlight pole structure and the receivers sensor. Using small angle approximations it is possible to reduce the overall complexity of obtaining the perturbed DC channel response through eliminating parameters that do not affect the perturbed response. Furthermore, for the proposed application, it is shown that the physical perturbations can be reliably ignored for a sensor that is placed within the luminaire illumination zone.

Two channel parameters which are usually derived for communication channels are the channel RMS delay spread and the channel capacity. The channel RMS delay spread, which gives a measure of the ISI free transmission rate, is a function of LED geometry and DC channel response. By replacing the LED array by its single LED equivalency, it is shown that it is possible to obtain accurately the RMS channel delay spread while reducing the computation complexity. The results obtained for the average channel capacity and channel RMS delay spread indicates that high speed

transmissions on the high speed roadways are limited by the modulating bandwidth (BW) of the LED used in the luminaire. This effect culminates into an observed penalty of around 11 fold when comparing the constrained channel capacity to the ISI free transmission. However, it is also shown that data rates above 25Mbps can be achieved, thus opening the prospects of high speed roadways VLC.

Table of Contents

Table of Acronyms

ITS	**Intelligent Transport System**
VLC	**Visible Light Communication**
LED	**Light Emitting Diode**
HB-LEDs	**High Brightness – Light Emitting Diodes**
IM	**Intensity Modulation**
Tx	**Transmitter**
PD	**Photodiode**
DD	**Direct Detection**
Gbps	**Giga bits per second**
Mbps	**Mega bits per second**
kbps	**kilo bits per second**
BW	**Bandwidth**
RMS	**Root Mean Square**
Rx	**Receiver**
I2V	**Infrastructure to vehicle**
V2V	**Vehicle to Vehicle**
V2I	**Vehicle to Infrastucture**
ISI	**Intersymbol Interference**
OWC	**Optical Wireless Communication**
IR	**Infra-red**
UV	**Ultra-Violet**
FSO	**Free Space Optical**
VLCC	**Visible Light Communication Consortium**

OMEGA	**HOME Gigabit Access**
Li-Fi	**Light Fidelity**
Wi-Fi	**Wireless Fidelity**
CMOS	**Complementary Metal Oxide Semiconductor**
APD	**Avalanche Photodiode**
RF	**Radio Frequency**
EMI	**Electromagnetic Interference**
COTS	**Commercial Off the Shelf**
PLC	**Powerline Communication**
WLAN	**Wireless Local Area Network**
SSL	**Solid State Light**
BER	**Bit Error Rate**
DoT	**Department of Transport**
ITSA	**Intelligent Transportation Society of America**
ERTICO	**ITS Europe**
GPS	**Global Positioning System**
RFID	**Radio Frequency Identification**
DSRC	**Dedicated Short Range Communication**
HPS	**High Pressure Sodium**
OOK	**On Off Keying**
SNR	**Signal to Noise Ratio**
FOV	**Field of View**
CSK	**Color Shift Keying**
PHY	**Physical Layer**
PPM	**Pulse Position Modulation**
PWM	**Pulse Width Modulation**
OOK-NRZ	**On Off Keying – Non Return to Zero**
IoT	**Internet of Things**
SM	**Spatial Modulation**
SSK	**Spatial Shift Keying**
GSSK	**Generalized Spatial Shift Keying**
SPPM	**Spatial Pulse Position Modulation**
BPF	**Band Pass Filter**
RSU	**Road Side Units**

DSSS	**Direct Sequence Spread Spectrum**
LOS	**Line of Sight**
NLOS	**Non-Line of Sight**
fps	**Frames per Second**
OCI	**Optical Communications Image**
FV	**Forward Vehicle**
BV	**Back Vehicle**
PAR	**Packet Arrival Rate**
CSI	**Channel State Information**
SIR	**Signal to Interference Ratio**
SC-BPSK	**Single Carrier Binary Shift Keying**
CIR	**Channel Impulse Response**
OFDM	**Orthogonal Frequency Division Multiplexing**
SUV	**Sports Utility Vehicle**
CAN	**Controller Area Network**
PDF	**Probability Density Function**
FEM	**Finite Element Method**
AASHTO	**American Association of State Highway and Transportation Officials**
MV/LV	**Medium Voltage to Low Voltage**
LV	**Low Voltage**
MV	**Medium Voltage**
MIMO	**Multiple Input Multiple Output**
WA	**Western Australia**
IRC	**Inner Road Curvature**
ORC	**Outer Road Curvature**
TOA	**Time of Arrival**
RV	**Random Variable**
iid	**independent and identically distributed**
MGF	**Moment Generating Function**
ML	**Maximum Likelihood**
RC	**Raised Cosine**
FET	**Field Effect Transistor**

Chapter 1

Introduction

1.1 Motivation

Road safety issues are of great concern in most road applications and services. This concern is greatly amplified by observing that the number of road accident related deaths in the US alone is more than 30,000 in the past two decades [1]. Car accidents often incur the deaths of multiple members of a family, especially for those taking the road on long journeys. To curb the negative impact of road accidents on society, the intelligent transport system (ITS) has been introduced. In effect, it has been envisaged that an ITS solution could manage roadways in multiple ways. Firstly, it could channel traffic through the most convenient routes, thereby smoothing traffic flow. By thinning traffic, road occupants become more tolerable to one another. Secondly, by maintaining the traffic flow, it becomes possible to reduce the required time of delivery, which will definitely impact the economy of a country in a positive manner. Finally and most critically, it could be used for crash warning, crash avoidance and crash reporting.

Successful deployment of an all round ITS requires the reliable exchange of information between vehicles and all concerned parties. In the case of crashes, road monitoring authorities should be capable of transmitting accurate information regarding the crash to ambulance services. A quick ambulance dispatch could be the difference between life and death to the injured involved. Furthermore, sharing the whereabouts of a crash on a road with other road occupants within the vicinity, could be critical in avoiding multiple crashes. In this case a method to broadcast the information over the road stretch becomes a priority.

One method of exchanging information over roadways, could be by deploying wireless radio. However, due to the relatively congested radio spectrum, dedicating a slice of the valuable spectrum for ITS could be a costly endeavor. To circumvent this problem, the option of using wireless devices based upon the IEEE 802.11 standard, could be adopted. On the downside, implementing an integrated ITS using this approach will require building a new radio network. Moreover, the distance coverage of such devices are limited. This limitation will ultimately translate into the procurement of a large number of transmitters required for sufficient signal coverage over the entire road network.

Visible light communication (VLC) is an emerging communications technique that utilizes the free visible light spectrum for communication based applications. To communicate by means of light requires that a modulating signal be applied to the light carrier. The point of attraction of adopting VLC can be directly related to the large available light spectrum that can be harnessed freely for communication purposes. Moreover, light under normal circumstances is non-harmful. However, if light does become an intrusive element, it can be blocked quite easily. Finally, non-coherent light, such as that emitted by light emitting diodes (LEDs), are at present commonly used for area illumination.

The smart city push instilled by governments, is usually bolstered by any underlying economic savings that can be achieved. One eminent source of economic expenditure is in electrical power generation and distribution, which must satisfy a continuous increasing demand of electricity. This increase in demand is mainly driven by the expansion of urbanized areas, factories and businesses, which all require laying out afresh a complete supporting infrastructure. In particular, the expanding electrical grid will connect a diversity of electrical loads, some that have been designed on the foundations of high power efficiency, while others not. Light bulbs, installed in public and private premises alike, are no exception to this, and therefore come in a variety of types and forms. Through the introduction of high brightness – light emitting diodes (HB-LEDs), it became a reality that power bills associated with illlumination can be drastically reduced. This potential has made road operators, whether government or private, to reconsider replacing older luminaires on roadways

with HB-LEDs.

Research into the benefits of adopting HB-LEDs has identified yet another possible benefit, applying modulation to light. In this case the LEDs can be used for the dual purpose of illumination and communications. With HB-LEDs replacing older luminaires on roadways, a possible alternative to radio communication for ITS becomes a reality. This simple transformation of luminaires, could promote VLC into a truly ubiquitous form of digital communications.

Through changing the light intensity by a method known as intensity modulation (IM) each streetlight luminaire is transformed into a VLC transmitter (Tx). On the other end, photo diode (PD) sensors mounted on the roofs of vehicles detect the differences in illumination in a direct detection (DD) scheme.

The combination of IM/DD is currently being vigorously investigated at many level, such as in [2]. However, it is mainly driven by the prospect of delivering Gbps data connectivity applicable to the indoor environment. This high speed transmission is based upon the extremely large bandwidth (BW) associated with the data carrier, namely the visible light. By utilizing the light spectrum rather than the highly contested radio spectrum, could allow in the near future, the possibility of offloading some radio communication services to VLC. Light, too, is a free commodity, which makes VLC all the more appealing. Compared to fiber optics light wave communications, VLC liberates itself from delivering communication services through a constricted fiber optic waveguide. To this extent, the VLC implementation is free from any waveguide specific infrastructure. The ubiquitous nature of light bulbs, in the sense of penetrating into most man made infrastructures, is also a clear indicator into the limitless possibilities of integrating VLC within the telecommunications realm.

Light too has its limitations. The light carrier can easily be blocked by obstacles in its path. Although there have been a number of successful demonstrations of VLC by reflecting light on walls, such communication method is inefficient as compared to unobstructed VLC. Compared to the confinement of the indoor environment, the

outdoor counterpart can be challenging due, in essence, to the existence of a large number of environmental variations. The variations, which can be attributed largely to the weather, introduces a number of uncertainties into the free air channel. Rain, fog and dust can all introduce channel attenuation and multipath effect, where the latter is the phenomenon that arises due to the reception of multiple copies of the transmitted signal. Air turbulence, a direct consequence of the thermal properties of air, causes a focused beam of light to scintillate. The effect of wind on structures housing focused light at the transmission end further complicate matters, by causing the light beam to wander at the receiving end.

It has been initially associated with outdoor VLC that the predominant Txs suitable for the outdoor environment were devices based on lasers. However, LEDs are currently entering into the field. Unlike lasers, that have primarily been used for long range point-to-point communications, the communication range of LED is much shorter. With an unfocused light beam, the output from LEDs are much broader compared to the light output from lasers. It is this feature that makes LEDs an ideal element for short range broadcast in the sphere of VLC. Capitalizing on this feature along with the highly prioritized safety applications in ITS, has spawned the idea of broadcast using LED based traffic lights.

As LEDs have only begun emerging into the lighting infrastructure, studies into the environmental impact onto VLC have only recently started to draw interest. With the indoor environment more predictable in terms of variability, compared to the outdoor, along with the large potential of VLC for indoor personal communications, a number of channel studies had been conducted for the indoor environment [3]. The studies focused on obtaining the channel responses derived from the direct non obstructed and reflected light components. Direct non obstructed channels are obtained in terms of the DC channel response whilst reflected channels are obtained in terms of the multipath channel. Moreover, key channel parameters, in the form of the channel root mean square (RMS) delay and channel capacity can be produced as demonstrated in [4].

In VLC studies retaining to the indoor environment, it is acknowledged that LED

based light fixtures are usually composed from a large number of LEDs. Each LED in the fixture can be viewed as a single point source that individually affects the outcome of the channel response. The contribution from every LED is required to obtain an exact channel response, which becomes a computationally intensive task. The computations of the channel response can be further increased under the realization that multiple light fixtures are typically installed within a single indoor environment. To obtain a measure on some key parameters while reducing the number of computations, in some researches on the indoor channel, it has been suggested to replace each light fixture by an equivalent single LED light source. Similarly, the outdoor environment that utilizes multiple LED light fixtures could also benefit from this simplification.

VLC in ITS can have either two setups, an inter-vehicle setup or an infrastructure vehicle setup. An inter-vehicle setup is one in which VLC is used to deliver information between vehicles, whereas in the latter information is shared between the infrastructure and vehicles. In each setup there are two type of VLC Txs, headlamps and taillights for the former, while for the latter, traffic lights and streetlights have to be also included. On the receiver (Rx) side, there are mainly two types of sensors, namely the PD and camera. In the arena of high speed communication of infrastructure to vehicle (I2V), it is typical that PD are favored over camera based sensors. Conversely, for low speed VLC, that could utilize multiple VLC Txs, the adoption of camera based sensors is believed to have the upper hand.

Streetlights have been designed to illuminate the surface of the road in an even manner. LEDs on the other hand, tend to focus their light output onto specific points. To accommodate LEDs for road illumination requires adopting secondary optics that redistributes the light intensity for even road surface illumination. Such type of lenses, also known as freeform lenses, exhibit a light intensity distribution that bears resemblance to bat wings, and are therefore known as bat wing distributions. Modeling of streetlights using this model has been shown in [5].

VLC channel studies for road setups have been, in most cases, based upon experimentation or simulation of specific road scenarios. To the authors knowledge,

only a single analytical study on each of I2V and vehicle to vehicle (V2V) cases has been performed [6][7]. In particular, with respect to the first case, the particularity of the light intensity distribution associated with roadway lighting have altogether been discarded.

Almost all studies of I2V VLC channel have been exclusively undertaken for the cases of metropolitan and urban road scenarios. In contrast, high speed roadways VLC channel studies have yet to be performed, to the best of the authors knowledge. The importance of studying the VLC channel of the high speed roadway environment can be highlighted through the deep impact it could have on peoples lives. This is especially true in circumstances whereby loved ones are lost in fatal road accidents, that could have been avoided altogether. For such reasons, this thesis aims at studying the VLC channel of high speed roadways specific to I2V streetlight LED transmissions. Particular emphasis, in this study, is given to relevant roadway parameters that are typically applied in highway construction, which influences the I2V VLC channel.

As this thesis pioneers on the I2V VLC channel study for high speed roadways, it should be specified that it is impossible to accommodate the complete set of variables that would naturally influence the channel. As a consequence, the thesis is confined to the study of the unobstructed VLC DC channel and its possible perturbations under the assumption of clear night sky condition only. The motivation of conducting the study on this basis, abides to the known manner to which initial VLC channel studies are undertaken in a new environment. In this respect, the study achieves to uncover the high speed roadway streetlight parameters that greatly affects the outcome of the DC channel response, while, foremost, verifying the ability to communicate using an I2V VLC system. The study is also extended to include perturbations that will influence the outcome of the DC channel response Subsequently, from the outcome of the DC channel response, two important parameters, that provides an invaluable insight into the achievable transmission rates within the high speed roadway environment, are shown. The two parameters are namely the channel RMS delay and channel capacity.

It is clear that the DC channel response is the crucial parameter within this study. The DC channel response can be obtained by means of two methods, namely, a direct and an indirect method. The direct method is based upon accounting for the complete set of LEDs in a light fixture, in contrast to the indirect method. An equivalent LED representation of all LEDs within the light fixture is the basis upon which the indirect method is composed. Importance of conducting the study using the later method, highlights the significance of reducing the computational complexity of obtaining the channel parameters, while maintaining the accuracy as compared to the former method.

1.2 Thesis Objectives:

The thesis undertakes the following objectives towards studying the I2V VLC unobstructed channel under clear sky night time conditions, in the framework that vehicles are constrained to known paths on the road surface:

1. Obtain the exact DC channel response based upon the proposed street light model.
2. Derive an analytic model for a simplified DC channel response.
3. Undertake a perturbations analysis considering possible rotation and translation movement of the streetlight pole or sensor.
4. Highlight the prevalent perturbation parameters that affect the DC channel response.
5. Evaluate the channel RMS delay through a direct and an indirect method.
6. Extend the channel RMS delay to obtain a measure of the possible bit rate for intersymbol interference (ISI) free transmission.
7. Obtain the channel capacity of the system.

1.3 Thesis Contribution:

To the best of the authors understanding, this thesis is the first to model and analyze a VLC system for high speed roadways. The thesis contribution is supported by the

following findings:

1. A framework for an accurate methodology of modeling the high speed roadways with streetlights centered between both roads. Moreover, the framework takes into account specifics of the physical roadway specifications. This is shown in chapter 3.
2. The DC channel response over a complete stretch of light coverage zone while considering the different highway scene settings is shown. The DC channel response, furthermore, takes into account an accurate streetlight model of the light intensity distribution. Furthermore, it is shown that for VLC communications the effect of light spilled over from the luminaire from the opposite side of the road is negligible, and therefore causes no interference. Moreover, it is shown that it is possible to efficiently and accurately model the DC channel response using a single LED equivalency model in place of the complete LED array. This can be observed in chapter 4.

3. A plausible method of lumping all physical perturbations into the Rx and/or Tx is demonstrated. Furthermore, the perturbed system is analyzed analytically through obtaining the DC channel responses of rotation and translation perturbations. Simultaneously, the parameters, distance, polar and azimuthal angles and sensor to LED viewing angle, are all assessed upon their significance towards the perturbed DC channel response. It is shown that the DC channel response is insignificantly perturbed by physical perturbation of the luminaire or the sensor, for a sensor placed within the illumination zone. This can be obtained within chapter 5.

4. Demonstrate the channel RMS delay for the different possible types of roadway configurations. Furthermore, it is shown that by using a simplified method it is possible to obtain accurately the channel RMS delay spread for a predetermined geometrical layout of LEDs. Similarly, the channel capacity of the high speed roadways has been demonstrated. This all can be seen in chapter 6.

5. Establish that the system has the potential of delivering high speed data, but is limited due to the light emitting property associated to the LED coating, as demonstrated in chapter 7.

1.4 Thesis Outline:

To gain an insight into the studied channel, this thesis is structured according to the following manner,

- Chapter 2 is a literature survey that is conducted into VLC communications. Particular attention is given to VLC applied to the field of ITS and its associated systems and channel analysis.
- Chapter 3 provides a detailed description of an envisaged high speed roadway VLC system which sets the scene for studying the VLC channel.
- Chapter 4 is used to produce the analysis of the DC channel response and its analytical simplification.
- Chapter 5 is used to analyze the effect of rotation and translation perturbations on the DC channel response.
- Chapter 6 shows the analysis of two channel parameters, namely the channel RMS delay spread and channel capacity.
- Chapter 7 demonstrates the complete set of results associated with the DC channel response and its simplification, perturbations, RMS delay spread and channel capacity, of the system.
- Chapter 8 provides the conclusion and future works.

Chapter 2

Literature Review

2.1 Introduction:

VLC is an implementation of optical wireless communication (OWC) that includes the infra-red (IR), visible light and ultra violet (UV) spectrum for communications purposes. In particular, VLC is an attractive opportunity for ubiquitous high speed data communications by means of switching states of light sources. The main driving factor of VLC adoption can be returned to the commercialization of LEDs as an efficient means of illumination. By varying the light source intensity at relatively high frequencies, at rates imperceptible to the human eyes, communication through illumination is made possible.

The technique of using light to carry information is not new and can be traced to the use of fire as light beacons in times of war and light houses for maritime purposes in ship navigation [8]. The modern adoption of VLC has been initially targeting the high end market. Within that sphere, the vision was to build a high speed point-to-point communication system as an alternative backbone to fiber optics, using air, rather than fiber, as the channel. Consistently, lasers were used as Txs, owing this to its inherently confined low beam divergence [9] and its ability of high speed modulation [10]. Therefore, synonymous to outdoor free space optic (FSO) communication, a niche was carved for laser transmissions. In contrast, the introduction of LEDs, more specifically HB-LEDs, that are capable of high speed switching, has seen the laser dominance curbed in the field of short range VLC. Accompanied by the adoption of HB-LEDs for VLC is the realization of a potential landmark transformation in the VLC arena.

Caching on this realization, numerous groups, in the form of government backed bodies, companies and academic institutions have been formed to investigate the potentials, promote and drive to standardize VLC. In 2003, the Visible Light Communication Consortium (VLCC) was formed in Japan [11] Europe formed the HOME Gigabit Access (OMEGA) project aiming at integrating communications from radio, power line cables and light to deliver data at 1Gbps to the home or office end user [12]. On a larger scale, in 2009 the IEEE Visible Light Communication Task Group was formed to create the new IEEE802.15.7 standard for VLC [13]. From the academic environment, VLC has been promoted by Prof. Haas, who is a leading figure from one of the leading institutions in the field, Edinburgh's Institute for Digital Communications. Specifically, in a TED Global talk 2011, he introduced the acronym light fidelity (Li-Fi), which bears similarity to wireless fidelity (Wi-Fi). The popularity of the acronym has been accepted ever since, to the extent that some have identified as the next technology in wireless communication to accommodate enhanced data transmission rates [14][15]. Companies homing on the potential of VLC have emerged, such as pureLiFi and Stins Coman. Similarly, partnerships between industry and academia are also being continually forged, an example is San'an Opto and Shanghai Institute of Aerospace and Electronics [16]. While targeting the mobile handsets, successful demonstration of the seamless integration of VLC into mobile handsets has been promoted in CES 2014 by Oledcomm [17].

The composition of a VLC system, in its most basic from, includes a Tx, channel and a Rx. Currently, there are two common types of Txs, namely lasers and LEDs. With respect to LED Txs, most commercial LEDs produce white light and are usually of the HB-LED type. Similarly, commercial LEDs can be subdivided into two groups, phosphor coated and colored. The choice of the appropriate Tx is grossly driven by the type of application, and if applicable, the lighting requirement. The channel medium is usually air, but support for underwater VLC is also being addressed [18]. However, the air itself, can be divided into two types, an air medium that is either indoor or outdoor. Finally, Rxs too can be subdivided according to the receiver sensor. Typical sensors are either imaging, complementary metal-oxide semiconductor (CMOS) based, or non-imaging PD based. Furthermore, PD based

Rxs can also be subdivided into PD only based or avalanche PD (APD) Rxs. The choice of Rx type is mainly a function of the received signal power and data transmission rates [19]. Whereby CMOS has slow response times, compared to PD based Rxs, however, the former can support parallel data transmission of LEDs and not the latter. On the other hand, high speed VLC is usually handled by PD sensors. In cases where the light levels could be critically low, APD could substitute PD but with the penalty of reduced data transmission rates. Lenses, too, can be attached to Txs and Rxs to enhance a VLC systems performance. It is therefore important to appropriately choose the Tx, Rx and all necessary lenses that best suites the VLC systems application.

It could be argued that VLC, the optical counterpart to radio, may be inferior to radio frequency (RF) communications. However, there are a number of benefits of adopting VLC over RF. For one the visible light is unlicensed, which could support idealistically free communications. It could also aid in offloading particular portions of the RF spectrum that are required by critical applications. This can be easily achieved knowing that the optical frequency band is ten thousand times wider than the RF spectrum [20]. Subsequently, through proper modulations schemes, VLC can technically support extremely fast transmission rates without a complete infrastructure overhaul. In contrast, new RF design implementations are mostly plagued by the latter. From a health aspect, VLC signals in general can be contained and do not pose any adverse health effects, unlike high power RF signals. Consequently, in locations which are sensitive to electromagnetic interference (EMI), such as certain areas within hospitals, clearly a VLC implementation should be favored over RF. Furthermore, caching on the nature of light to travel in a straight path, it is easy to direct the transmitted light towards an intended Rx. This ultimately makes the communication more secure when compared to RF. In relation to indoor secure communication, the ability of RF signals to penetrate walls, can be problematic when eavesdroppers are available. In contrast, within a VLC system, the transmitted light can be easily confined within walled up spaces for indoor communications, hence VLC in this respect is inherently more secure as compared to an RF approach. VLC can also be easily adopted through procurement and implementation of commercial off the shelf (COTS) products. Furthermore, VLC

signals, unlike RF, do not suffer from multipath fading, where light waves from a single source add constructively and destructively.

On the other hand, VLC does suffer from a few drawbacks, especially applicable to the outdoor environment. Compared to the RF footprint, VLC suffers from its relatively small communication coverage area, that can hinder its wide spread use. Moreover, in outdoor applications, whereby the environment is dynamic, signals could be easily blocked by unconstrained factors, such as birds and animals crossing the communication path. The dynamic weather condition, too, could have adverse effect on the quality of VLC signals. This is especially true in circumstances when aerosols in the form of smog and fog are prevalent [21].

One particularly interesting aspect of VLC is its potential to support other forms of communications, such as wireless and powerline communications (PLC). In light of radio communications, rather than seeing VLC as a competitor to radio communications, VLC can be easily integrated into radio devices [22][23]. Through applying VLC alongside radio communications, a new layer of communication channel can be generated, as shown in the EU OMEGA project [12]. Furthermore, VLC could potentially be implemented as a last mile access of data networks, where users lack fiber optic connectivity and internet penetration is sparse [24]. In one specific proposal, a probable scenario for VLC market penetration could see VLC operating alongside a wireless local area network (WLAN) for information transfer between the user and infrastructure [25].

Of particular interest is the integration of VLC and PLC [26]. One of the pioneering works on the integration is shown in [27] and [28] and further developed in [29] and [30] targeting indoor application. The concept of the integrating both communication types is backed by the concept that the PLC channel is a ubiquitous medium capable of transport information between rooms within a building. Upon data delivery into the target room, the data is subsequently handled by the VLC portion to deliver data to and from the end user [31]. An interesting application to this form of integration is proposed in [32], whereby the integration targets a hospital building that is sensitive to EMI. However, there are a number of problems that must be addressed in terms of

system interoperability. Most of the related work on PLC/VLC integration addresses the PLC side. This in part is due to the fact that it is the PLC end that suffers greatest from channel impairments [31]. Further support of this shown in [33], whereby PLC channel equalization has been addressed to alleviate the channel impairments.

2.2 Smart City, ITS and LEDs:

An emerging concept that is clearly shaping the infrastructure of cities of the future is the inclination towards adopting green technologies. The concept of green technologies can be summed into reducing the emission footprint of CO2 and other harmful wastes into the environment, without compromising an individual's activity. To achieve this goal, the harmful emitters must be replaced by their friendlier to the environment counterparts. From this emerged the concept of the smart city, which in part, integrates a smart lighting infrastructure. Smart lighting can be defined as lighting that embodies energy efficient bulbs and sensors, which operate in concert to reduce energy consumption. The lighting infrastructure can inherently include some form of communications, which could be based upon VLC [34]. One such concept of smart city is given by LightNET [35]. Moreover, the concept of smart city is inclusive of traffic flow and its environmental impact from which is tightly bound to the concept of ITS. The importance of efficient transport cannot be overstated as can be evidently observed by recurring yearly events, the likings of the ITS World Congress Conference [36] and the IEEE Executive Committee Meetings [37].

In recent years, great emphasis has been made towards replacing inefficient electrical devices which consumes large power with low power devices. In [38] it is indicated that in the US over 20% of the total electrical power consumption is dedicated to lighting during 2009. In the developing world this figure even greater. Five years later, it has been projected that lighting in the US is estimated to consume a total of 11% from the total consumption, as shown in the 2015 Annual Energy Outlook, published by the US Energy Information Administration [39]. This significant drop in the lighting consumption could be attributed, although not in entirety, to replacing older inefficient light bulbs with significantly more efficient ones. The drop in price

and widespread commercialization of LED light bulbs were two key milestones in the industry and governments adopting LEDs for energy saving purposes.

For mainstream lighting, the key factors to the adoption of solid state lights (SSL), besides the cost and efficiency factors, are the bulb lifespan and color of the output light [38]. Adoption of light bulbs whose chromatic output bears resemblance to sunlight has been aggressively pursued in the LED light bulb manufacturing realm [40]. Furthermore, as multiple LEDs must be mounted onto a single panel to extract practical amounts of light from the panel, it is thus possible to obtain a large swath of colors through mounting an array of multicolor LEDs [41]. By adjusting the output light intensity of the different multicolor LEDs, it becomes possible to accommodate different light settings that is best suited to different times of the day. It has been mentioned within researches on tunable chromatic LED sources that human's well being can be induced through appropriate lighting [42].

The chromatic output from LED bulbs is normally created using two methods. In the case of controllable chromatic output, a light bulb could simultaneously include 3 different LEDs, namely a red, green and blue LED. By increasing the brightness of each LED, different chromatic output can be achieved. On the other hand, a constant white output can be created using a yellow phosphor coated LED. This type of LED is the predominant type used in illumination, whose functioning is as follows. The LED module harbors a blue LED at its core. Once activated, the emitted light from the blue LED excites the yellow phosphor coating of the LED module. The mixing of the yellow and blue lights produces the required white colored light [43].

Realization of the benefits of LEDs and the potential of it replacing older types of light bulbs while producing similar chromatic output, has led to the pioneering work on LED based VLC. It has been shown in [44] and [45] that it is possible to transmit a data signal, in this case an audio signal, using LED based traffic lights over the free air medium. In their proposed setup, the audio signal was used to modulate a square wave carrier signal of 100kHz. The modulating signal deviated the carrier by ±50kHz. At the receiving end, the free space signal was first detected by a PD then amplified and reproduced on a speaker. The system had been successfully

demonstrated for a Tx/Rx separation distance of 20m.

However, unlike the pioneering work shown in [44] and [45], which utilize different colored LEDs for transmission, the current HB-LED usage is directly linked to area illumination, due to their high efficiency. Such bulbs are usually of the phosphor coated type. With focus to VLC, a main disadvantage to high speed data transmission using this type of LED is directly related to the production mechanism of the light itself. It has been shown that the on-off switching speed of light from the LED coating is a magnitude of order slower than the blue LED seated in the core of the LED module [46]. In fact, the applicable modulation BW of the phosphor white LEDs is only a few MHz as shown in [47]. To circumvent this problem, a simple and cost effective solution can be adopted in the form of inserting a blue optical filter at the Rx side. In its first demonstration, blue filtering of the white LED has been shown to be promising, as it achieved 125 Mb/s over a distance of 5m [46] within an indoor environment. Alternatively, in [48] another method to circumvent the problem has been proposed in the form of a simple first order equalizer and a predistortion filter. It has been demonstrated that a white phosphor HB-LED with a BW of 1MHz can easily transmit data of 10 Mb/s with a bit error rate (BER) as low as $1x10^{-10}$ using this method.

In tandem to the concept of smart city is the concept of an ITS as previously indicated. A transportation system that embeds intelligence at its core, is a transportation system that gathers relevant information of moving vehicles or people within it and utilizes that information to its benefit. The information can be used to reduce transfer time, increase productivity, improve road safety and reduce fuel burn. The applications of ITS can range from basic road traffic management for dynamic traffic routing [49], such as controlling traffic light signals by cameras [50], to more advanced applications, for example parking information, guidance to parking spots and parking payment systems [51].

The benefits of ITS has been realized by many governments and societies around the globe. Specifically, in the US, the Department of Transportation (DoT) has created the Intelligent Transportation Systems Joint Program Office dedicated to ITS [52].

Similarly, the Intelligent Transportation Society of America (ITSA) [53] has been created in 1991, whose members includes over 450 members from both public and private sectors. In Europe, ITS Europe (ERTICO) has been founded by members of the EU states and includes approximately 100 members from companies and institutions working on developing the European ITS [54]. Similarly, ITS Australia has been established in 1992 to bring together users, government, academia and businesses to serve the purpose of ITS within the country [55].

To support ITS it is essential to include some form of communications means, either between vehicles, or between the infrastructure and vehicles. Inter-vehicle communications is referred to as V2V communications, while the communications between the vehicle and infrastructure can have two forms depending upon the direction of information transfer. A vehicle that is transmitting its information to the infrastructure is known as a V2I communications. On the other hand, a vehicle on the receiving end of the communication link is known as I2V communications.

Current communications technology applied to ITS are mainly radio based. It includes global positioning system (GPS) satellite signals used in vehicle navigation. Mobile and cellular signals can further assist the GPS signals in navigation through triangulation. Meanwhile, radio frequency identification (RFID) used in vehicle sensing applications and Wi-Fi IEEE 802.11p standard in inter-vehicle communication can be applied for dedicated short range communications (DSRC). Apart from these forms, information of traffic can further be obtained from road side video, acoustic and sensors [56].

The emergence of VLC as a novel and promising technology has also been viewed as another communications potential in ITS. This is especially true with the emergence of HB-LEDs. As previously mentioned, the earliest adoption of VLC had been applied to traffic lights, [44], for I2V. However, with the introduction of white light HB-LEDs into vehicle for forward lighting and tail lighting, VLC for V2V has also been proposed in [57]. To this extent, it was envisaged that adding communication signaling to road illumination into vehicles can easily be adopted. This can simply be achieved by replacing the vehicles lighting elements with LEDs.

An early proposed system of using road illumination for I2V communications is shown for Japan in [6]. The authors conducting the study, had the realization that the dawn of LED street lighting has commenced. With the transfer from high pressure sodium (HPS) to LED luminaires, the seamless adoption for the luminaires to become communication devices has been proposed. Specifically, the authors targeted safety related applications. Given that the study was targeting the Japanese roads, the authors firstly addressed the road illumination requirement of the country, for a pole to pole spacing of 30m. Upon proving the validity of integrating LEDs for adequate street lighting purposes, simulations were conducted on the VLC side. The VLC portion consisted of a Rx placed in a traveling vehicle that was pointed towards the streetlight luminaire, in an I2V VLC setting. The vehicle has been assumed to be traveling at a consistent speed of 60km/hr. Data modulation using on-off keying (OOK) has been further assumed. From the system simulation it has been shown that low data rate communication can be attained all over the road surface. However, in the event of reliable high speed communications at data rates around 1Mbps and BERs less than 1×10^{-6} , it is required that the signal to noise ration (SNR) is at least 13dB. Furthermore, it has been shown that the sensors field of view (FOV), its tilt towards the luminaire and its placing on the road surface, all effect the systems performance. For a vehicle placed in the first lane, an advantageous tilt angle and FOV was observed to be 60^{o} and 20^{o} respectively, for a data rate of 100kbps. For faster data rates of 100Mbps, the advantageous tilt angle of 40^{o} has been observed.

The possibility of utilizing streetlights for area illumination and VLC has opened up new avenues for ITS. However, the complete integration of VLC systems for ITS has to overcome a number hurdles. According to [58], the main hurdles are related to the Tx and Rx separation distance along with the relative position of each Tx, and Rx. Furthermore, it has been pointed out that light from other sources operating within the vicinity of the Tx and Rx, will contribute towards degrading the overall VLC systems performance.

Within the realm of experimental VLC focused towards an ITS solution, the

prevailing concept concentrated upon developing I2V systems. More specifically, as demonstrated by one of the earliest works in the field, it is demonstrated in [59] that data transfer via traffic light LEDs to a vehicle is feasible. In fact, it has been shown that audio signal transmitted via visible light over a distance of 20m using the modulation and detection techniques known as IM and DD.

2.3 The IEEE802.15.7 Standard:

The success of a new communications scheme is directly linked to its adoption by the industry and the adherence of the industry to a specific set of standards. These standards provides devices from different manufacturers the ability to communicate seamlessly. Consequently, to suite the VLC channel, many proposed modulation schemes have been proposed for the outdoor VLC channel. However, the new IEEE802.15.7 standard for VLC, which inspires the industry, has adopted three modulation types into the standard [60-62]. Specifically these modulations are OOK, variable pulse position modulation (VPPM) and color shift keying (CSK). The IEEE802.15.7 standard, moreover, specifies three different physical layers (PHY), PHY I, PHY II and PHY III [63], which are crucially linked to the channel modulation. The PHY I has been specifically designed for the outdoor environment, with low data rates (266.6kbps). In contrast, the PHY II and III are designed for indoor VLC application that can sustain moderate to high data rates, up to 96Mbps.

For the outdoor environment with respect to the PHY I layer, and as dictated by the IEEE802.15.7 standard the modulation should be performed using either OOK or VPPM. In OOK modulation, the light output changes between two different states, according to the transmitted bit. However, specific to VLC, OOK modulation does not require that the lights be completely turned off. The two different levels thus only change the intensity of the output light. On the other hand, VPPM modulation combines two modulation techniques, pulse position modulation (PPM) and pulse width modulation (PWM). The PPM portion is used to eliminate flicker, by making the light intensity vary faster than the human eye can perceive. While the PWM portion is used for dimming purposes.

With the prospect of including VLC into vehicles, one proposed type of modulation referred to as group waveform-coded pulse width position modulation has been proposed in [64]. In essence this modulation is simply VPPM. The data is subdivided into two groups, one group modulates waveforms according to PWM while the second group modulates waveform according to PPM. The signals are next combined and transmitted via the vehicles LED lighting system. This scheme has been shown by the authors to increase data rate transmission while permitting dimming control of the lights.

However, in most implementations of VLC for ITS, it has been observed that OOK is favored over VPPM. For light that has been modulated by OOK a Rx set within the variable luminosity environment senses differences in light intensity. OOK light modulation is a form of IM while its detection is performed using a PD in a DD method. As such, the system operation is referred to as an IM/DD system. This system has been demonstrated in the pioneering work on VLC in [59][61].

Although in some research assessing different modulations for VLC has pointed to the limited transmission rates of OOK, it has been demonstrated in [65] that it is possible to achieve 614Mb/s using a signaling scheme known as duobinary signal modulation. The demonstration has been conducted using an RGB-type white LED in an indoor environment, which is in contrast to the outdoor high speed roadways and utilized type of LEDs considered in the study herein. However, the viability of OOK to deliver high data rates is nonetheless encouraging. Moreover, it is worthwhile mentioning that using duobinary modulation can, in theory, improve the maximum transmission speed three fold compared to on-off keying – non-return to zero (OOK-NRZ) as given in [65].

Research into applying the IEEE802.15.7 standard for ITS based services, has been proposed in [66]. Driven by road safety related applications, the authors in the study aimed at building a VLC prototype using low COTS embedded systems. The prototype system uses a PD Rx, and has shown acceptable performance within a range of 10m. Furthermore, it has been shown that such a system, with the proposed

hardware, can easily integrate the IEEE802.15.7 standard. The adoption of the standard is seen as a potential advantage towards the drive for an internet of things (IoT). However, due to the limited range of LED based VLC systems, the realization of a handover mechanism to radio is seen as a potential possible fix for successful deployment of the system.

Outdoor roadways are a dynamic environment, which holds the possibility that VLC Txs and Rxs could both be mobile. Accordingly, it is typical that the issue of Doppler shift of the transmitted signal is addressed. The effect of Doppler shift has been considered in [67]. The authors consider a system with BPSK modulation utilizing a visible light carrier. In the analysis, no specifics with respect to the optical Doppler effect have been given, with exception to the results drawn from simulations. It has only been mentioned that the within the simulation the effect of a moving vehicle between 1 – 5 km/hr has been included. For the proposed BPSK system, the authors identified that severe degradation on VLC signals occur, even at speeds as low as 5km/hr. However, under the proposed IEEE802.15.7 standard, Doppler shift should be of no concern in ITS applications, due to the lack of a carrier.

Increasing the transmission rate in VLC could potentially be achieved by adding a new dimension to the modulation scheme. This extra dimension could be obtained from the locations of LEDs based upon the fact that LED light sources typically consist of multiple LED elements. Such type of modulation is referred to as spatial modulation (SM) [68]. There are numerous types of SMs, such as spatial shift keying (SSK), generalized SSK (GSSK) and spatial PPM (SPPM). In SSK only a single LED in an LED array is active at any one time instant, while in GSSK multiple LEDs can be active in the array. For SPPM, rather than transmitting using a single LED array, there are a number of optical sources, each capable of transmitting a number of unique patterns. At any instant of time, in SPPM, only a single source transmits one of its unique patterns.

SM could be potentially adopted to both indoor and outdoor VLC, with the latter implementing a CMOS based Rx. However, for indoor VLC, it has been shown that SM is influenced by a number of factors. One main contributing factor is the ratio of

the path gain, or equivalently path loss, between the strongest and all other incoming paths. In the event of a four source optical Tx, with the path gain ratios of 0.5, it has been shown that the required SNR for reliable communications is around 32dB. Subjecting the channel to different conditions has shown that the required SNR can decrease drastically. The influence of different optical path power gain ratios can be viewed in light of a mobile Rx, whereby the path lengths, albeit path gains, changes according to the Rx's location.

The effect of applying different line coding techniques to VLC, has also been considered. Two types line encoding schemes have been applied to the aforementioned proposed I2V VLC system based on OOK modulation. Namely, Manchester and Miller line encoding for which details can be found in [69]. The results reflect on the difficulties of communication links of length 50m and beyond, while clearly drawing attention to the advantage of augmenting the range of I2V link by RF transmission. This work has been extended in [70] to a development prototype.

Line coding to enhance V2V VLC systems performance has also been considered. A line modulation technique known as sub-pulse Manchester modulation has been introduced in [71]. The authors identify that low frequency artificial light from other vehicles and streetlights can possibly interfere with the desired received signal at frequencies below 2kHz. To accomplish better BER performance sub-pulse line encoding is used to introduce sub-pulses into a single high level pulse state within a Manchester signal. This technique eliminates the low frequency content within the modified and transmitted Manchester encoded signal. Furthermore, given the signal has no low frequency content, it then becomes advantageous to use a simple band pass filter (BPF) to extract the signal, while eliminating the interference, namely the low frequency background light.

2.4 Implementations of VLC in V2V and I2V Applications:

Developing VLC systems for V2V or I2V communications, inclusive of ITS

applications or not has been without doubt of great interest. One such system is proposed in [72]. The system employs VLC alongside RF to location based services and navigation for ITS application. In lane specific services, vehicles extract information from the road infrastructure using VLC, due to the lights inherent straight travel path. This can be achieved with high positional accuracy. It then follows that in areas where VLC can be challenging, radio services effectively complement the VLC portion. The authors define the area which the BER will be less than 1×10^{-6} as the coverage area. Through simulation, it has been shown that a VLC system coverage area decreases with increased bit rate. Namely, the coverage area for 1 Mbps, 10Mbps and 100Mbps is 117m, 61m and 15m, respectively. Augmenting VLC with radio coverage, can considerably extend the effective area, as shown for a hybrid configuration transmitting at 100Mbps and an effective area of 1200m.

A more comprehensive system architecture for the integration of VLC into an ITS infrastructure has been proposed in [73]. A traffic light is used as a road side unit (RSU) that broadcast road safety related information. Ultimately, the RSUs was conceived to effectively ease traffic flow and reduce accidents. Through an experimental setup, that included transmitting information at 20kbps between a traffic light and a mobile unit, it has been shown that communication is broad daylight can be achieved. In the experiment, both Tx and Rx units were set at a height of 1.5 with no inclination, using direct sequence spread spectrum (DSSS) for signal modulation. Under this setup a link distance of 40m could be achieved.

In a similar study to [73], the authors in [74] have experimentally demonstrated the ability of transmitting data at 100kbps for road safety applications. It is assumed that for such applications, priority should favor sustainable flow of data over high speed data transfer. Under this reasoning, in the proposed system data modulation was performed using DSSS. The authors show that for sustainable communications, whereby the BER doesn't exceed 1×10^{-6} , a SNR of approximately 8 to 10 dB is required.

Yet in another study targeting the use of RSU in ITS the range limitation of RSUs

using VLC has been addressed and investigated in [75][76]. Conceptually, the study proposes that RSUs, in this case traffic lights, transmits information to vehicle sensors. The received information can then be forwarded to other vehicles via the receiving vehicles taillights. By adopting this proposed method, it then becomes feasible to communicate beyond the service area of the RSU. Targeting applications of road safety, it has been shown experimentally, that communication at BERs of 1×10^{-7} is achievable for a communication link of 18m in length. This distance is a composite distance. The first part of the link is the I2V link and the second part is the V2V part. The achievable ranges for each of the I2V and V2V portions is respectively 15m and 3m.

V2V communication extended to a fleet of vehicles, or a platoon, has been pioneering in [77] and [78]. The investigated system is based upon a the line of sight (LOS) communication link starting from a lead vehicle tail light and captured by the rear vehicle PD. The PD is mounted at an advantageous location on the front portion of the vehicle. The information is then transferred from a vehicles sensor to its taillights where the next vehicle in line receives a copy of the information. The process continues to the last vehicle in the fleet. Such systems have been adopted using RF techniques, however, herein the focus is on substituting the radio signal transmission with visible light. The authors identified the limiting factor of VLC in such a setup. To the authors it is the FOV of the Rx that is the constraining factor, which, by no suprise, is a general problem with all VLC systems. Specific to the case at hand, for a fleet of vehicles, the problem is amplified when conducting sharp turns. Such maneuver could severely effect the link, if not disrupt the communication altogether. To overcome this problem, the authors propose a tracking arm, which will automatically align the rear vehicles sensor to the taillights of the vehicle in front. For correct tracking, positional information from the front vehicle is transmitted to the rear vehicle. The proposed system has been simulated in Simulink [79] for a fleet of four vehicles traveling at a constant speed of 20m/s, with an inter-vehicle distance of 4m. Through this implementation, the authors have shown that it is possible to overcome the FOV limitation for any trajectory, provided that the tracking arm is correctly chosen. However, for further research, the influence of vibrations on the optical received signal and its effect on the receiver must be undertaken.

One particular application of V2I has been proposed in a vehicle theft recovery system [80]. The system operating in UV light is perceived as an alternative to RFID, and is hence dubbed UVID. Based on OOK modulation and the inherent ability of UV systems to communicate in a non-line of sight (NLOS) mode, the system operates by continuously transmitting a vehicles tag number to the road infrastructure. In the proposed system, UV LED transmitters can be placed within the vehicles exterior lighting compartment. Rxs, located along the road, pickup the continuous transmission which can then be directed to the party of interest in case of vehicle theft.

A key aspect of VLC is its inherent positioning accuracy, which could be garnered towards end user location applications. Successful implementation of such systems have been demonstrated with exceptional accuracy in the indoor environment [81]. Applications, such as object identification and indoor tracking [82], could be the driving force behind the commercialization of these systems. In the automotive industry too there have been proposed systems for a driver awareness system, that gathers information from a vehicles surrounding [83], subsequently serving the vehicle's driver. The position accuracy means that vehicles can use the information in application whereby GPS position fixes must be augmented by other techniques.

Promoting V2V VLC to the masses requires simple and versatile systems that can be easily integrated into vehicles. This concept has been the foundation of demonstrating a prototype system composed from a development board, based on an ARM processor at its core, for V2V VLC road safety applications [84]. Unlike other systems which attempt to combine the vehicles headlamps and taillights into the communication process, this system includes its own COTS LED HB lamp. By placing different lens types in front of the LED Tx, it is possible to change the beam divergence angle, from 120^{o} (no lens) to 18^{o} (with lens). At the receiving end, a PD sensor is used, which also can include an optional lens. Using the default bit rate supplied by the boards manufacturer, it has been shown experimentally, that it is possible to communicate in links of up to 31m error free, in a controlled test lab environment. However, realistically the issue of glare sourced by the mounted HB-

LED lamp could adversely effect drivers and become in itself a hazard.

An alternative method of promoting VLC for wireless communications has been shown through Wi-Fi signaling. In perspective, popularity of the numerous Wi-Fi protocols, has led to the investigation of applying the Wi-Fi signal format to transmissions of VLC. This mode of signal transmission has been shown in one such study [68]. The authors in the study has considered using the vehicles exterior lighting to transfer data within a femtocell light footprint, that has been generated by the vehicles lighting.

2.5 LED Street Illumination:

To study an I2V VLC system with streetlights as Txs, it is important to obtain a reasonable model of the transmitted visible light radiation. A unique study with respect to modeling the illumination of LED based street lights, the authors in [5] have produced an analytical description for the radiated pattern. The proposed model, can easily be inclusive of the effect of varying pole heights, LED positions and tilt angles on the intensity profile. By describing the street lighting through theoretical means, it becomes possible to leverage a fundamental understanding on the influence of different streetlight parameters on I2V VLC.

VLC channel modeling is greatly influenced by the light intensity distribution that is radiated from the LED surface. In most HB-LED bulbs, the light emitters are seldom exposed directly to the illuminated medium, rather they are encapsulated by a lens. The lens acts to direct and focus the light onto the intended area of illumination, suitable to the application. Therefore, lighting for spot illumination requires different lens types as compared to area illumination.

Accordingly, a direct link to this case study, is the effect of the lens on the output light distribution over an illuminated road surface. It is known that the light intensity of streetlights spreads the light over the road surface in a rectangular fashion. To reduce the effect of light wastage, the light must be primarily confined to the road

surface. Furthermore, the streetlight illumination design must consider the driver's safety. With respect to this issue, the light should not produce any form of glare [85]. Hence, for the development of such illumination type, designers have generally resorted to free-form optics [86]. However, due to the complexity surrounding free-form optics, there have been great emphasis on the use of simulation software for streetlight illumination design. One popular software is LightTools [87]. Such software types have been effectively applied for assessing of I2V VLC systems, as shown in [88].

In most studies conducted on channel modeling for ITS VLC, LEDs are considered as Lambertian emitters. A Lambertian emitter is one whose intensity distribution is a cosine function with respect to the viewing angle [89]. As this is inconsistent with practical applications then according to the definition, LEDs should be considered as imperfect Lambertian rather than Lambertian emitters. However, it could be argued that approximating the LED by a Lambertian emitter holds well, especially with respect to V2V related VLC [7].

In contrast, I2V illumination can be viewed differently. In the case of traffic light emitters, the argument that the LEDs are Lambertian emitters, could still hold [90]. However, with respect to road illumination that should exhibit uniformity on the road surface, the model is inaccurate due to the lens impact on the light distribution [91]. The problem of lens design for applications requiring uniform surface illumination has been highly pursued in multiple investigations, such as in [91]-[94]. Such lenses are known as free-form lenses, and are often implemented in streetlight LED modules as secondary lenses.

2.6 VLC Receivers:

In VLC systems the choice of either two primary types of Rxs, either CMOS or PD, should be made as to fulfill the applications requirement. For Rxs utilizing imaging sensors, or equivalently CMOS devices, in the application of VLC to ITS, a good survey can be found in [95]. A CMOS device is essentially an array of PD that can

distinguish different intensity levels within the PD array. One key parameter of CMOS devices, over single PD Rxs, is its ability to distinguish between different light sources. By utilizing image processing techniques, it is possible to estimate position and distinguish between still and moving objects. This is in contrast to the single PD device.

Single PD sensors can become saturated when operated under direct sunlight, and will therefore, require adequate means to reduce the background illumination. In comparison, using an imaging sensor with multiple PD elements, full image saturation is almost unlikely. The PD saturation problem could be partially solved by blocking off-axis direct light through narrowing the FOV of the PD Rx. However, this can be an impractical solution in the integration of VLC into mobile handset devices.

A prominent advantage of using single PD sensors, is its ability to quickly detect different illumination levels giving this sensors type its low response time, when compared to CMOS devices. In contrast, CMOS devices are commercially tailored to suite the human response. With a common frame rate of 60 frames per second (fps) in most commercial devices, it is clear that CMOS is unsuitable for high speed signal reception as that required in time critical ITS applications. The application of CMOS is further constrained in an environment with high speed moving vehicles. To overcome this limitation, it becomes necessary to implement high frame rate CMOS devices in automotive applications. Using high frame rate cameras for VLC ITS has been demonstrated in [96].

An alternative solution to the expensive adoption of commercial high frame rate camera is to build a suitable application specific CMOS sensor for VLC ITS application. One such CMOS device tailored for V2V communication has been demonstrated in [97] and [98]. The authors name this type of CMOS sensor an optical communications image (OCI) sensor. Within it are two types of picture elements. It harbors communication pixels, tailored to receive high intensity light only, along with the usual imaging pixels. The authors main motivation of developing a specific sensor for V2V application, is that V2V requires quick and

accurate LED detection along with high speed data reception. The detector design interleaves two 321×480 pixel arrays of communication and imaging pixels, in the specific hybrid communication and imaging CMOS device. Each communication pixel can achieve 20Mbps optical signal reception. To validate their design, an experimental system setup consisting of two vehicles, a forward vehicle (FV) and a back vehicle (BV), were made to communicate. Video of varying average frame rates are captured from a 320×640 pixel camera mounted on the FV dashboard. This video is suitably converted for transmission by a pair of 10×10 LED arrays mounted at the rear of the FV. Subsequently, a camera mounted on the dashboard of the BV, which includes the OCI device, captures the information transmitted by the rear mounted FV LED arrays. The data received by the BV is then transferred to a PC which can process and compares the received data to the FV transmitted data. The frame rate changed according to the time of day, with 15fps during daylight hours and 10fps at night. The experiment was subdivided into two components. First, it was demonstrated that the OCI device can adapt to varying day and night time conditions. For this part, the evaluation metric was the number of packet arrival rate (PAR). Secondly, the system was evaluated based upon the BER of the original and reconstructed images. It has been shown that for the first part, the OCI device operated with a PAR of 91%. For the second part, it has been show that the system is capable attaining BERs of 1.14×10^{-4} and 1.94×10^{-6} for an uncoded and coded system respectively. For the coded system, bits were coded using an encoder that provided a 1-bit error correction capability.

Following in suite of I2V study cases, in [96] the investigation of obtaining the channel state information (CSI) of a traffic light Tx through high speed camera Rx. The CSI is then handled by the error code block to reduce the systems errors. In their setup, the Tx consists of a 16×16 LED array that operates at a rate of 500 Hz. The Rx is a high speed camera with a frame rate of 1000 fps, and a resolution of 256×256 pixels. The system was evaluated in the distance range of 20m to 70m. For the proposed system, it is envisaged that data can be segmented into three ranges, long, medium and short. Of highest priority is the long range data, whereby it the application is specific to safety applications. The other two ranges could further add different types of information that is not safety related. In the design, the CSI is

obtained through computing the signal to interference ratio (SIR) of the 2D LED array received image. By applying this technique, it has been shown that the system can improve on the BER.

There have been numerous studies and demonstrations of I2V VLC, in which either imaging or PD have been implemented. In one particular study [99], it had been further suggested that both sensors could be fused together to garner the benefits of each sensor to the others advantage. Tracking of the luminaire source, in this case a traffic light, could be performed using the wide FOV of the imaging sensor. The PD, armed with its relatively narrower FOV could then be pointed to the lights using the information from the imaging sensor. Using this method, the narrower FOV of the PD reduces the ambient noise, whilst permitting connectivity at 48m and data rates of 10Mbps.

The effect background light source on ITS VLC has been considered in [100], through the analysis of the systems SNR in diurnal metropolitan road conditions. In this particular study, two scenarios have been simulated, a V2I scenario and a V2V scenario. However the explanation provided by the authors suggests that the first scenario in reality is V2I. With this understanding, it is clear that signal transmission in both scenarios, is performed using the vehicles headlamps. However, in obtaining the light intensity distribution, the authors model two light sources, a car headlamp and a street lamp. The authors use a simulation software, namely Dialux [101], to obtain the light intensity distribution. The study simply concluded the effects of daylight on VLC. As per the authors, simulating a V2I VLC system has proven that daytime communications is feasible, however, for V2V it is important to effectively mitigate the noise for reliable communications. This conclusion has been drawn without the authors presenting any results.

2.7 System Analysis and Channel Studies:

Unlike the most study cases of ITS VLC that are based on experiments, in [90] pioneering work into the study of applying LED traffic lights to ITS is undertaken

through analysis. The system is based on two types of modulation schemes. Modulation composed from OOK and single carrier binary phase shift keying (SC-BPSK) for the transmission of visible light from traffic lights to vehicles. In the analysis, the authors show the amount of receivable information, in bits, as a function of vehicle speed and the applicable coverage area of the VLC signal. In the analysis, the communication range of up to 75m while simultaneously vehicle speeds of 70km/hr had been investigated. The authors indicate the importance of the SNR in the BER of both investigated modulation types. However no analytical expressions quantifying the importance of the SNR are produced. On the other hand, the simulations have shown that by implementing SC-BPSK, it is possible to attain BER 1×10^{-6} at a maximum data rate of 3.56Mbps within the 75m range. The results were drawn with no reference to the effect of possible carrier Doppler shift that could be associated with SC-BPSK modulation. The authors did mention that the communication link will be affected by the vehicles position on the road surface, due to the angle between the Rx PD and Tx traffic light. However, the analysis falls short of giving an insight into the simulation results.

With respect to the VLC channel modeling geared towards ITS, it is first required to define the possible different channel types encountered in a VLC implementation. The DC channel response is a widely adopted channel model in VLC and has been studied extensively for the indoor environment [102][103]. In particular, VLC channels can been subdivided into three types, LOS, diffuse and NLOS. The LOS channel is a channel whereby both Tx and Rx are directed towards each other with no obstacles breaking the link. On the other hand, in the diffuse channel, only reflections off walls of the transmission are received. The third channel type, is viewed as the combination of both LOS and diffuse and can be considered as the most realistic channel model.

The VLC channel can be characterized in a manner that is similar to the mobile channel, in terms of the RMS channel delay spread [104] and SIR [2]. It is known that the RMS delay spread is an informative metric on the achievable data rate. This metric characterizes the channels time dispersion property that will effect the signal. The SIR metric is a measure on the ratio of the received power of the desired signal

component to the undesired interfering signal component. The interference could be of two types. The first type is attributed to delayed copies of a signal arriving outside the allocated symbol duration. While the second type is attributed to different signals emitted by different sources. In an indoor environment, in which broadcasting of signals is common, the first type of SIR arises. In an outdoor environment, where two adjacent light sources transmit different data into overlapping zones, the second type of SIR will be observed. A study based upon these two metrics had been conducted for mid and large sized indoor rooms in [105]. It has been shown that the indoor channel RMS delay spread is in the order of 1.08ns and 3.35ns for both types of room sizes, respectively. These values have been obtained as maximum values, where the Rx had been located along the rooms edges.

The outdoor VLC channel is a dynamic channel that can induce a large number of impairments to the systems performance, in particular affecting the received signal. In relation to terrestrial FSO channels, the impairments includes aerosol scattering, atmospheric turbulence and building sway [106]. Dense fog, one of the most degenerating forms of aerosol to VLC, can restrict communications to a mere few hundred meters by introducing high attenuation levels into the channel [107]. In clear weather, variations in the airs refractive index introduces atmospheric turbulence. Under such condition, VLC systems performance is adversely impacted when the length of the communication links exceeds 1km [9]. Finally, building sway could be the result of thermal expansion, wind loading or weak Earth tremors as listed in [108].

By inspecting the impairments of terrestrial FSO channels and comparing it to the VLC channel within this study, it becomes evident that the influence of aerosols and atmospheric turbulence on the channel can both be discarded. This returns to the fact that the studied channel is clear and constrained to lengths much shorter than 100 meters. According to the studies related to VLC for road vehicles, it is shown in [109] that the received signal is greatly influenced by the relative positions of the Tx and Rx [58]. However, the number of studies that have contributed towards understanding this effect in an I2V VLC setup has been left largely unexplored. The exception to this statement is the work conducted in [6].

A study on the V2V VLC channel with respect to link duration has been conducted in [109], for a CMOS type Rx. Based upon experimental data captured by a video recorder, it has been shown that the inter-vehicle link duration, could be modeled by a generalized Pareto distribution. Furthermore, the link duration has been observed to be in the order of a few seconds. To arrive to these results the authors performed post processing on 30hrs of gathered video with respect to the duration that taillights remaining in segments of video. From the results, the authors indicate that conditional distributions of the link could also be obtained, through analyzing the different conditions of the vehicles taillight. Such conditions would be added value to understanding the circumstances when an active link can be terminated.

Channel modeling for V2V is not confined to cars as had been shown in [109]. The channel study is conducted on the taillight of scooters that include COTS LED lights. The taillight is used as a Tx with 4-PPM modulation, data transmission rate of 20kbps and a half power angle of 20^{o} . The authors used a Lambertian light intensity model, which was applied to the channel DC gain. The DC channel gain was computed around the scooters taillights at to a maximum angle and distance of 35^{o} and 10m. Subsequently, the systems SNR, which is a function of the channel DC gain, could be substituted into BER formula for PPM. Comparison of the experimental data has shown that there is good correlation between the developed analysis and gathered data. One particular aspect that had been demonstrated and greatly impacts the systems performance is the FOV. It has been shown that the received power drops significantly if the FOV angle is 20^{o} or greater.

Most studies conducted for V2V communications have been conducted based upon simulation tools and for specific road scenarios. In [7], the authors aimed at producing analytical results that could be used to predict the systems performance under different road scenarios. The analyzed system has been based upon a BV headlight transmission and a FV rear reception PD system. By analyzing the LOS and road surface reflected NLOS components, an analytical expression of the received power, Rx noise and SNR were all derived. Furthermore, it has been shown through simulation of a typical VLC system configuration within a vehicle, that the placement height of the PD sensor effects the BER performance. Sensors that are

mounted closer to the ground, specifically at 0.2m, show lower BER than their counterparts at higher levels, such as at 0.6m, at greater distances. This observation confirms that the intensity of the forward lights of vehicles are directed towards a particular spot on the ground ahead of the vehicle. A Rx moving towards that point will observe lower BERs. To this extent, the study has shown that it is possible to establish VLC at a separation distance of 20m between vehicles for data rates of 2Mbps with the PD sensor placed at 0.2-0.4m above the ground.

In [110] the authors looked into characterizing the channel fading of V2V VLC. The main fading parameters obtained from the study are the channel path loss and channel coherence time. However, prior to obtaining the two fading parameters, three key parameters associated with V2V channel fading for moving vehicles were identified. The three parameters are the separation distance, irradiance angle and incidence angle of the incoming light signal. The fading parameters were obtained through experimental means. In the setup the Tx is the taillight of the FV and the Rx is a camera located in the BV. Using video recordings and resorting to computer vision, accurate estimates of the positions all taillights in the recording images could be obtained relative to the cameras position. Subsequently, knowing that the angles of irradiance and incidence are both functions of the Tx location relative to the Rx, these angles could be easily obtained from the images. Furthermore, the channel DC component and hence received power, could then be computed from known formulas. The results have shown that the 50% and 90% coherence times of the VLC channel are in the hundreds and tens of milliseconds respectively, which is a magnitude larger than the RF V2V channel. Accordingly, the VLC V2V channel perceives much slower time variations compared to the RF V2V case.

Data transmission rates in VLC systems could also be influenced by the geometric configuration of the Tx LEDs. It is known that almost all types of LED bulbs are composed from a plural number of LEDs. To study this effect, in [3], the relation due to plural signal transmission in both LOS and NLOS channels had been performed. The study sheds light on the optical path difference in an indoor environment. The system employing a typical type of white LED, has been shown to produce multiple optical paths in the indoor scene due to the composite received signal from LOS and

reflected light. The difference in optical paths can be captured in the resulting shape of the channel impulse response (CIR). The multiple paths within the CIR will eventually effect the amount of ISI introduced in high speed VLC transmission, through the RMS time delay of the channel. In their investigation, two systems were simulated, a OOK-NRZ and an orthogonal frequency division multiplexing (OFDM) systems. By introducing a guard interval into OFDM symbols, it has been shown that the BER results of OFDM are lower than OOK-NRZ. However, the authors did not clearly mention the data rate nor the RMS delay spread of the investigated channel.

Similarly, the effect of the lighting source geometry on the channel response with respect to varying the inter-LED spacing has been investigated for the indoor environment in [4]. In this particular study, six configurations have been assessed, from 4cm to 24cm LED spacings. It has been shown through simulation, that the RMS delay spread increases with LED spacing.

To attain an accurate VLC channel model, the effect of all LEDs contributing towards the channel response, must be individually considered, as each LED is a transmission device. In the indoor environment, there can be a large number of LEDs within a single luminaire. Such luminaire configuration can conversely lead to high computation cost for evaluating the channel response. To reduce the computational complexity, channel simplification, in the form of treating the luminaire as a single LED, has been proposed. However, the effect of this channel model simplification for indoor VLC can severely undermine the accuracy of the channel model, as shown in [111] and [112]. The deviation of the channel parameters from their exact value is most notable with respect to the channel RMS delay spread.

Unlike in [61] that looked into the simple demonstration, in [58] roadside VLC was investigated taking into consideration the potential problems of an I2V scenario. The I2V system under consideration was a traffic light Tx and a moving vehicle Rx. The problems associated with VLC in this setup could be enumerated as, large separation distance and variable position between Tx and Rx. Furthermore, the reception has to overcome the surrounding optical noise for proper signal reception. To solve the distance related problem, a hybrid system that includes a camera only and a

combined camera and lens setup, has been proposed. For long distance reception, which requires a small FOV, the Rx switches to the camera and lens configuration. In the short range, which requires a large FOV, utilizes the camera only as the Rx. Furthermore, the authors propose the use of galvanometer mirrors that can track the traffic light signals. Although the proposed system has been suggested for communications within the Mbps range and around 100m separation distance, however, experiments have shown that using the proposed setup it is not feasible.

A follow on to the study of an I2V system using an LED array Tx and high frame rate camera, mounted within a vehicle as the Rx, is shown in [113-116]. In [116], the camera operates at 250fps whereas in [113] and [114] it operates at 1000fps. The authors, in [113], clearly state the problems associated with this system in terms of the loss of received image components with high spatial frequency. This is primarily a situation when vehicles are far from the Tx, and the system looses focus. To alleviate the problem, the authors propose a hierarchical coding scheme, whereby information is sorted into high and low priorities. In the low priority transmission, data is generated using high spatial frequency content. Meanwhile, the high priority transmission generates data with low spatial frequency content. Accordingly, the high priority can be received at much farther distances compared to the low priority data. The system was tested for a vehicle traveling towards the Tx at a speed of 30km/hr. The reception distance range of 80m to 25m has been investigated for OOK data modulation of a 16×16 LED array. The results indicated that error free communications in the envelope of operation is feasible. This type of system, as suggested in [116], is theoretically capable of delivering data at 1Mbps.

In a simulation based study that follows on [100], in [88] the author show two different road scenarios, a metropolitan crossroad and a metropolitan stretch of road. The metropolitan cross road is simulated as a scene in which a four way traffic light cross road includes vehicles in opposite directions. In the case of the metropolitan stretch of road, the simulation includes high rise buildings on either side of the road. The received impulse responses from the different scenarios is obtained via Dialux simulation. From their observations, the authors identify that the V2V channel have relatively smaller RMS delay spreads as compared to the V2I channel. In terms of

channel model, the metropolitan stretch of road has been identified to be viewed as a multiple LOS and NLOS channels. This scenario shows that the channel possess a relatively large delay compared to the cross road scenario.

In a continuation on the channel study presented in [100], the authors in [117] obtain the channel delay profile of both metropolitan crossroad and road stretch scenarios for both V2V and V2I cases. In all cases, except for the crossroad V2I scenario, it has been shown that the channel delay can be adequately modeled using either a 3 or 4 tap delay line. To obtain these results, the simulation software, LightTools [87] and CATIA V5 [118] have been applied to the four particular metropolitan scenarios.

To demonstrate the ability of V2V communication during daylight hours, in [119] a setup using the vehicles LED headlamps for transmission in the BV and a rear mounted PD in the FV has been demonstrated. In this successful demonstration the VLC signal was modulated using 4-PPM. With this specific setup, it has been shown that communication up to 20m at a data rate of 10kbps is achievable, even in daylight.

The possibility in which LEDs are used to relay information to drivers with respect to range finding has also been considered. In [120], the authors proposed a system setup that uses LED Tx and a camera based monitoring for the application. An LED is used to illuminate a particular zone around the vehicle. The light passes through a series of slits, transforming it into a diffuse source. Using this method, it is assumed that the radiated light will have a normal distribution over the illuminated surface. Reflections of the radiated light from surfaces within the zone induces shifts to the presumed normal illumination density. To obtain the range, the author have suggested using an expectation maximization algorithm to the shifted received light distribution. The proposed method has returned positive results in the application whereby the detected objects are simple shapes. However, for commercial application further research has to be undertaken.

In a variation to the studied VLC channels related to the field of ITS, in [121] and [122] the interior of a sports utility vehicle, (SUV), is physically modeled to obtain

the physical channel. The envisioned transmission system is based upon an IR LED, while signal reception points consisted of 3000 different locations within the SUV. The results reflects upon the received power, BW and RMS delay spread of the particular channel. Using MATLAB [123] ray-tracing software package and by simulating the SUV interior, the results indicate that the received power is $49\mu W$, for a BW greater than 300MHz and negligible RMS delay. These results were obtained for the rear passengers side of the SUV. In contrast, around the driver and front passenger headrest areas, support of 48MHz BW and received signal power of $4.9\mu W$ has been observed.

2.8 Noise in the VLC Environment:

Ambient light in VLC systems operating in either indoor or outdoor environments, is a source of noise. Consequently, there have been a number of studies that have targeted the issues of decreasing the effect of ambient light in VLC systems, such as in [124] and [125]. An interesting study of ambient light has bee conducted in [124], in which the authors study the effect of fluorescent and AC-powered LED lighting on indoor VLC. The study shows that both light sources can impede the transmission of indoor OFDM VLC systems even when the LOS Tx/Rx distance is just over 1m. However, by implementing simple equalization techniques, it is possible to increase the data rates from 1Mbps up to 12Mbps. In contrast, the authors in [125], deemed that VLC still lacks maturity to be deployed into the market. Furthermore, it is claimed that VLC is suitable to be used only in closed and confined spaces. Those claims can be viewed as overly pessimistic and requires more support. To investigate such claims research into outdoor VLC in sunlight had been conducted.

Outdoor VLC deployment for ITS application a Rx must be capable of adapting to different sky conditions. In most cases of ITS, VLC will suffer from the ambient daylight. A system that circumvents this problem through selective combining and background light rejection has been shown in [126]. The system is composed from two sets of Rxs with narrowband optical filters, hemispherical lenses and low noise trans-impedance pre-amplifiers. Light from a traffic light, which is used as a Tx,

enters into either Rx set, depending on the active color of the light. Selective combining is then used to choose the signal with the greatest SNR from both sets of Rxs, while rejecting the other. Simulation results have pointed that in such a system, the Rx is susceptible to background noise variation of around 20 dB between the early morning and afternoon. A further 3.5 dB of variation can also occur due to the clear sky variability. Simulation of the systems performance revealed that this type of Rx configuration can extend the VLC operations range.

Furthermore, the effect of sunlight on a PD has been studied through experimentation in [127] for V2V communication that implements a controller area network (CAN). It is known that under direct sunlight or strong ambient light, it is possible that a PD receiver becomes driven into saturation. A saturated PD cannot receive VLC signals and is therefore useless. Therefore, the motivation of improving V2V communication by using the vehicles head and tail LED lamps is demonstrated under such conditions. The system performance is augmented through implementing suitable optical arrangements and by including appropriate filtering. Through experimentation, the authors demonstrate that significant improvement can be made by placing a light shield in front of the Rx. The effective shielding reflects upon the fact that a PD in V2V VLC is usually placed vertically, facing the Tx lights. In contrast, the sun can be considered as a point source that is on a horizontal plane high above the Rx. Furthermore, it has been shown that by placing a red optical filter in front of the Rx improves only slightly the reception. Finally, it was demonstrated that by placing the Tx and Rx 0.2m above the ground and including a lens module to the Tx it is possible to obtain a BER as low as 1×10^{-9} over a link separation distance of 20m, for both rear and forward light Txs. In comparison, a system that lacks the lens shows extremely poor performance. The study, however, had been conducted in a controlled stationary environment, that lacks the movement aspect of practical V2V communications. Furthermore, placing a lens front of the Tx within either headlamps or tail lights, will alter the focal point of the light beam, hence effecting the quality of illumination. Although the effect had been observed, however, no explicit details on the lens setup has been provided by the authors.

A study in [128] has targeted the link performance of the traffic light to vehicle I2V

through experimentation. COTS LEDs have been chosen for the transmitters, while including for the noise the compound effect of solar radiation, using the SPCTRAL2 model [129], and artificial light sources. One of the constraining factors for high speed transmission using COTS LEDs is due to the limited 3-5MHz modulation BW of phosphor coated white HB-LEDs. From the experiments, it has been shown that transmission of 1Mbps at a range of 75m is achievable for a BER of 1×10^{-2} .

2.9 Clear Night Sky Light Perturbations over Roadways:

As aforementioned the effect of relative motion of the Tx and Rx influences the performance of VLC systems. Targeting outdoor VLC, one cause of motion arises from the perturbations induced by wind. In most studies dedicated to outdoor VLC, specifically to point-to-point laser FSO communications, the effect of wind has been either totally disregarded [130] or lumped into the effect of turbulence [131][132]. Accordingly, from an FSO perspective implementing laser Txs, the wind factor is usually accounted within the study of scintillation and beam wander [133]. In a FSO link, air pockets, which are caused by wind and varying temperature gradients within the FSO path, are the main causes of scintillation and beam wander. The air pockets have rapidly varying optical indices that cause unpredictable atmospheric turbulence. The observed received signal will tend to move due to this varying air indices as well as fluctuate in its brightness. The effect of pointing errors on the BER of PPM has been analyzed in [134] for a system that includes multiple hops. To understand the turbulent channel, it has been considered that in the case of weak turbulence, the channel characteristic can be adequately modeled by a log-normal channel. In [135] the study of average channel capacity assuming a log-normal channel probability density function (PDF) of the normalized irradiance has been given for a system implementing OOK. Alternatively, in [136], a channel model with a gamma-gamma distribution which presumably accounts for all turbulence conditions had been used in the study of FSO system capacity. Moreover, in [137] the authors have looked at the correlations of particular wind parameters and the refractive index of the air to obtain better measures on the effect of wind on the channel. The effect of such turbulence on a VLC system, can be embodied in terms of the instantaneous

fluctuations in the luminous irradiance, which directly affects the systems SNR [107]. From the study, it had been ascertained that turbulence will directly induce uncertainties into the received SNR.

In a broader perspective, pointing errors could also occur due to the mechanical misalignment of both Tx and Rx [130]. Then alternative to air turbulence, in one particular study on optical tracking [138], it had been indicated that the effect of Tx and Rx misalignment, primarily a result of building sway, could decrease the reliability of FSO communication systems. In the most severe of cases, misalignment errors could culminate to a VLC system grinding into a complete halt. Such errors due to building sway, has been further supported by the research in [139]. The atmospheric cause of building sway is wind, as had been identified in [130], and results in pointing errors. It has been suggested in [140] that pointing errors can be adequately modeled by a Gaussian distribution on each of the planar x and y axes perpendicular to the traveling light. In each axis, the two Gaussian distributions, as shown in the study, are independent from one another.

A number of papers such as [141][142], has reported that in long terrestrial FSO communications, atmospheric turbulence plays a major role with respect to the systems performance. In contrast, for short links of the type concerned within this study, turbulence can be altogether ruled out. In spite that turbulence can be ignored for the links herein, misalignment caused by relative motion of the Tx and Rx must be considered.

In the study conducted in [143] the displacements of a slender structure, namely a streetlight pole, is evaluated at times of wind with and without gust. Quantifying the amount of displacement in the pole structure has been undertaken using the finite element method (FEM). Accordingly, three standards could be compared, namely the American Association of State Highway and Transportation Officials (AASHTO) CODE 2001, UBC 97 and IS857 Part 3 1997. The study looked into poles with single and double luminaires. From the results, it has been observed that at times of wind with gust, the maximum displacement is 143.00mm and 119.7mm for the single and double luminaire respectively. While at times with wind only, the maximum

displacement of 121.6mm and 80.1mm has been noted for single and double luminaire respectively. For all results it has been assumed that the wind speed is 10m/s, pole height is 19m and the boom length of the streetlight pole is 1.8m.

In [144] the modes of vibration of a streetlight pole influenced by external forces, have been clearly identified. There are typically two modes of vibrations, a first and second mode. The first mode is also referred to as sway. In this mode the vibration occurs at an approximate frequency of 1Hz. This mode of vibration is observed at wind speeds of about 1 to 7 mph. The center of the deflection is observed to be located around the poles center. In this case, the amount of vibration is large. The case of the second mode vibration, which is also known as vortex shedding, will occur at wind speeds of approximately 8 to 20 mph. This mode is the result of the synchronization of the poles natural vibration frequency and the wind frequency [145]. The resulting oscillations lies between 3 and 8 Hz. As compared to the first mode, the resulting deflection of the luminaire is relatively smaller.

On the other hand, a traveling vehicle along a streets lane can also experience perturbations that result in the vehicles deviation away from the lanes center line. These perturbations can be due to the imperfectly flat road surface, tires and road interaction, motion of the vehicles suspension and driver's constantly changing inputs. These small scale deviations from the ideal center of path produces variations in the separation distance between a vehicles sensor and LED luminaire.

2.10 The Incomplete Picture:

To sum up on the research conducted on VLC in the field of ITS, to the best of the author's knowledge, it is clear that the field at large is still at its infancy. It is, therefore, a natural effect that studies related to the VLC channel devoted to ITS applications remains largely unexplored. In support of this, it is clearly indicated in [110] that unlike the extensive work done on modeling the V2V RF channel, the V2V VLC channel has attracted little attention. This same argument can be extended to modeling of both the I2V and V2I VLC channels. As a consequence and for the sake

of studying VLC channels devoted to high speed roadways, an appropriate VLC system setup, forming the basis of this study, is given in chapter 4. Each of the various systems components are clearly shown and their functions and method of integration is detailed. The design clearly indicates an opportunity awaiting VLC for ITS, and is therefore considered as a prelude to the channel study.

Chapter 3

System Design

3.1 Overview:

The proposed system within this study is one that transmits road specific information to moving vehicles along high speed roadways. This I2V mode of communication is analogous to the downlink portion of a satellite or mobile communication systems. One form of transmission suitable for this I2V system configuration, is to employ light as the viable mode of transport, with the air as the communication medium. This has been made possible by introducing LED type luminaires to the streetlight infrastructure. Within the current chapter, a description of such a system, on the macroscopic scale, will be given. The system will be described for only a section of a highway.

High data rate signals are exchanged between highways and a telecommunications infrastructure at particular points along the highway. These points, or preferably nodes, could comprise the medium voltage to low voltage (MV/LV) transformers that are located at approximately constant intervals along the highway stretch. The data at these nodes could be received from the telecommunications infrastructure via RF waves, fibre-optics or by any other means. The signals received at the nodes are next appropriately converted to be transported over the low voltage (LV) power lines that connect all streetlight poles, using PLC techniques. The signals modulates the AC voltage and is delivered to the street lighting. A modulation scheme that has been adopted for VLC using LEDs is known as OOK. In OOK the light intensity is varied in accordance to the information signal. This modulated light is next transmitted through the air towards the road surface.

Concerns regarding varying light intensities, with respect to highway safety, must be addressed. Care must be taken such that a minimum light intensity, specified by road

regulations, should always be maintained. Any modulation, therefore, should occur above a prescribed minimum light level. Furthermore, the modulation should occur at a rate that is imperceptible to the human eye. The unnoticeable light modulation, under this constraint, must be flicker free, for all concerns related to roadway safety standards.

The road highways, in this scenario, will not be solely considered as a medium of transporting people and physical goods, but rather is also transformed into a complementary high speed data transmission pathway. Road operators could also view this as an opportunity to embed a high speed network that is independent of the other services. Under this view, radio airwaves occupied by road operators, could be spared for other use. Furthermore, as time critical and life saving information are the highest priorities envisaged to be transported along the highway, the combination of PLC and VLC could provide a relatively secure mode of information transport.

The transmission component of the downlink side of the proposed highway VLC system is clearly visible in figure 3.1 below.

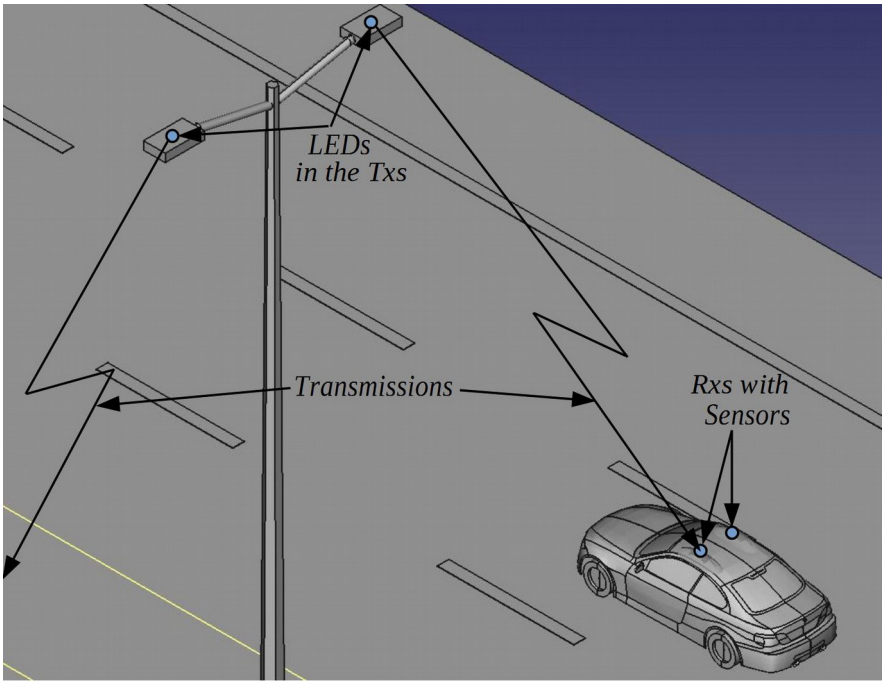

Figure 3.1. Downlink transmission end of the highway VLC system.

In the figure, a light source on either side of a streetlight pole is shown. The light source emits light that is a combination of an information bearing signal and the illumination lighting. Each lighting element transmits signals towards the road surface it is intended to illuminate only. A moving vehicle, with sensors located at its highest unobstructed vantage point, captures both the signal and the illumination light along its path. The information bearing signal is then extracted from the ambient lighting for further processing. As shown in the figure, vehicles can be equipped with multiple receivers for signal reception.

3.2 Power Connectivity of Streetlight Poles:

The power connection of the streetlight poles along a highway is shown in figure 3.2. In the figure, a highway section of streetlights are shown. The power to the highway section is obtained from a three phase medium voltage (MV) transmission line. The three phases are down converted using an appropriate MV/LV transformer, into its LV counterpart. In addition to the phases lines, both ground and neutral cables are available on the LV end. Light poles along the highway are connected successively to each of the three LV phase lines. Furthermore, the ground and neutral lines are connected directly to all poles. Under this configuration the load is balanced between the three LV lines. Finally, although a switch mechanism, that controls the On/Off light state, is essential, however it has been deliberately omitted, as it is not critical to this study.

At the copper end of the communications system which is proposed to be designed around a PLC system, it could be desirable to bind into the system existing powerline modems. Such modems, although preferably used for an indoor environment, have been designed specifically for LV lines to deliver high speed data. Such modems could be easily adapted for highway PLC while delivering high data rates for a relatively cheap price. If the same signals must be delivered to each streetlight pole, then all three phases will concurrently deliver the same signal. It is, therefore, interesting to note that each pole has at its disposal three wires for communications, a

single phase, the neutral and ground wires. Such an investigation is related to the PLC side and is, therefore, not further pursued in this study.

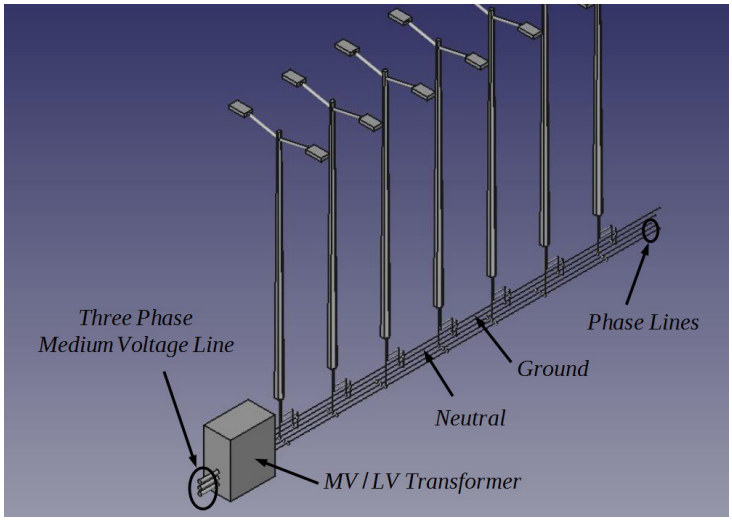

Figure 3.2. Highway streetlight power connection.

Signals fed by a specific MV/LV transformer along a highway section will require regeneration, due to the length of the cables and the associated cable attenuation. The regeneration of signals must be made while eliminating the noise that occurs along the cables. Although it is well known that the powerline channel is categorically a challenging medium for signal transmission, in this particular case signal regeneration could be easier to handle than that found in similar LV powerline channels. To observe this fact, at the regeneration point, the single source of noise generated over the powerline stems solely from the LEDs and its drivers. The underlying assumption of this fact is based upon the acknowledgment that power cables for highways are generally isolated from other LV devices.

The power is then delivered to a driver circuit that connects to the light source. Under the consideration that an LED source consumes less power than other types of lamps, the lighting element in this study will focus on the application of LEDs only. Furthermore, even though only a portion of a LV streetlight cable is regarded in this study, the following specification can be assumed with respect to the complete stretch of LV cable. A single LV cable connects on average 15 streetlight poles on each of the three phases. Perfect signal regeneration is conducted over each phase. All

luminaires deliver the same amount of light intensity without failure. Using the current state of the art LV indoor power line modems, transmission rates up to 500Mbs can be delivered along the line.

3.3 The Highway Streetlight:

There are a number of forms of lights that are used for typical road light illumination. Such types can be categorized as center or side lane illuminations, fancy or plain, HPS lamps or more recently LEDs. In the following it will be assumed that the streetlight type used are center lane LED streetlight, specifically designed for high speed road ways.

A streetlight is composed from multiple components, that can be easily described using a figure. In figure 3.3, the top most section of a typical highway street light is shown, with an elevated road surface plane as a reference.

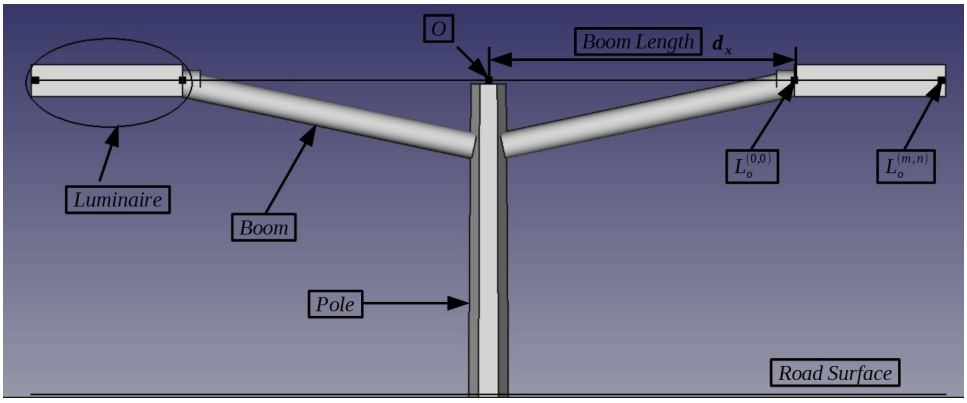

Figure 3.3. A typical highway street light.

Indicated in the figure is the simplest form of a typical highway street light that is composed from a single pole, two booms and two luminaires. The pole is the perpendicular element, also known as a pole mast, that elevates the lighting elements to a specified height, h , over the road surface. The boom is the element that connects the lighting elements to the pole at a prescribed height. The length of the boom, which will be denoted by d_x , overhangs the lighting elements over the road surface to aid in directing the light in an effective manner. The booms, for a highway

illuminated at its center, are typically offset by 180° from each other. Finally, the luminaire houses the lighting elements. The typically used lighting elements on most highways are HPS lamps. However, illumination modifications on existing highways and the illumination requirement on newer ones are strongly favoring LEDs over HPS lamps.

To suffice both communication and illumination, this study focuses on an implementation based upon LED luminaire. A typical configuration of LEDs within a luminaire is shown in figure 3.4, as seen by an observer directly underneath the streetlight luminaire.

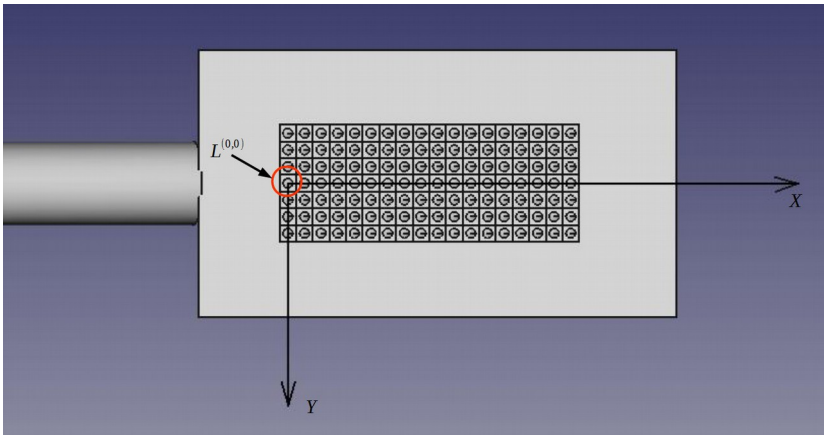

Figure 3.4. Typical LED setting in a streetlight luminaire.

In the specified configuration, there are a number of LEDs placed within a rectangular grid. All LEDs within the grid are placed at the same level. Accordingly, this reference level for the LEDs shall be referred to as the LED plane. Marked in the figure are the x and y axes of the LED plane, with the z axis directed towards the observer. The axes are placed at the center of a reference LED indicated by LED $L^{(0,0)}$ on the LED grid – encircled in red. Each luminaire is composed from a rectangular array of $(N)\times(2M-1)$ LEDs positioned parallel to the x and y axes. The center of all LEDs are offset by an equal amount. The offset along the x and y axes is referred to by Δx and Δy respectively. An LED offset by an amount $m\Delta x$ and $n\Delta y$ will be denoted by LED $L^{(m,n)}$. Specifically,

$$L^{(m,n)}=\left(L_x^{(m,n)},L_y^{(m,n)},L_z^{(m,n)}\right) \quad \text{with} \quad -(M-1)\le m\le M-1 \quad \text{and} \quad 0\le n\le N-1 \quad .$$

It can be observed from figure 3.3 that the luminaire is parallel to the road surface. The directed light, however, from each LED is not directed perpendicular to the road surface. Rather it is inclined by an angle so as to provide adequate highway illumination. It shall be assumed in this study that the optical inclination of all the LEDs within a luminaire are equal. This point shall be elaborated upon further in the following chapter.

From the signaling perspective, the electrical signal, that includes the data signal, is fed into an LED driver within the luminaire fixture. The driver produces the required output illumination according to both a baseline illumination and a subtle superimposed variable illumination. This subtle illumination is then detected by the receiver and further processed.

3.4 Typical Highway Configurations:

In this study, two typical road configurations are going to be analyzed as clearly depicted within figure 3.5.

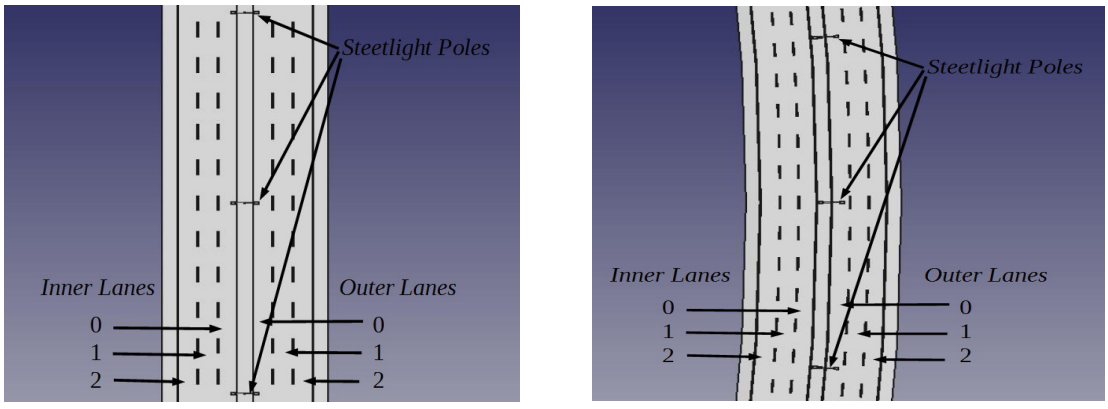

(a) (b)

Figure 3.5. The two highway configuration under study, (a) straight and (b) curved.

In both figures, the highway consists of three lanes that direct traffic in opposite

directions. The lanes are indicated as lanes 0, 1 and 2 with lane 0 regarded as the innermost lane while lane 2 as the outermost lane. Each lane is assumed to be 3.5m wide. Beyond lane 2 lies the highway shoulder of around 2.5m. Figure 3.5a shows a configuration for a straight highway segment, while figure 3.5b shows a segment of a curved highway. Finally, from both figures, it can be observed that the streetlight poles are placed at a relatively constant distant from one another. This distance will be referred to as the pole spacing, and is considered in this study to be 40m.

Highways that are curved tend to be elevated by an amount prescribed by highway engineers. The inclination is such that the side of the road towards the inner portion of the curvature, indicated in figure 3.5(b) by the inner lanes, is lower in elevation than the side of the road on the outer portion of curvature. The outer portion of the curvature is indicated in figure 3.5(b) by the outer lanes. By considering a cross-section of the road surface, the inclination can be easily visualized, as illustrated in figure 3.6.

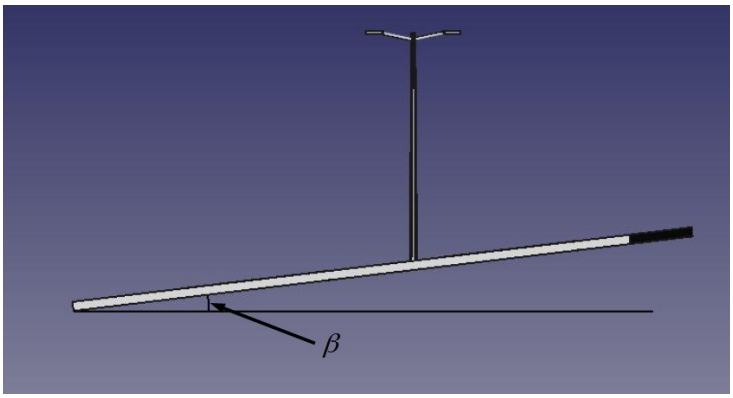

Figure 3.6. Curved highway cross-section demonstrating super elevation angle β .

The inclination angle, also known by the cross road elevation angle, is denoted by β . It is interesting to observe that although there is a road inclination, the streetlight poles remain perpendicular to the horizon level. In the figure this level is indicated by the horizontal line.

Analysis of the system will be done for a two road configurations as shown in figures 3.5. In the case of the inclined surface, the analysis will assume the maximum

allowable road inclination. Accordingly, by considering the curved road, for the maximum tolerable inclination, it should be evident that the analysis is inclusive of two extreme cases. Both extreme cases are linked to the maximum inclination angle of the streetlight poles, of the inner and outer curves. As the road direction changes, the inclination gradually disappears at the point when the road follows a straight path. It can therefore be considered that the straight path is the middle point between both extremities.

3.5 The Receiver:

As shown in figure 3.1, there could be numerous receivers fixed onto a vehicle. For example, in a two receiver configuration, each receiver could appropriately be directed to observe a current and an incoming luminaire. In this configuration, a single light sensitive sensor within the receiver has to be motorized ideally to maximize the amount of captured light. Alternatively, a receiver could house multiple sensors. For such a configuration, sensors should be placed at a predetermined angle from one another within the receiver. The angles should be chosen so as to maximize the amount of received photons from the intended luminaire along a road strip. In this case, sensors do not require a motor to direct them towards the luminaire.

To visualize this, figure 3.7 demonstrates the envisaged receiver with a multiple sensor configuration. The receiver has two main components, the sensors and the sensor housing. The sensor housing should be large enough to adequately accommodate all sensors, while also being transparent to permit the desired light signal through. Moreover, the housing should remain as transparent as possible for correct light level reception. In countries where heat is a concern, the housing must be made such as to reflect off as much heat while maintaining a functional environment for the sensors.

Clearly demonstrated within figure 3.7 is the different angles required by each sensor. Consider that such such a receiver is fixed to the rooftop of a vehicle, with the vehicles front end positioned towards the top left corner in the figure. It is clear that a

vehicle approaching a streetlight will activate the sensors within the first row initially. As the vehicle moves closer, the second row of sensors will receive an illumination that will be greater than the first row. Once the vehicle is directly under the streetlight, the middle row will receive the greatest illumination. As the vehicle moves away from the streetlight, the rows towards the end of the vehicle become successively active.

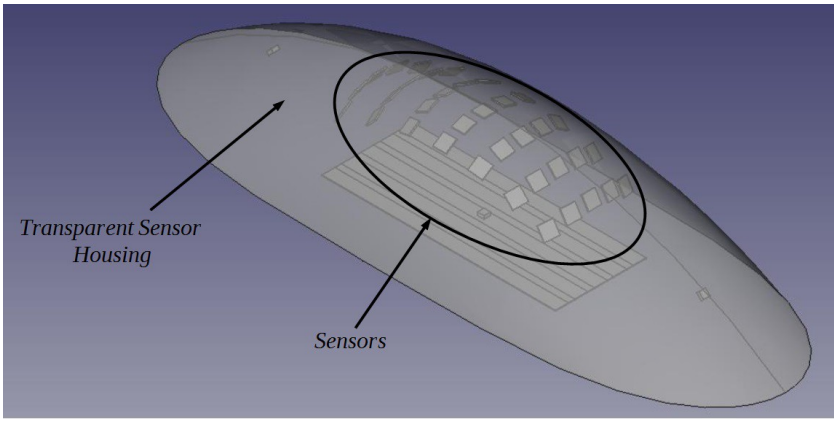

Figure 3.7. Envisaged receiver of the system.

The advantage of this sensor configuration could be viewed in light of receiving multiple forms of the signal, opening the door for a multiple input multiple output (MIMO) system implementation, as opposed to the single sensor configuration. However, the housing of this receiver type could be bulkier than its single sensor counterpart, for equal sensor size. The increased size could be aesthetically unpleasant for both vehicle manufacturers and buyers, and thus would require the attention of designers to the matter. Furthermore, as vehicles become more fuel efficient, a smaller aerodynamic footprint becomes essential.

In this study, however, as the main concern is to obtain meaningful results as to the VLC end of the system, it shall be assumed that the system is composed from a single receiver and a single sensor. The sensor is assumed to be motorized, such that it maintains fixture to the center of the luminaire at all times.

3.6 The Sensor:

Sensors that are used in VLC communications can be divided into two main groups, imaging and non-imaging sensors, as had been previously mentioned. There are a number of parameters that are critical to the operation of the sensors. From them are the sensor sensitivity and the FOV. The sensor sensitivity is related to the minimum amount of signal level that can be distinguished from the sensor generated noise. For the FOV, it can be easily described by referring to figure 3.8 below.

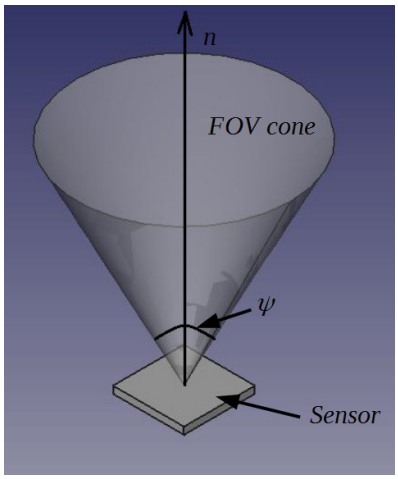

Figure 3.8. Sensor and FOV angle.

Consider that the unit normal vector to the sensor surface is denoted by n . Accordingly, the FOV angle, denoted by ψ , can be defined as the maximum angle about n that the sensor is capable of detecting photons. In this study, the sensor type for the system is nonessential other than that it should have an adequate FOV to detect the light emitted by all LEDs housed within a specific streetlight luminaire.

3.7 Variable Design Elements and Study Focus:

To study the system, a vehicle will be allowed only to travel on specific tracks on the road surface. Each lane will have 4 prescribed tracks, Tr_i , $i=\{0,1,2,3\}$, with $i=0$ and $i=3$ indicating a lanes inner and outer tracks, respectively. This is

clearly shown in figure 3.9.

There can be numerous factors that could effect the variable illumination. The factors affecting the quality of the received variable illumination could be ideally subdivided into electrical, infrastructure, illumination, weather and vehicle. Each factor can hinder the transmission in its own way, which in turn will change the available data rate.

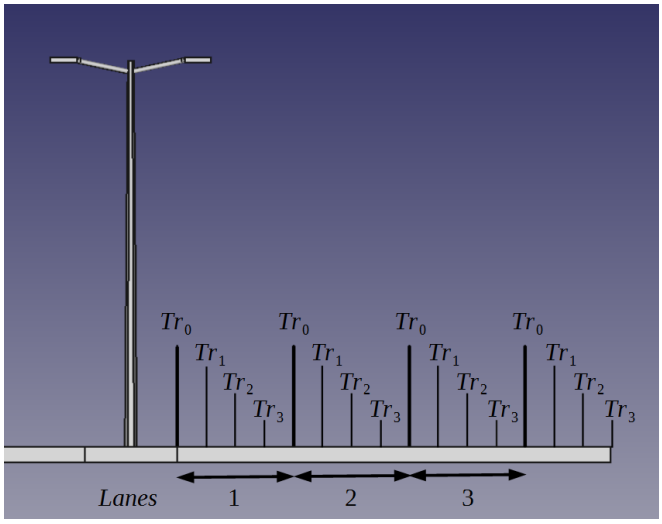

Figure 3.9. Highway lanes and vehicle tracks

Electrical factors that contribute towards inconsistent transmission rates could be related to all electrical driven devices. These includes the LEDs, LED drivers and the AC power transmitted along the power cables. Mass manufacturing of LEDs could lead to LED defects. Such defects could change the electrical to optical conversion over a single luminaire LED array. Moreover, LEDs have a lifespan that, although is relatively long as compared to other lamps, remains limited. As such, the effect of LED malfunctions cannot be ignored. The LED driver too, could deliver inaccurate power levels over the LED array. As a single luminaire houses multiple LEDs, synchronization of LEDs is of paramount importance. Delays caused by the driving circuitry could then become a limiting factor of high speed data transmission at the VLC side. Finally, electrical variations over the power cables due to variable power factors or changing load conditions can inadvertently change the received signal power level, thus impacting data rates.

The infrastructure related factors could be returned to the imperfect streetlight alignments, in all three axes with respect to both streetlights and road surface. Misalignment in both x and y axes, will change the pole spacing, which in turn will change the time of delay of signals for different poles. A y and z axes misalignment could increase the illumination from the other end of the road while minimizing it at the vehicles side. Similarly, an inconsistent super-elevation angle could also alter the amount of light falling onto the sensor, as the normal to the sensor will not be constant across different lanes under the same streetlight. Moreover, inaccurate boom lengths will alter the luminaire overhang along the highway, which in turn will lead to inconsistent received light levels. Another factor that could also be of importance, is the imperfect luminaire/pole and luminaire/luminaire alignment that will introduce variations in the light levels. Added to this are the effect of induced streetlight vibrations due to the passing of heavy vehicles along the highway. Then finally, inaccurate LED positioning on the LED plane and manufacturing defects in both LED and secondary LED lens could all be contributing factors.

With respect to the illumination factor, two elements could come into play. Prior to fixing the streetlights, the lighting level is usually computed by aide of a simulation software, such a DIALux, CalcuLux and Zemax. Input to the program are related to road measurements and drawings. After fixing the streetlights, engineers then assess the amount of light along the highway using photometric devices. Inconsistent measurements prior and after of light fixing could both contribute towards inaccurate lighting levels along highways.

The effect of weather on the quality of the illumination can be returned to temperature, rain, fog, time of day, sand and wind factors. LEDs are temperature sensitive devices with chromatic and power output levels that change according to different temperature conditions. Elevated temperature levels tends to weaken the light power output. To ensure adequate light and an acceptable chromatic output, LEDs require an effective cooling mechanism, in the form of heat sinks. The time of day at which the lights are switched on usually occurs during the dusk hours. During

this period within the day, until the fall of complete darkness, the effect of the background ambient light could alter the power level at the receiver end. Rain, fog and sand particles can all be grouped together as parameters that will alter the propagation path of the signal or partially block it. In the case of altering the light path, whereby it is assumed that an obstructed path towards the receiver exists, a number of different paths could be obtained from the same light source. The condition gives rise to the well known multipath effect. The multiple signals at the receiver end up being summed either constructively or destructively. On the other hand, in the case of an obstruction that partially blocks the signal, the light level at the receiver will be attenuated. If the particles in the air is not constant at different locations then the received power level will eventually fluctuate. Finally, the wind factor, could contribute to the movement of particles in the air. On the other hand, even under perfect link conditions between transmitter and receiver, the wind could sway the streetlight poles. This streetlight movement will contribute to the changing light levels at the receiver.

Finally, in terms of the factors related to the vehicle, these can be enumerated as inaccurate alignment of the sensor to the vehicles frame, vehicle to road misalignment, opaque sensor housing and variable vehicle conditions. The inaccuracy in fixing the sensor could lead to a non-optimum sensor to LED FOV. In the case of the vehicle to road misalignment, due to different tire inflation levels, a multiple sensor receiver will have to cope with inaccurate power level readings. In this case, prior calibration of the system would be required for best results. Similarly, an opaque sensor housing, that could be the effect of the accumulation of dust, will clearly generate an obstruction that will attenuate the received signal. And finally, variable vehicle conditions, such as movement within the vehicle and small scale road bumps, will also contribute towards the fluctuation in the received signal levels.

The aforementioned enlisted factors that influences the quality of the received light signal is extensive, and should be viewed as a subset of all potential deviations from the ideal condition. To make this study tractable, therefore, the focus will be on the effect of translational and rotational perturbations at the transmitter end and its influence on the optical signal. For such reasons, in concert with studying the optical

highway channel, a number of assumptions will be made. First, the signal is transmitted only in the dark hours of the night. Second, the transmission of the light signal to the receiver is unhindered, thus eliminating the effect of particles in the air making up a multipath channel. Third, vehicles are constrained onto a well predefined tracks over the highway. Fourth, all of the studied fluctuations are grouped into the transmitter end. Fifth, LED defects and malfunctions are not included, hence it is assumed that all LEDs deliver an equal power output. Sixth, fluctuations due to temperature effect on all LEDs be disregarded. Finally, it is assumed that all LEDs are in perfect synchronization.

Looking at the envisaged system in its entirety, to the best of the author's knowledge, such a system for communications over high speed roadways is unique, and its implementation has not been observed anywhere. This statement is made with the acknowledgment that LED highway street lighting is picking up traction in certain countries, such as Malaysia. Even within the State of Western Australia (WA), a sincere will to adopt LED street lighting can be observed. A good example of this is the LED streetlights along the new roads about the vicinity of Perth airport.

Adopting the complete envisaged system, especially over the WA freeways, has its own challenges. With the freeway as the target area of application, it is reasonable to assume that the current light pole spacing is greater than that catered for within this study. Under the current status of LED luminaires for high speed roadways, it is reasonable to assume that further luminaire development is required to adequately span the established pole spacing along the WA freeways. Moreover, this study focuses only on one type of highway streetlight configuration. This configuration can be observed over the major stretch of the WA freeway. However, for a truly complete adoption of the system, all possible high speed roadway lighting configurations, such as entries to and exits from the freeway, must also be taken into accounted. And finally, the integration of PLC over the outdoor LV cables and VLC, will have to overcome its own set of problems. Addressing these problems such as the electrical to optical signal conversion, is crucial for the seamless data delivery to the end user.

By conducting this primer study of adopting VLC for high speed roadways, a

reasonable choice of system parameters have been made. Firstly, center lane streetlight has been chosen as a representation of typical roadway lighting configuration. Secondly, assumption that data delivery to the luminaires by means of PLC is well established. And finally, perfect streetlight pole placement and perfect luminaire operation are both assumed. Accordingly, for the chosen configuration and system parameters, the VLC channel can now be studied in detail, while assuming the Tx and Rx configuration as described herein.

Chapter 4

Analysis of an Ideal System

4.1 Introduction:

In this chapter the derivation of the DC channel response will be undertaken using an analytical streetlight intensity distribution. Due to the underlying complexity of the DC channel response, and the numerous LEDs populating the LED luminaire, an attempt to simplify the response using differentials is outlined. However, as shown, a simplification attempt using this method instead increases the complexity of the DC channel response and thus should be avoided. Another method of simplification is conducted under the assumption that the complete LED array can be replaced by a single equivalent LED element. Accordingly, in the following section, a details of the channel are discussed, followed by the required coordinate frame transformations. The DC channel response for the intensity distribution is shown in section 4.3. Section 4.4 demonstrates the differential analysis attempt for DC response simplification. Finally, section 4.5 shows the single LED equivalent that can substitute the complete LED array for all DC channel response computations.

4.2 System Parameters and Coordinate Frames:

The system analysis will constitute the VLC portion of the complete system proposed in chapter 3. An illustration of this portion of the system is first described according to figure 4.1.

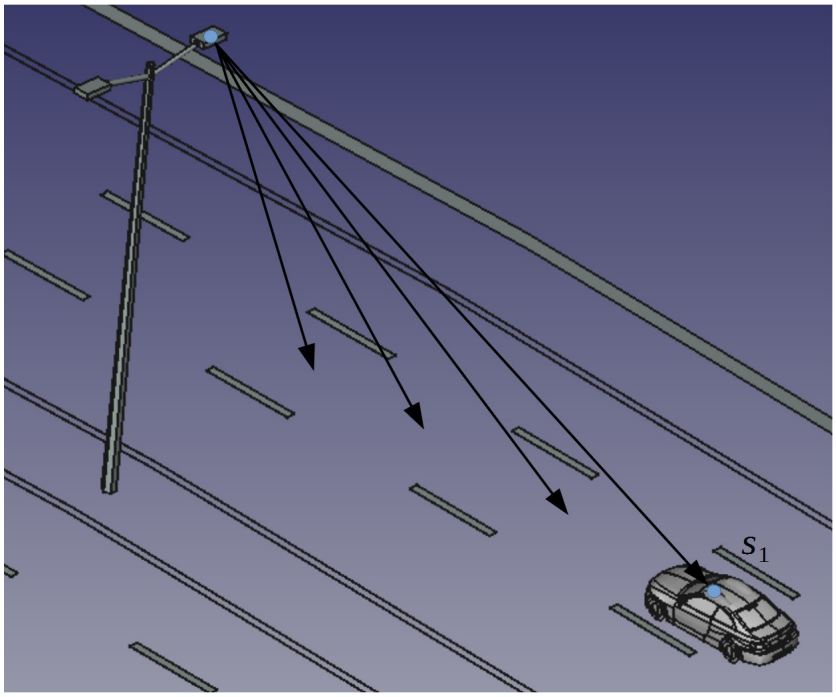

Figure 4.1 A center pole I2V VLC transmission over a high speed road configuration.

4.2.1 System Parameters:

In the figure, a sensor located on the roof of a moving vehicle receives signals from a streetlight LED. The vehicle follows a known path along the highway, while maintaining reception of the broadcast signal emitted from the LED. With the vehicle movement restricted over the road surface, it will be assumed that the *z*-coordinate, which extends upwards from the road surface, remains constant. To this extent, a vehicle will be confined in movement over the XY-plane only.

As roads tend to curve inwards and outwards, it is appropriate to describe the road curvature. To be begin with, consider a road section that is straight. This road neither curves inwards or outwards. If a road changes direction, it will naturally follow a curved path. By extending a small section of this curved path it is easy to observe that the extended portion inscribes a circle of radius R_s . Accordingly, it can be assumed that about a single streetlight that the road curvature follows a circular path which can be appropriately described by the equation of a circle,

$$\frac{x^2}{R_s^2}+\frac{y^2}{R_s^2}=1 \tag{4.1}$$

where, R_s is the radius of a curved road section.

From another perspective, all road sections can be appropriately described by equation (4.1). For a straight highway section, ideally the highway curvature should by infinity. However, for all practical reasons, a sufficiently large radius, such as 1000km, can nicely approximate the curvature for a straight highway.

The parameter R_s is determined by the minimum allowable radius at the inner portion of the road, and is a function of the road super elevation rate e_1, or equivalently the cross-road slope β, with $\beta = e_1$, as indicated in figure 3.6. Furthermore, R_s is a function of the velocity of the traveling vehicles u as well as the friction factor between the tires and the road, f. The expression of R_s is given by [146],

$$R_s = \frac{u^2}{127(f + e_1)} \tag{4.2}$$

with u in km/hr and in R_s meters, while certain values, although conservative, have been published by AASHTO [147]. Figure 4.2 can be used to visualize the *x* and *y* axes and variable R_s.

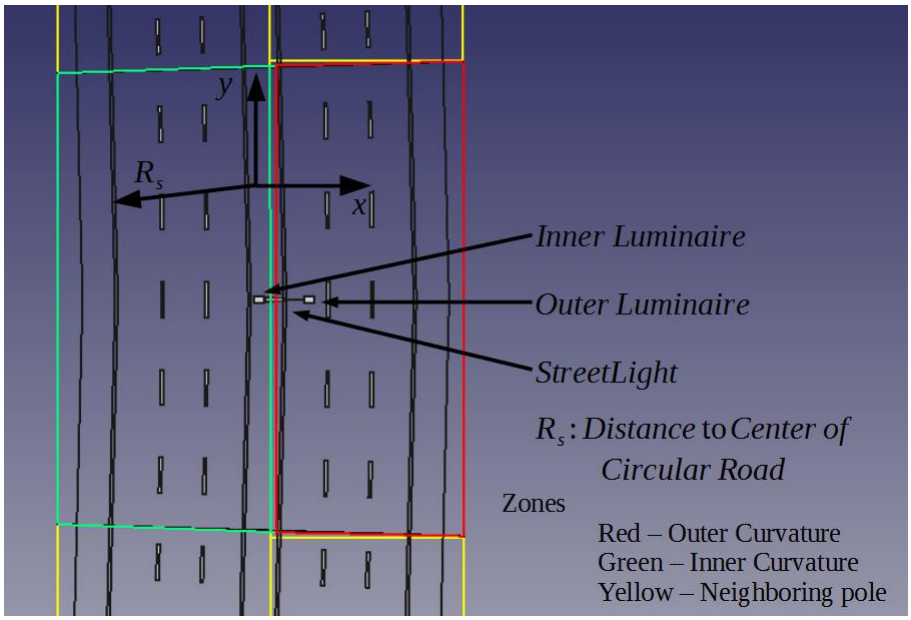

Figure 4.2 Illustration depicting the road surface along with the illumination zones of a single streetlight.

The equation of the sensor path can be described in terms of a parametric equation, $s_1(t)=(s_{1,x}(t),s_{1,y}(t),s_{1,z}(t))$ as,

$$s_1(t)=R_s\cos(\nu(t))i+R_s\sin(\nu(t))j+s_{1,z}k \tag{4.3}$$

with $\nu(t)=\nu_0+t\Delta_\nu$ and components $\Delta_\nu=u/(2\pi R_s)$ and ν_0 is the angle at the initial time instant.

Similarly, angle $\nu(t)$ can be obtained from the position of the sensor as,

$$\nu(t)=\tan^{-1}(s_{1,x}(t)/s_{1,y}(t)) \tag{4.4}$$

The components along the x , y and z axes are linked to the normalized 3-d vector components i , j and k .

The road curvature, sensor location and LED transmission are the variables that constitute the scene. Therefore, a few terminologies are going to be given prior to the analysis, which can all be appropriately obtained from figure 4.2. An inner road curvature (IRC) will be linked to a sensor or a luminaire that are located in the portion of the road that is closer to the center of the circle described by equation (4.1). Similarly, reference to an outer road curvature (ORC) will be linked to a sensor or a luminaire that are located in the portion that is further away from the center of the circle described by equation (4.1). According to the definitions of IRC and ORC, the streetlight luminaires serving each side of the road are designated as inner and outer luminaires.

A transmitting LED that is located on the same side of the highway as the sensor while located on a pole closest in range to the sensor, will be referred to as the transmitter. All other transmitting LEDs on other poles at the same side of the highway are considered interferences. Similarly, in the case that the transmitting LED and sensor are on opposite sides of the highway, then the transmitting LEDs are also referred to as interference.

As a final note on the axis placement in figure 4.2, the demonstrated *x* and *y* axes should strictly be placed at the center of the path inscribed by the curved road section. As such, the axis would have been placed at the roads origin or equivalently

at the roads center. However, due to the large value of R_s , placing the axes at the center would have made viewing the road section difficult. Accordingly, the axis has been shifted onto the road for the sake of clarity only.

For a sensor located in the red zone, the ORC zone, the wanted signal is transmitted from the luminaire in the red zone. Other signal transmissions from all other zones are considered as interferences. If the sensor is located in the green zone, in the IRC region, the desired signal is transmitted from the luminaire within the zone, while the remaining signals from the other zones are interferences.

In the analysis, three different planes are going to be regularly used. The first plane, particular to the sensor, will be referred to as the sensor plane. This plane is parallel to the road surface and is elevated by an amount of $s_{i,z}$, $\forall i=1,2$ above the ground. A typical value for $s_{i,z}$ can be considered 1.5m for high speed vehicles, where a sensor sits above the roof by 10cm. The second plane is referred to as the LED plane. This plane is inclined by angle β and is the physical plane at which all LEDs of a streetlight are fixed. Finally, the optical axis plane, that will be referred to by *OC*, is the plane normal to the optical axis of the LED. This will be defined as the center of the light intensity distribution curve. As neighboring LEDs are offset by an amount Δx and Δy from one another, each LED will be associated with its specific *OC* plane. However, it is assumed throughout this work that the optical axes of all LEDs are parallel, hence the *OC* planes of all LEDs are also parallel.

4.2.2 Coordinate Frames:

To analyze the system it is convenient to define a set of appropriate coordinate frames to work within. The first coordinate frame will be associated with the highway curvature. The second and third coordinate frames will be related to a reference LED $L^{(0,0)}$ inclined at an angle ζ specific to the IRC and ORC.

Initially all points in the 3D space are defined in the highway coordinate frame. A street light pole is fixed along the *x*-axis at a point $P=(P_x,0,0)^T$ on the center of the road surface at a distance R_s away from this coordinate frame origin. A sensor

located on the highway can be given by its 3D-coordinates as $s_1=(s_{1,x},s_{1,y},s_{1,z})^T$. The sensor could equally be translated to a coordinate frame that is centered about the base of a single streetlight pole. Denoted as s_1^P , the sensor translation is given by operation,

$$s_1^P=s_1-\boldsymbol{T}_{\boldsymbol{p}} \tag{4.5}$$

where $\boldsymbol{T}_{\boldsymbol{p}}$ is the translation vector to the pole base, and is given by,

$$\boldsymbol{T}_{\boldsymbol{p}}=\begin{bmatrix}-R_s\\0\\0\end{bmatrix} \tag{4.6}$$

In a similar manner, translation of the origin from the road coordinate frame to the center of a reference LED $L^{(0,0)}=(L_x^{(0,0)},L_y^{(0,0)},L_z^{(0,0)})$ can then be obtained as,

$$L^{(0,0)'}=\ \boldsymbol{T}_{\boldsymbol{L}^{(0,0)}}\ L^{(0,0)} \tag{4.7}$$

where $\boldsymbol{T}_{\boldsymbol{L}}^{(\boldsymbol{0,0})}$ is the translation vector to the LED center, and is given by,

$$\boldsymbol{T}_{\boldsymbol{L}^{(0,0)}}=\begin{bmatrix}-R_s-L_x^{(0,0)}\\0\\-L_z^{(0,0)}\end{bmatrix} \tag{4.8}$$

Because there are two luminaires that are referenced in opposite directions, a coordinate system that is referenced to the transmitting luminaire is to be considered separately. Accordingly, a distinction will be made for the translation to reference LED in the IRC and ORC Tx conditions, by denoting $\boldsymbol{T}_{\boldsymbol{L}_i^{(0,0)}}$ and $\boldsymbol{T}_{\boldsymbol{L}_o^{(0,0)}}$ for each respective translation vector. Then following from equation (4.8), $\boldsymbol{T}_{\boldsymbol{L}_i^{(0,0)}}$ and $\boldsymbol{T}_{\boldsymbol{L}_o^{(0,0)}}$ will be given as,

$$\boldsymbol{T}_{\boldsymbol{L}_i^{(0,0)}}=\begin{bmatrix}-R_s-L_{x,i}^{(0,0)}\\0\\-L_{z,i}^{(0,0)}\end{bmatrix} \tag{4.9.a}$$

$$\boldsymbol{T}_{L_o^{(0,0)}}=\begin{bmatrix} -R_s-L_{x,o}^{(0,0)} \\ 0 \\ -L_{o,i}^{(0,0)} \end{bmatrix} \tag{4.9.b}$$

Rotation of the origin within an LED reference can be given generally with respected to the axis of rotation. For each axis, therefore, a specific rotation matrix can be identified. The rotations in the *x, y* and *z* axes can be denoted respectively as $\boldsymbol{R}_x$, $\boldsymbol{R}_y$ and $\boldsymbol{R}_z$. Each rotation matrix can respectively be defined according a rotation angle γ_x , γ_y and γ_z about the *x* *y* and *z* axes. Following these definitions, the rotation matrices $\boldsymbol{R}_x$, $\boldsymbol{R}_y$ and $\boldsymbol{R}_z$ will be given as,

$$\boldsymbol{R}_x(\gamma_x)=\begin{bmatrix} 1 & 0 & 0 \\ 0 & \cos(\gamma_x) & -\sin(\gamma_x) \\ 0 & \sin(\gamma_x) & \cos(\gamma_x) \end{bmatrix} \tag{4.10.a}$$

$$\boldsymbol{R}_y(\gamma_y)=\begin{bmatrix} \cos(\gamma_y) & 0 & -\sin(\gamma_y) \\ 0 & 1 & 0 \\ \sin(\gamma_y) & 0 & \cos(\gamma_y) \end{bmatrix} \tag{4.10.b}$$

$$\boldsymbol{R}_z(\gamma_z)=\begin{bmatrix} \cos(\gamma_z) & -\sin(\gamma_z) & 0 \\ \sin(\gamma_z) & \cos(\gamma_z) & 0 \\ 0 & 0 & 1 \end{bmatrix} \tag{4.10.c}$$

Subsequently, by applying the appropriate transformations, it is now possible to describe the process of shifting an origin from the road center to the Tx LED reference. For each coordinate frame, IRC and ORC, two steps are required, a translation to the center of the reference LED, followed by the axis rotation. The translation for both frames follows along the *x*-axis, and as shown previously, is given by $\boldsymbol{T}_{L_i^{(0,0)}}$ and $\boldsymbol{T}_{L_o^{(0,0)}}$, for IRC and ORC, respectively.

Focus now will be given to the axis rotations, with reference to the relevant angles. To begin with, figure 4.3 shows illustrates angles α , β and ξ in relation to the road surface.

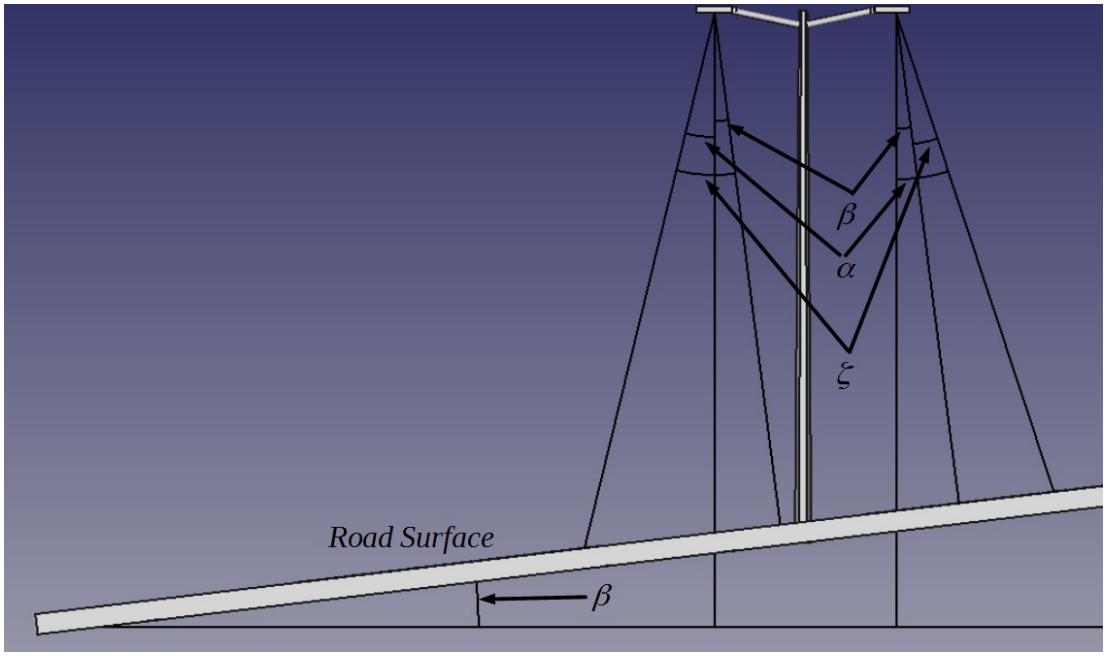

Figure 4.3 Illustration of angles α , β and ζ with reference to road surface.

The illustration depicts a vertical pole placed onto an inclined road surface. The diagram demonstrates that angle β referenced from the luminaire, is constant for both IRC and ORC. In contrast, the *OC* angle inclination α is referenced from the vertical of the pole towards the inner or outer road centers, for each of the IRC or ORC luminaires, respectively. The angle ζ which relates α and β together can be given respectively for the IRC and ORC cases as,

$$\zeta_i = \alpha + \beta \tag{4.11}$$

and

$$\zeta_o = \alpha - \beta \tag{4.12}$$

where

ζ_i and ζ_o refers to the optical axis inclination from the normal of the road surface in both IRC and ORC cases, respectively.

Then for the rotation step, in the case of ORC, a single rotation to align the negative *z*-axis with the optical axis is required. In the case of the ORC, two rotations are required. The first is required to point the new origin *x*-axis away from the pole, in the direction of the road center. This can be achieved using the 180^o rotation about the *z*-axis, $\boldsymbol{R}_z(\pi)$. This is then followed by a rotation about the *y*-axis to align the *z*-axis with the reference LED optical axis. The rotation of the optical axis, in both

cases, is similar, and can be given as,

$$\boldsymbol{R}_y(\alpha)=\begin{bmatrix}\cos(\alpha) & 0 & -\sin(\alpha)\\ 0 & 1 & 0\\ \sin(\alpha) & 0 & \cos(\alpha)\end{bmatrix} \tag{4.13}$$

Whereby it has been assumed in the previous equation that the road is parallel to the LED plane. If a super elevation angle β exists, then matrix $\boldsymbol{R}_y(\alpha)$ is converted into either $\boldsymbol{R}_y(\zeta_i)$ or $\boldsymbol{R}_y(\zeta_o)$ for the IRC and ORC system setup, respectively.

While for the IRC rotation matrix $\boldsymbol{R}_z(\pi)$, it is given by the identity,

$$\boldsymbol{R}_z(\pi)=\begin{bmatrix}-1 & 0 & 0\\ 0 & -1 & 0\\ 0 & 0 & 1\end{bmatrix} \tag{4.14}$$

Then transforming a point $p=(p_x,p_y,p_z)$ from the road coordinate frame into the optical axis ORC coordinate frame, p' can be achieved using,

$$p' = \boldsymbol{R}_y(\zeta_o)(\boldsymbol{T}_{\boldsymbol{L}_o^{(0,0)}}+p) \tag{4.15}$$

Using the same principles, a point p' in the IRC coordinate frame will be obtained using,

$$p' = \boldsymbol{R}_y(\zeta_o)\boldsymbol{R}_z(\pi)(\boldsymbol{T}_{\boldsymbol{L}_o^{(0,0)}}+p) \tag{4.16}$$

Finally, it should be remembered that multiplication of matrices is not associative, therefore the order of the multiplication must be maintained.

The first is required to align the *x*-axis away from the pole center, while at the same time pointing the *z*-axis to towards the ground. The second rotation is a rotation of ζ about the *y*-axis to align the system with the LED OC plane. For each of the IRC and ORC, the rotations will be different. Both rotations for the IRC will be given by matrix $\boldsymbol{R}_i$ as,

$$\boldsymbol{R}_i=\begin{bmatrix}\cos(\pi-\zeta) & 0 & -\sin(\pi-\zeta)\\ 0 & 1 & 0\\ \sin(\pi-\zeta) & 0 & \cos(\pi-\zeta)\end{bmatrix} \tag{4.17}$$

Using the identities $\cos(\pi-a)=-\cos(a)$ and $\sin(\pi-a)=\sin(a)$, $\boldsymbol{R}_i$ can be

reduced into,

$$\boldsymbol{R_i}=\begin{bmatrix}-\cos(\zeta) & 0 & -\sin(\zeta)\\ 0 & 1 & 0\\ \sin(\zeta) & 0 & -\cos(\zeta)\end{bmatrix} \tag{4.18}$$

For the ORC, the rotation matrix is denoted by $\boldsymbol{R_o}$ and is given by,

$$\boldsymbol{R_o}=\boldsymbol{R}_{y(-\xi)}\ \boldsymbol{R_x} \tag{4.19}$$

where, $\boldsymbol{R_x}$ is a rotation of π about the *x*-axis,

and $\boldsymbol{R}_{y(-\xi)}$ is a rotation of $-\zeta$ about the new *y*-axis.

By performing the multiplication $\boldsymbol{R_o}$ will have the form,

$$\boldsymbol{R_o}=\begin{bmatrix}\cos(\zeta) & 0 & \sin(\zeta)\\ 0 & -1 & 0\\ \sin(\zeta) & 0 & -\cos(\zeta)\end{bmatrix} \tag{4.20}$$

Finally, the position of a sensor s_1 given in the highway coordinate frame, can be transformed into $s_1^{'}=(s_{1,x}^{'},s_{1,y}^{'},s_{1,z}^{'})^T$ within the LED OC coordinate frame using the sequence of translations and rotations. For the highway IRC, $s_1^{'}$ will be given as,

$$s_1^{'}=\boldsymbol{R_i}\ (s_1-\boldsymbol{T_p}-L^{(0,0)'}) \tag{4.21}$$

with components $s_{1,x}^{'}$, $s_{1,y}^{'}$ and $s_{1,z}^{'}$ given by,

$$\begin{aligned}s_{1,x}^{'}=&(-s_{1,x}+R_s+(L_{i,x}^{(0,0)}\cos(\beta)-L_{i,z}^{(0,0)}\sin(\beta)))\cos(\zeta)\\ &-(s_z-(L_{i,x}^{(0,0)}\sin(\beta)+L_{i,z}^{(0,0)}\cos(\beta)))\sin(\zeta)\end{aligned} \tag{4.22}$$

$$s_{1,y}^{'}=s_{1,y}-L_{i,y}^{(0,0)} \tag{4.23}$$

$$\begin{aligned}s_{1,z}^{'}=&(s_{1,x}-R_s-(L_{i,x}^{(0,0)}\cos(\beta)-L_{i,z}^{(0,0)}\sin(\beta)))\sin(\zeta)\\ &-(s_z-(L_{i,x}^{(0,0)}\sin(\beta)+L_{i,z}^{(0,0)}\cos(\beta)))\cos(\zeta)\end{aligned} \tag{4.24}$$

Similarly, the position of sensor s_1 on the ORC can be directly obtained as,

$$s_1^{'}=\boldsymbol{R_o}\ (s_1-\boldsymbol{T_p}-L^{(0,0)'}) \tag{4.25}$$

with components $s_{1,x}^{'}$, $s_{1,y}^{'}$ and $s_{1,z}^{'}$ given by,

$$s'_{1,x} = (-s_{1,x} + R_s + (L_{i,x}^{(0,0)}\cos(\beta) - L_{i,z}^{(0,0)}\sin(\beta)))\cos(\zeta) + (s_z - (L_{i,x}^{(0,0)}\sin(\beta) + L_{i,z}^{(0,0)}\cos(\beta)))\sin(\zeta) \tag{4.26}$$

$$s'_{1,y} = -s_{1,y} + L_{i,y}^{(0,0)} \tag{4.27}$$

$$s'_{1,z} = (s_{1,x} - R_s - (L_{i,x}^{(0,0)}\cos(\beta) - L_{i,z}^{(0,0)}\sin(\beta)))\sin(\zeta) + (s_z - (L_{i,x}^{(0,0)}\sin(\beta) + L_{i,z}^{(0,0)}\cos(\beta)))\cos(\zeta) \tag{4.28}$$

4.2.3 System Angles and Planes:

This section will be confined to the description of the angles and how it relates to the different planes. An understanding of the angles is core to the analysis of the system.

Angles α , β and ζ will contribute towards the light intensity distribution, I , over the road surface. In turn, the light intensity distribution can be expressed in terms of two angles, a polar angle, θ , and an azimuthal angle, φ . Then I can be given in terms of θ and φ as $I(\theta,\varphi)$. With reference to sensor s_1 and optical axis OC , angle θ is the angle formed from s_1 passing through the center of the LED and connecting OC . The azimuthal angle φ is described as the angle centered at OC between the *y*-axis and sensor s_1 on the plane normal to OC which contains s_1 . As the single light pole fixture includes numerous LEDs, then for a specific LED, $L^{(m,n)}$, and sensor s_1 , the intensity distribution will be referred to by $I_{s1}^{(m,n)}(\theta,\varphi)$. In this definition, it is implied that polar and azimuthal angles are specific to the sensor/LED pair.

Next consider a typical road scene, where two sensors are located on opposite sides of a highway with a single streetlight pole in the middle. Consider that a luminaire contains a single pair of LEDs. To distinguish between the LEDs from either luminaire, the IRC and ORC LED pairs will be denoted by $(L_i^{(0,0)}, L_i^{(m,0)})$ and $(L_o^{(0,0)}, L_o^{(m,0)})$, respectively. In all that follows, the subscript indicating the IRC and ORC will be dropped, except when explicitly mentioned. Then for both pairs, $L^{(0,0)}$ represents the reference LED of the luminaire. Moreover, both LED pairs are located

on the *x*-axis. The sensors, too, can be distinguished from each other. A sensor that is located on the transmission side will be denoted from this point forward as s_1 , with $s_1=(s_{1,x},s_{1,y},s_{1,z})$. The sensor on the opposite side, which is not intended to receive the transmission, will be denoted by s_2 , with $s_2=(s_{2,x},s_{2,y},s_{2,z})$. For the analysis it will be assumed that $s_{i,z}=s_{1,z}=s_{2,z}$. The complete scene for the respective cases of IRC and ORC transmissions is given in figures 4.4 and 4.5.

Indicated in each of figures 4.4 and 4.5 is the origin that is centered within the reference LED. However, this origin is meant for clarity purposes only, and should not be confused with the origin aligned with the OC axis.

In each figure, the ground, or road surface, and LED plane are clearly marked. In addition, four other parallel planes marked as P_0 , P_m , P_1 and P_2 are given. Planes P_0 and P_m are the OC axis planes centered within LEDs $L^{(0,0)}$ and $L^{(m,0)}$ respectively. While planes P_1 and P_2 are the *OC* planes centered within sensors s_1 and s_2 respectively. Further marked for reference in the figures are angles α , β and ζ . There are two polar angle pairs indicated in both figures, each linked to sensors s_1 and s_2 respectively. Angle pair $(\theta_{s1}^{(0,0)},\theta_{s1}^{(m,0)})$ is associated with receiving sensor s_1 while angle pair $(\theta_{s2}^{(0,0)},\theta_{s2}^{(m,0)})$ is associated with receiving sensor s_2 .

From the figures, the following two observations can be made. Primarily, the intersection of both LEDs *OC* axes with either planes P_1 or P_2 gives the projection of the LED separation on the *OC* plane. From the figures, this projection is obtained as $\Delta x\cos(\alpha)$. Secondly, the observation that angle pair $(\theta_{s2}^{(0,0)},\theta_{s2}^{(m,0)})$ will generally be larger than angle pair $(\theta_{s1}^{(0,0)},\theta_{s1}^{(m,0)})$, which is due to the super-elevation of the roadway.

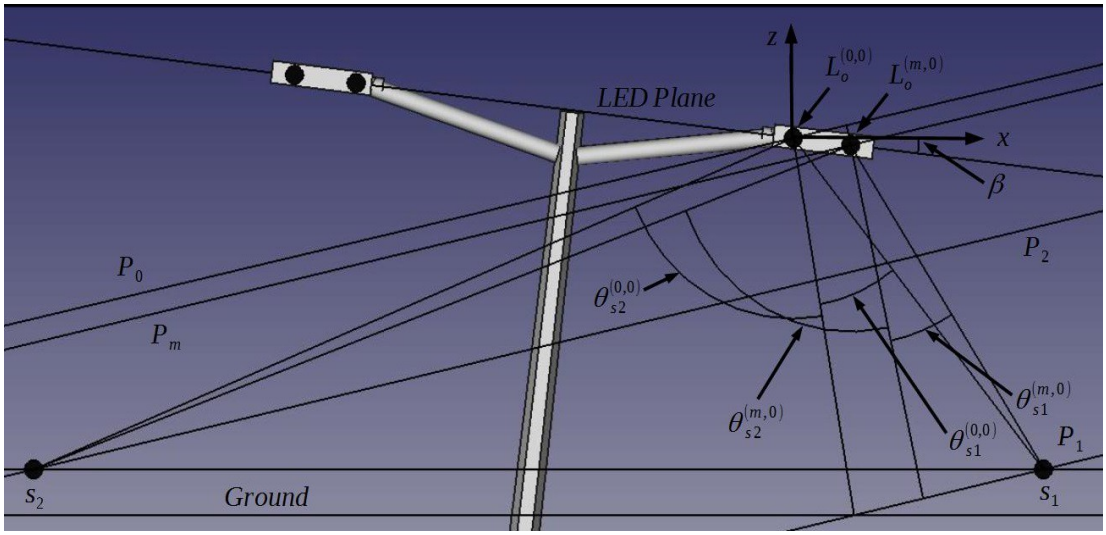

Figure 4.4. Arrangement of s_1 and s_2 for an IRC luminaire transmission.

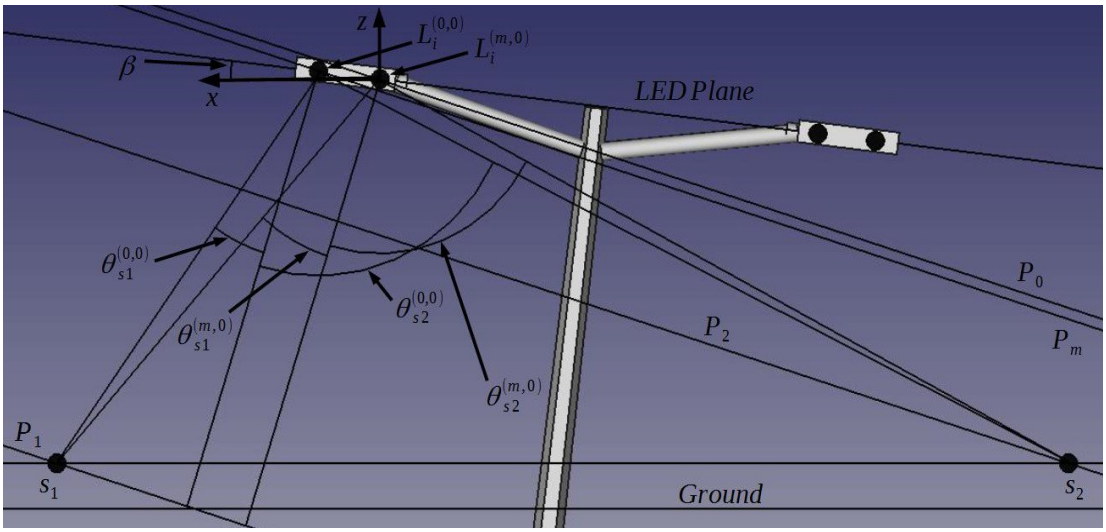

Figure 4.5. Arrangement of s_1 and s_2 for an ORC luminaire transmission.

In relation to the azimuthal angle φ , figure 4.6 shows the OC axis of 4 LEDs intersecting the OC plane that includes sensor s_1 , for the IRC.

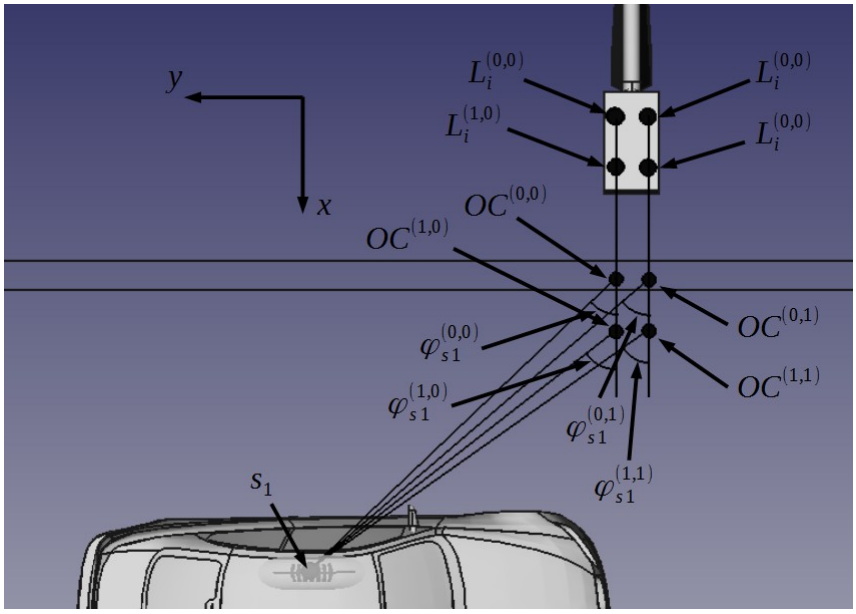

Figure 4.6. Plan view demonstration of sensor azimuthal angle relative to four LEDs optical axes.

Notice that the LEDs are spaced by an amount of Δx and Δy on the LED array plane. However, due to the OC tilt of α relative to the LED plane, the projected spacing of each axes on the OC plane becomes $\Delta x \cos(\alpha)$ and Δy on the respective *x* and *y* axes.

4.3 The DC Channel Response:

4.3.1 Generalized DC Channel Response:

It is known that light traveling from its source to destination follows a straight path. In an atmosphere that is free from all air particles, a Rx will receive the transmitted visible light signal via an obstructed LOS path only. Then following the argument from [148], the LOS channel response will be independent from frequency, and can be conveniently to as the DC channel response. Following the suite of [2] and [104], the DC channel response is known to be a function of the Tx/Rx separation distance, light intensity distribution, sensor surface area, light incidence angle with respect to the receivers axis, and the optical gains of the Tx and Rx. To obtain the DC channel

response, first consider a receiving element of physical area *A*, that will have an effective area $A_{s1}(\psi)$ with respect to an incoming signal of incidence angle ψ relative to receiver $s1$ axis as,

$$A_{s1}(\psi)=\begin{cases} A\cos(\psi), & 0\le\psi\le\pi/2 \\ 0, & \psi>\pi/2 \end{cases} \tag{4.29}$$

If the optical system includes optical concentrators at the Tx and Rx sides, then $A_{s1}(\psi)$ will be modified into,

$$A_{s1}(\psi)=\begin{cases} A\,G(\psi)G_{s1}(\psi)\cos(\psi), & 0\le\psi\le\psi_{FOV} \\ 0, & \psi>\psi_{FOV} \end{cases} \tag{4.30}$$

where,

$G(\psi)$ and $G_{s1}(\psi)$ are the optical gains of the transmitter and receiver respectively, and ψ_{FOV} is the FOV angle which is a parameter specified by the PD manufacturers [149].

The DC channel response H_{s1} can now be evaluated for an isotropic radiating light source at distance d_{s1} away from receiving element $s1$ as,

$$H_{s1}(0)=\begin{cases} \dfrac{A}{d_{s1}^2}G(\psi)G_{s1}(\psi)\cos(\psi), & 0\le\psi\le\psi_{FOV} \\ 0, & \psi>\psi_{FOV} \end{cases} \tag{4.31}$$

However, if the light radiating from the source is non isotropic, then H_{s1} should be modified to include the luminous intensity flux, I , in the form of,

$$H_{s1}(0)=\begin{cases} \dfrac{A}{d_{s1}^2}I_{s1}(\theta,\varphi)G(\psi)G_{s1}(\psi)\cos(\psi), & 0\le\psi\le\psi_{FOV} \\ 0, & \psi>\psi_{FOV} \end{cases} \tag{4.32}$$

where, $I(\theta,\varphi)$ is the luminous intensity flux that is defined in both polar, θ , and azimuthal, φ , angles.

Under this definition of the DC channel response, each of its constituent parameters are to be derived in each of the following subsection specific to the streetlight LED

luminaires. The parameters will then be included to obtain the DC channel response specific to the streetlight case.

4.3.2 LED to Sensor Distance:

The first step in analyzing the system is to determine the separation distance of sensor s_1 and any LED within the LED array. Although the distance can be obtained directly without any system coordinate transformations, however, to gain insight into the effect of the variations in system parameters, the distance will be obtained for the two aforementioned cases. Accordingly, the sensors location must be first obtained for either case.

Considering a sensor located on either IRC or ORC. The sensor position on the OC plane can be obtained after translation and rotation of the origin at LED $L^{(0,0)}$ center as,

$$s_1^{'}(t)=s_{1,x}^{'}(t)\,i+s_{1,y}^{'}(t)\,j+s_{1,z}^{'}(t)\,k \tag{4.33}$$

whereby the components $s_{1,x}^{'}(t)$, $s_{1,y}^{'}(t)$ and $s_{1,z}^{'}(t)$ are given as,

$$s_{1,x}^{'}(t)=(R_s\cos(\zeta(t))-L_x^{(0,0)})\cos(\alpha)+(s_{1,z}(t)-L_z^{(0,0)})\sin(\alpha) \tag{4.34}$$

$$s_{1,x}^{'}(t)=(s_{1,x}(t)-L_x^{(0,0)})\cos(\alpha)+(s_{1,z}(t)-L_z^{(0,0)})\sin(\alpha) \tag{4.35}$$

$$s_{1,y}^{'}(t)=s_{1,y}(t)-L_y^{(0,0)} \tag{4.36}$$

$$s_{1,z}^{'}(t)=-(R_s\cos(\zeta(t))-L_x^{(0,0)})\sin(\alpha)+(s_{1,z}(t)-L_z^{(0,0)})\cos(\alpha) \tag{4.37}$$

$$s_{1,z}^{'}(t)=-(s_{1,x}(t)-L_x^{(0,0)})\sin(\alpha)+(s_{1,z}(t)-L_z^{(0,0)})\cos(\alpha) \tag{4.38}$$

If the sensor location is to be computed for only a single time instant, then it could be assumed that the sensor location is independent from all other time instants. For such an assumption, it is possible to drop the time dependency in the previous equations and write the sensor distance to $L^{(0,0)}$ with origin at LED center, for only a particular time instant will be,

$$D_{s1}^{(0,0)}=\sqrt{(s_{1,x}^{'})^2+(s_{1,y}^{'})^2+(s_{1,z}^{'})^2} \tag{4.39}$$

Similarly, the distance to sensor $L^{(m,n)}$ with the origin at LED $L^{(0,0)}$ center will be given by,

$$D_{s1}^{(m,n)}=\sqrt{(s_{1,x}^{(m,n)'})^2+(s_{1,y}^{(m,n)'})^2+(s_{1,z}^{(m,n)'})^2} \tag{4.40}$$

Substituting for components $s_{1,x}^{(m,n)'}$, $s_{1,x}^{(m,n)'}$ and $s_{1,x}^{(m,n)'}$ into $D_{s1}^{(m,n)}$ gives,

$$D_{s1}^{(m,n)}=\sqrt{(s_{1,x}^{'}-m\Delta x\cos(\alpha))^2+(s_{1,y}^{'}+n\Delta y)^2+(s_{1,z}^{'}-m\Delta x\sin(\alpha))^2} \tag{4.41}$$

that can also be more conveniently written in the form of,

$$D_{s1}^{(m,n)}=\sqrt{(D_{s1,x}^{'}-m\Delta x\cos(\alpha))^2+(D_{s1,y}^{'}+n\Delta y)^2+(D_{s1,z}^{'}-m\Delta x\sin(\alpha))^2} \tag{4.42}$$

Considering a sensor located on the IRC. The sensor position on the LED array plane can be obtained after translation and rotation of the origin to the center of LED $L^{(0,0)}$ will become,

$$s_1^{''}(t)=s_{1,x}^{''}(t)i+s_{1,y}^{''}(t)j+s_{1,z}^{''}(t)k \tag{4.43}$$

with components $s_{1,x}^{''}(t)$, $s_{1,y}^{''}(t)$ and $s_{1,z}^{''}(t)$ given by,

$$s_{1,x}^{''}(t)=(R_s\cos(\zeta(t))-L_x^{(0,0)})\cos(\beta)+(s_{1,z}(t)-L_z^{(0,0)})\sin(\beta) \tag{4.44}$$

$$s_{1,x}^{''}(t)=(s_{1,x}(t)-L_x^{(0,0)})\cos(\beta)+(s_{1,z}(t)-L_z^{(0,0)})\sin(\beta) \tag{4.45}$$

$$s_{1,y}^{''}(t)=R_s\sin(\zeta(t))-L_y^{(0,0)} \tag{4.46}$$

$$s_{1,y}^{''}(t)=s_{1,y}(t)-L_y^{(0,0)} \tag{4.47}$$

$$s_{1,z}^{''}(t)=-(R_s\cos(\zeta(t))-L_x^{(0,0)})\sin(\beta)+(s_{1,z}(t)-L_z^{(0,0)})\cos(\beta) \tag{4.48}$$

$$s_{1,z}^{''}(t)=-(s_{1,x}(t)-L_x^{(0,0)})\sin(\beta)+(s_{1,z}(t)-L_z^{(0,0)})\cos(\beta) \tag{4.49}$$

Then by dropping the time notation, then the sensor distance to $L^{(0,0)}$ with origin at LED center, for only a particular time instant will be,

$$d_{s1}^{(0,0)}=\sqrt{(s_{1,x}^{''})^2+(s_{1,y}^{''})^2+(s_{1,z}^{''})^2} \tag{4.50}$$

and the distance to sensor $L^{(m,n)}$ with the origin at LED $L^{(0,0)}$ center will be given by,

$$d_{s1}^{(m,n)}=\sqrt{\left(s_{1,x}^{(m,n)''}\right)^2+\left(s_{1,y}^{(m,n)''}\right)^2+\left(s_{1,z}^{(m,n)''}\right)^2} \tag{4.51}$$

Substituting for components $s_{1,x}^{(m,n)''}$, $s_{1,x}^{(m,n)''}$ and $s_{1,x}^{(m,n)''}$ into $d_{s1}^{(m,n)}$ gives,

$$d_{s1}^{(m,n)}=\sqrt{\left(s_{1,x}^{''}-m\Delta x\right)^2+\left(s_{1,y}^{''}+n\Delta y\right)^2+\left(s_{1,z}^{''}\right)^2} \tag{4.52}$$

It can be noticed from equation (4.52) that the distance is a function of only the variation in the new systems coordinates *x* and *y* along the LED array surface.

Moreover, equation (4.52) represents the distance between LED and sensor as a discrete. This function is discrete due to the fact that the transmitting LED occupies a specific location on the LED array plane. As the spacing between the LEDs could be chosen in a random fashion, it would be intuitive to allow for a continuous representation of the LEDs positions. In this case, Δx simply becomes x and Δy changes into y . Using this configuration, equation (4.52) can be represented in a more compact form of,

$$d_{s1}^{(m,n)}=\left(A_2x^2+A_1x+B_2y^2+B_1y+A_0\right)^{1/2} \tag{4.53}$$

with coefficients A_2 , A_1 , A_0 , B_2 and B_1 given as,

$$A_2=1 \tag{4.54}$$

$$A_1=-2s_{1,x}^{''} \tag{4.55}$$

$$B_2=1 \tag{4.56}$$

$$B_1=-2s_{1,y}^{''} \tag{4.57}$$

$$A_0=\left(s_{1,x}^{''}\right)^2+\left(s_{1,y}^{''}\right)^2+\left(s_{1,z}^{''}\right)^2 \tag{4.58}$$

4.3.3 Sensor Normal Vector:

In a similar way that the sensor position had been computed relative to the new systems coordinate, the normal vector to the sensor surface must, too, be recomputed. Then considering an initial normal vector $n_{s1}=\left(n_{s1,x}i,n_{s1,y}j,n_{s1,z}k\right)$ to sensor s_1 surface. In terms of the 3D vector components i , j and k , this vector

will vary in relation to the circular path of motion of the vehicle that has been given by equation (4.3). The sensor normal vector with respect to the LED array plane can be obtained using the translation and rotation with the center located at the center of LED $L^{(0,0)}$, $n_{s1}^{''}(t)$, will be given as,

$$n_{s1}^{''}(t)=n_{s1,x}^{''}(t)\,i+n_{s1,y}^{''}(t)\,j+n_{s1,z}^{''}(t)\,k \tag{4.59}$$

with components $n_{s1,x}^{''}(t)$, $n_{s1,y}^{''}(t)$ and $n_{s1,z}^{''}(t)$ given by,

$$n_{s1,x}^{''}(t)=(n_{s1,x}\cos(\xi(t))-L_x^{(0,0)})\cos(\beta)+(n_{s1,z}-L_z^{(0,0)})\sin(\beta) \tag{4.60}$$

$$n_{s1,x}^{''}(t)=(n_{s1,x}^{'}(t)-L_x^{(0,0)})\cos(\beta)+(n_{s1,z}^{'}-L_z^{(0,0)})\sin(\beta) \tag{4.61}$$

$$n_{s1,y}^{''}(t)=n_{s1,y}\sin(\xi(t))-L_y^{(0,0)} \tag{4.62}$$

$$n_{s1,y}^{''}(t)=n_{s1,y}^{'}(t)-L_y^{(0,0)} \tag{4.63}$$

$$n_{s1,z}^{''}(t)=-(n_{s1,x}\cos(\xi(t))-L_x^{(0,0)})\sin(\beta)+(n_{s1,z}-L_z^{(0,0)})\cos(\beta) \tag{4.64}$$

$$n_{s1,z}^{''}(t)=-(n_{s1,x}^{'}(t)-L_x^{(0,0)})\sin(\beta)+(n_{s1,z}^{'}-L_z^{(0,0)})\cos(\beta) \tag{4.65}$$

By dropping the time dependance, the components of $n_{s1}^{''}$ can be expressed in a more compact form by defining the following variables,

$$C_0=n_{s1,x}^{'} \tag{4.66}$$

$$C_1=n_{s1,z}^{'} \tag{4.67}$$

$$C_2=n_{s1,y}^{'} \tag{4.68}$$

Then $n_{s1}^{''}$ components will be given in the form of,

$$n_{s1,x}^{''}=C_0\cos(\beta)+C_1\sin(\beta) \tag{4.69}$$

$$n_{s1,y}^{''}=C_2 \tag{4.70}$$

$$n_{s1,z}^{''}=-C_0\sin(\beta)+C_1\cos(\beta) \tag{4.71}$$

Alternatively, for a sensor surface that is always normal to the vector connecting

LED $L^{(0,0)}$ and the center of s_1 , the normal component can be computed within the OC coordinate frame as,

$$\boldsymbol{n}_{\boldsymbol{s1}}^{(\boldsymbol{0,0})}=(-s_{1,x}^{'}\boldsymbol{i},-s_{1,y}^{'}\boldsymbol{j},-s_{1,z}^{'}\boldsymbol{k})/d_{s1} \tag{4.72}$$

where the center of the coordinate frame is located at LED $L^{(0,0)}$ center and $d_{s1}^{(0,0)}$ is the LED to sensor separation distance.

Then for a fixed normal vector to any other point (*m*,*n*) on the LED array, it can be simply obtained through,

$$\boldsymbol{n}_{\boldsymbol{s1}}^{(\boldsymbol{m,n})}=\frac{(m\Delta x\cos(\alpha)-s_{1,x}^{'}\ \boldsymbol{i},\ n\Delta y-s_{1,y}^{'}\ \boldsymbol{j},\ m\Delta x\sin(\alpha)-s_{1,z}^{'}\ \boldsymbol{k})}{d_{s1}^{(m,n)}} \tag{4.73}$$

with $d_{s1}^{(m,n)}$ can be obtained by equation (4.53).

4.3.4 The Luminous Intensity Distribution I :

The luminous intensity distribution, $I(\theta,\varphi)$, as had been briefly described for street lighting applications, acquires a particular form that resembles the wings of a bat. This type of illumination distribution is therefore suitably referred to as a bat wing distribution [150][151]. One such bat wing distribution pattern is shown in figures 4.7.

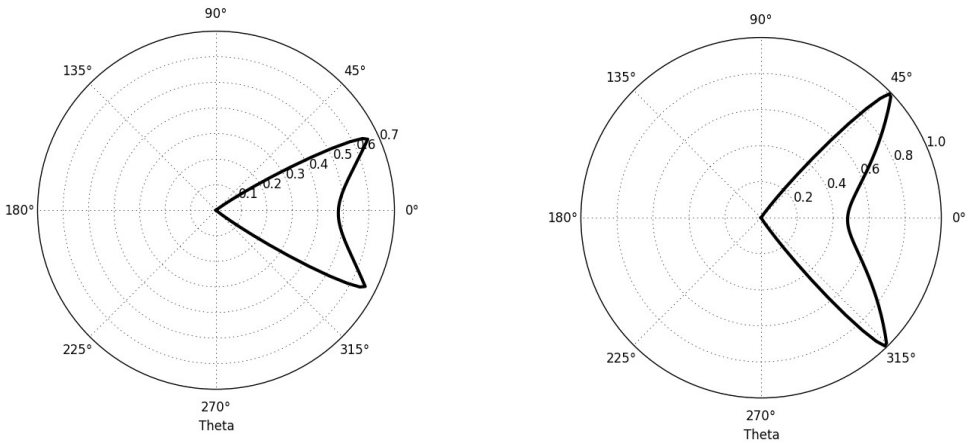

(a) (b)

Figure 4.7. Polar plot of luminous intensity distribution,, $I(\theta,\varphi)$ in planes (a) XZ and (b) YZ for street lighting

From the figure, the two curves are shown for the pattern in the XZ and YZ planes. The symmetrical pattern about the LED light fixture is clear with its resemblance to the wings of a bat. Also visible in the diagram is the difference in pattern in either plane. The pattern is elongated along the YZ plane, the length of the road, relative to the XZ plane, the breadth of the road. This is due to the simple fact that the illumination must cover the length and breadth of road surface. The distribution, as given in [5], is a function of both polar angle θ and azimuthal angle φ . It is described by,

$$I(\theta,\varphi)=U\,G(\theta)+(1-U)G(\theta_p(\varphi))e^{-g_0(\varphi)(|\theta|-\theta_p(\varphi))^2} \tag{4.74}$$

with parameter U and functions $g_0(\varphi)$, $\theta_p(\varphi)$ and $G(\theta)$ all described as follows,

$$U=\begin{cases}1, & \text{if } |\theta|<\theta_p(\varphi)\\ 0, & \text{if } |\theta|>\theta_p(\varphi)\end{cases} \tag{4.75}$$

$$g_0(\varphi)=\frac{g_{0,x}g_{0,y}}{\sqrt{(g_{0,x}\sin(\varphi))^2+(g_{0,y}\cos(\varphi))^2}} \tag{4.76}$$

$$\theta_p(\varphi)=\tan^{-1}\left(\frac{\tan(\theta_{p,x})\tan(\theta_{p,y})}{\left[(\tan(\theta_{p,x})\sin(\varphi))^{m_{SE}}+(\tan(\theta_{p,y})\cos(\varphi))^{m_{SE}}\right]^{(1/m_{SE})}}\right) \tag{4.77}$$

$$G(\theta)=g_1-g_2e^{-g_3(|\theta|-g_4)^2} \tag{4.78}$$

with parameters g_i , $i=\{1,2,3,4\}$, $g_{0,x}$ and $g_{0,y}$ are constants representing a specific intensity distribution.

Specifically, the functions $g_0(\varphi)$ and $\theta_p(\varphi)$, trace a super-ellipse over the optical axis plane. A super-ellipse can be generally generated using the equation,

$$\left|\frac{x}{a}\right|^n+\left|\frac{y}{b}\right|^n=1 \tag{4.79}$$

Finally, parameter m_{SE} defines the sharpness of the super-ellipse. The larger the value of m_{SE} the sharper the super-ellipse will be around the edges. Parameters $g_{0,x}$ and $g_{0,y}$ give the x and y axis intercept of ellipse $g_0(\varphi)$ Similarly,

parameters $\tan(\theta_{p,x})$ and $\tan(\theta_{p,y})$ give the x and y axis intercepts of super-ellipse $\theta_p(\varphi)$ as a function of the respective x and y peak angles $\theta_{p,x}$ and $\theta_{p,y}$.

The complete set of aforementioned equations of $I(\theta,\varphi)$ shows that the distribution is in reality a mix of two Gaussian functions. The switch parameter is U . From this aspect, parameter g_3 can be viewed as the inverse square of the variance of $G(\theta)$. The parameter values that are used in this study are given in table 4.1 below [5], where justification of $\theta_{p,y}=74^{\circ}$ is taken from lighting project shown in [152].

Table 4.1 Required parameters for $I(\theta,\varphi)$ computation.

Parameter	Value	Parameter	Value
m_{SE}	12	g_1	36.73
$\theta_{p,x}$	27.125	g_2	36.00
$\theta_{p,y}$	74.0	g_3	7.237×10^{-6}
g_0	0.027	g_4	0.0

4.3.5 Polar angle θ :

The normalized vector to LED $L^{(m,n)}$ which coincides with the LEDs OC axis can be defined by vector $n^{(m,n)}$. Equivalently, the normalized direction vector of sensor s_1 with the origin centered at LED $L^{(0,0)}$ is denoted by $s_1^{'}$. Then the angle, $\theta_{s1}^{(m,n)}$ which is the polar angle between both vectors, can be obtained through obtaining the inverse cosine of the dot product of the normalized vectors $n^{(m,n)}$ and $s_1^{'}$. This is given formally as,

$$\theta_{s1}^{(m,n)}=\cos^{-1}\left(n_x^{(m,n)}s_{1,x}^{'}+n_y^{(m,n)}s_{1,y}^{'}+n_z^{(m,n)}s_{1,z}^{'}\right) \tag{4.80}$$

Given that all LEDs share a common OC axis then the normalized vectors can be given as,

$$n^{(m,n)}=n^{(0,0)},\forall m,n \tag{4.81}$$

Then by inferring that the origin is placed at the center of LED $L^{(0,0)}$ and with the

OC axis aligned to a local -z-axis, $n^{(0,0)}$ can be described by vector $n^{(0,0)}=(0i,0j,-1k)$. Accordingly, $\theta_{s1}^{(m,n)}$ will be simplified to,

$$\theta_{s1}^{(m,n)}=\cos^{-1}\left(n_z^{(m,n)}s_{1,z}^{'}\right) \tag{4.82}$$

In the following analysis the polar angle centered at LED $L^{(0,0)}$ will be described. This will be followed by the analysis of the general case for the polar angle centered at LED $L^{(m,n)}$, which is a direct extension from the analysis of LED $L^{(0,0)}$.

1. Angle at center of LED $L^{(0,0)}$, $\theta_{s1}^{(0,0)}$:

From the distance of s_1 to LED $L^{(0,0)}$ using the OC plane, the angle $\theta_{s1}^{(0,0)}$ can be computed using,

$$\theta_{s1}^{(0,0)}=\cos^{-1}\left(s_{1,z}^{'}/d_{s1}^{(0,0)}\right) \tag{4.83}$$

2. Angle at center of LED $L^{(m,n)}$, $\theta_{s1}^{(m,n)}$:

From the distance of s_1 to LED $L^{(m,n)}$ using the OC plane, the angle $\theta_{s1}^{(m,n)}$ can be computed using,

$$\theta_{s1}^{(m,n)}=\cos^{-1}\left(\left(s_{1,z}^{'}-m\Delta x\sin(\alpha)\right)/d_{s1}^{(m,n)}\right) \tag{4.84}$$

By considering that the spacing could assume any arbitrary value then for the analysis it is assumed that Δx and Δy both become x and y on the LED array surface, and $\theta_{s1}^{(m,n)}$ can be transformed into a continuous function θ_{s1} . Angle θ_{s1} can then be written in the form of,

$$\theta_{s1}=\cos^{-1}\left(E/d_{s1}\right) \tag{4.85}$$

with the numerator E given by,

$$E=s_{1,z}^{'}-x\ \sin(\alpha) \tag{4.86}$$

4.3.6 Azimuthal angle φ :

With reference to figure 4.6, the azimuthal angles can then be easily computed from the distance $d_{s1}^{(m,n)}$ using,

$$\varphi_{s1}^{(m,n)} = \tan^{-1}\left(s_{1,y}^{(m,n)'} / s_{1,x}^{(m,n)'}\right) \tag{4.87}$$

substituting for $s_{1,x}^{(m,n)'}$ and $s_{1,y}^{(m,n)'}$ the angle $\varphi_{s1}^{(m,n)}$ can be given as,

$$\varphi_{s1}^{(m,n)} = \tan^{-1}\left(\frac{s_{1,y}^{'} + n\Delta y}{s_{1,x}^{'} - m\Delta x\cos(\alpha)}\right) \tag{4.88}$$

Again, invoking the assumption that Δx and Δy both become x and y for the case the analysis of the infinitely small spacing of LED elements, $\varphi_{s1}^{(m,n)}$ can be written as,

$$\varphi_{s1} = \tan^{-1}\left(\frac{s_{1,y}^{'} + y}{s_{1,x}^{'} - x\cos(\alpha)}\right) \tag{4.89}$$

4.3.7 Sensor to LED Viewing Angle ψ :

The visibility of an LED at the surface of s_1 can be given relative to the angle it makes with the normal vector pointing in the direction towards the LED center. This angle will be denoted by ψ and can be computed from the positions of both s_1 and a particular LED. To obtain ψ , it is imperative to define the normal vector to the surface of sensor s_1 , $n_{s1}(t)$, and the normalized direction vector from s_1 to LED $L^{(m,n)}$, $p_{s1}^{(m,n)}(t)$. Both vectors can be defined relative to the LED array plane. Then for the observation of LED $L^{(m,n)}$, the angle $\psi_{s1}^{(m,n)}(t)$ is obtained through invoking the dot product of the two normalized vectors $p_{s1}^{(m,n)}(t)$ and $n_{s1}^{''}(t)$ as follows,

$$\psi_{s1}^{(m,n)}(t) = \cos^{-1}\left(p_{s1,x}^{(m,n)}(t)n_{s1,x}^{''}(t) + p_{s1,y}^{(m,n)}(t)n_{s1,y}^{''}(t) + p_{s1,z}^{(m,n)}(t)n_{s1,z}^{''}(t)\right) \tag{4.90}$$

with the components of $p_{s1}^{(m,n)}(t)$ are given by,

$$p_{s1,x}^{(m,n)}(t) = \frac{L_x^{(m,n)} - s_{1,x}^{''}(t)}{d_{s1}^{(m,n)''}(t)} \tag{4.91}$$

$$p_{s1,y}^{(m,n)}(t) = \frac{L_y^{(m,n)} - s_{1,y}^{''}(t)}{d_{s1}^{(m,n)''}(t)} \tag{4.92}$$

$$p_{s1,z}^{(m,n)}(t)=\frac{L_z^{(m,n)}-s_{1,z}^{''}(t)}{d_{s1}^{(m,n)''}(t)} \tag{4.93}$$

For the single instant of time observation, the time dependence can be removed from the previous equations. By substituting for $L_x^{(m,n)}$, $L_y^{(m,n)}$ and $L_z^{(m,n)}$ the identities can therefore be given as,

$$p_{s1,x}^{(m,n)}=\frac{L_x^{(0,0)}-m\Delta x-s_{1,x}^{''}}{d_{s1}^{(m,n)''}} \tag{4.94}$$

$$p_{s1,y}^{(m,n)}=\frac{L_y^{(0,0)}+n\Delta y-s_{1,y}^{''}}{d_{s1}^{(m,n)''}} \tag{4.95}$$

$$p_{s1,z}^{(m,n)}=\frac{L_z^{(0,0)}-s_{1,z}^{''}}{d_{s1}^{(m,n)''}} \tag{4.96}$$

The components of $p_{s1}^{(m,n)}$ can be further written in a more compact form by defining the following variables,

$$C_3=-s_{1,x}^{''} \tag{4.97}$$

$$C_4=-s_{1,y}^{''} \tag{4.98}$$

$$C_5=-s_{1,z}^{''} \tag{4.99}$$

Then using these variables and substituting the previous identities for $\psi_{s1}^{(m,n)}(t)$ while dropping the time notation, $\psi_{s1}^{(m,n)}$ can be written as,

$$\psi_{s1}^{(m,n)}=\cos^{-1}\left(\left(\left(C_3-m\Delta x\right)n_{s1,x}^{''}+\left(C_4+n\Delta y\right)n_{s1,y}^{''}+C_5n_{s1,z}^{''}\right)/d_{s1}^{(m,n)''}\right) \tag{4.100}$$

Furthermore, using the reasoning that the LEDs could be placed at random spacing, then for analyzing the effect of spacing, it could be assumed that the spacing between the LED elements becomes infinitely small. Under such an assumption it can be considered practically that Δx and Δy both become x and y and $\psi_{s1}^{(m,n)}$

can be written in the following compact form,

$$\psi_{s1}=\cos^{-1}\left(\left(D_2x+D_1y+D_0\right)/d_{s1}\right) \tag{4.101}$$

with coefficients D_0 , D_1 and D_2 given by,

$$D_0=C_2C_4+\left(C_0C_3+C_1C_5\right)\cos\left(\beta\right)+\left(C_1C_3-C_0C_5\right)\sin\left(\beta\right) \tag{4.102}$$

$$D_1=C_2 \tag{4.103}$$

$$D_2=-\left(C_0\cos\left(\beta\right)+C_1\sin\left(\beta\right)\right) \tag{4.104}$$

In certain circumstances, interest is given to the cosine of the angle rather than the angle per se. Therefore the variable $\psi_{s1}^{'}$ can be defined as,

$$\psi_{s1}^{'}=\cos\left(\psi_{s1}\right) \tag{4.105}$$

which can then be equally expanded into,

$$\psi_{s1}^{'}=\frac{D_2x+D_1y+D_0}{\left(A_2x^2+A_1x+B_2y^2+B_1y+A_0\right)^{1/2}} \tag{4.106}$$

4.3.8 The Streetlight DC Channel Response $H_{s1}(0;t)$:

In the VLC system, the DC channel gain can be defined as the gain observed by the receiver of the direct LOS path from the emitter to the receiver. With knowledge of $I(\theta,\varphi)$ and angle $\psi_{s1}^{(m,n)}(t)$, the direct LOS DC channel gain $H_{s1}^{(m,n)}(0;t)$, between LED $L^{(m,n)}$ and sensor s_1 can be computed at a particular location. Using the approach shown in [2], $H_{s1}^{(m,n)}(0;t)$ is computed as,

$$H_{s1}^{(m,n)}(0;t)=\begin{cases}\left(\dfrac{A_{s1}}{\left(d_{s1}^{(m,n)}(t)\right)^2}\right)I_{s1}^{(m,n)}(\theta,\varphi)G^{(m,n)}(\psi_{s1}^{(m,n)}(t)) & \\ \quad\times G_{s1}(\psi_{s1}^{(m,n)}(t))\cos(\psi_{s1}^{(m,n)}(t)), & 0\le\psi_{s1}^{(m,n)}(t)\le\psi_{FOV} \\ 0, & \psi_{s1}^{(m,n)}(t)>\psi_{FOV}\end{cases} \tag{4.107}$$

where,

$G^{(m,n)}(\psi_{s1}^{(m,n)}(t))$ and $G_{s1}(\psi_{s1}^{(m,n)}(t))$ are the optical gains of the transmitter and receiver respectively, $\psi_{s1}^{(m,n)}(t)$ is the angle between LED $L^{(m,n)}$

and the normal vector to the sensor plane and ψ_{FOV} is the FOV angle which is a parameter specified by the PD manufacturers [149]. Angle $\psi_{s1}^{(m,n)}(t)$ is also referred to as the incidence angle of the optical ray from the LED to sensor. A nominal value for the ψ_{FOV} is 60˚. In the expression of the DC channel response, the time parameter, t , has been explicitly dropped.

Herein, it will be assumed that $G^{(m,n)}(\psi_{s1}^{(m,n)}(t))$ is unity, while $G_{s1}(\psi_{s1}^{(m,n)}(t))$ is given by,

$$G_{s1}(\psi_{s1}^{(m,n)}(t))=\begin{cases}\dfrac{n_i^2}{\sin^2(\psi_{s1}^{(m,n)}(t))}, & 0\le\psi_{s1}^{(m,n)}(t)\le\psi_{FOV}\\ 0, & \psi_{s1}^{(m,n)}(t)>\psi_{FOV}\end{cases} \tag{4.108}$$

In most literature, the expression of $G_{s1}(\psi_{s1}^{(m,n)}(t))$ is simplified through the assumption that a hemispherical concentrator is utilized [153]. In this configuration, the expression of $G_{s1}(\psi_{s1}^{(m,n)}(t))$ will be,

$$G_{s1}(\psi_{s1}^{(m,n)}(t))=\begin{cases}\dfrac{n_i^2}{\sin^2(\psi_{FOV})}, & 0\le\psi_{s1}^{(m,n)}(t)\le\psi_{FOV}\\ 0, & \psi_{s1}^{(m,n)}(t)>\psi_{FOV}\end{cases} \tag{4.109}$$

The equation clearly shows that the $G_{s1}(\psi_{s1}^{(m,n)}(t))$ is independent of the incidence angle over the entire FOV of the receiver.

Using gains $G^{(m,n)}(\psi_{s1}^{(m,n)}(t))$ and $G_{s1}(\psi_{s1}^{(m,n)}(t))$ simplification, the equation of the DC channel gain can be modified into,

$$H_{s1}^{(m,n)}(0;t)=\begin{cases}\dfrac{A_{s1}n_i^2}{\sin^2(\psi_{FOV})(d_{s1}^{(m,n)})^2}I_{s1}^{(m,n)}(\theta,\varphi)\cos(\psi_{s1}^{(m,n)}), & 0\le\psi_{s1}^{(m,n)}\le\psi_{FOV}\\ 0, & \psi_{s1}^{(m,n)}>\psi_{FOV}\end{cases} \tag{4.110}$$

Finally, the overall DC channel gain, $H_{s1}(0;t)$, can be determined from the individual DC channel gains $H_{s1}^{(m,n)}(0;t)$ for all $(N)\times(2M-1)$ LEDs. This is given in the form of,

$$H_{s1}(0;t)=\sum_{m=0}^{M-1}\sum_{n=1-N}^{N-1}H_{s1}^{(m,n)}(0;t) \tag{4.111}$$

Then using the identity of the DC channel gain,

$$H_{s1}(0;t_0)=\int_{-\infty}^{\infty}h_{s1}(t;t_0)dt \tag{4.112}$$

The impulse response, $h_{s1}(t;t_0)$ can be obtained from $H_{s1}^{(m,n)}(0;t_0)$ through,

$$h_{s1}(t;t_0)=\sum_{m=0}^{M-1}\sum_{n=1-N}^{N-1}H_{s1}^{(m,n)}(0;t_0)\delta(t_0-t_{m,n}) \tag{4.113}$$

where $\delta(t_{m,n})$ is the time of arrival (TOA) delay of the LOS component emanating from LED $L^{(m,n)}$.

Finally, the impulse response could also be represented in it usual form, for any location on the tracks surface through,

$$h_{s1}(t)=\sum_{m=0}^{M-1}\sum_{n=1-N}^{N-1}H_{s1}^{(m,n)}(0)\delta(t-t_{m,n}) \tag{4.114}$$

where DC component $H_{s1}^{(m,n)}(0)$ represents the DC channel gain at an arbitrary point on the roads surface.

4.4 A Differential Analysis of the DC Channel Response:

In the previous section it had been shown that $H_{s1}(0;t)$ is the accumulated effect of every LED element within an LED luminaire. Furthermore, obtaining $H_{s1}(0;t)$ over the road surface requires that computations be repeated at every location on the road surface. In terms of computation, this can be viewed as an intensive operation, especially when the number of LEDs is large.

Knowing that the LEDs are placed within close proximity on an LED panel, the aim herein is to investigate the possibility of reducing the required computations by considering the differential DC channel response effect of the LEDs onto a single reference LED. Accordingly, it is hypothesized that it is sufficient to obtain the exact DC channel response of a single reference LED and extend the effect of all

remaining LEDs through each individual LEDs differential DC channel response contribution. Towards achieving this, derivation of the DC channel response differential equations is undertaken, for all parameters that constituent the DC channel response shown in equation (4.110). The methods complexity will compared to the exact DC channel response.

4.4.1 Differential Analysis of $H_{s1}(0;t)$:

Consider that the DC channel response is to obtained over an entire rectangular array plane. It could be assumed that the plane contains an infinite number of LEDs each producing an identical intensity distribution with identical optical axes, *OC*. A sensor observing the LED array will observe a DC response equivalent to the effects of the individual LEDs. This variation in the DC channel response over the entire array plane extending in the *x* and *y* axes can be determined from the expression,

$$dH = \frac{\partial}{\partial x} H\, dx + \frac{\partial}{\partial y} H\, dy \tag{4.115}$$

It is therefore meaningful to represent the equation of $H_{s1}(0)$ whose variables are in terms of x and y . By defining a variable V , as $V = 1/d_{s1}^2$, this can be achieved using,

$$H_{s1}(0) = \begin{cases} \dfrac{A_{s1} n_i^2}{\sin^2(\psi_{FOV})} V_{s1}(x,y) I_{s1}(x,y) \psi'_{s1}(x,y), & 0 \le \psi_s \le \psi_{FOV} \\ 0, & \psi_{s1} > \psi_{FOV} \end{cases} \tag{4.116}$$

From equation (4.116), it is clear that $H_{s1}(0)$ is characterized by the three variables $V_{s1}(x,y)$, $I_{s1}(x,y)$ and $\psi'_{s1}(x,y)$. Then the differential $dH_{s1}(0)$ can be obtained using the identities,

$$\frac{\partial}{\partial x}(V_{s1} I_{s1} \psi'_{s1}) = \frac{A_{s1} n_i^2}{\sin^2(\psi_{FOV})} \left((V_{s1} I_{s1}) \frac{\partial \psi'_{s1}}{\partial x} + (V_{s1} \psi'_{s1}) \frac{\partial I_{s1}}{\partial x} + (I_{s1} \psi'_{s1}) \frac{\partial V_{s1}}{\partial x} \right) \tag{4.117}$$

$$\frac{\partial}{\partial y}(V_{s1} I_{s1} \psi'_{s1}) = \frac{A_{s1} n_i^2}{\sin^2(\psi_{FOV})} \left((V_{s1} I_{s1}) \frac{\partial \psi'_{s1}}{\partial y} + (V_{s1} \psi'_{s1}) \frac{\partial I_{s1}}{\partial y} + (I_{s1} \psi'_{s1}) \frac{\partial V_{s1}}{\partial y} \right) \tag{4.118}$$

Where it is required to obtain the partials derivatives of $V_{s1}(x,y)$, $I_{s1}(x,y)$ and $\psi_{s1}^{'}(x,y)$ over the road surface.

The DC channel gain can then finally be represented using the ensemble of differential equations of all three parameters along the x and y axes over the road surface as,

$$H_{s1}(0)=\begin{cases}\sum_{m=-M+1}^{M-1}\sum_{n=0}^{N-1}\left(H_{s1}^{(0,0)}(0)+\frac{\partial}{\partial x}H_{s1}(0)\,dx_n+\frac{\partial}{\partial y}H_{s1}(0)\,dy_m\right), & 0\le\psi_{s1}\le\psi_{FOV}\\ 0, & \psi_{s1}>\psi_{FOV}\end{cases} \tag{4.119}$$

Including the three variables that $H_{s1}(0)$ depends on, there are a further two indirectly related variables to $H_{s1}(0)$, namely θ and φ . These two variables are directly connected to the evaluation of $I(\theta,\varphi)$. Therefore, in the following sections, the differential of the three variables and all the dependent variables, required in the evaluation of equation (4.116) and hence (4.119), is going to be outlined.

4.4.2 Differential of d_{s1} with respect to x and y :

The distance partial differential with respect to the *x* and *y* axes, $\frac{\partial V}{\partial x}$ and $\frac{\partial V}{\partial y}$, can be obtained as,

$$\frac{\partial V}{\partial x}=-(2A_2x+A_1)V \tag{4.120}$$

and

$$\frac{\partial V}{\partial y}=-(2B_2y+B_1)V \tag{4.121}$$

4.4.3 Differential of $\psi_{s1}^{'}$ with respect to x and y :

For $\psi_{s1}^{'}$, the partial derivatives with respect to axes *x* and *y*, $\frac{\partial \psi_{s1}^{'}}{\partial x}$ and $\frac{\partial \psi_{s1}^{'}}{\partial y}$, can be respectively obtained as,

$$\frac{\partial \psi_{s1}^{'}}{\partial x}=\frac{2D_2 d_{s1}^2-(2A_2 x+A_1)(D_2 x+D_1 y+D_0)}{2d_{s1}^3} \tag{4.122}$$

and

$$\frac{\partial \psi_{s1}^{'}}{\partial y}=\frac{2D_2 d_{s1}^2-(2B_2 y+B_1)(D_2 x+D_1 y+D_0)}{2d_{s1}^3} \tag{4.123}$$

4.4.4 Differential of θ_{s1} with respect to x and y :

Using the fact that $sec^{-1}(x)=\cos^{-1}(1/x)$ along with the following integral,

$$\int \frac{du}{u\sqrt{u^2-a^2}}=\frac{1}{a}sec^{-1}(\frac{u}{a}) \tag{4.124}$$

the partial derivatives of θ_{s1} along the *x* and *y* axes, $\frac{\partial}{\partial x}\theta_{s1}$ and $\frac{\partial}{\partial y}\theta_{s1}$, are respectively given as,

$$\frac{\partial}{\partial x}\theta_{s1}=\frac{E(2A_2 x+A_1)-2d_{s1}^2\sin(\alpha)}{2d_{s1}^2 E\left((\frac{d_{s1}}{E})^2-1\right)^{1/2}} \tag{4.125}$$

$$\frac{\partial}{\partial y}\theta_{s1}=\frac{2B_2 y+B_1}{2d_{s1}^2\left((\frac{d_{s1}}{E})^2-1\right)^{1/2}} \tag{4.126}$$

4.4.5 Differential of φ_{s1} with respect to x and y :

It should be realized that angle φ_{s1} is defined over the OC plane. For such reasons, the vehicle position must first be transformed onto the OC plane prior to obtaining the differential of φ_{s1} .

The partial derivatives along the axes, the respective variation along the *x* and *y* axes, $\frac{\partial}{\partial x}\varphi_{s1}$ and $\frac{\partial}{\partial y}\varphi_{s1}$, can be derived by utilizing the identity,

$$\int \frac{du}{u^2+a^2}=(\frac{1}{a})\tan^{-1}(\frac{u}{a}) \tag{4.127}$$

The derived $\frac{\partial}{\partial x}\varphi_{s1}$ and $\frac{\partial}{\partial y}\varphi_{s1}$ will then respectively be,

$$\frac{\partial}{\partial x}\varphi_{s1}=\frac{(s'_{1,y}+y)\cos(\alpha)}{(s'_{1,x}-x\cos(\alpha))^2+(s'_{1,y}+y)^2} \tag{4.128}$$

$$\frac{\partial}{\partial y}\varphi_{s1}=\frac{s'_{1,x}-x\cos(\alpha)}{(s'_{1,x}-x\cos(\alpha))^2+(s'_{1,y}+y)^2} \tag{4.129}$$

4.4.6 Differential of $I(\theta,\varphi)$ with respect to x and y :

The luminous intensity, $I(\theta,\varphi)$, is clearly a function of angles θ and φ . In turn, a number of derived relations for both angles relative to axes *x* and *y* have been established as shown in section (4.3.3). With this, the variation of $I(\theta,\varphi)$ relative to the *x* and *y* axes can be obtained using the chain rule. Accordingly, the derivative with respect to the *x* and *y* axes will be,

$$\frac{d}{dx}I=\frac{\partial I}{\partial\theta}\frac{\partial\theta}{\partial x}+\frac{\partial I}{\partial\varphi}\frac{\partial\varphi}{\partial x} \tag{4.130}$$

$$\frac{d}{dy}I=\frac{\partial I}{\partial\theta}\frac{\partial\theta}{\partial y}+\frac{\partial I}{\partial\varphi}\frac{\partial\varphi}{\partial y} \tag{4.131}$$

Equations (4.130) and (4.131) require partial differentials $\frac{\partial\theta}{\partial x}$, $\frac{\partial\theta}{\partial y}$, $\frac{\partial\varphi}{\partial x}$ and $\frac{\partial\varphi}{\partial y}$ that have been previously obtained in sections (4.4.4) and (4.4.5). The remaining quantities required in both equations are partial differentials $\frac{\partial I}{\partial\theta}$ and $\frac{\partial I}{\partial\varphi}$. To obtain these two partial differentials it is necessary to delve further into the luminous intensity equations.

The luminous intensity is a non-continuous function that takes two distinct forms that depends on relative magnitude of θ and $\theta_p(\varphi)$, as indicated by equation (4.75). To distinguish between both cases, the case with $|\theta|<\theta_p(\varphi)$ shall be considered as case 1 and that with $|\theta|>\theta_p(\varphi)$ as case 2.

4.4.6.1 Case 1:

In this case $I(\theta,\varphi)$ will reduce to,

$$I(\theta,\varphi)=G(\theta) \tag{4.132}$$

From the equation it is clear that $I(\theta,\varphi)$ is independent of angle φ such that $I(\theta,\varphi)=I(\theta)$ for this case. To obtain the change of the intensity with respect to θ, the differential $\frac{dI(\theta)}{d\theta}$ must be derived. Using the identity,

$$\frac{d|\theta|}{dx}=\frac{\theta\times\theta'}{|\theta|} \tag{4.133}$$

the derivative $\frac{dI(\theta)}{d\theta}$ is obtained as follows,

$$\frac{dI(\theta)}{d\theta}=\frac{dG(\theta)}{d\theta}=2g_2g_3(|\theta|-g_4)\frac{\theta}{|\theta|}e^{-g_3(|\theta|-g_4)^2} \tag{4.134}$$

Equivalently, for this case equations (4.130) and (4.131) reduces into,

$$\frac{d}{dx}I=\frac{\partial I}{\partial\theta}\frac{\partial\theta}{\partial x} \tag{4.135}$$

$$\frac{d}{dy}I=\frac{\partial I}{\partial\theta}\frac{\partial\theta}{\partial y} \tag{4.136}$$

4.4.6.2 Case 2:

From equation (4.74), $I(\theta,\varphi)$ can be explicitly written, for this specific case, as,

$$I(\theta,\varphi)=G(\theta_p(\varphi))e^{-g_0(\varphi)(|\theta|-\theta_p(\varphi))^2} \tag{4.137}$$

that is a function of both θ and φ. To obtain $dI(\theta,\varphi)$ it is necessary to derive the partial derivatives with respect to θ and φ.

The partial derivative with respect to θ will be,

$$\frac{\partial}{\partial\theta}I(\theta)=-2G(\theta_p(\varphi))g_0(\varphi)(|\theta|-\theta_p(\varphi))\frac{\theta}{|\theta|}e^{-g_0(\varphi)(|\theta|-\theta_p(\varphi))^2} \tag{4.138}$$

Next, the differential $\frac{\partial I(\theta,\varphi)}{\partial\varphi}$ is to be derived. From the equation of $I(\theta,\varphi)$, variables $g_0(\varphi)$, $\theta_p(\varphi)$ and $G(\theta_p(\varphi))$ are all dependent on φ.

Therefore, the differential of each of the three parameters with respect to φ has to be initially obtained as shown within the following expression of $\frac{\partial I(\theta,\varphi)}{\partial \varphi}$,

$$\frac{\partial I(\theta,\varphi)}{\partial \varphi}=\frac{\partial I(\theta,\varphi)}{\partial g_0(\varphi)}\frac{\partial g_0(\varphi)}{\partial \varphi} + \frac{\partial I(\theta,\varphi)}{\partial \theta_p(\varphi)}\frac{\partial \theta_p(\varphi)}{\partial \varphi} + \frac{\partial I(\theta,\varphi)}{\partial G(\theta_p(\varphi))}\frac{\partial G(\theta_p(\varphi))}{\partial \varphi} \tag{4.139}$$

From the previous equation (4.139), it is clear that the equation is composed from three terms, and that with each term in turn composed from two other terms. Each of the first, second and third terms correspond to functions of $g_0(\varphi)$, $\theta_p(\varphi)$ and $G(\theta_p(\varphi))$ respectively. Then for the first term in equation (4.139), the partial differential term $\frac{\partial I(\theta,\varphi)}{\partial g_0(\varphi)}$ can be is obtained as,

$$\frac{\partial I(\theta,\varphi)}{\partial g_0(\varphi)}=-G(\theta_p(\varphi))(|(\theta)|-\theta_p(\varphi))^2 e^{-g_0(\varphi)(|(\theta)|-\theta_p(\varphi))^2} \tag{4.140}$$

And subsequently the partial differential term $\frac{dg_0(\varphi)}{d\varphi}$, will be,

$$\frac{dg_0(\varphi)}{d\varphi}=\frac{-g_{0,x}g_{0,y}\cos(\varphi)\sin(\varphi)(g_{0,x}^2-g_{0,y}^2)}{((g_{0,x}\sin(\varphi))^2+(g_{0,y}\cos(\varphi))^2)^{3/2}} \tag{4.141}$$

Next, the partial derivative of $\frac{\partial I(\theta,\varphi)}{\partial \theta_p(\varphi)}$ can be obtained in the form of

$$\frac{\partial I(\theta,\varphi)}{\partial \theta_p(\varphi)}=2G(\theta_p(\varphi))g_0(\varphi)(|(\theta)|-\theta_p(\varphi))e^{-g_0(\varphi)(|(\theta)|-\theta_p(\varphi))^2} \tag{4.142}$$

And subsequently the second partial differential term in term 2, $\frac{\partial \theta_p(\varphi)}{\partial \varphi}$, is evaluated as,

$$\frac{\partial \theta_p(\varphi)}{\partial \varphi}=\frac{-A_x A_y (B_x^{m_{SE}}+B_y^{m_{SE}})^{\frac{-1-m_{SE}}{m_{SE}}}}{1+\left(\frac{A_x A_y}{(B_x^{m_{SE}}+B_y^{m_{SE}})^{1/m_{SE}}}\right)^2}\times\left(\frac{B_x^{m_{SE}}\cos(\varphi)}{\sin(\varphi)}-\frac{B_y^{m_{SE}}\sin(\varphi)}{\cos(\varphi)}\right) \tag{4.143}$$

where,

$$A_x = \tan(\theta_{p,x}) \tag{4.144}$$

$$A_y = \tan(\theta_{p,y}) \tag{4.145}$$

$$B_x = A_x \sin(\varphi) \tag{4.146}$$

$$B_y = A_y \cos(\varphi) \tag{4.147}$$

Finally, for the third partial differential term, the derivative of $\frac{\partial I(\theta,\varphi)}{\partial G(\theta_p(\varphi))}$ can be obtained as,

$$\frac{\partial I(\theta,\varphi)}{\partial G(\theta_p(\varphi))} = e^{-g_0(\varphi)(|(\theta)|-\theta_p(\varphi))^2} \tag{4.148}$$

And the second partial differential term within the third term, $\frac{\partial G(\theta_p(\varphi))}{\partial \varphi}$, must be evaluated using the following expression,

$$\frac{\partial G(\theta_p(\varphi))}{\partial \varphi} = \frac{\partial G(\theta_p(\varphi))}{\partial \theta_p(\varphi)} \frac{\partial \theta_p(\varphi)}{\partial \varphi} \tag{4.149}$$

where $\frac{\partial G(\theta_p(\varphi))}{\partial \theta_p(\varphi)}$ is given by,

$$\frac{\partial G(\theta_p(\varphi))}{\partial \theta_p(\varphi)} = -2 g_2 g_3 (|\theta_p(\varphi)| - g_4) \frac{\theta_p(\varphi)}{|\theta_p(\varphi)|} e^{-g_3(|\theta_p(\varphi)|-g_4)^2} \tag{4.150}$$

and $\frac{\partial \theta_p(\varphi)}{\partial \varphi}$ has been evaluated earlier in equations (4.143).

4.4.7 Complexity of the Method:

The proposed method in this section is based upon obtaining the DC channel response of an LED luminaire through applying the differential responses to a single reference LEDs exact response. However, obtaining the differential responses, has proven to be more complex, in terms of computational effort, as opposed to directly obtaining $H_{s1}^{(m,n)}(0;t)$ for each LED. Henceforth, applying this method will not be

further used within this study.

4.5 Single LED Equivalent $H_{s1}(0;t)$ for an LED Array:

This proposed method is again based upon the fact that the distance between LEDs is small compared to the distance from an LED to sensor. Accordingly, it can be hypothesized that for a sensor placed within the LED illumination zone, that

$$H_{s1}^{(m,n)}(0;t) \approx \frac{1}{N_{LED}} H_{s1}(0;t) \tag{4.151}$$

where N_{LED} is the total number of LEDs within a luminaire.

Under this proposed method for outdoor VLC it is, therefore, sufficient to obtain the DC channel response of a single LED and multiply by the total number of LEDs. To this effect, the DC channel response with respect to the single reference LED becomes,

$$\left(H_{s1}(0;t)\right)' = N_{LED} H_{s1}^{(m,n)}(0;t) \tag{4.152}$$

which is a much simpler representation as compared to equation (4.111).

However, from equation (4.111), it is clear that the position of each LED on the LED array will effect the DC channel response differently. Therefore, it is important to choose the position of the reference LED that will attain greatest accuracy as compared to the exact $H_{s1}(0;t)$. A possible choice for this is to place the reference LED at the middle point of the LED array. Accordingly, if M is odd, $H_{s1}(0;t)$ becomes,

$$\left(H_{s1}(0;t)\right)' = N_{LED} H_{s1}^{(M/2,0)}(0;t) \tag{4.153}$$

While for M even, $H_{s1}(0;t)$ is,

$$\left(H_{s1}(0;t)\right)' = N_{LED}\left(H_{s1}^{(M/2-1,0)}(0;t) + H_{s1}^{(M/2+1,0)}(0;t)\right)/2 \tag{4.154}$$

Chapter 5

Perturbations Analysis

5.1 Introduction:

In this chapter two types of perturbations are to be analyzed. The first kind is due to the translation of a luminaire while the second is due to its rotation. Each type will be analyzed separately under the consideration that each of the two perturbations are independent from the other. Although both types, in reality, can effect the luminaire at the same time instant, however, the objective herein is to obtain a measure on the effect of each type on the channels response. To be more specific, as it had been shown in chapter 4, the DC channel response is a function of angles θ , φ and ψ . Moreover, the luminous intensity distribution, $I(\theta,\varphi)$, is a function of the first two angles. To establish the amount of perturbation the luminaire will undergo, it is imperative to obtain a measure on the effect of the luminaires rotation and translation on each of the angles. With the effect of the perturbations on the angles known, it will then be possible to find the effect of both types of perturbations on $I(\theta,\varphi)$. Subsequently, it will then be possible to determine the effect of both perturbation types on the DC channel response, $H(0)$, of equation (4.114).

Prior to proceeding with the analysis, it is first required to obtain the amount of movement that a luminaire can undertake. This will be shown in the following section, 5.2. In section 5.3, the analysis of the rotation perturbation will be developed followed by the translation perturbations in section 5.4. As the channel response is partly a function of the light intensity distribution, therefore, in section 5.5 the analysis on the effect of each parameter constituting $I(\theta,\varphi)$ will be demonstrated. The section will terminate by outlining a pick of the most important factors will be

used for the perturbed channel response. Finally, in section 5.6, the analysis will be extended to the overall channel response.

5.2 Perturbation Range:

Streetlight poles can shift under the influence of external forces, thereby perturbing the VLC link between the Tx and Rx. The number of external forces are numerous, such as wind, gust and tremors. However, the outcome effect of each type of external force will amount to either a rotation or a translation or a combination of both rotation and translation onto the transmitting luminaire. Therefore, irrespective of the type of external force acting on the luminaire, the concern herein amounts to the overall influence such forces will induce variations to the VLC channel. In light of this view, it can be perceived that a traveling vehicle, which is currently occupying a lane center, will continue to follow this perfect lane center. All perturbations will be induced at the transmitting luminaire end only. From another perspective, the light pole can be imagined to be stationary with the cause of all variations encapsulated into the moving vehicle. However, from either perspective the resultant analysis should remain the same, because the relative motion of Tx and Rx is what matters. Then by using the second perspective, the overall effect of all these variations can be viewed in light of the small scale deviations of a vehicle from the lanes center it is currently occupying. The deviation will result in variations to the separation distance of vehicle sensors and LED luminaire. Under the same reasoning, angles θ , φ and ψ will all experience an amount of small scale variations.

To address the problem of the amount of perturbation which will alter the DC channel response, the first perspective will be adopted. A quantitative measure on the amount of deviation a luminaire will be subjected to is to be undertaken herein. Accordingly, it has been indicated in [143] that the approximate maximum deviations a slender light pole will experience due to wind is $\delta_w = 120.0\,mm$. As the authors in [143] did not indicate to whether this deviation is in the *x*, *y* or *z* axes, it will be assumed that the luminaire can shift freely a maximum of δ_w in any of the three

axes. Furthermore, from [154], it is observed that the luminaires rotates about a point located approximately $2/3$ of the pole height. The range of permissible rotation of the LED array plane about any of its axes, can therefore be determined by the help of figure 5.1.

In the figure, the 6 blue circles each represent an LED. Pairs of LEDs are connected by a line, indicative of the LED plane. A pair of LED that experiences no perturbation remains on the horizontal slope. In the event of a perturbation, the LED pair will ultimately experience a maximum shift. This shift results to the LED plane moving to the point of the maximum or minimum LED slopes as indicated in the figure. To determine the maximum rotation angle, it shall be firstly required to relocate the origin within the pole at the height of $2/3$ above the ground. Furthermore, with reference to the figure, it shall be considered that the maximum displacement occurs around the *z*-axis only.

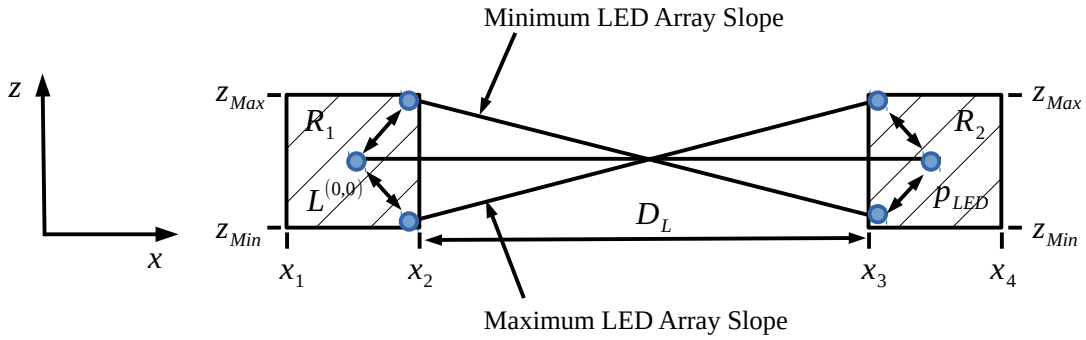

Figure 5.1. The maximum and minimum LED slope due to rotation perturbation.

The displacement of LED $L^{(0,0)}$ along the *z* axis will then be determined from,

$$L_{z2}^{(0,0)} = L_{z1}^{(0,0)} + \delta \tag{5.1}$$

where,

δ and $L_{z1}^{(0,0)}$ are the half axis displacement and pole height from the new origin. As such both δ and $L_{z1}^{(0,0)}$ are,

$$\delta = \delta_w / 2 = 0.6\,m \tag{5.2}$$

and

$$L_{z1}^{(0,0)} = 13.5 - 2/3 \times 13.5 = 4.5\,m \tag{5.3}$$

Next, the *x* coordinate of $L^{(0,0)}$ is given by $L_{x1}^{(0,0)}$ and for an average 13.5 m pole will be,

$$L_{x1}^{(0,0)} = 1.83\,m \tag{5.4}$$

Using this information, it is now possible to determine the luminaire rotation angle, γ_R, that will result in this maximum displacement. For this the following equation for γ_R has to be solved,

$$L_{z2}^{(0,0)} = -L_{z2}^{(0,0)}\sin(\gamma_R) + L_{z1}^{(0,0)}\cos(\gamma_R) \tag{5.5}$$

To solve for γ_R the following two identities can be used,

$$\sin(x) = \frac{2t}{1+t^2} \tag{5.6}$$

and

$$\cos(x) = \frac{1-t^2}{1+t^2} \tag{5.7}$$

with,

$$t = \tan(x/2) \tag{5.8}$$

Equation (5.5) can now be written in a quadratic form of,

$$(L_{z2}^{(0,0)} + L_{z1}^{(0,0)})t^2 - 2L_{x1}^{(0,0)}t + (L_{z2}^{(0,0)} - L_{z1}^{(0,0)}) = 0 \tag{5.9}$$

Substituting all values within equation (5.9) and solving for t while choosing the smaller of the two solutions for the required angle, gives $\gamma_R = 1.962^\circ$. This value can now be regarded as the maximum value of γ_R about the *x* axis, (i.e. $-1.962^\circ \le \gamma_R \le 1.962^\circ$).

5.3 Rotation Perturbations:

5.3.1 Prelimenaries:

Consider a coordinate frame reference O. If the reference is rotated about its center, then all objects within the environment shall be apparently rotated relative to the new coordinate reference O'. There are three possible independent rotations

about O , that shall be given as R_x R_y and R_z for the respective rotations about the x y and z axes. The rotation matrices will follow suite the definitions shown for the axes rotations in chapter 4. The rotation angles about each of the x , y and z axes will respectively be denoted by γ_x , γ_y and γ_z .

Next, consider a scenario where a reference LED $L^{(0,0)}$ is positioned such that the coordinate frame origin is fixed at its center. In this scenario, all remaining LEDs that are allocated fixed positions on the LED array plane. Then any rotation experienced by the reference LED will also be experienced by the remaining LEDs on the plane.

Now consider that the environment includes a single sensor s_1 . If the reference LED $L^{(0,0)}$ is free to rotate on any of its three axes. Then it is possible to enumerate all possible combinations of the rotation matrix $\boldsymbol{R}_{\boldsymbol{\gamma}}$. By using the fact that matrix order is important in matrix multiplications, $\boldsymbol{R}_{\boldsymbol{\gamma}}$ can acquire any of the following six forms,

$$\boldsymbol{R}_1 = \boldsymbol{R}_x \boldsymbol{R}_y \boldsymbol{R}_z \tag{5.10.a}$$

$$\boldsymbol{R}_2 = \boldsymbol{R}_x \boldsymbol{R}_z \boldsymbol{R}_y \tag{5.10.b}$$

$$\boldsymbol{R}_3 = \boldsymbol{R}_y \boldsymbol{R}_x \boldsymbol{R}_z \tag{5.10.c}$$

$$\boldsymbol{R}_4 = \boldsymbol{R}_y \boldsymbol{R}_z \boldsymbol{R}_x \tag{5.10.d}$$

$$\boldsymbol{R}_5 = \boldsymbol{R}_z \boldsymbol{R}_x \boldsymbol{R}_y \tag{5.10.e}$$

$$\boldsymbol{R}_6 = \boldsymbol{R}_z \boldsymbol{R}_y \boldsymbol{R}_x \tag{5.10.f}$$

The restriction to only six rotations, is established from the assumption that no repeated rotations along a single axis is permissible. Then by denoting $s_{\gamma_A} = \sin(\gamma_A)$ and $c_{\gamma_A} = \cos(\gamma_A)$, the matrix $\boldsymbol{R}_i$, with $i = \{1,\ldots,6\}$, will have the following constituents,

$$\boldsymbol{R_1}=\begin{bmatrix} c_{\gamma_Y}c_{\gamma_Z} & -c_{\gamma_Y}s_{\gamma_Z} & s_{\gamma_Y} \\ s_{\gamma_X}s_{\gamma_Y}c_{\gamma_Z}+c_{\gamma_X}s_{\gamma_Z} & -s_{\gamma_X}s_{\gamma_Y}s_{\gamma_Z}+c_{\gamma_X}c_{\gamma_Z} & -s_{\gamma_X}c_{\gamma_Y} \\ -c_{\gamma_X}s_{\gamma_Y}c_{\gamma_Z}+s_{\gamma_X}s_{\gamma_Z} & c_{\gamma_X}s_{\gamma_Y}s_{\gamma_Z}+s_{\gamma_X}c_{\gamma_Z} & c_{\gamma_X}c_{\gamma_Y} \end{bmatrix} \tag{5.11.a}$$

$$\boldsymbol{R_2}=\begin{bmatrix} c_{\gamma_Y}c_{\gamma_Z} & -s_{\gamma_Z} & s_{\gamma_Y}c_{\gamma_Z} \\ c_{\gamma_X}c_{\gamma_Y}s_{\gamma_Z}+s_{\gamma_X}s_{\gamma_Y} & c_{\gamma_X}c_{\gamma_Z} & c_{\gamma_X}s_{\gamma_Y}s_{\gamma_Z}+s_{\gamma_X}c_{\gamma_Y} \\ s_{\gamma_X}c_{\gamma_Y}s_{\gamma_Z}-c_{\gamma_X}s_{\gamma_Y} & s_{\gamma_X}c_{\gamma_Z} & s_{\gamma_X}s_{\gamma_Y}s_{\gamma_Z}+c_{\gamma_X}c_{\gamma_Y} \end{bmatrix} \tag{5.11.b}$$

$$\boldsymbol{R_3}=\begin{bmatrix} s_{\gamma_X}s_{\gamma_Y}s_{\gamma_Z}+c_{\gamma_Y}c_{\gamma_Z} & s_{\gamma_X}s_{\gamma_Y}c_{\gamma_Z}-c_{\gamma_Y}s_{\gamma_Z} & c_{\gamma_X}s_{\gamma_Y} \\ c_{\gamma_X}s_{\gamma_Z} & c_{\gamma_X}c_{\gamma_Z} & -s_{\gamma_X} \\ s_{\gamma_X}c_{\gamma_Y}s_{\gamma_Z}-s_{\gamma_Y}c_{\gamma_Z} & s_{\gamma_X}c_{\gamma_Y}c_{\gamma_Z}+s_{\gamma_Y}s_{\gamma_Z} & c_{\gamma_X}c_{\gamma_Y} \end{bmatrix} \tag{5.11.c}$$

$$\boldsymbol{R_4}=\begin{bmatrix} c_{\gamma_Y}c_{\gamma_Z} & -c_{\gamma_X}c_{\gamma_Y}s_{\gamma_Z}+s_{\gamma_X}s_{\gamma_Y} & s_{\gamma_X}c_{\gamma_Y}s_{\gamma_Z}+c_{\gamma_X}s_{\gamma_Y} \\ s_{\gamma_Z} & c_{\gamma_X}c_{\gamma_Z} & -s_{\gamma_X}c_{\gamma_Z} \\ -s_{\gamma_Y}c_{\gamma_Z} & c_{\gamma_X}s_{\gamma_Y}s_{\gamma_Z}+s_{\gamma_X}c_{\gamma_Y} & -s_{\gamma_X}s_{\gamma_Y}s_{\gamma_Z}+c_{\gamma_X}c_{\gamma_Y} \end{bmatrix} \tag{5.11.d}$$

$$\boldsymbol{R_5}=\begin{bmatrix} -s_{\gamma_X}s_{\gamma_Y}s_{\gamma_Z}+c_{\gamma_Y}c_{\gamma_Z} & -c_{\gamma_X}s_{\gamma_Z} & s_{\gamma_X}c_{\gamma_Y}s_{\gamma_Z}+s_{\gamma_Y}c_{\gamma_Z} \\ s_{\gamma_X}s_{\gamma_Y}c_{\gamma_Z}+c_{\gamma_Y}s_{\gamma_Z} & c_{\gamma_X}c_{\gamma_Z} & -s_{\gamma_X}c_{\gamma_Y}c_{\gamma_Z}+s_{\gamma_Y}s_{\gamma_Z} \\ -c_{\gamma_X}s_{\gamma_Y} & s_{\gamma_X} & c_{\gamma_X}c_{\gamma_Y} \end{bmatrix} \tag{5.11.e}$$

$$\boldsymbol{R_6}=\begin{bmatrix} c_{\gamma_Y}c_{\gamma_Z} & s_{\gamma_X}s_{\gamma_Y}c_{\gamma_Z}-c_{\gamma_X}s_{\gamma_Z} & c_{\gamma_X}s_{\gamma_Y}c_{\gamma_Z}+s_{\gamma_X}s_{\gamma_Z} \\ c_{\gamma_Y}s_{\gamma_Z} & s_{\gamma_X}s_{\gamma_Y}s_{\gamma_Z}+c_{\gamma_X}c_{\gamma_Z} & c_{\gamma_X}s_{\gamma_Y}s_{\gamma_Z}-s_{\gamma_X}c_{\gamma_Z} \\ -s_{\gamma_Y} & s_{\gamma_X}c_{\gamma_Y} & c_{\gamma_X}c_{\gamma_Y} \end{bmatrix} \tag{5.11.f}$$

A perturbed luminaire, influenced by a force that will allow it to rotate only, experiences a small amount of rotation within a small increment in time. Within this time increment the following small angle approximations are valid,

$$\cos(\gamma) \approx 1 \tag{5.12.a}$$

$$\sin(\gamma) \approx \gamma \tag{5.12.b}$$

$$\tan(\gamma) \approx \gamma \tag{5.12.c}$$

Then by observing the components of the rotation matrices, the following identities are applicable,

$$c_{\gamma_A}c_{\gamma_B} \approx 1 \tag{5.13.a}$$

$$s_{\gamma_A} s_{\gamma_B} s_{\gamma_C} \approx 0 \tag{5.13.b}$$

Finally,

$$s_{\gamma_A} s_{\gamma_B} c_{\gamma_C} + s_{\gamma_C} c_{\gamma_A} \approx \gamma_c \tag{5.13.c}$$

which is obtained by establishing that,

$$s_{\gamma_A} s_{\gamma_B} c_{\gamma_C} < s_{\gamma_C} c_{\gamma_A} \tag{5.13.d}$$

By substitution of these identities based upon the small angle approximations, into $\boldsymbol{R_5}$, will result to the simplification,

$$\boldsymbol{R_5} \approx \begin{bmatrix} 1 & -\gamma_z & \gamma_y \\ \gamma_z & 1 & -\gamma_x \\ -\gamma_Y & \gamma_x & 1 \end{bmatrix} \tag{5.14}$$

An interesting feature of the simplified form of $\boldsymbol{R_5}$ is that this approximation holds valid for the complete set of rotation matrices. Therefore, with $\boldsymbol{R_\gamma} = \boldsymbol{R_5}$, the generalization for the rotation matrix will be,

$$\boldsymbol{R_\gamma} = \boldsymbol{R_i} \quad \forall i = \{ 1, \dots , 6 \} \tag{5.15}$$

By applying the rotations $\boldsymbol{R_\gamma}$ to the current sensor position, the new position of s_1 can be obtained through,

$$\boldsymbol{s_1^{'(P)}} = \boldsymbol{R} \ \ \boldsymbol{s_1^{'}} \tag{5.16}$$

Expanding $\boldsymbol{s_1^{'(P)}}$ yields,

$$s_{1,x}^{'(P)} = s_{1,x}^{'} - \gamma_z s_{1,y}^{'} + \gamma_y s_{1,z}^{'} \tag{5.17.a}$$

$$s_{1,y}^{'(P)} = \gamma_z s_{1,x}^{'} + s_{1,y}^{'} - \gamma_x s_{1,z}^{'} \tag{5.17.b}$$

$$s_{1,z}^{'(P)} = -\gamma_y s_{1,x}^{'} + \gamma_x s_{1,y}^{'} + s_{1,z}^{'} \tag{5.17.c}$$

For the rotational perturbation to encapsulate the effect of the various different types of forces that could act upon the luminaire, it will be assumed that all axial rotations are decoupled from one another. As it has been indicated earlier that there exists a maximum limit to the rotation angle on every axis. This maximum rotation angle

centered at a prescribed mean angle, will be denoted by $\pm\gamma_R$. This angle shall be assumed equal for all axes.

Through enumerating every possible type of force acting on the streetlight pole, and hence affecting the luminaire position, it is possible to obtain an exact model to the rotation perturbation. However, this method of analysis is excessively difficult, if not all together impossible to implement. Moreover, such an approach would also be largely inefficient. To circumvent this problem, while realistically accounting for all possible effects, it will be assumed that each rotation is a random variable (RV) that can be described by its probabilistic distribution. Although idealistically the distributions governing the rotation must be truncated, however, for the tractability of the analysis, it will be further considered that all distributions follows a normal distribution. Then for each of the rotation angles within the system, the RV will have a PDF defined by $\gamma_x \sim N(\mu_x, \sigma_x^2)$, $\gamma_y \sim N(\mu_y, \sigma_y^2)$ and $\gamma_z \sim N(\mu_z, \sigma_z^2)$ with μ and σ^2 defining the means and variances of the respective distributions. To accommodate the truncation, even though the normal distribution is defined over the interval $\{-\infty, \infty\}$, using the well established 3-sigma rule implies that $3\sigma = \gamma_R$ for the univariate normally distribution perturbation. The application of the referred three sigma rule, ensures that on average a RV γ will exceed 3σ only 3 times in a thousand trials. In this case the tail probabilities of the distribution beyond 3σ becomes insignificant from a practical perspective. Accordingly, the perturbation angles γ_x , γ_y and γ_z can now be viewed in light of independent and identically distributed (iid) normal RVs whose means and variances are respectively $\mu_x = \mu_y = \mu_z = 0$ and $\sigma_x^2 = \sigma_y^2 = \sigma_x^2 = \sigma^2$. In accord to the data shown in [143], it will be assumed that γ_R is confined to $\pm 2^o$, ie $\sigma = \pm 2/3^o$.

Then for a normal RV W, its PDF, $p_W(w)$, can be parametrized through its mean μ and variance σ^2 according to,

$$p_W(w) = \frac{1}{\sqrt{2\pi\sigma^2}} e^{\frac{-(w-\mu)^2}{2\sigma^2}} \tag{5.18}$$

It is now possible to interpret equations (5.17.a)-(5.17.c) in light of the normal

distribution. It is clear that each component of the perturbed rotated sensor $\boldsymbol{s}_1^{p\,''}$ will be centered about unperturbed component. The perturbation effects the other two components, such that the resultant perturbed component can be viewed as the sum of two weighted Gaussian RVs. Then for the general structure of equation set (5.17.a)-(5.17.c), the perturbed resulting Gaussian distribution can be determined using the identities of the mean and variance of the sum of independent Gaussian RVs yielding,

$$s_i^{'(P)} \sim N\left(\left(s_i^{'}+s_j^{'}\mu_A+s_k^{'}\mu_B\right),\left(\left(s_j^{'}\right)^2\sigma_A^2+\left(s_k^{'}\right)^2\sigma_B^2\right)\right) \tag{5.19}$$

for general component

$$s_i^{(P)}=s_i^{'}+s_j^{'}\gamma_A+s_k^{'}\gamma_B \tag{5.20}$$

and

$\{ i, j, k, A, B \}\in\{ x, y, z \}$, $\gamma_A\sim N\left(\mu_A,\sigma_A^2\right)$ and $\gamma_B\sim N\left(\mu_B,\sigma_B^2\right)$.

In the specific condition at hand, the probability distributions of each of the perturbed components in $\boldsymbol{s}_1^{'(P)}$ will become,

$$s_{1,x}^{'(P)} \sim N\left(s_{1,x}^{'},\left(\left(s_{1,y}^{'}\right)^2+\left(s_{1,z}^{'}\right)^2\right)\sigma^2\right) \tag{5.21.a}$$

$$s_{1,y}^{'(P)} \sim N\left(s_{1,y}^{'},\left(\left(s_{1,x}^{'}\right)^2+\left(s_{1,z}^{'}\right)^2\right)\sigma^2\right) \tag{5.21.b}$$

$$s_{1,z}^{'(P)} \sim N\left(s_{1,z}^{'},\left(\left(s_{1,x}^{'}\right)^2+\left(s_{1,y}^{'}\right)^2\right)\sigma^2\right) \tag{5.21.c}$$

From equation (5.21.a)-(5.12.c), it is evident that the new perturbed axes components are too normal RVs. Then an alternative form of equation (5.16) can be realized in the form of,

$$\begin{bmatrix} s_{1,x}^{'(P)} \\ s_{1,y}^{'(P)} \\ s_{1,z}^{'(P)} \end{bmatrix}=\begin{bmatrix} 0 & -s_{1,z}^{'} & s_{1,y}^{'} \\ s_{1,z}^{'} & 0 & -s_{1,x}^{'} \\ -s_{1,y}^{'} & s_{1,x}^{'} & 0 \end{bmatrix}\begin{bmatrix} \gamma_x \\ \gamma_y \\ \gamma_z \end{bmatrix}+\begin{bmatrix} s_{1,x}^{'} \\ s_{1,y}^{'} \\ s_{1,z}^{'} \end{bmatrix} \tag{5.22.a}$$

that can be written in a more compact form of,

$$\boldsymbol{s}_1^{'(P)} = \boldsymbol{R}\boldsymbol{\gamma} \;+\; \boldsymbol{s}_1^{'} \tag{5.22.b}$$

Using this format, and the definition of the sum of weighted Gaussian RVs, a mean vector, $\boldsymbol{\mu}_{s'}$, can be obtained in the form of,

$$\boldsymbol{\mu}_{s'}=\boldsymbol{s}'_1 \tag{5.23}$$

Similarly, a covariance matrix, $\boldsymbol{C}=\boldsymbol{E}[\boldsymbol{R}\boldsymbol{\gamma}\boldsymbol{\gamma}^{T}\boldsymbol{R}^{T}]$, for the new normal RVs can be found as,

$$\boldsymbol{C}=\begin{pmatrix} (s'_{1,y})^2+(s'_{1,z})^2 & -s'_{1,x}s'_{1,y} & -s'_{1,x}s'_{1,z} \\ -s'_{1,x}s'_{1,y} & (s'_{1,x})^2+(s'_{1,z})^2 & -s'_{1,y}s'_{1,z} \\ -s'_{1,x}s'_{1,z} & -s'_{1,y}s'_{1,z} & (s'_{1,x})^2+(s'_{1,y})^2 \end{pmatrix}\sigma^2 \tag{5.24}$$

The format of the covariance matrix as shown in equation (5.24) is a real symmetric matrix, and hence, matrix $\boldsymbol{C}$ is positive definite. Under this condition, the joint PDF of $\boldsymbol{s}_{\boldsymbol{1}}^{'(\boldsymbol{P})}$, $f_{\boldsymbol{S}'^{(P)}}(\boldsymbol{s}'^{(\boldsymbol{P})})$ can be written in the form of the multivariate normal distribution as,

$$f_{\boldsymbol{S}'^{(P)}}(\boldsymbol{s}'^{(\boldsymbol{P})})=\frac{1}{\sqrt{(2\pi)^3|\boldsymbol{C}|}}e^{-\frac{1}{2}(\boldsymbol{\gamma}-\boldsymbol{\mu}_{s'})^{T}\boldsymbol{C}^{-1}(\boldsymbol{\gamma}-\boldsymbol{\mu}_{s'})} \tag{5.25}$$

Equation (5.25), however, cannot be used further, due to the singularity of $\boldsymbol{C}$. Therefore, the analysis of rotation perturbations must be considered differently.

5.3.2 Effect of Rotation Perturbation on the Polar Angle θ_{s1} :

The perturbation effect on the polar angle can be obtained in terms of the cosine of the polar angle. In turn, the cosine of the polar angle is simply the normalized dot product between the optical axis negative *z* component and the vector connecting both the center of LED $L^{(0,0)}$ and sensor s_1 . Then from this depiction it is formally given by,

$$\cos(\theta_{s1}^{'(P)})=-s_{1,z}^{(0,0)(P)}/d_{s1}^{(0,0)(P)} \tag{5.26}$$

with $d_{s1}^{(0,0)(P)}$ representing the perturbed distance RV and is given by,

$$d_{s1}^{(0,0)(P)}=\sqrt{((s_{1,x}^{'(P)})^2+(s_{1,y}^{'(P)})^2+(s_{1,z}^{'(P)})^2)} \tag{5.27}$$

where, $s_{1,x}^{'(P)}$ $s_{1,y}^{'(P)}$ and $s_{1,z}^{'(P)}$ are given by equation (5.22.a).

To capture the effect of the small scale variations, the left hand side of equation (5.26) can be re-expressed in the form,

$$\cos\left(\theta_{s1}^{'(P)}\right)=\cos\left(\theta_{s1}+\delta\theta\right) \tag{5.28}$$

where θ_{s1} is the unperturbed polar angle to sensor s_1 ,

and $\delta\theta$ represents the polar angle perturbations.

Expanding (5.28) and applying the small angle approximations, the equation can be given in the approximate format,

$$\cos\left(\theta_{s1}^{'(P)}\right)\approx\cos\left(\theta_{s1}\right)-\sin\left(\theta_{s1}\right)\delta\theta \tag{5.29}$$

Then substitution of equation (5.29) into (5.26) yields,

$$\delta\theta^{(0,0)}=\cot\left(\theta^{(0,0)}\right)+\frac{s_{1,z}^{'}}{d_{s1}^{(0,0)(P)}\sin\left(\theta^{(0,0)}\right)}+\frac{s_{1,y}^{'}\gamma_x-s_{1,x}^{'}\gamma_y}{d_{s1}^{(0,0)(P)}\sin\left(\theta^{(0,0)}\right)} \tag{5.30}$$

In the analysis of the rotation perturbation for a single sensor, two cases can be identified. Firstly, the rotation perturbation linked to LED $L^{(0,0)}$ and secondly, the rotation perturbation linking the remaining LEDs to s_1 . For each case the analysis is undertaken in the following to subsections.

5.3.2.1 Case with LED $L^{(0,0)}$:

For the first case, a sensor that is rotated about LED $L^{(0,0)}$ the distance $d_{s1}^{(0,0)(P)}$ remains constant, i.e. $d_{s1}^{(0,0)(P)}=d_{s1}^{(0,0)}$. Applying this piece of information to equation (5.30) shows that only the third term is a RV. Through this observation, it can be deduced that the polar angle perturbation PDF is a Gaussian function. Then $\delta\theta^{(0,0)}\sim N\left(\mu_{\delta\theta^{(0,0)}},\sigma^2_{\delta\theta^{(0,0)}}\right)$ with mean and variance given respectively as,

$$\mu_{\delta\theta^{(0,0)}}=\cot\left(\theta^{(0,0)}\right)+\frac{s_{1,z}^{'}}{d_{s1}^{(0,0)}\sin\left(\theta^{(0,0)}\right)} \tag{5.31}$$

$$\sigma^2_{\delta\theta^{(0,0)}}=\frac{\left(\left(s_{1,x}^{'}\right)^2+\left(s_{1,y}^{'}\right)^2\right)\sigma^2}{\left(d_{s1}^{(0,0)}\sin\left(\theta^{(0,0)}\right)\right)^2} \tag{5.32}$$

5.3.2.2 Case with LED $L^{(m,n)}$:

In the previous sub-section, the analysis of the effect of rotation perturbation of a

single LED on the polar angle has been shown. However, the system comprises multiple LEDs that are arranged in a planar array fashion. It is therefore necessary to extend the analysis such that the effect of rotation perturbation of the complete set of LEDs on the polar angle.

A sensor s_1 is rotated about reference LED $L^{(0,0)}$ to its new perturbed position s_1^P with components given by equation set (5.21.a)-(5.21.c). The distance between the reference LED and the sensor remains constant for all rotations about $L^{(0,0)}$ as previously mentioned. This distance shall be denoted as $d_{s1}^{(0,0)}$ and is given in terms of its new perturbed position as shown by equation (5.27). In contrast, the distance between s_1 and any other LED $L^{(m,n)}$ is not constant.

As a preliminary, it is necessary to restate the LED offsets from the origin on the LED plane. An LED $L^{(m,n)}$ is offset by an amount of δx , δy and δz from the origin along the systems coordinate frame principle axes. Recalling from the previous chapter, the three offset terms evaluated within the OC coordinate frame for a rectangular LED arrangement is determined by,

$$\delta x = m \Delta x \cos(\alpha) \tag{5.33.a}$$

$$\delta y = n \Delta y \tag{5.33.b}$$

$$\delta z = -m \Delta x \sin(\alpha) \tag{5.33.c}$$

where m, n represent the LED number,

and $\Delta x, \Delta y$ are the spacing between neighboring LEDs,

and α is the inclination angle of the OC plane and the LED plane.

Now the required changes to equation (5.30) can be included, such that equation (5.33) will be modified into,

$$\delta\theta^{(m,n)} = \cot\left(\theta^{(m,n)}\right) + \frac{s_{1,z}^{'} + \delta z}{d_{s1}^{(m,n)(P)} \sin\left(\theta^{(m,n)}\right)} + \frac{\left(s_{1,y}^{'} + \delta y\right)\gamma_x - \left(s_{1,x}^{'} + \delta x\right)\gamma_y}{d_{s1}^{(m,n)(P)} \sin\left(\theta^{(m,n)}\right)} \tag{5.34}$$

where $d_{s1}^{(m,n)(P)}$ represents the perturbed distance between LED $L^{(m,n)}$ and s_1^P .

Unlike equation (5.30), it is clear that the distance now is a RV that will modify the second and third terms in equation (5.34). For the second term, the numerator is constant and the randomness is caused by the denominator only. While for the third term, both numerator and denominator comprise a ratio RV, with the former regarded as a Gaussian RV as shown in the previous subsection. Equivalently, it will be advantageous to group the random component together, terms 2 and 3, and rewrite equation (5.34) as,

$$\delta\theta^{(m,n)} = \cot\left(\theta^{(m,n)}\right) + \theta_N^{(m,n)} / \theta_D^{(m,n)} \tag{5.35}$$

where $\theta_N^{(m,n)}$ is the sum of the numerators of terms 2 and 3,

and $\theta_D^{(m,n)}$ is the denominator of terms 2 and 3.

From equation (5.35), the numerator PDF can be defined as $\theta_N^{(m,n)} \sim N\left(\mu_{\theta_N}, \sigma_{\theta_N}^2\right)$ with mean and variances given by,

$$\mu_{\theta_N} = s_{1,z}^{'} + \delta z \tag{5.36.a}$$

$$\sigma_{\theta_N}^2 = \left(s_{1,x}^{'} + \delta x\right)^2 + \left(s_{1,y}^{'} + \delta y\right)^2 \tag{5.36.b}$$

For the denominator in equation (5.35), it is clear that $d_{s1}^{(m,n)(P)}$ is the random component. For such reasons, the distribution of the distance $d_{s1}^{(m,n)(P)}$ is sought.

To begin with, the distance between LEDs $L^{(0,0)}$ and $L^{(m,n)}$, which is constant for any particular luminaire, can be obtained through,

$$d^{(m,n)} = \sqrt{\left(\delta x^2 + \delta y^2 + \delta z^2\right)} \tag{5.37}$$

By implementing the law of cosines for triangles, $d_{s1}^{(m,n)}$ can be found as,

$$d_{s1}^{(m,n)(P)} = \sqrt{\left(d^{(m,n)}\right)^2 + \left(d_{s1}^{(m,n)}\right)^2 - 2\left(\delta x\, s_{1,x}^{'(P)} + \delta y\, s_{1,y}^{'(P)} + \delta z\, s_{1,z}^{'(P)}\right)} \tag{5.38}$$

The above equation can be written in terms of the rotation angles γ_x, γ_y and γ_z using the small angle approximations as,

$$\begin{aligned}\left(d_{s1}^{(m,n)}\right)^2 = {} & \left(d^{(m,n)}\right)^2 + \left(d_{s1}^{(m,n)}\right)^2 - 2\delta x\left(s_{1,x}^{'} + s_{1,z}^{'}\gamma_y - s_{1,y}^{'}\gamma_z\right) \\ & -2\delta y\left(s_{1,y}^{'} + s_{1,x}^{'}\gamma_z - s_{1,z}^{'}\gamma_x\right) - 2\delta z\left(s_{1,z}^{'} - s_{1,x}^{'}\gamma_y + s_{1,y}^{'}\gamma_x\right)\end{aligned} \tag{5.39}$$

Grouping both the deterministic and random variables into variables A_0 and A_1 respectively, $d_{s1}^{(m,n)}$ can be finally given in form of,

$$d_{s1}^{(m,n)} = \sqrt{A_0 + A_1} \tag{5.40}$$

with parameters A_0 and A_1 given by,

$$A_0 = \left(d^{(m,n)}\right)^2 + \left(d_{s1}^{(m,n)}\right)^2 - 2\left(\delta x\, s'_{1,x} + \delta y\, s'_{1,y} + \delta z\, s'_{1,z}\right) \tag{5.41}$$

$$A_1 = 2\left(\left(s'_{1,z}\delta y - s'_{1,y}\delta z\right)\gamma_x + \left(s'_{1,x}\delta z - s'_{1,z}\delta x\right)\gamma_y + \left(s'_{1,y}\delta x - s'_{1,x}\delta y\right)\gamma_z\right) \tag{5.42}$$

Distance $d_{s1}^{(m,n)}$ can be rearranged as the ratio of A_0 to A_1 under the root as,

$$d_{s1}^{(m,n)} = \sqrt{A_0}\sqrt{1 + A_1/A_0} \tag{5.43}$$

The square root operation can now be approximated when the ratio $\left|\frac{A_1}{A_0}\right| < 1$ using the identity,

$$\sqrt{1+x} \approx 1 + \frac{x}{2} \tag{5.44}$$

The distance $d_{s1}^{(m,n)}$ can then be written in its approximated form of,

$$d_{s1}^{(m,n)} \approx B_0 + B_1 \tag{5.45}$$

with

$$B_0 = \sqrt{A_0}$$

and

$$B_1 = \frac{A_1}{2\sqrt{A_0}}$$

From this approximation it is easy to identify that the distribution of $d_{s1}^{(m,n)}$ is a Gaussian function with a given distribution of $d_{s1}^{(m,n)} \sim N\left(\mu_{d_\theta}^{(m,n)}, \left(\sigma_{d_\theta}^{(m,n)}\right)^2\right)$ for which the mean and variance are respectively given as,

$$\mu_{d_\theta}^{(m,n)} = \sqrt{A_0} \tag{5.46}$$

$$\left(\sigma_{d_\theta}^{(m,n)}\right)^2 = \left(\left(s'_{1,z}\delta y - s'_{1,y}\delta z\right)^2 + \left(s'_{1,x}\delta z - s'_{1,z}\delta x\right)^2 + \left(s'_{1,y}\delta x - s'_{1,x}\delta y\right)^2\right)\sigma^2/A \tag{5.47}$$

From this relation it can be observed that the variance of distance $d_{s1}^{(m,n)}$ tends to zero as the LEDs becomes closer to the center of the rotation.

Finally, the distribution of the denominator in the ratio will be $\theta_D^{(m,n)} \sim N\left(\mu_{\theta_D}^{(m,n)}, \left(\sigma_{\theta_D}^{(m,n)}\right)^2\right)$, with the mean and variance respectively given as,

$$\mu_{\theta_D}^{(m,n)} = \mu_{d_\theta}^{(m,n)} \tag{5.48.a}$$

$$\left(\sigma_{\theta_D}^{(m,n)}\right)^2 = \left(\sigma_{d_\theta}^{(m,n)}\right)^2 \left(\sin\left(\theta^{(m,n)}\right)\right)^2 \tag{5.48.b}$$

In light of this, $\delta\theta^{(m,n)}$ can be regarded as the ratio of two Gaussian RVs centered about the unperturbed polar angle $\theta^{(m,n)}$.

5.3.3 Effect of Rotation Perturbation on the Azimuthal Angle $\varphi^{(m,n)}$:

In a similar fashion to the analysis that has been undertaken for the rotation perturbation effect on the polar angle, in this section, the effect on the azimuthal angle shall be analyzed. Recalling that the azimuthal angle of LED $L^{(m,n)}$ to s_1 is given by equation (4.82), the equivalent form with a rotation perturbation, $\varphi^{(m,n)(P)}$, can be given as,

$$\tan\left(\varphi^{(m,n)(P)}\right) = s_{1,y}^{'(m,n)(P)} / s_{1,x}^{'(m,n)(P)} \tag{5.49}$$

The event of such a perturbation can be captured by expanding the azimuthal angle into its components of,

$$\varphi^{(m,n)(P)} = \varphi^{(m,n)} + \delta\varphi^{(m,n)} \tag{5.50}$$

with $\delta\varphi^{(m,n)}$ representing the perturbation component.

Using the equivalent ratio of representation of $\tan(x) = \sin(x)/\cos(x)$ and using the small angle approximation of $\cos(x)$ given by equation (5.29) and that for $\sin(x)$ as,

$$\sin(u + \delta u) \approx \sin(u) + \cos(u)\delta u \tag{5.51}$$

equation (5.49) can be expressed as,

$$\delta\varphi^{(m,n)} = \frac{\cos\left(\varphi^{(m,n)}\right)\left(s_{1,y}^{'(m,n)(P)} / s_{1,x}^{'(m,n)(P)}\right) - \sin\left(\varphi^{(m,n)}\right)}{\sin\left(\varphi^{(m,n)}\right)\left(s_{1,y}^{'(m,n)(P)} / s_{1,x}^{'(m,n)(P)}\right) + \cos\left(\varphi^{(m,n)}\right)} \tag{5.52}$$

Then by algebraic manipulation, $\delta\varphi^{(m,n)}$ can be expressed as the ratio of two correlated Gaussian RVs in the form of,

$$\delta\varphi^{(m,n)}=\frac{\varphi_N^{(m,n)}}{\varphi_D^{(m,n)}} \tag{5.53}$$

with $\varphi_N^{(m,n)}\sim N(\mu_{\varphi_N},\sigma_{\varphi_N}^2)$ and $\varphi_D^{(m,n)}\sim N(\mu_{\varphi_D},\sigma_{\varphi_D}^2)$ are the numerator and denominator RVs of the ratio.

Substituting for $s_{1,x}^{'(m,n)(P)}$ and $s_{1,y}^{'(m,n)(P)}$, the mean and the variance of each of the numerator and denominator can be evaluated as,

$$\mu_{\varphi_N}=\cos(\varphi^{(m,n)})(s_{1,y}^{'}+\delta y)-\sin(\varphi^{(m,n)})(s_{1,x}^{'}+\delta x) \tag{5.54.a}$$

$$\sigma_{\varphi_N}^2=(\cos(\varphi^{(m,n)})(s_{1,x}^{'}+\delta x))^2+(\sin(\varphi^{(m,n)})(s_{1,y}^{'}+\delta y))^2+(s_{1,z}^{'}+\delta z)^2 \tag{5.54.b}$$

$$\mu_{\varphi_N}=\cos(\varphi^{(m,n)})(s_{1,x}^{'}+\delta x)+\sin(\varphi^{(m,n)})(s_{1,y}^{'}+\delta y) \tag{5.54.c}$$

$$\sigma_{\varphi_D}^2=(\sin(\varphi^{(m,n)})(s_{1,x}^{'}+\delta x))^2+(\cos(\varphi^{(m,n)})(s_{1,y}^{'}+\delta y))^2+(s_{1,z}^{'}+\delta z)^2 \tag{5.54.d}$$

The above expressions can be further simplified under the assumption that $s_{1,x}^{'}\gg\delta x$ and $s_{1,y}^{'}\gg\delta y$. In this case the numerator and denominator means and variances simplifies into,

$$\mu_{\varphi_N}=\cos(\varphi^{(m,n)})s_{1,y}^{'}-\sin(\varphi^{(m,n)})s_{1,x}^{'} \tag{5.55.a}$$

$$\sigma_{\varphi_N}^2=(\cos(\varphi^{(m,n)})s_{1,x}^{'})^2+(\sin(\varphi^{(m,n)})s_{1,y}^{'})^2+s_{1,z}^{'\,2} \tag{5.55.b}$$

$$\mu_{\varphi_N}=\cos(\varphi^{(m,n)})s_{1,x}^{'}+\sin(\varphi^{(m,n)})s_{1,y}^{'} \tag{5.55.c}$$

$$\sigma_{\varphi_D}^2=(\sin(\varphi^{(m,n)})s_{1,x}^{'})^2+(\cos(\varphi^{(m,n)})s_{1,y}^{'})^2+s_{1,z}^{'\,2} \tag{5.55.d}$$

5.3.4 Effect of Rotation Perturbation on Sensor Viewing Angle $\psi_{s1}^{'(m,n)}$:

In this portion, the rotational perturbation onto the sensor to LED viewing angle, $\psi_{s1}^{'(m,n)(P)}$, will be demonstrated. By recalling the equation of $\psi_{s1}^{'(m,n)}$, shown in (4.90), its perturbed counterpart can be evaluated, through the dot product of the

normal vector to the sensor surface and the vector connecting an LED element on the LED array. For this, focus shall be given to obtaining the two normal vectors.

To commence with, it is assumed that the normal vector to sensor s_1 , $\boldsymbol{n}_{\boldsymbol{s1}}^{(\boldsymbol{L_x},\boldsymbol{L_y})}$, is fixed to the center of a rectangular LED array of size $2(L_x \times L_y)$ for all relative motion of the sensor along its perceived path. This vector can be given as,

$$\boldsymbol{n}_{\boldsymbol{s1}}^{(\boldsymbol{L_x},\boldsymbol{0})} = (L_x^{'} - s_{1,x}^{'})\ \boldsymbol{i},\ -s_{1,y}^{'}\ \boldsymbol{j},\ -L_z^{'} - s_{1,z}^{'}\ \boldsymbol{k})/d_{s1}^{(L_x,0)} \tag{5.56}$$

where for the assumed coordinate frame, the center of the luminaire is aligned along the *x*-axis. Moreover, it has been assumed $\boldsymbol{n}_{\boldsymbol{s1}}^{(\boldsymbol{L_x},\boldsymbol{0})}$ is computed based on the OC plane, and that $L_x^{'} = L_x \cos(\alpha)$ and $L_z^{'} = L_x \sin(\alpha)$ are the appropriate transformations onto the OC plane.

Then for the analysis, the system shall be first demonstrated for the specific case of LED $L^{(0,0)}$ followed by the generalization for LED $L^{(m,n)}$.

Consider the normal vector to LED $L^{(0,0)}$, $\boldsymbol{n}_{\boldsymbol{s1}}^{(\boldsymbol{0},\boldsymbol{0})}$. This vector will be given as,

$$\boldsymbol{n}_{\boldsymbol{s1}}^{(\boldsymbol{0},\boldsymbol{0})} = (-s_{1,x}^{'}\ \boldsymbol{i},\ -s_{1,y}^{'}\ \boldsymbol{j},\ -s_{1,z}^{'}\ \boldsymbol{k})/d_{s1}^{(0,0)} \tag{5.57}$$

Including the rotation perturbation modifies equation (5.57) into,

$$\boldsymbol{n}_{\boldsymbol{s1}}^{(\boldsymbol{0},\boldsymbol{0})(\boldsymbol{P})} = (-s_{1,x}^{'(P)}\ \boldsymbol{i},\ -s_{1,y}^{'(P)}\ \boldsymbol{j},\ -s_{1,z}^{'(P)}\ \boldsymbol{k})/d_{s1}^{(0,0)} \tag{5.58}$$

with the perturbation components $s_1^{'(P)}$ is appropriately given by equation set (5.17.a)-(5.17.c).

Similarly, a rotational perturbation modifies $\boldsymbol{n}_{\boldsymbol{s1}}^{(\boldsymbol{L_x},\boldsymbol{0})}$ into its perturbed form, $\boldsymbol{n}_{\boldsymbol{s1}}^{(\boldsymbol{L_x},\boldsymbol{0})(\boldsymbol{P})}$,

$$\boldsymbol{n}_{\boldsymbol{s1}}^{(\boldsymbol{L_x},\boldsymbol{0})(\boldsymbol{P})} = (n_{s1,x}^{c(P)}\boldsymbol{i},\ n_{s1,y}^{c(P)}\boldsymbol{j},\ n_{s1,z}^{c(P)}\boldsymbol{k}) \tag{5.59}$$

which by substituting for its components is,

$$\boldsymbol{n}_{\boldsymbol{s1}}^{(\boldsymbol{L_x},\boldsymbol{0})(\boldsymbol{P})} = \frac{((L_x^{'} - s_{1,x}^{'})^{(P)}\boldsymbol{i},\ -s_{1,y}^{'(P)}\boldsymbol{j},\ (L_z^{'} - s_{1,z}^{'})^{(P)}\boldsymbol{k})}{\sqrt{((L_x^{'} - s_{1,x}^{'})^{(P)})^2 + ((s_{1,y}^{'})^{(P)})^2 + ((L_z^{'} - s_{1,z}^{'})^{(P)})^2}} \tag{5.60}$$

It is clear from equation (5.60) that the distance is also perturbed, in contrast to that

shown by equation (5.59). The cosine of the perturbed sensor looking angle can now be evaluated as,

$$\psi_{s1}^{'(L_x,0)(P)}=\frac{s_{1,x}^{'(P)}\left(s_{1,x}^{'}-L_x^{'}\right)^{(P)}+s_{1,y}^{'(P)}s_{1,y}^{'(P)}+s_{1,z}^{'(P)}\left(s_{1,z}^{'}-L_z^{'}\right)^{(P)}}{d_{s1}^{(0,0)}d_{s1}^{(L_x,0)(P)}} \tag{5.61}$$

Equation (5.61) can be modified for the general case of LED $L^{(m,n)}$ into,

$$\psi_{s1}^{'(m,n)(P)}=\frac{\left(L_x^{'(m,n)}-s_{1,x}^{'(P)}\right)\left(L_x^{'}-s_{1,x}^{'}\right)^{(P)}+\left(L_y^{'(m,n)}-s_{1,y}^{'(P)}\right)s_{1,y}^{'(P)}+\left(L_z^{'(m,n)}-s_{1,z}^{'(P)}\right)\left(L_z^{'}-s_{1,z}^{'}\right)^{(P)}}{d_{s1}^{(m,n)(P)}d_{s1}^{(L_x,0)(P)}} \tag{5.62}$$

Rather than attempting to directly obtain $\psi_{s1}^{'(m,n)(P)}$ from the form given by equation (5.62), it may be more convenient to adopting the approach of fixing $\boldsymbol{n}_{\boldsymbol{s1}}^{(\boldsymbol{L_x},\boldsymbol{0})}$ in space while making $\boldsymbol{n}_{\boldsymbol{s1}}^{(\boldsymbol{m},\boldsymbol{n})}$ variable. This can be easily done by transforming equation (5.62) into,

$$\psi_{s1}^{'(m,n)(P)}=\frac{\left(L_x^{'(m,n)}-s_{1,x}^{'(P)}\right)^{(-P)}\left(L_x^{'}-s_{1,x}^{'}\right)+\left(L_y^{'(m,n)}-s_{1,y}^{'(P)}\right)^{(-P)}s_{1,y}^{'}+\left(L_z^{'(m,n)}-s_{1,z}^{'(P)}\right)^{(-P)}\left(L_z^{'}-s_{1,z}^{'}\right)}{\left(d_{s1}^{(m,n)(P)}\right)^{(-P)}d_{s1}^{(L_x,0)}} \tag{5.63}$$

By substituting the components of $\boldsymbol{n}_{\boldsymbol{s1}}^{(\boldsymbol{L_x},\boldsymbol{0})}$, equation (5.63) can be written more compactly as,

$$\psi_{s1}^{'(m,n)(P)}=\frac{v_x^{(-P)}n_{s1,x}^{c}+v_y^{(-P)}n_{s1,y}^{c}+v_z^{(-P)}n_{s1,z}^{c}}{d_v^{(-P)}} \tag{5.64}$$

where $v_x^{(-P)}$, $v_y^{(-P)}$ and $v_z^{(-P)}$ are the *x*, *y* and *z* components of the perturbed vector and $d_v^{(-P)}$ is the length of the vector.

The length $d_v^{(-P)}$ is appropriately given as,

$$d_v^{(-P)}=\sqrt{\left(v_x^{(-P)}\right)^2+\left(v_y^{(-P)}\right)^2+\left(v_z^{(-P)}\right)^2} \tag{5.65}$$

Performing the rotations and simplifications gives each component of the perturbed vector as follows,

$$v_x^{(-P)}=L_x^{'(m,n)}-s_x+L_y^{'(m,n)}\gamma_z-L_z^{'(m,n)}\gamma_y+\left(s_y\gamma_y+s_z\gamma_z\right)\gamma_x-s_x\left(\gamma_y^2+\gamma_z^2\right) \tag{5.66.a}$$

$$v_y^{(-P)}=L_y^{'(m,n)}-s_y+L_z^{'(m,n)}\gamma_x-L_x^{'(m,n)}\gamma_z+\left(s_x\gamma_x+s_z\gamma_z\right)\gamma_y-s_y\left(\gamma_x^2+\gamma_z^2\right) \tag{5.66.b}$$

$$v_z^{(-P)} = L_z^{'(m,n)} - s_z + L_x^{'(m,n)}\gamma_y - L_y^{'(m,n)}\gamma_x + (s_x\gamma_x + s_y\gamma_y)\gamma_z - s_z(\gamma_x^2 + \gamma_y^2) \quad (5.66.c)$$

Through substitution of these values into equation (5.63), it can be observed that the problem becomes quite involved which could lead to difficult evaluation of parameter $\psi_{s1}^{'(m,n)(P)}$. This fact could be returned to the rotation and the anti-rotation which have to be performed. For such reasons, a better approach to the problem can be devised through fixing the location of sensor s_1 while permitting the rotation of the luminaire about the reference LED $L^{(0,0)}$. This is in contrast to the method used for all of the other analysis. In this configuration, equation (5.64) can be easily modified into,

$$\psi_{s1}^{'(m,n)(P)} = \frac{v_x^{(P)} n_{s1,x}^c + v_y^{(P)} n_{s1,y}^c + v_z^{(P)} n_{s1,z}^c}{d_{v^{(P)}}} \quad (5.67)$$

where $v_x^{(P)}$, $v_y^{(P)}$ and $v_z^{(P)}$ are the *x*, *y* and *z* components of the perturbed vector and $d_{v^{(P)}}$ is the length of the vector.

While the components of $\boldsymbol{n}_{\boldsymbol{s1}}^{(\boldsymbol{L_x},\boldsymbol{0})}$ remains the same, $v_x^{(P)}$, $v_y^{(P)}$ and $v_z^{(P)}$ are given as,

$$v_x^{(P)} = L_x^{'(m,n)} - s_x + L_y^{'(m,n)}\gamma_z - L_z^{'(m,n)}\gamma_y \quad (5.68.a)$$

$$v_y^{(P)} = L_y^{'(m,n)} - s_y + L_z^{'(m,n)}\gamma_x - L_x^{'(m,n)}\gamma_z \quad (5.68.b)$$

$$v_z^{(P)} = L_z^{'(m,n)} - s_z + L_x^{'(m,n)}\gamma_y - L_y^{'(m,n)}\gamma_x \quad (5.68.c)$$

From the outset, it is clear that equation set (5.68.a)-(5.68.c) is relatively simpler compared to equation set (5.66.a)-(5.66.c). Distance $d_{v^{(P)}}$ will then be,

$$d_{v^{(P)}} = \sqrt{(v_x^{(P)})^2 + (v_y^{(P)})^2 + (v_z^{(P)})^2} \quad (5.69)$$

Expanding $d_{v^{(P)}}$ and collecting the perturbed and unperturbed distance components, equation (5.69) can be shown to be,

$$d_{v^{(P)}}^{(m,n)} = \sqrt{(d_{s1}^{(m,n)})^2 + C_R^2(\gamma)} \quad (5.70)$$

with $d_{s1}^{(m,n)}$ and $C_R(\gamma)$ represent respectively the unperturbed and perturbed separation distance components of sensor s_1 and LED $L^{(m,n)}$.

The grouped terms show that $(d_{s1}^{(m,n)})^2$ and $C_T^2(\gamma)$ are evaluated in the form of,

$$\begin{aligned}(d_{s1}^{(m,n)})^2 = s_{1,x}^2 + s_{1,y}^2 + s_{1,z}^2 + (L_{1,x}^{'})^2 + (L_{1,x}^{'})^2 \\ + (L_{1,x}^{'})^2 - 2(L_{1,x}^{'} s_{1,x} + L_{1,y}^{'} s_{1,y} + L_{1,z}^{'} s_{1,z})\end{aligned} \tag{5.71}$$

$$\begin{aligned}C_R^2(\gamma) = (L_y^{'(m,n)} + L_z^{'(m,n)})\gamma_x^2 + (L_x^{'(m,n)} + L_z^{'(m,n)})\gamma_y^2 + (L_x^{'(m,n)} + L_y^{'(m,n)})\gamma_z^2 \\ -2(L_x^{'(m,n)} L_y^{'(m,n)}\gamma_x\gamma_y + L_x^{'(m,n)} L_z^{'(m,n)}\gamma_x\gamma_z + L_y^{'(m,n)} L_z^{'(m,n)}\gamma_y\gamma_z) \\ +2\left((L_z^{'(m,n)} s_{1,y} - L_y^{'(m,n)} s_{1,z})\gamma_x + (L_x^{'(m,n)} s_{1,z} - L_z^{'(m,n)} s_{1,x})\gamma_y + (L_y^{'(m,n)} s_{1,x} - L_x^{'(m,n)} s_{1,y})\gamma_z\right)\end{aligned} \tag{5.72}$$

Given that $(d_{s1}^{(m,n)})^2 > C_R^2(\gamma)$ permits invoking the square root approximation of equation (5.70) such that its inverse can be written in the form of,

$$\frac{1}{d_{v^P}^{(m,n)}} = \frac{1}{d_{s1}^{(m,n)}}\left(1 - \frac{1}{2}\frac{C_R^2(\gamma)}{(d_{s1}^{(m,n)})^2}\right) \tag{5.73}$$

Then substituting (5.73) into (5.67) yields the approximation to $\psi_{s1}^{'(m,n)(P)}$, $(\psi_{s1}^{'(m,n)(P)})_A$, in the form of,

$$\psi_{s1}^{'(m,n)(P)} = \frac{v_x^{(P)} n_{s1,x}^c + v_y^{(P)} n_{s1,y}^c + v_z^{(P)} n_{s1,z}^c}{d_{s1}^{(m,n)}}\left(1 - \frac{1}{2}\frac{C_R^2(\gamma)}{(d_{s1}^{(m,n)})^2}\right) \tag{5.74}$$

Equation (5.74) then can be written in a similar fashion to that shown in the analysis of the translation perturbations as,

$$(\psi_{s1}^{'(m,n)(P)})_A = \psi_{s1}^{'(m,n)} + (\delta\psi_{s1,R}^{'(m,n)})_1 + (\delta\psi_{s1,R}^{'(m,n)})_2 \tag{5.75}$$

whereby the first term is the unperturbed viewing angle and the remaining terms are perturbed components.

The unperturbed component from equation (5.75) evaluates into,

$$\psi_{s1}^{'(m,n)} = (L_x^{'(m,n)} - s_{1,x})n_{s1,x}^c + (L_y^{'(m,n)} - s_{1,y})n_{s1,y}^c + (L_z^{'(m,n)} - s_{1,z})n_{s1,z}^c / d_{s1}^{(m,n)} \tag{5.76}$$

which is similar to the component observed in the case of the translational perturbation, as excepted.

On the other hand, the perturbed components can be each expressed as follows,

$$\begin{aligned}\left(\delta\psi_{s1,R}^{'(m,n)}\right)_1=&\left(\left(L_z^{'(m,n)}\gamma_y-L_y^{'(m,n)}\gamma_z\right)n_{(s1,x)}^c+\left(L_x^{'(m,n)}\gamma_z-L_z^{'(m,n)}\gamma_x\right)n_{(s1,y)}^c\right.\\&\left.+\left(L_y^{'(m,n)}\gamma_x-L_x^{'(m,n)}\gamma_y\right)n_{(s1,z)}^c\right)/d_{s1}^{(m,n)}\end{aligned}\tag{5.77}$$

$$\left(\delta\psi_{s1,R}^{'(m,n)}\right)_2=\frac{-1}{2\left(d_{s1}^{(m,n)}\right)^2}\left(\psi_{s1}^{'(m,n)}+\left(\delta\psi_{s1,R}^{'(m,n)}\right)_1\right)C_R^2(\gamma)\tag{5.78}$$

Next define for ease of notation the following,

$$v_{ab}^{(m,n)(\boldsymbol{n})}=L_a^{(m,n)}n_{s1,b}^c-L_b^{(m,n)}n_{s1,a}^c\tag{5.79.a}$$

$$v_{ab}^{(m,n)(\boldsymbol{s})}=L_a^{(m,n)}s_{1,b}-L_b^{(m,n)}s_{1,a}\tag{5.79.b}$$

$$\left(v_{ab}^{(m,n)}\right)^2=\left(L_a^{'(m,n)}\right)^2+\left(L_b^{'(m,n)}\right)^2\tag{5.79.c}$$

$$v_{ab}^{(m,n)}=L_a^{'(m,n)}L_b^{'(m,n)}\tag{5.79.d}$$

and $\left(\psi_{s1}^{'(m,n)}\right)_N$ as the numerator of (5.76).

Then expanding equation (5.78) in terms of (5.79.a) and (5.79.b) yields,

$$\begin{aligned}\left(\delta\psi_{s1,R}^{'(m,n)}\right)_3=&\left(v_{yz}^{(m,n)}\right)^2v_{yz}^{(m,n)(\boldsymbol{n})}\gamma_x^3+\left(v_{xz}^{(m,n)}\right)^2v_{xz}^{(m,n)(\boldsymbol{n})}\gamma_y^3+\left(v_{xy}^{(m,n)}\right)^2v_{xy}^{(m,n)(\boldsymbol{n})}\gamma_z^3\\&+\left(v_{xy}^{(m,n)}v_{xy}^{(m,n)(\boldsymbol{n})}+v_{xz}^{(m,n)}v_{xz}^{(m,n)(\boldsymbol{n})}+v_{yz}^{(m,n)}v_{yz}^{(m,n)(\boldsymbol{n})}\right)\gamma_x\gamma_y\gamma_z\\&+\left(v_{yz}^{(m,n)}\right)^2v_{zx}^{(m,n)(\boldsymbol{n})}-2\left(\left(v_{xy}^{(m,n)}\right)^2v_{yz}^{(m,n)(\boldsymbol{n})}\right)\gamma_x^2\gamma_y\\&+\left(v_{yz}^{(m,n)}\right)^2v_{xy}^{(m,n)(\boldsymbol{n})}-2\left(\left(v_{xz}^{(m,n)}\right)^2v_{yz}^{(m,n)(\boldsymbol{n})}\right)\gamma_x^2\gamma_z\\&+\left(v_{xz}^{(m,n)}\right)^2v_{yz}^{(m,n)(\boldsymbol{n})}-2\left(\left(v_{xy}^{(m,n)}\right)^2v_{zx}^{(m,n)(\boldsymbol{n})}\right)\gamma_x\gamma_y^2\\&+\left(v_{xy}^{(m,n)}\right)^2v_{yz}^{(m,n)(\boldsymbol{n})}-2\left(\left(v_{xz}^{(m,n)}\right)^2v_{xy}^{(m,n)(\boldsymbol{n})}\right)\gamma_x\gamma_z^2\\&+\left(v_{xz}^{(m,n)}\right)^2v_{xy}^{(m,n)(\boldsymbol{n})}-2\left(\left(v_{yz}^{(m,n)}\right)^2v_{zx}^{(m,n)(\boldsymbol{n})}\right)\gamma_y^2\gamma_z\\&+\left(v_{xy}^{(m,n)}\right)^2v_{zx}^{(m,n)(\boldsymbol{n})}-2\left(\left(v_{yz}^{(m,n)}\right)^2v_{xy}^{(m,n)(\boldsymbol{n})}\right)\gamma_y\gamma_z^2\\&+\left(\left(v_{yz}^{(m,n)}\right)^2\left(\psi_{s1}^{'(m,n)}\right)_N+2v_{zy}^{(m,n)(\boldsymbol{s})}v_{yz}^{(m,n)(\boldsymbol{n})}\right)\gamma_x^2\\&+\left(\left(v_{xz}^{(m,n)}\right)^2\left(\psi_{s1}^{'(m,n)}\right)_N+2v_{xz}^{(m,n)(\boldsymbol{s})}v_{zx}^{(m,n)(\boldsymbol{n})}\right)\gamma_y^2\\&+\left(\left(v_{xy}^{(m,n)}\right)^2\left(\psi_{s1}^{'(m,n)}\right)_N+2v_{yx}^{(m,n)(\boldsymbol{s})}v_{xy}^{(m,n)(\boldsymbol{n})}\right)\gamma_z^2\\&+2\left(v_{xz}^{(m,n)(\boldsymbol{s})}v_{yz}^{(m,n)(\boldsymbol{n})}+v_{zy}^{(m,n)(\boldsymbol{s})}v_{zx}^{(m,n)(\boldsymbol{n})}-v_{xy}^{(m,n)(\boldsymbol{s})}\left(\psi_{s1}^{'(m,n)}\right)_N\right)\gamma_x\gamma_y\\&+2\left(v_{xz}^{(m,n)(\boldsymbol{s})}v_{xy}^{(m,n)(\boldsymbol{n})}+v_{yx}^{(m,n)(\boldsymbol{s})}v_{zx}^{(m,n)(\boldsymbol{n})}-v_{yz}^{(m,n)(\boldsymbol{s})}\left(\psi_{s1}^{'(m,n)}\right)_N\right)\gamma_y\gamma_z\\&+2\left(v_{yx}^{(m,n)(\boldsymbol{s})}v_{yz}^{(m,n)(\boldsymbol{n})}+v_{zy}^{(m,n)(\boldsymbol{s})}v_{xy}^{(m,n)(\boldsymbol{n})}-v_{xz}^{(m,n)(\boldsymbol{s})}\left(\psi_{s1}^{'(m,n)}\right)_N\right)\gamma_x\gamma_y\\&+2v_{zy}^{(m,n)(\boldsymbol{s})}\left(\psi_{s1}^{'(m,n)}\right)_N\gamma_x+2v_{xz}^{(m,n)(\boldsymbol{s})}\left(\psi_{s1}^{'(m,n)}\right)_N\gamma_y+2v_{yx}^{(m,n)(\boldsymbol{s})}\left(\psi_{s1}^{'(m,n)}\right)_N\gamma_z\end{aligned}\tag{5.80}$$

where,

$$\left(\delta\psi_{s1,R}^{'(m,n)}\right)_3=\left(d_{s1}^{(m,n)}\right)^2\left(\delta\psi_{s1,R}^{'(m,n)}\right)_2\tag{5.81}$$

Accordingly, equation (5.75) can be written as,

$$\left(\psi_{s1}^{'(m,n)(P)}\right)_A = \psi_{s1}^{'(m,n)} + \left(\delta\psi_{s1,R}^{'(m,n)}\right)_1 - \left(\delta\psi_{s1,R}^{'(m,n)}\right)_3 / 2\left(d_{s1}^{(m,n)}\right)^3 \tag{5.82}$$

From the last expression it is possible to approximate the equation under the realization that $\left|\cos\left(\delta\psi_{s1,R}^{'(m,n)}\right)_3 / \left(d_{s1}^{(m,n)}\right)^3\right| \ll \left|\left(\delta\psi_{s1,R}^{'(m,n)}\right)_1\right|$. It is subsequently possible to neglect the term $\left(\delta\psi_{s1,R}^{'(m,n)}\right)_1$ and consider that,

$$\left(\psi_{s1}^{'(m,n)(P)}\right)_A = \psi_{s1}^{'(m,n)} + \left(\delta\psi_{s1,R}^{'(m,n)}\right)_1 \tag{5.83}$$

From this analysis, the distribution of $\left(\psi_{s1}^{'(m,n)(P)}\right)_A$ will follow a normal distribution. If it can be assumed that $\psi_{s1}^{'(m,n)}$ is directly pointed towards the center of the luminaire, then the approximation $\psi_{s1}^{'(m,n)} \approx 0$ holds. In this case, $\left(\psi_{s1}^{'(m,n)(P)}\right)_A \sim N\left(0, \sigma_{\psi_N}^2\right)$ with zero mean and variance given by,

$$\sigma_{\psi_N}^2 = \left(\left(v_{zy}^{(m,n)(\boldsymbol{n})}\right)^2 + \left(v_{zx}^{(m,n)(\boldsymbol{n})}\right)^2 + \left(v_{xy}^{(m,n)(\boldsymbol{n})}\right)^2\right)\sigma^2 / \left(d_{s1}^{(m,n)}\right)^2 \tag{5.84}$$

It is clear that $\sigma_{\psi_N}^2$ will tend to zero when $m = n = 0$.

5.4 Translation Perturbation of Luminaire:

The luminaire, due to external factors, can undergo translation perturbation in any of the three coordinate axes, independently from one another. This uncoupled translation can be encapsulated as the relative motion of a sensor to a fixed luminaire. Furthermore, it shall be assumed that there is no restriction that the translation must occur in either the LED array coordinate or the OC coordinate frames. Under such freedom of choice and to simplify the analysis, the translation will be expressed within the OC coordinate frame.

Consider that the translation perturbation induces a relative positional change with respect to LED $L^{(0,0)}$, in each of the sensors *x*, *y* and *z* components, $\boldsymbol{s}_{\boldsymbol{1}}^{'(\boldsymbol{P})} = \left(s_{1,x}^{'(P)}, s_{1,y}^{'(P)}, s_{1,z}^{'(P)}\right)$, to the effect of,

$$s_{1,x}^{'(P)} = s_{1,x}^{'} + \eta_x \tag{5.85.a}$$

$$s_{1,y}^{'(P)} = s_{1,y}^{'} + \eta_y \tag{5.85.b}$$

$$s_{1,z}^{'(P)} = s_{1,z}^{'} + \eta_z \tag{5.85.c}$$

where $\boldsymbol{s_1^{'(P)}}$ represents the perturbed sensor position that is affected by random positional variation on each axes by the iid RVs η_x , η_y and η_z .

Using matrices, equation set (5.85) can be expressed as follows,

$$\begin{bmatrix} s_{1,x}^{'(P)} \\ s_{1,y}^{'(P)} \\ s_{1,z}^{'(P)} \end{bmatrix} = \begin{bmatrix} 1 & 0 & 0 \\ 0 & 1 & 0 \\ 0 & 0 & 1 \end{bmatrix} \begin{bmatrix} \eta_x \\ \eta_y \\ \eta_z \end{bmatrix} + \begin{bmatrix} s_{1,x}^{'} \\ s_{1,y}^{'} \\ s_{1,z}^{'} \end{bmatrix} \tag{5.86.a}$$

or in a more compact form of,

$$\boldsymbol{s_1^{'(P)} = I\eta + s_1^{'}} \tag{5.86.b}$$

In the aforementioned definition of the RVs it was assumed that each had its own mean. However, it could be assumed that the RVs are perturbed about the unperturbed sensors location $\boldsymbol{s_1^{'}} = (s_{1,x}^{'}, s_{1,y}^{'}, s_{1,z}^{'})$. Moreover, it could be assumed that the variances of the variables are equal. With these two statements, the RVs means and variances can be given as $\mu_x = \mu_y = \mu_z = 0$ and $\sigma_x^2 = \sigma_y^2 = \sigma_x^2 = \sigma_\eta^2$.

As the perturbation should be inclusive of a complete range of possible external forces acting upon the luminaire, the Gaussian distribution can be considered as a suitable distribution. Under these considerations, the *x*, *y* and *z* translation perturbation RVs can be formally given by $\eta_x \sim N(0, \sigma_\eta^2)$, $\eta_y \sim N(0, \sigma_\eta^2)$ and $\eta_z \sim N(0, \sigma_\eta^2)$.

The joint distribution, $f_{\boldsymbol{S}^{'(P)}}(\boldsymbol{s}^{'(P)})$, containing all three components can be written in the form of a multivariate normal distribution as follows,

$$f_{\boldsymbol{S}^{'(P)}}(\boldsymbol{s}^{'(P)}) = \frac{1}{\sqrt{(2\pi)^3 |\boldsymbol{C}|}} e^{-\frac{1}{2}(\boldsymbol{\eta} - \boldsymbol{\mu}_{s'})^T \boldsymbol{C}^{-1} (\boldsymbol{\eta} - \boldsymbol{\mu}_{s'})} \tag{5.87}$$

with $\boldsymbol{C}$ as the covariance matrix that can be evaluated through $\boldsymbol{C}=\boldsymbol{E}[\boldsymbol{\eta}\boldsymbol{I}\boldsymbol{I}^{T}\boldsymbol{\eta}^{T}]$. By performing the multiplication, the covariance matrix $\boldsymbol{C}$ will have the simple form of,

$$\boldsymbol{C}=\boldsymbol{I}\sigma^{2} \tag{5.88}$$

The effect of this type of perturbation on the DC channel response, $H_{s1}^{(m,n)}(0)$, will be the result of the change in angles $\theta^{(m,n)}$, $\varphi^{(m,n)}$ and $\psi(x,y)$ compounded by the change in the distance variable $V(x,y)$. All these variables require to be expressed in terms of an offset from the coordinate origin, which translates into computing the angles and distance to an arbitrary LED $L^{(m,n)}$ positioned on the LED array. Therefore, the offset must be written in terms of variables $L_x^{(m,n)}$ and $L_y^{(m,n)}$ and be accounted for in all computations. Moreover, this offset should subsequently be transformed into the OC frame which results into obtaining the equivalent variables $L_x^{'(m,n)}$, $L_y^{'(m,n)}$ and $L_z^{'(m,n)}$.

5.4.1 Effect of Translation Perturbation on distance $d_{s1}^{(m,n)}$:

In a similar fashion to the analysis carried out for the rotation perturbation, the effect of the displacement perturbation on the LED to sensor separation distance shall be demonstrated. To begin with, consider the following naming schemes. The unperturbed and perturbed distances between sensor s_1 and LED $L^{(0,0)}$ shall be respectively denoted by $d_{s1}^{(0,0)}$ and $d_{s1}^{(0,0)(P)}$. Similarly, the perturbed distance between s_1 and LED $L^{(m,n)}$ shall be denoted by $d_{s1}^{(m,n)}$. Finally, the fixed distance separating both LED $L^{(0,0)}$ and $L^{(m,n)}$ will be denoted by $d^{(m,n)}$.

Distances $d^{(m,n)}$ which has been given earlier by equation (5.37) is repeated for convenience herein,

$$d^{(m,n)}=\sqrt{\left(\left(L_x^{'(m,n)}\right)^2+\left(L_y^{'(m,n)}\right)^2+\left(L_z^{'(m,n)}\right)^2\right)} \tag{5.89}$$

while $d_{s1}^{(0,0)}$ is defined as,

$$d_{s1}^{(0,0)}=\sqrt{\left(s_{1,x}^{'}\right)^2+\left(s_{1,y}^{'}\right)^2+\left(s_{1,z}^{'}\right)^2} \tag{5.90}$$

The parameter $d_{s1}^{(0,0)(P)}$ under the effect of the translational perturbation is variable unlike the case of rotation perturbation. To obtain the variability of $d_{s1}^{(0,0)(P)}$, first define a constant vector from LED $L^{(0,0)}$ to s_1 and a random vector from $s_1^{'}$ to $s_1^{'(P)}$. Then $d_{s1}^{(0,0)(P)}$ can be computed from,

$$d_{s1}^{(0,0)(P)}=\sqrt{\left(s_{1,x}^{'}+\eta_x\right)^2+\left(s_{1,y}^{'}+\eta_y\right)^2+\left(s_{1,z}^{'}+\eta_z\right)^2} \tag{5.91}$$

By expanding equation (5.91) and gathering the deterministic and random terms together, equation (5.91) can be suitably expressed by,

$$d_{s1}^{(0,0)(P)}=\sqrt{A_2+A_3} \tag{5.92}$$

with parameters A_2 and A_3 defined as,

$$A_2=\left(d_{s1}^{(0,0)}\right)^2 \tag{5.93.a}$$

$$A_3=\eta_x^{'}\eta_x+\eta_y^{'}\eta_y+\eta_z^{'}\eta_z \tag{5.93.b}$$

with $\eta_x^{'}\sim N\left(2s_{1,x},\sigma_\eta^2\right)$, $\eta_y^{'}\sim N\left(2s_{1,y},\sigma_\eta^2\right)$ and $\eta_z^{'}\sim N\left(2s_{1,z},\sigma_\eta^2\right)$.

It is clear from equation (5.93.b) that RV A_3 is the sum of correlated normal products, with correlation coefficient $\rho=1$ for every product. Furthermore, for the random variables within each product, it is observed that $\mu_{\eta_i}=0,\ i=\{x,y,z\}$ and $\sigma_{\eta_i}=\sigma_{\eta_i^{'}}=\sigma_\eta^2$.

Proceeding by using the equivalent approach shown in the rotation perturbation, the approximation to the square root can be obtained through,

$$d_{s1}^{(0,0)(P)}\approx B_2+B_3 \tag{5.94}$$

with

$$B_2=\sqrt{A_2} \quad \text{and} \quad B_3=\frac{A_3}{2\sqrt{A_2}}.$$

The separation distance between LED $L^{(0,0)}$ and sensor s_1 obtained by equation (4.52) can be interpreted as a distance that is centered about variable B_2 and perturbed by RV B_3 . To this effect, it is necessary to determine the PDF of B_3 , or equivalently A_3 .

There have been a number of researched papers specific to determining the product of two normal RVs. Most notably are the papers given by [155]-[158]. Herein, the approach adopted by [157] will be followed. It has been shown that the product of two correlated normal RVs $W_1 \sim N(\mu_{1,}\sigma_1^2)$ and $W_2 \sim N(\mu_{2,}\sigma_2^2)$ with correlation coefficient ρ , $U = W_1 W_2$, can be equally expressed as,

$$U = (W_0 + V_0)(W_0 + V_1) \tag{5.95}$$

with

$W_0 \sim N(0, \rho\sigma_1\sigma_2)$, $V_1 \sim N(\mu_{1,}\sigma_1^2 - \rho\sigma_1\sigma_2)$ and $V_2 \sim N(\mu_{2,}\sigma_2^2 - \rho\sigma_1\sigma_2)$ are all uncorrelated normal RVs.

The moment generating function (MGF) of a RV U , $M_U(t)$ is given through,

$$M_U(t) = \int_{-\infty}^{\infty} e^{tu} f(u)\,du \tag{5.96}$$

Substitution of equation (5.95) into (5.96) it has been shown in [157] that $M_U(t)$ is,

$$M_U(t) = \frac{1}{\sqrt{B_4}} e^{\frac{B_5 t - B_6 t^2/2}{B_4}} \tag{5.97}$$

with parameters B_4 , B_5 and B_6 derived as,

$$B_4 = (1 - \rho\sigma_1\sigma_2 t)^2 - \sigma_1^2\sigma_2^2 t^2 \tag{5.98.a}$$

$$B_5 = \mu_1\mu_2 \tag{5.98.b}$$

$$B_6 = \mu_1^2\sigma_2^2 + \mu_2^2\sigma_1^2 - 2\rho\,\mu_1\mu_2\sigma_1\sigma_2 \tag{5.98.c}$$

Then by substituting for $\mu_1=0$, $\sigma_1^2=\sigma_2^2=\sigma^2$ and $\rho=1$, and proceeding as shown in appendix A.1, the mean, variance and skewness can all be respectively obtained as,

$$\mu_U=\sigma^2 \tag{5.99}$$

$$\sigma_U^2=\sigma^2(\mu^2+\sigma^2) \tag{5.100}$$

$$skew_U=\frac{\sigma(11\sigma^2+6\mu^2)}{(\sigma^2+\mu^2)^{3/2}} \tag{5.101}$$

$$kurt_U=\frac{3(18\sigma^4+20\mu^2\sigma^2+\mu^4)}{(\sigma^4+2\mu^2\sigma^2+\mu^4)} \tag{5.102}$$

From these generalized results, the values of μ can be interchanged by μ_{η_i}, $i=\{x,y,z\}$ while $\sigma^2=\sigma_\eta^2$. To conduct a simple analysis on the parameters $skew_U$ and $kurt_U$ it should first be noted that for all practical cases, $\mu_{\eta_i}\gg\sigma_\eta$. Accordingly, from equation (5.89) $skew_U\approx 0$ and from equation (5.102) $kurt_U-3\approx 0$.

An alternative approach to the above analysis can be obtained through expanding equation (5.91) into the root sum of a chi-squared and normal random variables as,

$$d_{s1}^{(0,0)(P)}=\sqrt{A_4+A_5} \tag{5.103}$$

with parameters A_4 and A_5 are respectively given by,

$$A_4=\eta_x^2+\eta_y^2+\eta_z^2 \tag{5.104}$$

and

$$A_5=2(s_{1,x}^{'}\eta_x+s_{1,y}^{'}\eta_y+s_{1,z}^{'}\eta_z)+(s_{1,x}^{'})^2+(s_{1,y}^{'})^2+(s_{1,z}^{'})^2 \tag{5.105}$$

By inspection of equation (5.104), A_4 it is known that the sum of *k* the squares of iid standard Gaussian RVs will produce a chi-squared RV of *k* degrees of freedom, $\chi^2(k)$. Although each of the three RVs in A_4 are not standard Gaussian RVs, however, it is simple to transform them into the standard form. Applying the

transformation will result in $A_4 \sim \sigma_\eta^2 \chi^2(k)$, which is simply a weighted chi-squared RV, with three degrees of freedom.

Equivalently, A_5 from equation (5.105) is observed to be a normal RV, $A_5 \sim N(\mu_{A_5}, \sigma_{A_5}^2)$, with mean and variance respectively given by,

$$\mu_{A_5} = (d_{s1}^{(0,0)})^2 \tag{5.106.a}$$

and

$$\sigma_{A_5}^2 = 4\sigma^2 (d_{s1}^{(0,0)})^2 \tag{5.106.b}$$

From inspecting equations (5.103)-(5.105), it is clear that for $|s_{1,i}^{'}| \gg \eta_i^2$, equation (5.103) can be approximated by,

$$d_{s1}^{(0,0)(P)} \approx \sqrt{A_5} \tag{5.107}$$

Approximation given by equation (5.107) holds true under all circumstances in the application of highway VLC. For the equation to hold true, the relation $|s_{1,z}^{'}| \gg \eta_z^2$ should be true over all highway configurations, even in the condition when $|s_{1,x}^{'}| < \eta_x^2$ and $|s_{1,y}^{'}| < \eta_y^2$ occurs. The condition physically implies that vehicles passing under street lights are always significantly lower than the allowable minimum sway along the *z* axis. This fact that is naturally true for all streetlight and vehicles traveling along the highway according to their specified functional design mode of operation.

From another aspect, equation (5.103) can be loosely interpreted as the square root of the convolution of a chi-squared and a normal RV, though strictly both RVs must be independent. In light of this, observing the variance of each function provides good insight into the relative shapes of the functions. Then under all practical VLC scenarios, the variance attached to the chi-squared RV, which is independent of sensor position, is observed to be much smaller compared to the normal RV counterpart. As such, the chi-squared RV tends towards an impulse as the sensor moves away from the streetlight. It can therefore be conjured that the normal RV predominates, and henceforth, equation (5.107) becomes an accurate approximation

of $d_{s1}^{(0,0)(P)}$.

The approximate distribution that follows from equation (5.107) for $d_{s1}^{(0,0)(P)}$ can be obtained directly. Then $d_{s1}^{(0,0)(P)} \sim N\left(\mu_{d_{s1}^{0,0}}, \sigma_{d_{s1}^{0,0}}^2\right)$ with the mean and variance respectively given as $\mu_{d_{s1}^{0,0}} = d_{s1}^{(0,0)}$ and $\sigma_{d_{s1}^{0,0}}^2 = \sigma^2$.

The focus next will be to obtain the displacement perturbation relative to $L^{(m,n)}$. The distance can be computed based upon the length of the vector connecting LED $L^{(m,n)}$ to $s_1^{'(P)}$. This vector is the resultant vector of the vector from LED $L^{(m,n)}$ to LED $L^{(0,0)}$, followed by the vector from LED $L^{(0,0)}$ to $s_1^{'}$ followed by the random vector from $s_1^{'}$ to $s_1^{'(P)}$. In light of this, the perturbed distance is given as,

$$d_{s1}^{(m,n)(P)} = \sqrt{\left(s_{1,x}^{'} + \delta x + \eta_x\right)^2 + \left(s_{1,y}^{'} + \delta y + \eta_y\right)^2 + \left(s_{1,z}^{'} - \delta z + \eta_z\right)^2} \tag{5.108}$$

with δx , δy and δz are the offset displacements of the LEDs on the LED plane in each of the *x*, *y* and *z* axes respectively.

Implementing an approach similar to the analysis shown for $d_{s1}^{(0,0)(P)}$, equation (5.108) can be expressed as,

$$d_{s1}^{(m,n)(P)} = \sqrt{A_4 + A_6} \tag{5.109}$$

with parameters A_4 as given by equation (5.104) and A_6 given by,

$$\begin{aligned} A_6 = 2\left[\left(s_{1,x}^{'} + \delta x\right)\eta_x + \left(s_{1,y}^{'} + \delta y\right)\eta_y + \left(s_{1,z}^{'} - \delta z\right)\eta_z\right] + \left(s_{1,x}^{'}\right)^2 + \left(s_{1,y}^{'}\right)^2 + \left(s_{1,z}^{'}\right)^2 \\ + \delta_x^2 + \delta_y^2 + \delta_z^2 + 2\left(s_{1,x}^{'}\delta x + s_{1,y}^{'}\delta y - s_{1,z}^{'}\delta z\right) \end{aligned} \tag{5.110}$$

From equation (5.110), it can be ascertained that $A_6 \sim N\left(\mu_{A_6}, \sigma_{A_6}^2\right)$, with μ_{A_6} and $\sigma_{A_6}^2$ given respectively as,

$$\mu_{A_6} = \left(s_{1,x}^{'}\right)^2 + \left(s_{1,y}^{'}\right)^2 + \left(s_{1,z}^{'}\right)^2 + \delta_x^2 + \delta_y^2 + \delta_z^2 + 2\left(s_{1,x}^{'}\delta x + s_{1,y}^{'}\delta y - s_{1,z}^{'}\delta z\right) \tag{5.111.a}$$

$$\sigma_{A_6}^2 = 4\sigma^2\left[\left(s_{1,x}^{'} + \delta x\right)^2 + \left(s_{1,y}^{'} + \delta y\right)^2 + \left(s_{1,z}^{'} - \delta z\right)^2\right] \tag{5.111.b}$$

Taking the same approximation as that shown for equation (5.103), $d_{s1}^{(m,n)(P)}$ can be approximated as,

$$d_{s1}^{(m,n)(P)} \approx \sqrt{A_6} \tag{5.112}$$

The approximation shows that $d_{s1}^{(m,n)(P)} \sim N\left(\mu_{d_{s1}^{(m,n)}}, \sigma^2_{d_{s1}^{(m,n)}}\right)$ with the mean and variances given as,

$$\mu_{d_{s1}^{m,n}} = \sqrt{\mu_{A_6}} \tag{5.113.a}$$

$$\sigma^2_{d_{s1}^{m,n}} = \sigma^2 \tag{5.113.b}$$

Although the analysis herein has been validated for $d_{s1}^{(m,n)(P)}$, this quantity is not explicitly used. Rather the quantity $1/d_{s1}^{(m,n)(P)}$ which often occurs within the computations. Hence by applying the identity

$$\frac{1}{\sqrt{1+x}} \approx 1 - \frac{x}{2} \tag{5.114}$$

the inverse of $d_{s1}^{(m,n)(P)}$ can be represented as,

$$1/d_{s1}^{(m,n)(P)} \approx B_4 - B_6 \tag{5.115}$$

with

$$B_4 = \sqrt{A_7} \tag{5.116}$$

$$B_6 = \frac{A_8}{2\sqrt{A_7}} \tag{5.117}$$

and variables A_7 and A_8 are given by,

$$A_7 = \left(d^{(m,n)}\right)^2 + \left(d_{s1}^{(m,n)}\right)^2 - 2\left(L_x^{'(m,n)} s'_{1,x} + L_y^{'(m,n)} s'_{1,y} + L_z^{'(m,n)} s'_{1,z}\right) \tag{5.118}$$

$$A_8 = 2\left(\left(s'_{1,x} - L_x^{'(m,n)}\right)\eta_x + \left(s'_{1,y} - L_y^{'(m,n)}\right)\eta_y + \left(s'_{1,z} - L_z^{'(m,n)}\right)\eta_z\right) + \eta_x^2 + \eta_y^2 + \eta_z^2 \tag{5.119}$$

Equation (5.119) can be expressed compactly as,

$$A_8 = 2C(\eta) + C(\eta^2) \tag{5.120}$$

Then by implementing the same justification as shown earlier, given that $2C(\eta) \gg C(\eta^2)$, it will be assumed that an appropriate approximation for A_8 will be,

$$A_8 \approx 2C(\eta) \tag{5.121}$$

By using this approximation, equation (5.115) demonstrates that $1/d_{s1}^{(m,n)(P)}$ can be approximated by a Gaussian RV identified by $1/d_{s1}^{(m,n)(P)} \sim N(\mu_d^{(m,n)}, (\sigma_d^{(m,n)})^2)$. The mean and variance, $\mu_d^{(m,n)}$ and $(\sigma_d^{(m,n)})^2$, are respectively given as,

$$\mu_d^{(m,n)} = \sqrt{A_7} \tag{5.122.a}$$

$$(\sigma_d^{(m,n)})^2 = 4\left((s'_{1,x} - L_x'^{(m,n)})^2 + (s'_{1,y} - L_y'^{(m,n)})^2 + (s'_{1,z} - L_z'^{(m,n)})^2\right)\sigma_y^2 \tag{5.122.b}$$

5.4.2 Effect of Translation Perturbation on Polar Angle $\theta^{(m,n)(P)}$:

Recalling the polar angle $\theta^{(m,n)}$ given by equation (4.82), the displacement perturbed equivalent form that is similar to the rotational perturbation is obtained as,

$$\cos(\theta_{s1}^{'(P)}) = -s_{1,z}^{(m,n)(P)} / d_{s1}^{(m,n)(P)} \tag{5.123}$$

It can be assumed that the effect of any translation will introduce an amount of small angle variation, that can be envisaged in the form shown by equation (5.28). The small scale translation perturbation effect can hence be given as,

$$\delta\theta = \theta_z^{(m,n)(P)} / d_{s1}^{(m,n)(P)} \tag{5.124}$$

with $d_{s1}^{(m,n)(P)}$ as shown by its approximate form, equation (5.112), and $\theta_z^{(m,n)(P)}$ given by,

$$\theta_z^{(m,n)(P)} = \frac{s'_{1,z} - L_z'^{(m,n)} + \eta_z + \cos(\theta^{(m,n)})}{\sin(\theta^{(m,n)})} \tag{5.125}$$

Then by substituting (5.125) into (5.124) and utilizing approximation (5.115), $\delta\theta$ can be expressed as,

$$\delta\theta^{(m,n)} = \theta^{(m,n)} + \delta\theta_1^{(m,n)} + \delta\theta_2^{(m,n)} \tag{5.126}$$

with the variables $\delta\theta_1^{(m,n)}$ and $\delta\theta_2^{(m,n)}$ containing all of the perturbed elements.

Variable $\delta\theta_1^{(m,n)}$ can be given as,

$$\delta\theta_1^{(m,n)}=\frac{\eta_z}{d_{s1}^{(m,n)}\sin\left(\theta^{(m,n)}\right)} \tag{5.127}$$

For variable $\delta\theta_2^{(m,n)}$ and to facilitate result interpretation, the following notation is introduced,

$$v_i^{(m,n)}=s_{1,i}-L_i^{(m,n)} \tag{5.128}$$

Similarly, consider $\delta\theta_3^{(m,n)}=\delta\theta_2^{(m,n)}/d_{s1}^{(m,n)}$, then $\delta\theta_3^{(m,n)}$ will be,

$$\begin{aligned}\delta\theta_3^{(m,n)}=&v_x^{(m,n)}v_z^{(m,n)}\eta_x+v_y^{(m,n)}v_z^{(m,n)}\eta_y+\left(v_z^{(m,n)}\right)^2\eta_z\\&+\frac{v_z^{(m,n)}}{2}\left(\eta_x^2+\eta_y^2+\eta_z^2\right)\end{aligned} \tag{5.129}$$

Then in terms of $\delta\theta_3^{(m,n)}$ equation (5.126) will become,

$$\delta\theta^{(m,n)}=\theta^{(m,n)}+\delta\theta_1^{(m,n)}+\delta\theta_3^{(m,n)}/d_{s1}^{(m,n)} \tag{5.130}$$

Finally, knowing that $\delta\theta_1^{(m,n)}\gg\delta\theta_3^{(m,n)}/d_{s1}^{(m,n)}$ it will be assumed that $\delta\theta^{(m,n)}$ can be further approximated through discarding the third term of equation (5.130). Accordingly, the approximate $\delta\theta^{(m,n)}$ is now,

$$\delta\theta^{(m,n)}=\theta^{(m,n)}+\delta\theta_1^{(m,n)} \tag{5.131}$$

where $\delta\theta_1^{(m,n)}$ is given by equation (5.127).

With η_z a normal distributed RV, it follows that $\theta_z^{(m,n)(P)}\sim N\left(\mu_{\theta_z},\left(\sigma_{\theta_z}\right)^2\right)$ with the mean and variance of $\theta_z^{(m,n)(P)}$ defined by,

$$\mu_{\theta_z}=\frac{s_{1,z}^{'}+\cos\left(\theta^{(m,n)}\right)}{\sin\left(\theta^{(m,n)}\right)} \tag{5.132}$$

$$\left(\sigma_{\theta_z}\right)^2=\sigma^2/\left(\sin\left(\theta^{(m,n)}\right)\right)^2 \tag{5.133}$$

5.4.3. Effect of Translation Perturbation on Azimuthal Angle $\varphi_{XY}^{(m,n)(P)}$:

The translational perturbation of the azimuthal angle can be demonstrated to follow a

similar format as given by equation (5.49). Accordingly, using the same logic as that shown for the derivation of the rotational perturbation, the small scale azimuthal angle disturbance due to the translational perturbation, $\delta\varphi_{xy}^{(m,n)}$, will follow equation (5.53) and is subsequently expressed as,

$$\delta\varphi_{xy}^{(m,n)}=\frac{\varphi_{xy,N}^{(m,n)}}{\varphi_{xy,D}^{(m,n)}} \tag{5.134}$$

It is now clear that the distribution of $\delta\varphi_{xy}^{(m,n)}$ is evaluated as the ratio of two normal RV functions, namely $\varphi_{xy,N}^{(m,n)}\sim N\left(\mu_{\varphi_{xy,N}},\sigma_{\varphi_{xy,N}}^2\right)$ and $\varphi_{xy,D}^{(m,n)}\sim N\left(\mu_{\varphi_{xy,D}},\sigma_{\varphi_{xy,D}}^2\right)$. Through the substitution for $s_{1,x}^{'(m,n)(P)}$ and $s_{1,y}^{'(m,n)(P)}$ using equations (5.13.a)-(5.13.b), the mean and variance of $\varphi_{xy,N}^{(m,n)}$ and $\varphi_{xy,D}^{(m,n)}$ is evaluated as,

$$\mu_{\varphi_{xy,N}}=\cos\left(\varphi^{(m,n)}\right)\left(s_{1,y}^{'}+\delta y\right)-\sin\left(\varphi^{(m,n)}\right)\left(s_{1,x}^{'}+\delta x\right) \tag{5.135.a}$$

$$\sigma_{\varphi_{xy,N}}^2=\left(\cos\left(\varphi^{(m,n)}\right)\left(s_{1,x}^{'}+\delta x\right)\right)^2+\left(\sin\left(\varphi^{(m,n)}\right)\left(s_{1,y}^{'}+\delta y\right)\right)^2 \tag{5.135.b}$$

$$\mu_{\varphi_{xy,D}}=\cos\left(\varphi^{(m,n)}\right)\left(s_{1,x}^{'}+\delta x\right)+\sin\left(\varphi^{(m,n)}\right)\left(s_{1,y}^{'}+\delta y\right) \tag{5.135.c}$$

$$\sigma_{\varphi_{xy,D}}^2=\left(\sin\left(\varphi^{(m,n)}\right)\left(s_{1,x}^{'}+\delta x\right)\right)^2+\left(\cos\left(\varphi^{(m,n)}\right)\left(s_{1,y}^{'}+\delta y\right)\right)^2 \tag{5.135.d}$$

5.4.4. Effect of Translation Perturbation on Sensor Viewing Angle $\psi_{s1}^{'(m,n)}$:

In this portion, the perturbation onto the sensor to LED viewing angle, $\psi_{s1}^{'(m,n)(P)}$, will be demonstrated. To commence with, it is assumed that the normal vector to sensor s_1 , $\boldsymbol{n}_{\boldsymbol{s1}}^{\boldsymbol{c}}$, is fixed to the center of a rectangular LED array of size $2\left(L_x\times L_y\right)$ for all relative motion of the sensor along its perceived path. This vector can be given as,

$$\boldsymbol{n}_{\boldsymbol{s1}}^{\boldsymbol{c}}=\left(n_{s1,x}^{c}\ \boldsymbol{i},\ n_{s1,y}^{c}\ \boldsymbol{j},\ n_{s1,z}^{c}\ \boldsymbol{k}\right) \tag{5.136}$$

with components $n_{s1,x}^{c}$ $n_{s1,y}^{c}$ and $n_{s1,z}^{c}$ given by,

$$n_{s1,x}^{c}=L_x^{'}-s_{1,x}^{'}/d_{s1}^{(L_x,0)} \tag{5.137.a}$$

$$n_{s1,y}^{c} = -s_{1,y}^{'} / d_{s1}^{(L_x,0)} \tag{5.137.b}$$

$$n_{s1,z}^{c} = L_z^{'} - s_{1,z}^{'} / d_{s1}^{(L_x,0)} \tag{5.137.c}$$

It is assumed that the center of the luminaire is aligned with the *x* axis. Moreover, the assumption is made that $\boldsymbol{n}_{\boldsymbol{s1}}^{\boldsymbol{c}}$ is computed aligned to the OC plane, such that $L_x^{'} = L_x \cos(\alpha)$ and $L_z^{'} = L_x \sin(\alpha)$ are the appropriate coordinate transformations from the LED array to the OC coordinate.

By recalling the equation of $\psi_{s1}^{'(m,n)}$, given by (4.106), its perturbed counterpart can be evaluated through the dot product of two vectors $\boldsymbol{n}_{\boldsymbol{s1}}^{\boldsymbol{c}}$ and $\boldsymbol{v}_{\boldsymbol{s1}}^{(\boldsymbol{m},\boldsymbol{n})(\boldsymbol{P})}$ as,

$$\cos(\psi_{s1}^{'(m,n)(P)}) = \boldsymbol{n}_{\boldsymbol{s1}}^{\boldsymbol{c}} \;.\; \boldsymbol{v}_{\boldsymbol{s1}}^{(\boldsymbol{m},\boldsymbol{n})(\boldsymbol{P})} \tag{5.138}$$

where $\boldsymbol{v}_{\boldsymbol{s1}}^{(\boldsymbol{m},\boldsymbol{n})(\boldsymbol{P})}$ indicates a normalized vector pointing to the observed LED $L^{(m,n)}$.

It is clear from the equation that the whole perturbation will be absorbed within $\boldsymbol{v}_{\boldsymbol{s1}}^{(\boldsymbol{m},\boldsymbol{n})(\boldsymbol{P})}$ while for all specific locations on the road, $\boldsymbol{n}_{\boldsymbol{s1}}^{\boldsymbol{c}}$ remains constant. The perturbed vector due to the translations, will then be,

$$\boldsymbol{v}_{\boldsymbol{s1}}^{(\boldsymbol{m},\boldsymbol{n})(\boldsymbol{P})} = \left(v_{s1,x}^{(m,n)(P)} \boldsymbol{i},\; v_{s1,y}^{(m,n)(P)} \boldsymbol{j},\; v_{s1,z}^{(m,n)(P)} \boldsymbol{k}\right) / d_{v^{(P)}} \tag{5.139}$$

where the *x*, *y* and *z* components of $\boldsymbol{v}_{\boldsymbol{s1}}^{(\boldsymbol{m},\boldsymbol{n})(\boldsymbol{P})}$ and its length are all denoted by $v_{s1,x}^{(m,n)(P)}$, $v_{s1,y}^{(m,n)(P)}$, $v_{s1,z}^{(m,n)(P)}$ and $d_{v^{(P)}}$ respectively.

For the components in $\boldsymbol{v}_{\boldsymbol{s1}}^{(\boldsymbol{m},\boldsymbol{n})(\boldsymbol{P})}$, each will be given by,

$$v_{s1,x}^{(m,n)(P)} = L_x^{'(m,n)} + \eta_x - s_{1,x} \tag{5.140.a}$$

$$v_{s1,y}^{(m,n)(P)} = L_y^{'(m,n)} + \eta_y - s_{1,y} \tag{5.140.b}$$

$$v_{s1,z}^{(m,n)(P)} = L_z^{'(m,n)} + \eta_z - s_{1,z} \tag{5.140.c}$$

Similarly, normalizing distance $d_{v^{(P)}}$ of $\boldsymbol{v}_{\boldsymbol{s1}}^{(\boldsymbol{m},\boldsymbol{n})(\boldsymbol{P})}$ evaluates as,

$$d_{v^{(P)}}=\sqrt{\left(L_x^{'(m,n)}+\eta_x-s_{1,x}\right)^2+\left(L_y^{'(m,n)}+\eta_y-s_{1,y}\right)^2+\left(L_z^{'(m,n)}+\eta_z-s_{1,z}\right)^2} \quad (5.141)$$

By expanding $d_{v^{(P)}}$ and collecting terms, equation (5.141) can be expressed as follows,

$$d_{v^{(P)}}=\sqrt{\left(d_{s1}^{(m,n)}\right)^2+C_T^2(\eta)} \quad (5.142)$$

with $d_{s1}^{(m,n)}$ and $C_T(\eta)$ represent respectively the unperturbed and perturbed separation distance components of sensor s_1 and LED $L^{(m,n)}$.

By appropriately grouping terms, both $\left(d_{s1}^{(m,n)}\right)^2$ and $C_T^2(\eta)$ are,

$$\left(d_{s1}^{(m,n)}\right)^2=s_{1,x}^2+s_{1,y}^2+s_{1,z}^2+\left(L_{1,x}^{'}\right)^2+\left(L_{1,x}^{'}\right)^2+\left(L_{1,x}^{'}\right)^2-2\left(L_{1,x}^{'}s_{1,x}+L_{1,y}^{'}s_{1,y}+L_{1,z}^{'}s_{1,z}\right) \quad (5.143)$$

$$C_{T,\psi}^2(\eta)=\eta_x^2+\eta_y^2+\eta_z^2+2\left[\left(L_x^{'}-s_{1,x}\right)\eta_x+\left(L_y^{'}-s_{1,y}\right)\eta_y+\left(L_z^{'}-s_{1,z}\right)\eta_z\right] \quad (5.144)$$

Under the realization that $\left(d_{s1}^{(m,n)}\right)^2 > C_{T,\psi}^2(\eta)$, it is now possible that the value of $1/d_{v^{(P)}}$ be approximated using,

$$\frac{1}{d_{v^P}}=1-\frac{1}{2}\frac{C_{T,\psi}^2(\eta)}{\left(d_{s1}^{(m,n)}\right)^2} \quad (5.145)$$

Substituting (5.145) into (5.139) and inserting the components of $\boldsymbol{n}_{\boldsymbol{s1}}^{\boldsymbol{c}}$ and $\boldsymbol{v}_{\boldsymbol{s1}}^{(\boldsymbol{m},\boldsymbol{n})(\boldsymbol{P})}$ into (5.138), the approximation to $\cos\left(\psi_{s1}^{'(m,n)(P)}\right)$, $\cos\left(\psi_{s1}^{'(m,n)(P)}\right)_A$, can be expressed as,

$$\cos\left(\psi_{s1}^{'(m,n)(P)}\right)_A = \frac{v_{s1,x}^{(m,n)(P)}n_{s1,x}^c+v_{s1,y}^{(m,n)(P)}n_{s1,y}^c+v_{s1,z}^{(m,n)(P)}n_{s1,z}^c}{\left(d_{s1}^{(m,n)}\right)}\left(1-\frac{1}{2}\frac{C_{T,\psi}^2(\eta)}{\left(d_{s1}^{(m,n)}\right)^2}\right) \quad (5.146)$$

Expanding equation (5.146) and collecting terms, $\cos\left(\psi_{s1}^{'(m,n)(P)}\right)_A$ becomes,

$$\cos\left(\psi_{s1}^{'(m,n)(P)}\right)_A=\cos\left(\psi_{s1}^{'(m,n)}\right)+\cos\left(\delta\psi_{s1}^{'(m,n)}\right)_1+\cos\left(\delta\psi_{s1}^{'(m,n)}\right)_2+\cos\left(\delta\psi_{s1}^{'(m,n)}\right) \quad (5.147)$$

where the first term in (5.147) represents the unperturbed viewing angle and all remaining terms represent the perturbations.

The unperturbed viewing angle will then be,

$$\cos\left(\psi_{s1}^{'(m,n)}\right)=\left(L_x^{'(m,n)}-s_{1,x}\right)n_{s1,x}^c+\left(L_y^{'(m,n)}-s_{1,y}\right)n_{s1,y}^c+\left(L_z^{'(m,n)}-s_{1,z}\right)n_{s1,z}^c/d_{s1}^{(m,n)} \quad (5.148)$$

Equivalently, each of the perturbed components will be expressed as follows,

$$\cos\left(\delta\psi_{s1}^{'(m,n)}\right)_1=\left(n_{s1,x}^c\eta_x+n_{s1,y}^c\eta_y+n_{s1,z}^c\eta_z\right)/d_{s1}^{(m,n)} \quad (5.149)$$

$$\cos\left(\delta\psi_{s1}^{'(m,n)}\right)_2=\frac{-1}{d_{s1}^{(m,n)}}\begin{pmatrix}\left(L_x^{'(m,n)}-s_{1,x}\right)n_{s1,x}^c+\left(L_y^{'(m,n)}-s_{1,y}\right)n_{s1,y}^c\\+\left(L_z^{'(m,n)}-s_{1,z}\right)n_{s1,z}^c+\left(\eta_x^2+\eta_y^2+\eta_z^2\right)\\+2\left(\left(L_x^{'(m,n)}-s_{1,x}\right)\eta_x+\left(L_y^{'(m,n)}-s_{1,y}\right)\eta_y+\left(L_z^{'(m,n)}-s_{1,z}\right)\eta_z\right)\end{pmatrix} \quad (5.150)$$

$$\cos\left(\delta\psi_{s1}^{'(m,n)}\right)_3=\frac{-1}{\left(d_{s1}^{(m,n)}\right)^3}\begin{pmatrix}n_{s1,x}^c\eta_x+n_{s1,y}^c\eta_y+n_{s1,z}^c\eta_z+\left(\eta_x^2+\eta_y^2+\eta_z^2\right)\\+2\left(\left(L_x^{'(m,n)}-s_{1,x}\right)\eta_x+\left(L_y^{'(m,n)}-s_{1,y}\right)\eta_y+\left(L_z^{'(m,n)}-s_{1,z}\right)\eta_z\right)\end{pmatrix} \quad (5.151)$$

Then let $v_{s1,i}^{(m,n)}=L_{s1,i}^{(m,n)}-s_{1,i}$, the sum of $\left(d_{s1}^{(m,n)}\right)^3\cos\left(\delta\psi_{s1}^{'(m,n)}\right)_2$ and $\left(d_{s1}^{(m,n)}\right)^3\cos\left(\delta\psi_{s1}^{'(m,n)}\right)_3$, $\cos\left(\delta\psi_{s1}^{'(m,n)}\right)_{23}$, evaluates into,

$$\begin{gathered}\cos\left(\delta\psi_{s1}^{'(m,n)}\right)_{23}=n_{s1,x}^c\eta_x^3+n_{s1,y}^c\eta_y^3+n_{s1,z}^c\eta_z^3\\n_{s1,x}^c\eta_x\left(\eta_y^2+\eta_z^2\right)+n_{s1,y}^c\eta_y\left(\eta_x^2+\eta_z^2\right)+n_{s1,z}^c\eta_z\left(\eta_x^2+\eta_y^2\right)\\+\left(3v_{s1,x}^{(m,n)}n_{s1,x}^c+v_{s1,y}^{(m,n)}n_{s1,y}^c+v_{s1,z}^{(m,n)}n_{s1,z}^c\right)\eta_x^2\\+\left(v_{s1,x}^{(m,n)}n_{s1,x}^c+3v_{s1,y}^{(m,n)}n_{s1,y}^c+v_{s1,z}^{(m,n)}n_{s1,z}^c\right)\eta_y^2\\+\left(v_{s1,x}^{(m,n)}n_{s1,x}^c+v_{s1,y}^{(m,n)}n_{s1,y}^c+3v_{s1,z}^{(m,n)}n_{s1,z}^c\right)\eta_z^2\\+2\left(v_{s1,x}^{(m,n)}n_{s1,y}^c+v_{s1,y}^{(m,n)}n_{s1,x}^c\right)\eta_x\eta_y\\+2\left(v_{s1,x}^{(m,n)}n_{s1,z}^c+v_{s1,z}^{(m,n)}n_{s1,x}^c\right)\eta_x\eta_z\\+2\left(v_{s1,y}^{(m,n)}n_{s1,z}^c+v_{s1,z}^{(m,n)}n_{s1,y}^c\right)\eta_y\eta_z\\+2\left(\left(v_{s1,x}^{(m,n)}\right)^2n_{s1,x}^c+v_{s1,x}^{(m,n)}v_{s1,y}^{(m,n)}n_{s1,y}^c+v_{s1,x}^{(m,n)}v_{s1,z}^{(m,n)}n_{s1,z}^c\right)\eta_x\\+2\left(v_{s1,x}^{(m,n)}v_{s1,y}^{(m,n)}n_{s1,x}^c+\left(v_{s1,y}^{(m,n)}\right)^2n_{s1,y}^c+v_{s1,y}^{(m,n)}v_{s1,z}^{(m,n)}n_{s1,z}^c\right)\eta_y\\+2\left(v_{s1,x}^{(m,n)}v_{s1,y}^{(m,n)}n_{s1,x}^c+v_{s1,y}^{(m,n)}v_{s1,z}^{(m,n)}n_{s1,y}^c+\left(v_{s1,z}^{(m,n)}\right)^2n_{s1,z}^c\right)\eta_z\end{gathered} \quad (5.152)$$

Finally, equation (5.147) can now be represented as,

$$\cos\left(\psi_{s1}^{'(m,n)(P)}\right)_A=\cos\left(\psi_{s1}^{'(m,n)}\right)+\cos\left(\delta\psi_{s1}^{'(m,n)}\right)_1-\cos\left(\delta\psi_{s1}^{'(m,n)}\right)_{23}/\left(d_{s1}^{(m,n)}\right)^3 \quad (5.153)$$

By a simple inspection of equation (5.153), it is revealed that $\left|\cos\left(\delta\psi_{s1}^{'(m,n)}\right)_{23}/\left(d_{s1}^{(m,n)}\right)^3\right|\ll\left|\cos\left(\delta\psi_{s1}^{'(m,n)}\right)_1\right|$. Using this realization, the third term in (5.153) can be neglected allowing for a further approximation of $\cos\left(\psi_{s1}^{'(m,n)(P)}\right)_A$ in the form of,

$$\cos\left(\psi_{s1}^{'(m,n)(P)}\right)_A=\cos\left(\psi_{s1}^{'(m,n)}\right)+\cos\left(\delta\psi_{s1}^{'(m,n)}\right)_1 \quad (5.154)$$

Then from equation (5.154) and in conjunction with equation (5.149), the mean and variance of $\cos\left(\psi_{s1}^{'(m,n)(P)}\right)_A$ will respectively be given as,

$$\mu_{c(\psi)_A}=\cos\left(\psi_{s1}^{'(m,n)}\right) \tag{5.155}$$

$$\sigma^2_{c(\psi)_A}=\left(\left(n^c_{s1,x}\right)^2+\left(n^c_{s1,y}\right)^2+\left(n^c_{s1,z}\right)^2\right)\sigma^2_\eta/\left(d_{s1}^{(m,n)}\right)^2 \tag{5.156}$$

A measure of the mean, $\mu_{c(\psi)_A}$, and variance, $\sigma^2_{c(\psi)_A}$, can be obtained from equations (5.155) and (5.156) under the practical consideration that $\psi_{s1}^{'(m,n)}\approx 1$ and $\left(d_{s1}^{(m,n)}\right)^2\gg\sigma^2_\eta$. For the first argument, it is considered that the sensor tracks perfectly the center of the unperturbed luminaire. The second states that the separation distance is practically much greater than the amount of shift a luminaire will undergo. Accordingly, it can be speculated that $\mu_{c(\psi)_A}\approx 1$ and $\sigma^2_{c(\psi)_A}\approx 0$.

5.5 Approximating the Intensity Distribution $I(\theta,\varphi)$:

The perturbations of angles θ and φ will influence on the outcome of $I(\theta,\varphi)$. Recalling from equation (4.70), it is shown that $I(\theta,\varphi)$ is a composite function composed from four other functions namely, U, $g_0(\varphi)$, $\theta_p(\varphi)$ and $G(\theta)$. To obtain an approximation of $I(\theta,\varphi)$ it is therefore important to investigate appropriate approximations of each of the four functions first.

Function U operates like a switch, dictated by the relation $\theta<\theta_p(\varphi)$, its effect will be observed as to give $I(\theta,\varphi)$ one of two different forms, as indicated by equation (4.70). From this relation the first function to be investigated will therefore be $\theta_p(\varphi)$. Furthermore, comparison of functions $g_0(\varphi)$ and $\theta_p(\varphi)$ with each other through equations (4.72) and (4.73) respectively, indicates that both functions bears strong resemblances. As such, an approximation of $g_0(\varphi)$ will follow suite. Next by assuming that, $U=0$ the intensity distribution, $I(\theta,\varphi)$, can be re-expressed as,

$$I(\theta,\varphi)=G(\theta_p(\varphi))e^{-w_0} \tag{5.157}$$

where,

$$w_0=g_0(\varphi)(|\theta|-\theta_p(\varphi))^2 \tag{5.158}$$

The final of the four functions, $G(\theta)$, which is given by equation (4.74), will subsequently be approximated, with $\theta_p(\varphi)$ replacing θ . After obtaining all necessary approximations of the four functions, the approximation of $I(\theta,\varphi)$ will finally be addressed.

5.5.1 Approximating $\theta_p(\varphi)$:

Recalling from equation (4.73), $\theta_p(\varphi)$ can be expressed through substitutions (4.139) and (4.140) as,

$$\theta_p(\varphi)=\tan^{-1}\left(\frac{A_xA_y}{\left[(A_x\sin(\varphi))^{m_{SE}}+(A_y\cos(\varphi))^{m_{SE}}\right]^{(1/m_{SE})}}\right) \tag{5.159}$$

Applying the Taylor series approximations of $\tan^{-1}(w_1)$ to the cube power of $\theta_p(\varphi)$ produces,

$$\theta_p(\varphi)\approx\begin{cases}\dfrac{\pi}{2}-\dfrac{(W_1(\varphi))}{A_xA_y}+\dfrac{(W_1(\varphi))^3}{3(A_xA_y)^3}, & w_1\geq 1 \quad (5.160.a)\\[2ex] \dfrac{A_xA_y}{(W_1(\varphi))}-\dfrac{A_xA_y^{\,3}}{3(W_1(\varphi))^3} & |w_1|<1 \quad (5.160.b)\end{cases}$$

with

$$w_1=\frac{A_xA_y}{\left[(A_x\sin(\varphi))^{m_{SE}}+(A_y\cos(\varphi))^{m_{SE}}\right]^{(1/m_{SE})}} \tag{5.161}$$

and

$$W_1(\varphi)=\left[(A_x\sin(\varphi))^{m_{SE}}+(A_y\cos(\varphi))^{m_{SE}}\right]^{(1/m_{SE})} \tag{5.162}$$

It can be observed from equations (5.160.a) and (5.160.b) that the approximation of $\theta_p(\varphi)$ will have two forms, determined by the value w_1 .

The next approximation considered is for $W_1(\varphi)$ in equation (5.162). Applying the Taylor series expansion, the first three terms of $W_1(\varphi)$ are,

$$W_1(\varphi)\approx\begin{cases} B_y[1+\frac{1}{m_{SE}}t_1^{m_{SE}}(\varphi)+(\frac{1-m_{SE}}{2m_{SE}^{\ 2}})t_1^{2m_{SE}}(\varphi)], & \tan(\varphi)<\frac{A_y}{A_x} \quad (5.163.a) \\ B_x[1+\frac{1}{m_{SE}}ct_1^{m_{SE}}(\varphi)+(\frac{1-m_{SE}}{2m_{SE}^{\ 2}})ct_1^{2m_{SE}}(\varphi)] & \tan(\varphi)>\frac{A_y}{A_x} \quad (5.163.b) \end{cases}$$

where,

B_x and B_y are given by equations (4.141) and (4.142) and $t_1(\varphi)=B_x/B_y$ and $ct_1(\varphi)=B_y/B_x$.

To simplify notations, the approximation to $W_1(\varphi)$ can be given as,

$$W_1(\varphi)\approx\begin{cases} (W_1(\varphi))_{1,} & \tan(\varphi)<\frac{A_y}{A_x} \quad (5.164.a) \\ (W_1(\varphi))_2 & \tan(\varphi)>\frac{A_y}{A_x} \quad (5.164.b) \end{cases}$$

It is clear from the equation pair (5.164.a) and (5.164.b) that there are two possible outcomes for $W_1(\varphi)$, depending upon the relation $\tan(\varphi)<A_y/A_x$. It is further possible to observe that $\theta_p(\varphi)$ can have four general outcomes. The four outcomes can be enumerated as,

$$\theta_p(\varphi)\approx\begin{cases} (\theta_p(\varphi))_{1,} & (w_1\geq 1),(\tan(\varphi)<\frac{A_y}{A_x}) \quad (5.165.a) \\ (\theta_p(\varphi))_{2,} & (w_1\geq 1),(\tan(\varphi)>\frac{A_y}{A_x}) \quad (5.165.b) \\ (\theta_p(\varphi))_{3,} & (|w_1|<1),(\tan(\varphi)<\frac{A_y}{A_x}) \quad (5.165.c) \\ (\theta_p(\varphi))_{4,} & (|w_1|<1),(\tan(\varphi)>\frac{A_y}{A_x}) \quad (5.165.d) \end{cases}$$

with $(\theta_p(\varphi))_1$ $(\theta_p(\varphi))_2$ $(\theta_p(\varphi))_3$ and $(\theta_p(\varphi))_4$ all given by,

$$(\theta_p(\varphi))_1=\frac{\pi}{2}-\frac{(W_1(\varphi))_1}{A_xA_y}+\frac{(W_1(\varphi))_1^3}{3(A_xA_y)^3} \quad (5.166.a)$$

$$(\theta_p(\varphi))_2=\frac{\pi}{2}-\frac{(W_1(\varphi))_2}{A_x A_y}+\frac{(W_1(\varphi))_2^3}{3(A_x A_y)^3} \tag{5.166.b}$$

$$(\theta_p(\varphi))_3=\frac{A_x A_y}{(W_1(\varphi))_1}-\frac{A_x A_y^{\,3}}{3(W_1(\varphi))_1^3} \tag{5.166.c}$$

$$(\theta_p(\varphi))_4=\frac{A_x A_y}{(W_1(\varphi))_2}-\frac{A_x A_y^{\,3}}{3(W_1(\varphi))_2^3} \tag{5.166.d}$$

5.5.2 Approximating $g_0(\varphi)$:

Again the same approximation principles as that shown for $\theta_p(\varphi)$ shall be applied to $g_0(\varphi)$. However, first $g_0(\varphi)$ in equation (4.72) can be re-expressed as,

$$g_0(\varphi)=\frac{g_{x,y}}{\sqrt{(B_{2,x})^2+(B_{2,y})^2}} \tag{5.167}$$

with,

$g_{x,y}=g_{0,x}g_{0,y}$, $B_{2,x}=g_{0,x}\sin(\varphi)$ and $B_{2,y}=g_{0,y}\cos(\varphi)$.

Then using the first three Taylor series expansion of $g_0(\varphi)$, the first three terms are,

$$g_0(\varphi)\approx\begin{cases}\dfrac{g_{x,y}}{B_{2,y}}(1-2t_2^2(\varphi)+3t_2^6(\varphi)) & \tan(\varphi)<\dfrac{g_{0,y}}{g_{0,x}} \quad (5.168.a)\\ \dfrac{g_{x,y}}{B_{2,x}}(1-2ct_2^2(\varphi)+3ct_2^6(\varphi)) & \tan(\varphi)>\dfrac{g_{0,y}}{g_{0,x}} \quad (5.168.b)\end{cases}$$

with,

$t_2=B_x/B_y$ and $ct_2=B_y/B_x$.

From the approximation of $g_0(\varphi)$, it is clear that there are two possible outcomes, depending upon the relation $\tan(\varphi)<g_{0,y}/g_{0,x}$.

5.5.3 Approximating $G(\theta)$:

The expression for $G(\theta)$ is given in equation (4.74). By grouping the terms in the exponent, $G(\theta)$ can be re-expressed as,

$$G(\theta)=g_1-g_2e^{-w_3} \tag{5.169}$$

where

$$w_3=g_3(\theta-g_4)^2 \tag{5.170}$$

It has been assumed that the value of θ remains positive for this application. Therefore, $|\theta|$ can be replaced by θ as shown in (5.170).

Then by applying the Taylor series expansion of e^{-w_3} , the first three terms of the approximation of $G(\theta)$ becomes,

$$G(\theta)\approx g_1-g_2(1-w_3+\frac{w_3^2}{2}) \tag{5.171}$$

This approximation can be directly used to obtain an approximation of $I(\theta,\varphi)$ in the case $U=1$. Then for this case, $I(\theta,\varphi)$ will be approximated as,

$$\begin{aligned} I(\theta) \approx & \frac{-g_2g_3^2}{2}\theta^4+2g_2g_3^2g_4\theta^3-g_2g_3(3g_3g_4^2+1)\theta^2 \\ & +2g_2g_3g_4(g_3g_4^2-1)\theta+g_1-g_2+g_2g_3g_4^2(1-g_3g_4^2) \end{aligned} \tag{5.172}$$

where the dependency of I on φ has been dropped.

On the other hand, if the requirement is to approximate $G(\theta_p(\varphi))$ rather than $G(\theta)$ then θ must be replaced by $\theta_p(\varphi)$ and w_3 be modified accordingly. This modification can be given in terms of,

$$w_{3,1}=g_3((\theta_p(\varphi))_1-g_4)^2 \tag{5.173.a}$$

$$w_{3,2}=g_3((\theta_p(\varphi))_2-g_4)^2 \tag{5.173.b}$$

$$w_{3,3}=g_3((\theta_p(\varphi))_3-g_4)^2 \tag{5.173.c}$$

$$w_{3,4}=g_3((\theta_p(\varphi))_4-g_4)^2 \tag{5.173.d}$$

As there are four possible outcomes for the approximation of $\theta_p(\varphi)$ then similarly $G(\theta_p(\varphi))$ too will retain four possible solutions. In general, the solution to $G(\theta_p(\varphi))$ for the specific $\theta_p(\varphi)$ will be,

$$G(\theta_p(\varphi))_i \approx g_1 - g_2\left(1 + w_{3,i} + \frac{w_{3,i}^2}{2}\right), \quad \forall i = 1,2,3,4 \tag{5.174}$$

5.5.4 Approximating $I(\theta,\varphi)$ for $U=0$:

For this case, a further approximation must be done to equation (5.157) with respect to the exponential. The general approximate of $I(\theta,\varphi)$ will be of the form,

$$I(\theta,\varphi) \approx G(\theta_p(\varphi))\left(1 + w_0 + \frac{w_0^2}{2}\right) \tag{5.175}$$

Applying this equation requires careful attention to the choice of the specific functions comprising w_0 , as given by equation (5.158). The specific choice can be obtained through inspection of $\tan(\varphi)$ in both $\theta_p(\varphi)$ and $g_0(\varphi)$. Introducing $g_{yx} = g_{0,y}/g_{0,x}$ and $A_{yx} = A_y/A_x$ it possible to enumerate all outcomes of $\tan(\varphi)$ for the condition $g_{yx} < A_{yx}$ as follows:

$$\tan(\varphi) \le g_{yx} < A_{yx} \tag{5.176.a}$$

$$g_{yx} \le \tan(\varphi) < A_{yx} \tag{5.176.b}$$

$$g_{yx} < A_{yx} \le \tan(\varphi) \tag{5.176.c}$$

A similar set of relations can be obtained for the condition when $A_{yx} < g_{yx}$. In this case the possibilities are,

$$\tan(\varphi) \le A_{yx} < g_{yx} \tag{5.177.a}$$

$$A_{yx} \le \tan(\varphi) < g_{yx} \tag{5.177.b}$$

$$A_{yx} < g_{yx} \le \tan(\varphi) \tag{5.177.c}$$

It is now possible to construct two tables that can assist in choosing the relevant set of equations for the approximation of $I(\theta,\varphi)$ in the case of $U=0$. Table 5.1

shows the set of equations that must be used when $g_{yx} < A_{yx}$ while Table 5.2 shows the equation set for $A_{yx} < g_{yx}$.

In the case at hand, the required values for the computation of g_{yx} and A_{yx} can be taken directly from table 4.1. The data gives $g_{yx} = 1$ and $A_{yx} = 2.728$, which clearly indicate that the parameters in table 5.1 should be chosen, while disregarding table 5.2.

Table 5.1. Equation set for $I(\theta, \varphi)$ approximation in case $U = 0$ and $g_{yx} < A_{yx}$.

$I(\theta, \varphi)$	Relation	Conditions	Equation set
$(I(\theta, \varphi))_1$	(5.176.a)	$w_1 < 1$	(5.165.a) (5.168.a) (5.174, i=1)
$(I(\theta, \varphi))_2$	(5.176.a)	$\lvert w_1 \rvert > 1$	(5.165.c) (5.168.a) (5.174, i=3)
$(I(\theta, \varphi))_3$	(5.176.b)	$w_1 < 1$	(5.165.a) (5.168.b) (5.174, i=1)
$(I(\theta, \varphi))_4$	(5.176.b)	$\lvert w_1 \rvert > 1$	(5.165.c) (5.168.b) (5.174, i=3)
$(I(\theta, \varphi))_5$	(5.176.c)	$w_1 < 1$	(5.165.b) (5.168.b) (5.174, i=2)
$(I(\theta, \varphi))_6$	(5.176.c)	$\lvert w_1 \rvert > 1$	(5.165.d) (5.168.b) (5.174, i=4)

Table 5.2. Equation set for $I(\theta, \varphi)$ approximation in case $U = 0$ and $A_{yx} < g_{yx}$.

$I(\theta, \varphi)$	Relation	Conditions	Equation set
$(I(\theta, \varphi))_7$	(5.177.a)	$w_1 < 1$	(5.165.a) (5.168.a) (5.174, i=1)
$(I(\theta, \varphi))_8$	(5.177.a)	$\lvert w_1 \rvert > 1$	(5.165.c) (5.168.a) (5.174, i=3)
$(I(\theta, \varphi))_9$	(5.177.b)	$w_1 < 1$	(5.165.b) (5.168.a) (5.174, i=2)
$(I(\theta, \varphi))_{10}$	(5.177.b)	$\lvert w_1 \rvert > 1$	(5.165.d) (5.168.a) (5.174, i=4)
$(I(\theta, \varphi))_{11}$	(5.177.c)	$w_1 < 1$	(5.165.b) (5.168.b) (5.174, i=2)
$(I(\theta, \varphi))_{12}$	(5.177.c)	$\lvert w_1 \rvert > 1$	(5.165.d) (5.168.b) (5.174, i=4)

It can be seen that evaluating an approximation to $I(\theta, \varphi)$ in the case of $U = 0$, is quite an involved process. Furthermore, it is known that this case will only occur when a sensor is in close proximity to the LED OC axis. In computing the perturbations, it can be considered that rotational perturbations will effect the sensor

most at the furthest point of signal detection. Within this region, computation of $I(\theta,\varphi)$ will be for the condition that $U=1$. In the case of translational perturbation, on the other hand, it will be assumed that the sensor still lies within the region $U=1$ but is at the closest point to the luminaire. The motivation for this is to produce a measure of the overall effect of the perturbations rather than to obtain exact values, while making the results tractable.

To obtain a measure on the perturbation on $I(\theta,\varphi)$ given by equation (5.172), polar angle θ must be replaced by $\theta+\delta\theta$ as,

$$I(\theta^P)=I(\theta+\delta\theta) \tag{5.178}$$

Accordingly, by including the small scale perturbations, equation (5.172) can be modified into,

$$I(\theta^P)\approx I(\theta)+I(\delta\theta) \tag{5.179}$$

where

$I(\theta)$ is the approximate given by equation (5.172) and $I(\delta\theta)$ is the small scale perturbations within $I(\theta^P)$.

This small scale perturbation can be given, to the second degree, by

$$I(\delta\theta)=g_2 g_3(1-3g_2 g_4^2)\delta\theta^2+2g_2 g_3 g_4(g_3 g_4^2-1)\delta\theta \tag{5.180}$$

Drawing that the perturbation of θ approximates to a Gaussian RV for both translation and rotation perturbations, then by inspection of equation (5.180) it is clear that the PDF of $I(\delta\theta)$ is the sum of a correlated Gaussian and chi-squared RVs.

5.6 Perturbed DC Channel Response:

Having determined the most influential parameters that constitute the channel response in the prior sections, in this section the effect of the perturbation on the DC response will be developed.

To commence, recall that the DC channel response, $H_{s1}(0)$, of a single LED at the origin, can be given by expression (4.110) as,

$$H_{s1}(0)=\begin{cases}\dfrac{C_H}{(d_{s1})^2}I_{s1}(\theta,\varphi)\cos(\psi_{s1}), & 0\le\psi_{s1}\le\psi_{FOV}\\ 0, & \psi_{s1}>\psi_{FOV}\end{cases} \tag{5.181}$$

where C_H is a constant that encapsulates all of the constants in equation (4.110).

Equation (5.181) can now be modified to include any gained insight to the effect of the perturbations on $I(\theta,\varphi)$ and $\cos(\psi_{s1})$. For all practical cases, a sensor that tracks the average luminaire center for a given vehicles position, it has been shown that $\cos(\psi_{s1})=1$ for both translational and rotational perturbations. Subsequently, it has been discussed that $I_{s1}(\theta,\varphi)$ in the case with $U=1$ is sufficient. In this case $I_{s1}(\theta,\varphi)=I_{s1}(\theta)$. The approximate perturbed DC channel response, $H_{s1}^{(P)}(0)$, can now be given as,

$$H_{s1}^{(P)}(0)=\frac{C_H}{(d_{s1}^{(P)})^2}I_{s1}^{(P)}(\theta) \tag{5.182}$$

where it is implied that the Rx tracks the center of the luminaire.

With $I_{s1}^{(P)}(\theta)$ given by equation (5.178), a generalized expression for $(d_{s1}^{(P)})^2$ is demonstrated. In general, $(d_{s1}^{(P)})^2$ can be represented by its unperturbed and perturbed components as,

$$(d_{s1}^{(P)})^2=d_{s1}^2+\delta d_{s1}^2 \tag{5.183}$$

with d_{s1}^2 and δd_{s1}^2 are the unperturbed and perturbed distance squared components.

The unperturbed component d_{s1}^2 will be given by,

$$d_{s1}^2=s_{1,x}^2+s_{1,y}^2+s_{1,z}^2 \tag{5.184}$$

For δd_{s1}^2 two expressions can be obtained, depending upon the type of

perturbation. In the case of a rotational perturbation, δd_{s1}^2 can be expressed as,

$$\begin{aligned}\delta d_{s1}^2 = &(s_{1,y}^2 + s_{1,z}^2)\gamma_x^2 + (s_{1,x}^2 + s_{1,z}^2)\gamma_y^2 + (s_{1,x}^2 + s_{1,y}^2)\gamma_z^2 \\ &-2s_{1,x}s_{1,y}\gamma_x\gamma_y - 2s_{1,x}s_{1,z}\gamma_x\gamma_z - 2s_{1,y}s_{1,z}\gamma_y\gamma_z\end{aligned} \tag{5.185}$$

While for the case of translational perturbations, δd_{s1}^2 becomes,

$$\delta d_{s1}^2 = \eta_x^2 + \eta_y^2 + \eta_z^2 + 2(s_{1,x}\eta_x + s_{1,y}\eta_y + s_{1,z}\eta_z) \tag{5.186}$$

It is now feasible to modify equation (5.181) to accommodate for the perturbations. Equation (5.182) will then be,

$$H_{s1}^{(P)}(0) = \frac{C_H}{d_{s1}^2 + \delta d_{s1}^2}(I_{s1}(\theta) + I_{s1}(\delta\theta)) \tag{5.187}$$

For all practical reasons, it could be considered that $\delta d_{s1}^2 \ll d_{s1}^2$, an assumption that allows $H_{s1}^{(P)}(0)$ to be represented by a Taylor series. Accordingly, $H_{s1}^{(P)}(0)$ expanded to the third degree becomes,

$$H_{s1}^{(P)}(0) \approx \frac{C_H}{d_{s1}^2}(I_{s1}(\theta) + I_{s1}(\delta\theta))\left(1 - \frac{\delta d_{s1}^2}{d_{s1}^2} + \frac{\delta d_{s1}^4}{d_{s1}^4} - \frac{\delta d_{s1}^6}{d_{s1}^6}\right) \tag{5.188}$$

Considering that the contribution of the terms of degree greater than 2 will have little influence on $H_{s1}^{(P)}(0)$, then

$$H_{s1}^{(P)}(0) \approx \frac{C_H}{d_{s1}^2} I_{s1}(\theta) + \frac{C_H}{d_{s1}^2} I_{s1}(\delta\theta) - \frac{C_H}{d_{s1}^4} I_{s1}(\theta)\delta d_{s1}^2 - \frac{C_H}{d_{s1}^4} I_{s1}(\delta\theta)\delta d_{s1}^2 \tag{5.189}$$

Finally, realizing that $\delta d_{s1}^2 \ll d_{s1}^4$, $H_{s1}^{(P)}(0)$ can be further reduced to,

$$H_{s1}^{(P)}(0) \approx H_{s1}(0) + \delta H_{s1}(0) \tag{5.190}$$

where,

$$H_{s1}(0) = \frac{C_H}{d_{s1}^2} I_{s1}(\theta) \tag{5.191}$$

and

$$\delta H_{s1}(0) = \frac{C_H}{d_{s1}^2} I_{s1}(\delta\theta) \tag{5.192}$$

This result indicates that the statistics of $H_{s1}^{(P)}(0)$ will be greatly influenced by the perturbation in $I(\theta)$ compared to the influence of all other parameters.

The PDF of $H_{s1}^{(P)}(0)$ can now be identified. Relating equation (5.192) with equation (5.180) shows that $H_{s1}^{(P)}(0)$ can be approximated as the sum of a correlated Gaussian and Chi-squared RVs. Then according to table 4.1, which indicates that parameter $g_4=0$, $\delta H_{s1}(0)$ for this special condition yields,

$$\delta H_{s1}(0)=\frac{C_H}{d_{s1}^2} g_2 g_3 (\delta\theta)^2 \tag{5.193}$$

where, parameters g_2 and g_3 are as given in Table 4.1.

Finally, the perturbed channel response becomes a chi-squared RV as per equation (5.193).

Chapter 6

Channel Capacity and RMS Time Delay Spread

6.1 Introduction:

In this chapter the channel capacity and the RMS time delay equations of the VLC system will be obtained through analysis. For both parameters, the equations will be shown for the perturbed and unperturbed cases. Accordingly, the following section is devoted to the channel capacity, whereas the RMS time delay is shown in section 6.3.

6.2 Channel Capacity:

It is assumed that the system utilizes IM/DD with OOK. Furthermore, it is assumed in the following that the signal is computed for a single point over the track. Henceforth, for the unperturbed channel it will be assumed that at any specific track location the channel is constant. In this condition the channel will be independent of time and therefore the time variable can be altogether ignored.

Consider the instantaneous optical power signal waveform, produced by an LED, is denoted by $G(t)$. Then from $G(t)$, the average transmitted power, P_t , over a time duration of $2T$, for the signal LED case, will be given as,

$$P_t = \frac{1}{2T}\int_0^{2T} G(t)\,dt \tag{6.1}$$

As each LED functions in both illumination and signaling modes, with the signal

superimposed over the illumination, an average transmitted power of $P_t = P_A$ will be observed for all operating LEDs. Moreover, it is reasonable to considered that for OOK operating over the illumination of streetlights that waveform $G(t)$ will only have two distinct levels, i.e. $G(t) \in \{U_{0,} U_1\}$. Then for OOK signaling, waveform $G(t)$ can assume,

$$G(t) = \begin{cases} P_A + P_{1,} & for\, b = 1 \\ P_A - P_{1,} & for\, b = 0 \end{cases} \tag{6.2}$$

Then the desired received power, according to [38], will be,

$$P_r = H_{0,1}(0) P_t \tag{6.3}$$

It will be considered that the channel is distortionless. The received light will be the combined light from the closest pole and the two neighboring poles. The light from the closest pole will include the light from the desired and non-desired luminaires. Then, the light from the desired luminaire will be the received signal and all remaining light are considered interferences. This received illumination will then be transformed into a current signal, $V(t)$, that can represented as,

$$V(t) = H_{0,0}(0) G(t) + \left(H_{0,1}(0) + \sum_{\substack{i=-1 \\ i \neq 0}}^{1} \sum_{j=0}^{1} H_{i,j}(0)\right) \; G(t) \tag{6.4.a}$$

or more compactly expressed in the form of,

$$V(t) = R_0(t) + I_0(t) + \sum_{\substack{i=-1 \\ i \neq 0}}^{1} \sum_{j=0}^{1} I_{i,j}(t) \tag{6.4.b}$$

In the event that the opposite side of the road luminaires, i.e. $j = 1$, contribute with an insignificant amount to $V(t)$ then expression (6.4.b) can be simplified into,

$$V(t) = R_0(t) + I_{-1,0}(t) + I_{1,0}(t) \tag{6.5}$$

A further simplification can be included within equation (6.5) under the proposed Rx design specification that incorporates a motor to the sensor. The motorized sensor will therefore, maintain a lock onto the desired luminaire center. This setup ensures that the closest interfering luminaire, located on the same end of the road as the Rx, will have no effect on the received signal level. According to this, at the Rx,

$I_{(-1,0)}(t)=I_{(1,0)}(t)=0$.

The received signal will also constitute a random noise component, $n(t)$, which in essence is the accumulation of numerous noise sources. According to [7] and [10], the noise can be divided into thermal and shot noise. Moreover, shot noise can be due to background radiation, received signal and dark current.

By adding the noise to the signal at the Rx location the received signal is defined as,

$$R(t)=V(t)+n(t) \tag{6.6}$$

where the noise can be appropriately modeled by white Gaussian noise.

For the given system, $n(t)$ will have power $P_n=4\sigma_n^2$ with variance σ_n^2 .

For a detector that operates on the maximum likelihood (ML) principle in Gaussian noise, a pulse can be distinguished from another pulse by defining the minimum distance, d_{min} , between two received signal levels. The minimum distance over a single bit duration, T_b , will then be,

$$d_{min}^2=\min_{i\neq j}\int_0^{T_b}(R_{0,i}(t)-R_{0,j}(t))^2dt \tag{6.7}$$

Substitution of equation (6.2) for OOK yields d_{min} as,

$$d_{min}^2=4T_bH_{0,1}^2P_t^2=\frac{4}{R_b}H_{0,1}^2P_t^2 \tag{6.8}$$

where $R_b=1/T_b$ is the bit rate in b/s.

Then for a ML detector, the probability of error, P_e , can be given in terms of the SNR as [126],

$$P_e=Q(\sqrt{(SNR)})=Q(\sqrt{(\frac{d_{min}^2}{4\sigma_n^2})}) \tag{6.9}$$

In turn, the SNR can be obtained in terms of the received power, P_r , sensor

sensitivity, r , and noise, N , as,

$$SNR = \frac{(r P_r)^2}{N} \tag{6.10}$$

Noise N , as mentioned earlier, is composed from two dominant noise sources, a shot noise component, σ_{shot}^2 , and a thermal noise component, $\sigma_{thermal}^2$, which is appropriately given as [2],

$$N = \sigma_{shot}^2 + \sigma_{thermal}^2 \tag{6.11}$$

The shot noise is the resultant from the combining of electron-hole pairs. When photons strike the sensors surface, electron-hole pairs are generated. The photons can be sourced by both the Tx and the sun, whereby the latter will attribute to the background noise. For such reasons, the shot noise is a function of both types of sources, and is given as [148],

$$\sigma_{shot}^2 = 2 q B_{eq} (r P_r + F_2 I_{bg}) \tag{6.12}$$

where,

q the electron charge, B_{eq} equivalent noise BW, F_2 noise BW factor and I_{bg} background noise current.

In contrast, the thermal noise is associated with the thermal characteristics of the Rx sensor, and can be given as [148],

$$\sigma_{thermal}^2 = \frac{8 \pi k T_A C_d A F_2 B_{eq}^2}{G} + \frac{16 \pi^2 k T_A \Gamma C_d^2 A^2 F_3 B_{eq}^3}{g_m} \tag{6.13}$$

with

k Boltzmann's constant, T_A absolute ambient temperature of the operating environment, C_d photodetector per unit area fixed capacitance, F_3 noise BW for a full raised cosine (RC) pulse, Γ Rx noise factor, G open loop voltage gain and g_m is the field effect transistor (FET) transconductance.

The values of the parameters in σ_{shot}^2 and $\sigma_{thermal}^2$ are listed in tables 6.1 and 6.2 according to [159].

By substituting the noise parameters from tables 6.1 and 6.2 for N in equation (6.10), the system capacity, C, in bits/s, can be evaluated directly using [160],

$$C = B\log_2(1+SNR) \tag{6.14}$$

where,

B is the modulation BW.

According to the system description given in chapter 3, it will be considered that each luminaire transmission is unique. In such a setup, the transmission rate of each luminaire will be 5.2Mbps under the assumption that the PLC channel operates at its specified maximum transmission rate.

Table 6.1 Receiver sensor shot noise σ^2_{shot} parameters.

Parameter	Value
q	$1.60\times10^{-19}C$
B_{eq}	$50\,MHz$
F_2	0.562
I_{bg}	$5100\,\mu A$
r	$0.54\,A/W$

Table 6.2 Receiver sensor thermal noise $\sigma^2_{thermal}$ parameters.

Parameter	Value
k	$1.38\times10^{-23}(m^2kg)/(Ks^2)$
T_A	$300\,K$
C_d	$1.12\,\mu F/m^2$
F_3	0.868
Γ	1.5
G	10
g_m	$30\,mS$

The given capacity that has been provided in equation (6.14) is particular to the unperturbed channel. In the case of channel perturbations, the channel capacity must

be modified to indicated the average channel capacity, C_{Ave} . The evaluation of C_{Ave} can be performed using [160],

$$C_{Ave}=\int_{-\infty}^{\infty} B\log_2(1+\Omega)\,p_{\Omega}(\Omega)\,d\Omega \tag{6.15}$$

where

Ω is the average SNR and $p_{\Omega}(\Omega)$ is the PDF of the perturbed system.

On the other hand, using the known logarithmic relation,

$$c\log(a+b)=c\log a+c\log(b/a) \tag{6.16}$$

Then by substituting for Ω using equation (5.190), C_{Ave} can be expressed as,

$$C_{Ave}=C_0+\int_{-\infty}^{\infty} B\log_2(\Omega_1)\,p_{\Omega_1}(\Omega_1)\,d\Omega_1+\int_{-\infty}^{\infty} B\log_2(\Omega_2)\,p_{\Omega_2}(\Omega_2)\,d\Omega_2 \tag{6.17}$$

where

C_0 is the unperturbed system capacity which is given by equation (6.14), and Ω_1 and Ω_2 are RVs given by the transform,

$$\Omega_1=\frac{2r^2P_T^2(H_{s1}(0))^2(\delta H_{s1}(0))^2}{(1+\Omega)N} \tag{6.18.a}$$

$$\Omega_2=\frac{2r^2P_T^2(\delta H_{s1}(0))^4}{(1+\Omega)N} \tag{6.18.b}$$

In the event that the variance of the RV $\delta H_{s1}(0)$ in equation (5.190), is insignificant compared to $H_{s1}(0)$ then the approximation $C_{Ave}\approx C_0$ can be used. Then C_{Ave} will be explicitly given as,

$$C_{Ave}=B\log_2\left(1+\frac{(r\,P_t\,H_{s1}(0))^2}{\sigma_{shot}^2+\sigma_{thermal}^2}\right) \tag{6.19}$$

6.3 RMS Channel Delay Spread:

In a system that employs a sensor that is mounted onto a motor, it is assumed that the

motor directs the sensor to the closest luminaire. Then it can be assumed by proper light shielding from all other light sources, that the only received light at the sensor is sourced by the closest luminaire. On the other hand, a system that employs a single sensor, with a hemispherical lens pointing up at the luminaires in general, would be subjected to the transmission from a number of luminaires. In effect, the received light will be primarily a function of the closest luminaire and the two adjacent luminaires.

The time delay analysis is essential to obtain a measure on possible systems ISI free transmission capability. It is known, as a rule of thumb, for ISI free transmission, that the symbol duration must be 10 time longer than the RMS delay spread of the channel. On this basis, the analysis of the RMS delay is essential to determining the possible data rates for ISI free reception. The analysis will be performed for both identified sensors configurations. As such, the RMS channel delay spread will be demonstrated first for the motor driven sensor and later extended for the hemispherical lens sensor.

6.3.1 Single Luminaire Time Delay:

The analysis is based upon obtaining the influence on the time delay difference due to adding new LEDs to an existing LED array Tx. The LEDs form a rectangular matrix with a constant inter-LED spacing. The array can be extended in either the *x*-axis, by increasing *m*, or in the *y*-axis, by increasing *n*, as per the LED array description given in section 3.3.

Consider a four LED luminaire configuration with LEDs $L^{(0,0)}$, $L^{(1,0)}$, $L^{(0,-1)}$ and $L^{(1,-1)}$. The position of each LED with reference to the street coordinate frame can be given as,

$$L^{(m,n)}=\left(R_s+m\,dx\,\boldsymbol{i}, n\,dy\,\boldsymbol{j}, z\,\boldsymbol{k}\right) \tag{6.20a}$$

or simultaneously as,

$$L^{(m,n)}=\left(L_x^{(m,n)}, L_y^{(m,n)}, L_z^{(m,n)}\right) \tag{6.20.b}$$

If the LEDs are spaced in a uniform manner over the x and y axes on the LED

plane, then dx can be related to dy by the ratio parameter r as $dx = r\,dy$.

If $r > 1$ then the LEDs position forms a rectangle of length dx and width dy . Similarly, for $r < 1$ the LEDs position forms a rectangle of length dy and width dx . Finally, with $r = 1$, the LEDs are positioned in a square configuration.

Next consider a vehicle traveling over the road surface given in the street coordinate frame

$$s_1 = \left(s_{1,x}\boldsymbol{i} + s_{1,y}\boldsymbol{j} + s_{1,z}\boldsymbol{k}\right) \tag{6.21}$$

Knowing that the track is circular defined by equation (4.3), and that $s_{1,z} = 0$, component $s_{1,x}$ can be written in terms of $s_{1,y}$ as,

$$s_{1,x} = \left(R_s^2 + s_{1,y}^2\right)^{1/2} \tag{6.22}$$

and the position s_1 , independent of time, becomes

$$s_1 = \left(\left(R_s^2 + s_{1,y}^2\right)^{1/2}\boldsymbol{i} + s_{1,y}\boldsymbol{j} + 0\,\boldsymbol{k}\right) \tag{6.23}$$

The time delay of the direct path for LED $L^{(m,n)}$, $t_{m,n}$, can be defined as,

$$t_{m,n} = d_{s1}^{m,n}/c \tag{6.24}$$

where c is the speed of light and $d_{s1}^{m,n}$ is the separation distance between the sensor and LED.

Consider $L^{(1,-1)}$ as the reference LED. The distance $d_{s1}^{1,-1}$ can be expressed as,

$$d_{s1}^{1,-1} = \left(\left(L_x - \left(R_s^2 + s_{1,y}^2\right)^{1/2}\right)^2 + \left(L_y - s_{1,y}\right)^2 + \left(L_z\right)^2\right)^{1/2} \tag{6.25}$$

Accordingly, the separation distance to LED $L^{(0,0)}$ will become,

$$d_{s1}^{0,0} = \left(\left(L_x + dx - \left(R_s^2 + s_{1,y}^2\right)^{1/2}\right)^2 + \left(L_y + dy - s_{1,y}\right)^2 + \left(L_z\right)^2\right)^{1/2} \tag{6.26}$$

The distances can be similarly obtained for an extended LED array where the number of elements in the x and y axes is $M+1$ and $N+1$, respectively. By choosing the reference LED as the furthermost LED from the pole, with LED coordinates given as $L^{(M,N)} = \left(L_x, L_y, L_z\right)$, a general expression of the distances can

be obtained in the form,

$$d_{s1}^{p,-q}=\left(\left(L_x+(M-p)\,dx-\left(R_s^2+s_{1,y}^2\right)^{1/2}\right)^2+\left(L_y+(q-N)\,dy-s_{1,y}\right)^2+\left(L_z\right)^2\right)^{1/2} \tag{6.27}$$

The previous equation has been established for a luminaire that is parallel to the road surface. In the event of an inclination angle β , the previous equation can be modified to accommodate the inclination such that $d_{s1}^{p,-q}$ becomes,

$$d_{s1}^{p,-q}=\left(\left(L_x+(M-p)\,dx\sin(\beta)-\left(R_s^2+s_{1,y}^2\right)^{1/2}\right)^2+\left(L_y+(q-N)\,dy\cos(\beta)-s_{1,y}\right)^2+\left(L_z\right)^2\right)^{1/2} \tag{6.28}$$

By acknowledging that the closest LED to sensor s_1 is the furthermost LED from the origin in the direction pointing towards s_1 . This assumes that s_1 will travel on a track that is located beyond the furthermost LED in the x axis. Accordingly, the time delay difference, δt , of each path that can be referenced to $t_{1,-1}$, the time delay to LED $L^{(1,-1)}$. Then δt can be given as,

$$\delta t_{m,n}=t_{m,n}-t_{1,-1},\ (m,n)\neq(1,-1) \tag{6.29}$$

However, in the general case, where $d_{s1}^{p,-q}$ is the shortest path length, the time delay difference between $d_{s1}^{p,-q}$ and LED $L^{(u_1,v_1)}$ on the same LED array is evaluated as,

$$\tau_{u,v}=\frac{d_{s1}^{(u_1,v_1)}-d_{s1}^{(p,-q)}}{c} \tag{6.30}$$

with

$$u=u_1-p \quad \text{and} \quad v=v_1+q$$

Subsequently, by simultaneously using equation (6.28) with equation (6.30), the time delay for each LED on the LED array can be directly obtained. The mean time delay difference, τ_μ , can then be evaluated using,

$$\tau_\mu=\frac{\sum_{\substack{i=0\\(i\neq p)}}^{M-1}\sum_{\substack{j=1-N\\(j\neq -q)}}^{N-1}\tau_{i,j}\left(H^{m,n}(0)\right)^2}{\sum_{\substack{i=0\\(i\neq p)}}^{M-1}\sum_{\substack{j=1-N\\(j\neq -q)}}^{N-1}\left(H^{m,n}(0)\right)^2} \tag{6.31}$$

and the RMS time delay spread, τ_{rms} , obtained from the relation,

$$\tau_{rms}=\frac{\sum_{\substack{i=0\\(i\neq p)}}^{M-1}\sum_{\substack{j=1-N\\(j\neq -q)}}^{N-1}(\tau_{i,j}-\tau_{\mu})^2\left(H^{m,n}(0)\right)^2}{\sum_{\substack{i=0\\(i\neq p)}}^{M-1}\sum_{\substack{j=1-N\\(j\neq -q)}}^{N-1}\left(H^{m,n}(0)\right)^2} \tag{6.32}$$

6.3.2 RMS Time Delay Spread using a Single Reference LED:

Given that the variability of the DC channel response for each LED is small, an approximation for both τ_{μ} and τ_{rms} can be obtained using the single reference LED response $H^{(p,-q)}(0)$ instead of the complete DC channel response $H^{(m,n)}(0)$. Correspondingly, the approximate mean time delay difference, $\tau_{\mu}^{'}$, and approximate RMS delay spread, $\tau_{rms}^{'}$, can be respectively obtained from the on luminaire LED geometry using,

$$\tau_{\mu}=\frac{\sum_{\substack{i=0\\(i\neq p)}}^{M-1}\sum_{\substack{j=1-N\\(j\neq -q)}}^{N-1}\tau_{i,j}\left(H^{(p,-q)}(0)d_{s1}^{(i,j)}/d_{s1}^{(p,-q)}\right)^2}{\sum_{\substack{i=0\\(i\neq p)}}^{M-1}\sum_{\substack{j=1-N\\(j\neq -q)}}^{N-1}\left(H^{(p,-q)}(0)d_{s1}^{(i,j)}/d_{s1}^{(p,-q)}\right)^2} \tag{6.33}$$

$$\tau_{rms}=\frac{\sum_{\substack{i=0\\(i\neq p)}}^{M-1}\sum_{\substack{j=1-N\\(j\neq -q)}}^{N-1}(\tau_{i,j}-\tau_{\mu})^2\left(H^{(p,-q)}(0)d_{s1}^{(i,j)}/d_{s1}^{(p,-q)}\right)^2}{\sum_{\substack{i=0\\(i\neq p)}}^{M-1}\sum_{\substack{j=1-N\\(j\neq -q)}}^{N-1}\left(H^{(p,-q)}(0)d_{s1}^{(i,j)}/d_{s1}^{(p,-q)}\right)^2} \tag{6.34}$$

6.3.3 RMS Time Delay Spread of an Adjacent Luminaire:

It can be hypothesized that luminaires along the same side of the Rx will have a significant impact on the outcome of the DC channel response. It is therefore, important to observe the contribution of each of the two adjacent luminaires on τ_{μ} and τ_{rms} . Similarly, the effect on the approximation $\tau_{\mu}^{'}$ and $\tau_{rms}^{'}$ can also be determined.

The adjacent luminaires can be designated by superscripts -1 and 1 for the previous

and the subsequent luminaires on the Rx side of the road. Then to include the effect of each, the distances to the vehicle sensor must first be computed. Knowing that each streetlight pole, and subsequently, luminaire, is rotated about the *z*-axis by angle ν_z with the respect to the roads curvature, the separation distance from luminaires -1, $d_{s1}^{-1,(p,-q)}$, and 1, $d_{s1}^{1,(p,-q)}$, can be respectively determined through,

$$d_{s1}^{1,(p,-q)}=\left(\left(d_{s1,x}^{(p,-q)}\cos(\nu_z)+d_{s1,y}^{(p,-q)}\sin(\nu_z)\right)^2+\left(d_{s1,y}^{(p,-q)}\cos(\nu_z)-d_{s1,x}^{(p,-q)}\sin(\nu_z)\right)^2+\left(d_{s1,z}^{(p,-q)}\right)^2\right)^{(1/2)} \tag{6.35}$$

and

$$d_{s1}^{-1,(p,-q)}=\left(\left(d_{s1,x}^{(p,-q)}\cos(\nu_z)-d_{s1,y}^{(p,-q)}\sin(\nu_z)\right)^2+\left(d_{s1,y}^{(p,-q)}\cos(\nu_z)+d_{s1,x}^{(p,-q)}\sin(\nu_z)\right)^2+\left(d_{s1,z}^{(p,-q)}\right)^2\right)^{(1/2)} \tag{6.36}$$

With components $d_{s1,x}^{(p,-q)}$, $d_{s1,y}^{(p,-q)}$ and $d_{s1,z}^{(p,-q)}$ given by,

$$d_{s1,x}^{(p,-q)}=L_x+(M-p)\,dx\sin(\beta)-\left(R_s^2+s_{1,y}^2\right)^{1/2} \tag{6.37}$$

$$d_{s1,y}^{(p,-q)}=L_y+(q-N)\,dy\cos(\beta)-s_{1,y} \tag{6.38}$$

$$d_{s1,z}^{(p,-q)}=L_z \tag{6.39}$$

The time delays associated with luminaires -1, $\tau_{(u,v),-1}$, and 1,, $\tau_{(u,v),1}$ can now be respectively evaluated through,

$$\tau_{(u,v),-1}=\frac{d_{s1}^{-1,(u_1,v_1)}-d_{s1}^{(p,-q)}}{c} \tag{6.40}$$

and

$$\tau_{(u,v),1}=\frac{d_{s1}^{1,(u_1,v_1)}-d_{s1}^{(p,-q)}}{c} \tag{6.41}$$

Subsequently, the RMS delays with respect to luminaires -1, $\tau_{rms,-1}$, and 1, $\tau_{rms,1}$, will be determined by applying,

$$\tau_{rms,p}=\frac{\sum_{i=0}^{M-1}\sum_{j=1-N}^{N-1}\left(\tau_{(i,j),p}-\tau_\mu\right)^2\left(H_p^{(m,n)}(0)\right)^2}{\sum_{i=0}^{M-1}\sum_{j=1-N}^{N-1}\left(H_p^{(m,n)}(0)\right)^2},\qquad p=-1,1 \tag{6.42}$$

with parameters τ_μ representing the mean delay of all luminaires

and $H_p^{(m,n)}(0)$ for $p=-1,1$ representing the DC channel responses for luminaires -1 and 1 respectively.

The mean delays accounting for all luminaires, τ_μ , is evaluated according to,

$$\tau_\mu = \frac{\sum_{k=-1}^{1} \sum_{i=0}^{M-1} \sum_{j=1-N}^{N-1} \tau_{(i,j),k} \left(H_k^{(m,n)}(0)\right)^2}{\sum_{k=-1}^{1} \sum_{i=0}^{M-1} \sum_{j=1-N}^{N-1} \left(H_k^{(m,n)}(0)\right)^2} \quad \begin{matrix} (if\ k=0\ i\neq p)\ (if\ k=0\ j\neq -q) \\ (if\ k=0\ i\neq p)\ (if\ k=0\ j\neq -q) \end{matrix} \tag{6.43}$$

where

$$k = \begin{cases} -1, & \textit{Past Luminaire} \\ 0, & \textit{Current Luminaire} \\ 1, & \textit{Next Luminaire} \end{cases}$$

and

$\tau_{rms,0}$ given by equation (6.32).

Finally, the total RMS delay while taking into account the adjacent luminaires becomes,

$$\tau_{rms,T} = \tau_{rms,0} + \tau_{rms,-1} + \tau_{rms,1} \tag{6.44}$$

Chapter 7

Results

7.1 Introduction:

The results shown herein correspond to the roadway configuration of a bi-directional 3-lane highway. Each lane, with a width of 3.5m, is subdivided further into 4 tracks, with offsets from the inner lane of 25% , 50% , 75% and 100% . Streetlight poles are spaced from each other at intervals of 40m along the highway. Three road configurations are tested, a straight road, an IRC and ORC. With the curved roads, a cross road angle, also known as a super-elevation, is included within the design considerations.

A few preliminary assumptions on the system setup are made for the simulations. Primarily, it is assumed that all poles and luminaires are equal in dimension and perfectly positioned. The impact of this assumption assures that the illumination of the road surface is equal under all poles and luminaires. Added to this assumption, it will be assumed that it is sufficient to simulate a single pole and infer that the results will be equal for all other poles. At the Rx side, it will be assumed that the Rx perfectly tracks the unperturbed luminaires center along any point on the road surface. This assumption is based upon a motorized sensor setup. Accordingly, it will be assumed that the Rx initial point of travel is 40m away from the pole. The Rx can only travel on a prescribed track and is not allowed to switch between tracks. A Rx will cover a total distance of 80m traveling initially in the direction towards the pole.
For this type of setup, the results are subdivided into three parts. In the first part, the simulations are related to the DC channel response. Firstly, the DC channel response to the different highway configurations is going to be demonstrated. Subsequently,

the channel response is simulated for an LED array approximated by the proposed single LED method applied to the three road configurations. The second part of the simulations are linked to the rotational and translational luminaire perturbations. Using the analysis shown in chapter 5 on perturbations, it will first be demonstrated the PDF of the variables that affect the DC channel response. For this part, the simulation will be undertaken for a sensor placed on the third lane 20m away from the pole. The choice of the point can be justified as belonging to the edge of luminaires coverage zone, that will give results of a worst case scenario on the road. In the final part, two important channel parameters are going to be shown, the RMS channel delay and the channel capacity. Both parameter are usually related to all conducted channel investigations, and are thus investigated herein. Both parameters will be obtained over the complete analyzed stretch of road, for the three road configurations.

7.2 DC Channel Response:

Figures 7.1 to 7.3 shows the response $H_{s1}(0)$ for a single LED at the center of the luminaire. The road configurations, in sequence from figures 7.1 to 7.3 are, straight, IRC and ORC. In all three figures, the sensor and the transmitting LED are on the same side of the road. In contrast, figure 7.4 shows the response $H_{s1}(0)$ of a single LED Tx on the straight whereby the Tx and Rx are on opposite sides of the road.

For a Rx that is placed on the same side of the road, it is clear that the Rx location and road configuration will effect $H_{s1}(0)$. From figures 7.1 to 7.3 it is quite clear that a Rx placed towards the highway center, will clearly have greater $H_{s1}(0)$ compared to a Rx placed on the outer lanes. This particular effect can be directly attributed to the smaller Tx/Rx separation distance observed by a Rx placed on the inner lanes as compared to the separation distance observed by a Rx on the outer. The particular shape of $H_{s1}(0)$ related to each track is observed to increase in an exponential manner, until a particular threshold distance away from the luminaire center. Beyond the threshold distance, however, the general observation which is

valid for all conditions, is that the curve of $H_{s1}(0)$ peaks approximately directly below the luminaire. For the cases of the straight and IRC curves, the threshold distance is approximately 10m away from the luminaire center, while for the ORC case it is 7.5m. This observation gives clearly gives the ORC curve a sharper response compared to the straight and IRC.

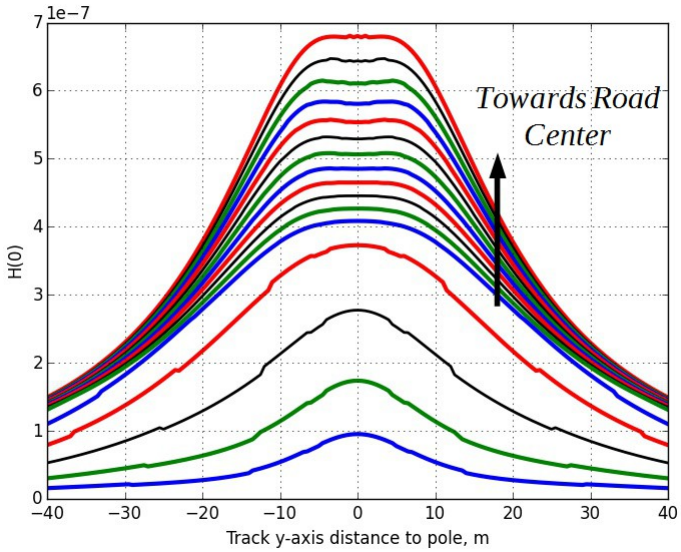

Figure 7.1 Channel response to single LED in straight road, sensor side.

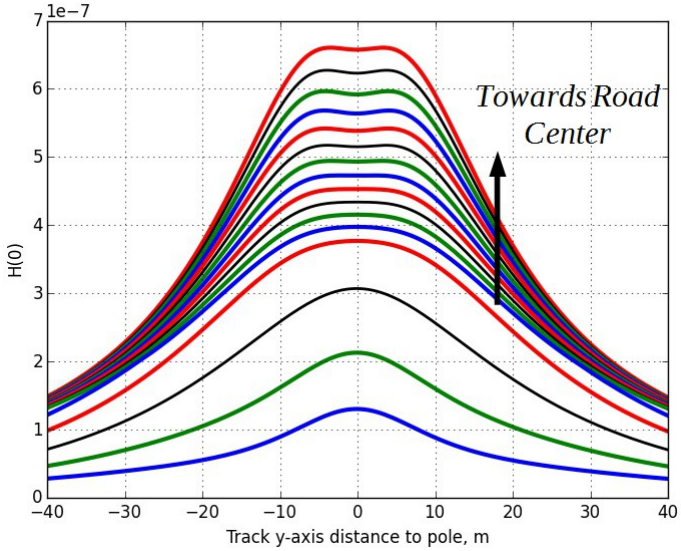

Figure 7.2 Channel response to single LED in curved road IRC.

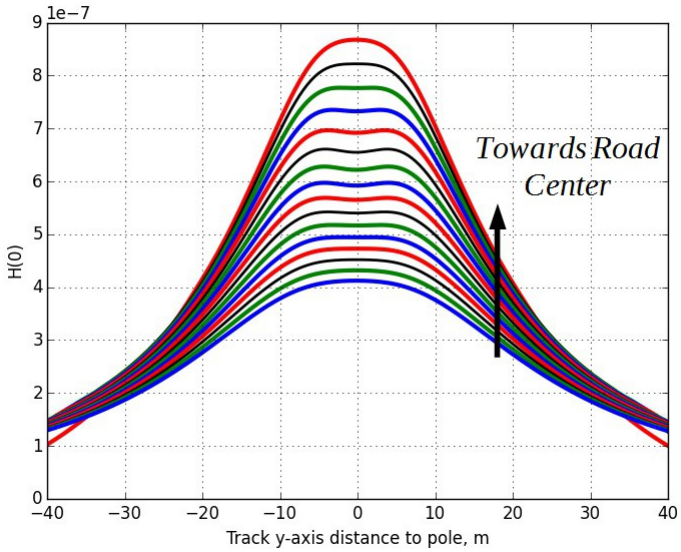

Figure 7.3 Channel response to single LED in curved road ORC.

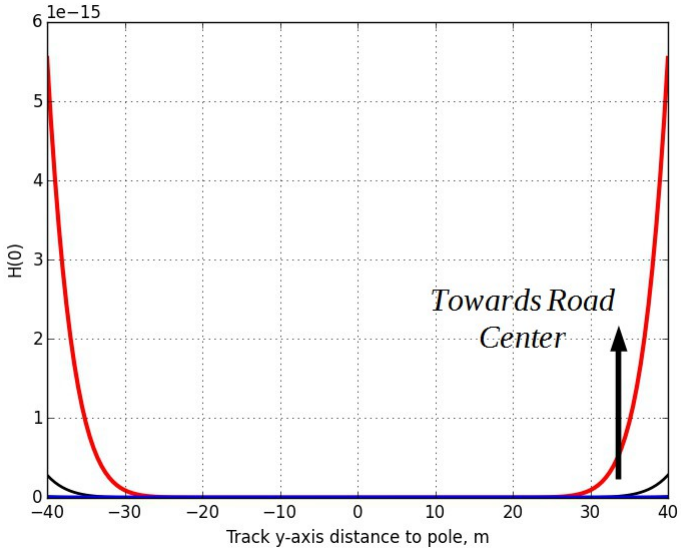

Figure 7.4 Channel response of single LED in straight road, opposite side.

Such observation is attributed to the relative inclination of the luminaire with respect to the road surface and OC, culminating in angle parameter ζ (equations (4.11) and (4.12)). Furthermore, the effect the Gaussian like visible feature in $H_{s1}(0)$ can be returned to the intensity distribution $I(\theta,\varphi)$ given by equation (4.74). Another feature in $H_{s1}(0)$ observed only for the straight is the discontinuity in the curves. This observation is limited to the tracks that are towards the road edges, and can be returned to parameter U which switches the state of $I(\theta,\varphi)$ according to

equation (4.75). Finally, comparing all three curves, it is clear that $H_{s1}(0)$ is narrower and exhibits a higher peak in the ORC case compared to the other two cases. Comparing the straight and IRC cases, only a marginal increase in $H_{s1}(0)$ is observed for the former over the latter. Again, this is attributed to the position of the sensor with respect to angle ζ . Given that $H_{s1}(0)$ is a function of $I(\theta,\varphi)$, then for a sensor elevated towards the luminaire in the ORC case, it is clear that the compound effect of shorter separation distance and higher illumination level, will make $H_{s1}(0)$ greater relative to the other two cases.

On the other hand, the effect of a single pole two luminaires output on the amount of light a sensor receives, can be directly observed through comparing figures 7.1 and 7.4. In the case of the luminaire and sensor are on the same side of the road, $H_{s1}(0)$ from the luminaire is an increasing function as the distance to pole decreases, figure 7.1. In contrast, for the luminaire directed to the other side of the road, it is clear from figure 7.4 that $H_{s1}(0)$ diminishes as the sensor moves towards the pole. This is due to the fact that $I(\theta,\varphi)$ from each luminaire is intentionally directed towards the side of road that includes the luminaire. Furthermore, the inclination of OC confines the light to diminutive amounts when observed around the other side of the pole. For all practical assumptions it can be observed that the backwash light from the opposite side luminaire is negligible. Henceforth, with respect to the visible light transmission side of the proposed system, it is clear for a streetlight pole with two luminaires on opposite ends, that the visible light radiated from one luminaire will not interfere with the light from the other luminaire. This makes the transmission from either luminaire interference free from the tranmission from the other luminaire.

7.3 LED Array DC Channel Response Simplification using a Single LED:

The results reflect upon the possibility of approximating the DC channel response of an LED array by a single LED. The results shown in this section are for the ratio test

of $r^{(0,0)}$, $r^{(M/2-1,0)}$ and $r^{(M/2+1,0)}$ and highway configurations $e=0$, $e=0.12$ IRC and $e=0.12$ ORC. Furthermore, it also demonstrates the choice of reference LED that should be taken in order to obtain the correct ratio. Ratio $r^{(0,0)}$ is particular to $L^{(0,0)}$, that has been considered primarily as the reference LED on the LED array in all the analysis. As the LED array assessed in this study contains 18×7 LEDs, it is clear that there is no center LED on the array. For such reasons, the choice of $r^{(M/2-1,0)}$ and $r^{(M/2+1,0)}$ is LED pair $L^{(0,0)}$ and $L^{(9,0)}$, which both reside on the *x*-axis. In this LED configuration the LED array center is located in between both LEDs.

In figures 7.5 to 7.7, highway configuration $e=0$ is shown for $r^{(0,0)}$, $r^{(M/2-1,0)}$ and $r^{(M/2+1,0)}$.

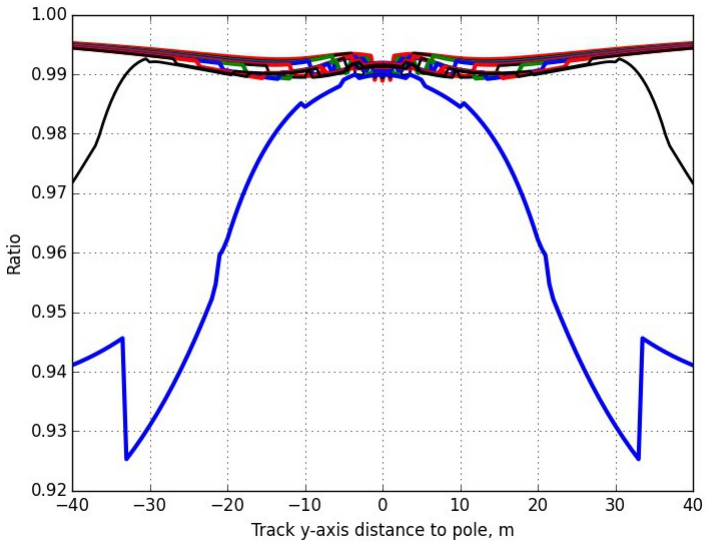

Figure 7.5 Ratio $r^{(0,0)}$ for highway configuration $e=0$.

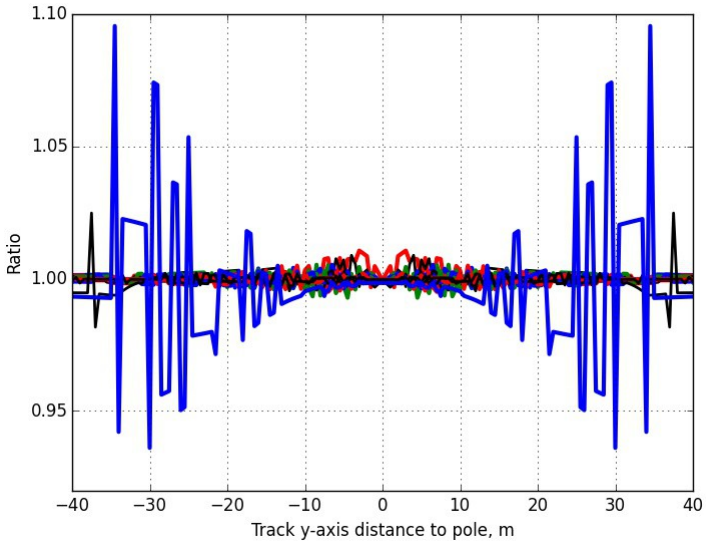

Figure 7.6 Ratio $r^{(M/2-1,0)}$ for highway configuration $e=0$.

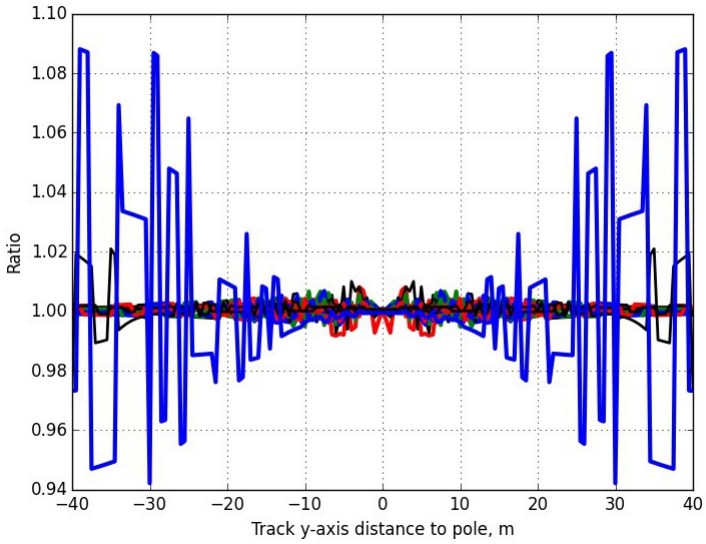

Figure 7.7 Ratio $r^{(M/2+1,0)}$ for highway configuration $e=0$.

In all figures, it is clear that the ratio test indicates that the ratios are overwhelmingly within 1% for all lanes and lane offsets, within the range of $-30m \leq y \leq 30m$. The exception to this is observed for the edge of lane 3, i.e. lane 3 with 100% offset, whereby the ratio is relatively larger. In particular, in the case of $r^{(0,0)}$, figure 7.5, the deviation increase relatively smoothly to approximately 7% at $y=30m$. In contrast, for the other two ratios, fluctuations about $r=1.0$ is observed, with a peak of approximately 8.75% in the case of $r^{(M/2+1,0)}$ at $y=30m$

.When comparing the ratios, it is clear that there is an advantage of selecting either $L^{(8,0)}$ or $L^{(9,0)}$ instead of $L^{(0,0)}$, for $e=0$. Therefore, it can be observed from this result, that selection of a representative LED to approximate the LED array is critical. Furthermore, the selection should be made closer to the LED array center.

In the following four figures, the ratios of $r^{(M/2-1,0)}$ and $r^{(M/2+1,0)}$ for highway configuration $e=0.12$ and the Tx located within the IRC and ORC. Specifically, figures 7.8 and 7.9 demonstrate the ratios for the IRC while figures 7.10 and 7.11 shows the ratios for the ORC.

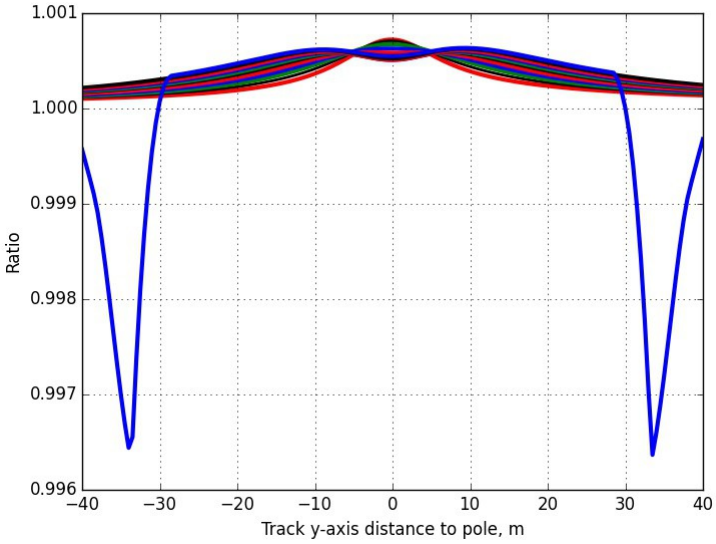

Figure 7.8 Ratio $r^{(M/2-1,0)}$ for IRC highway configuration with $e=0.12$.

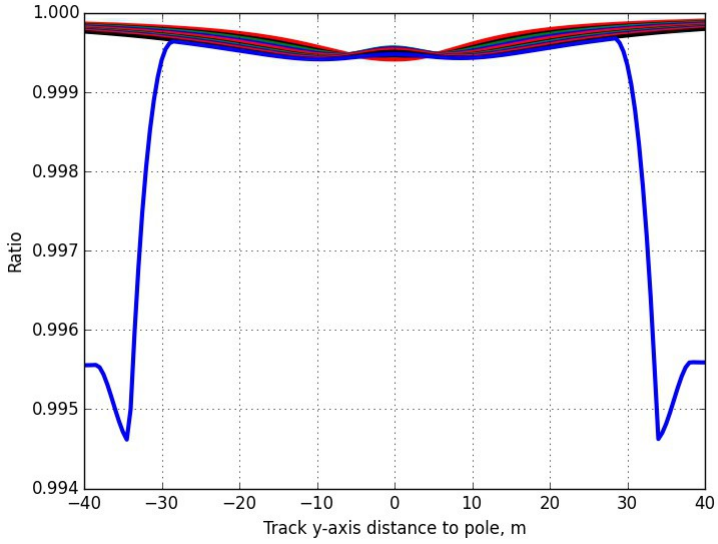

Figure 7.9 Ratio $r^{(M/2+1,0)}$ for IRC highway configuration with $e=0.12$.

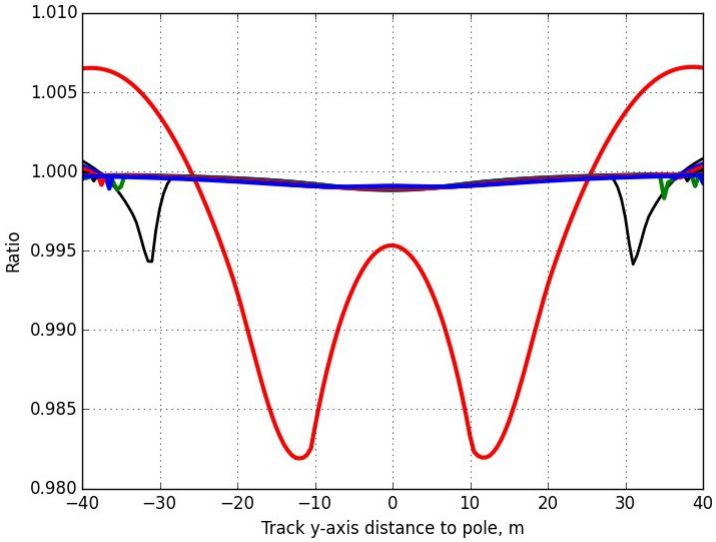

Figure 7.10 Ratio $r^{(M/2-1,0)}$ for ORC highway configuration with $e=0.12$.

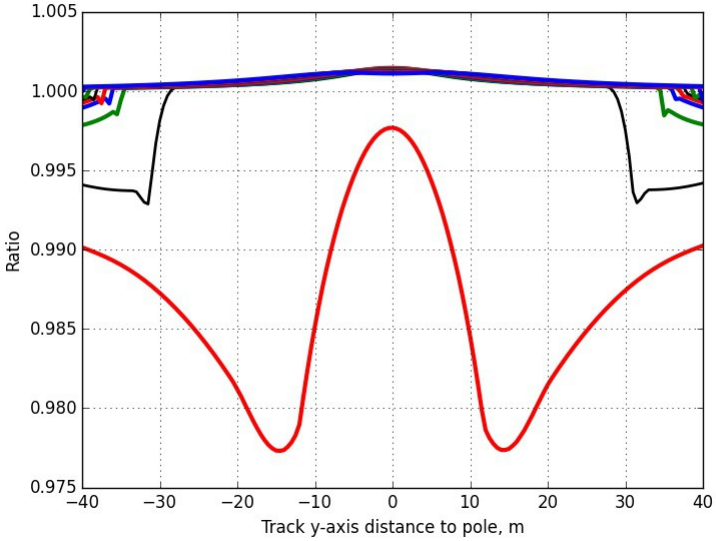

Figure 7.11 Ratio $r^{(M/2+1,0)}$ for ORC highway configuration with $e=0.12$.

From figure 7.8 and 7.9, it is clear again that the ratios $r^{(M/2-1,0)}$ and $r^{(M/2+1,0)}$ for LEDs $L^{(8,0)}$ and $L^{(9,0)}$ show good approximations, with the exception to this observation limited to lane 3 with a 100% lane offset, in the IRC case. However, unlike in case with $e=0$, all ratio curves are smooth. Furthermore, within the range of $-30m \leq y \leq 30m$ it is observed that the ratios are extremely close to 1.0. Upon closer inspection, it can further be observed that the ratios associated with LED $L^{(8,0)}$ are slightly over 1.0 within the range. In contrast, the ratio associated

with LED $L^{(8,0)}$ within the same range of distances, are slightly below 1.0.

In contrast to the IRC setup, in the ORC cases, figures 7.10 and 7.11, it is observed that the ratios offset from 1.0 is much larger. Specifically, in the case of lane 1 and a lane offset of 25% the maximum deviation from 1.0 is approximately 1.75% and 2.125% associated with LEDs $L^{(8,0)}$ and $L^{(9,0)}$ respectively. However, for the remaining lanes and offsets, in general the ratio deviates a maximum of 0.0025%. Furthermore, it can be observed that unlike in the IRC case, there is a relatively slight decrease in the ratio for LEDs $L^{(8,0)}$ and an increase in the ratio for LED $L^{(9,0)}$. Such an observation is clearly expected as the LED *OC* plane is rotated by angle α away from the IRC.

To verify if an improvement on the result can be obtained, rather than considering the individual responses, the ratio of the pair of LEDs DC channel response, r^c, is simulated for the configuration $e=0$ and both IRC and ORC cases with configuration $e=0.12$. These are respectively given in figures 7.12 through 7.14.

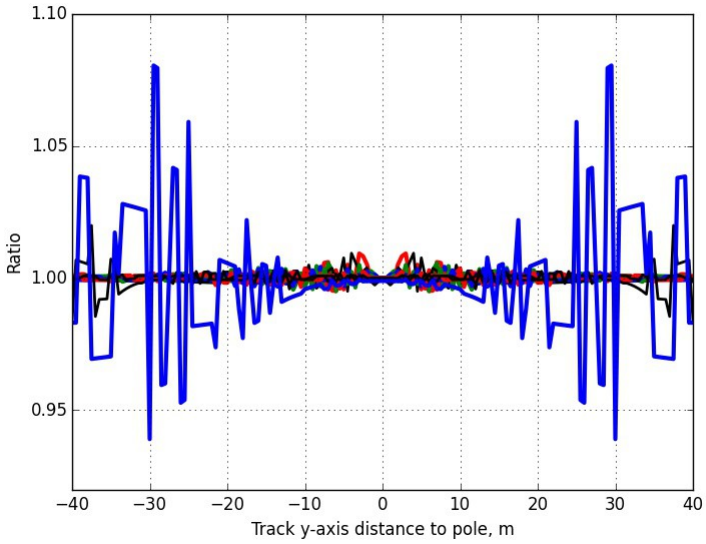

Figure 7.12 Ratio r^c of LED pair and highway configuration $e=0$.

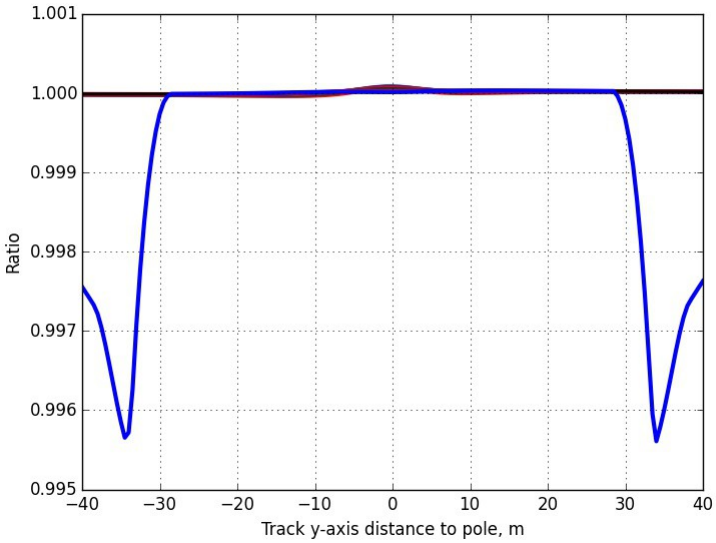

Figure 7.13 Ratio r^c of LED pair and IRC highway configuration $e=0.12$.

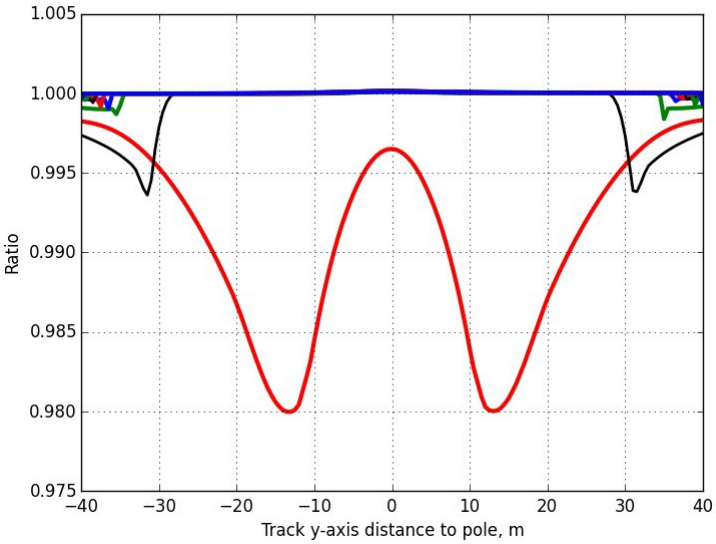

Figure 7.14 Ratio r^c of LED pair and IRC highway configuration $e=0.12$.

From figure 7.12, it is clear that no significant improvement is attained through considering the pair rather than the individual LEDs. In contrast, figures 7.13 and 7.14 both show marked improvement when comparing both to figure pairs (7.8, 7.9) and (7.10, 7.11). Within the *y* range, it has been observed that the variation due to either LEDs position away from the center, has been practically eliminated for almost all the curves. The exception to this is the remaining variation of the ratios over lanes 3 and 1 for offsets 100% and 25% away from the lane center, in the IRC and

ORC configurations, respectively. However, the level of both variations has slightly diminished, which for the IRC case, within the *y*-range, is negligible. For the ORC case, the variation has been diminished by approximately 0.025%.

Henceforth, from the results, it can be concluded that the DC channel response from an LED array can be obtained directly by replacing the LED array by a single LED at the array center, and solving for $H(0)$. Specifically, for the proposed system with an LED type luminaire as shown in figure 3.4 it suffices to account only the DC channel response of the center most LED in the array. The obtained single LED DC channel response is subsequently multiplied to account for all remaining LEDs on the array for $H(0)$. The results have shown in case of the proposed system, and under the streetlight illumination coverage area, that the proposed DC channel response approximation is accurate compared to the exact DC channel response.

7.4 Perturbation Effects:

In this section the effect of the rotation and translation perturbations will be demonstrated on the DC channel response. To obtain the resultant perturbed DC response, first the effect of the perturbations on polar angle θ and sensor to LED angle ψ will be shown. The azimuthal angle, φ , also is included in the DC response through the intensity density $I(\theta,\varphi)$. To demonstrate the perturbations, a representative point on the road surface is chosen at location 7.5m and 20m away from the luminaire center along the x and y axes respectively. At the chosen location on the road, it has been argued that $I(\theta,\varphi)$ is only a function θ . This fact stems from the established analysis that the predominant condition sets $U=1$ over the entire road surface. Accordingly, angle φ contributes insignificantly to the overall DC channel response and can therefore be totally discarded.

Figures 7.15 and 7.16 demonstrate the rotation and translation perturbations on θ .

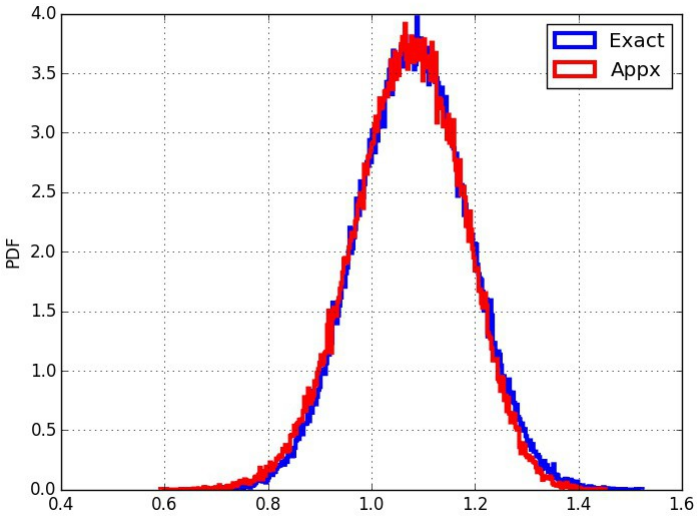

Figure 7.15 Effect of rotation perturbation on θ

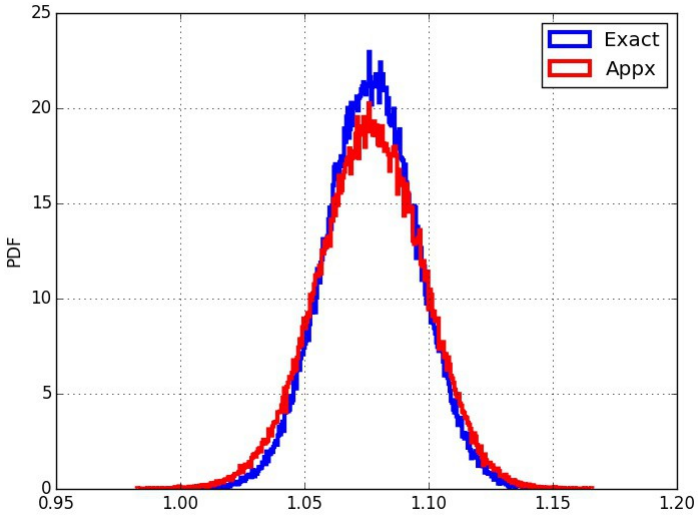

Figure 7.16 Effect of translation perturbation on θ

In both perturbations, the exact curve represents the exact simulation, while the approximate curve is evaluated using equations (5.30) and (5.131) for both cases of rotation and translation perturbations respectively.

From the rotation perturbation, it is clear that both curves show good agreement,

which indicates that the Gaussian approximation of θ is adequate. For the translation perturbation, however, a difference between both exact and approximate curves can be observed. However, such an outcome can be expected due to the approximations performed in obtaining a suitable approximate to the exact curve. On the other hand, the deviations from the exact curve can be considered acceptable over the range of values. Subsequently, θ , to a high degree of confidence, be approximated as a Gaussian RV whose parameters are defined by equations (5.30) and (5.131).

Figures 7.17 and 7.18 both demonstrate $\cos(\psi)$, rather than ψ , for the rotation and translation perturbation. Demonstrating the values of $\cos(\psi)$ is convenient as it appears in the DC response equation.

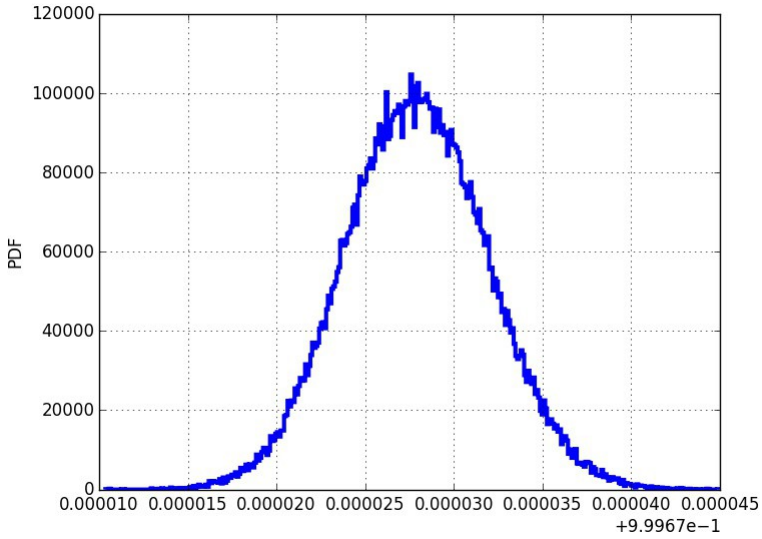

Figure 7.17 Effect of rotation perturbation on $\cos(\psi)$

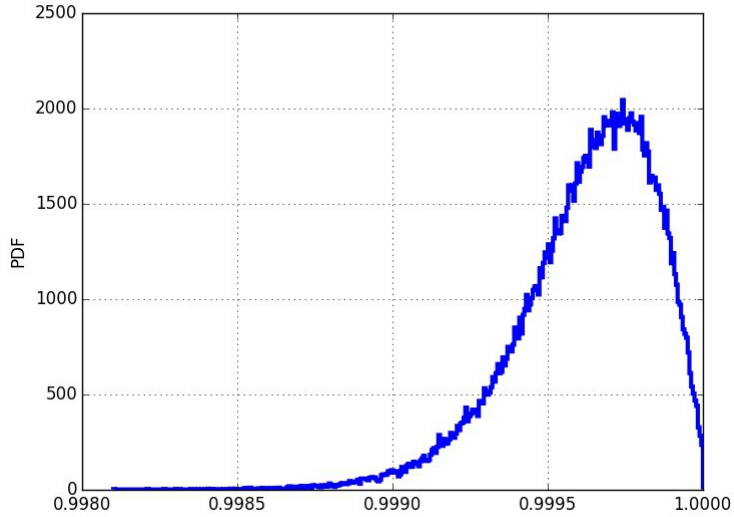

Figure 7.18 Effect of translation perturbation on $\cos(\psi)$

Evaluation of the exact PDF of the perturbed $\cos(\psi)$ indicates it follows a Beta distribution. For the case of the rotation perturbation, it can suffice to approximate the exact distribution by a truncated Gaussian RV. On the other hand, the translation perturbation, there is an apparent skew to the distribution, which indicates that a Gaussian approximation might not be adequate. However, it is interesting to observe the means and variances of both PDFs. For the rotation perturbation the mean and variance are respectively 0.99970 and 1.6187×10^{-11} . While for the translation perturbation, the mean and variance are respectively 0.99962 and 4.892×10^{-8} . It can therefore be confidently acknowledged that equations (5.84), (5.155) and (5.156) are good approximates. Then using the insight from the aforementioned equations, it can be stated with confidence, that for extremely small variance values, the relation $\cos(\psi)=1$ holds true. According to this statement, ψ becomes redundant in the DC channel response equation and can be adequately removed.

7.5 DC Channel Response Perturbations:

In this section the effect of rotation and translation perturbations on the DC channel response, $H_{s1}^{(P)}(0)$, in relation to equations (5.182) and (5.190), will be

demonstrated. The demonstration will be shown for all three road configurations, straight, IRC and ORC. Namely, figure set 7.19 and 7.20 show the results for a sensor on the straight path, while figure set 7.21 and 7.22 show the results for the IRC configuration. Finally, figure set 7.23 and 7.24 show the results for the ORC configuration. The purpose of demonstrating the three road configurations is to observe whether the super-elevation and OC axis tilts are pivotal to $H_{s1}^{(P)}(0)$.

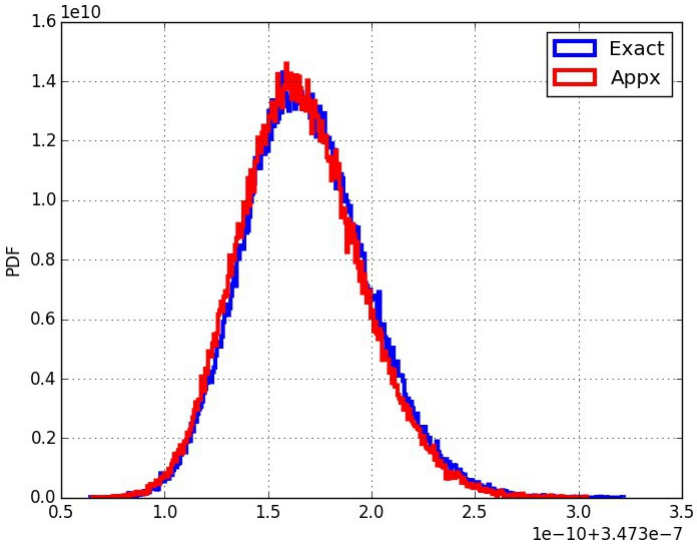

Figure 7.19 Rotation perturbed DC channel response $H_{s1}^{(P)}(0)$ in straight configuration.

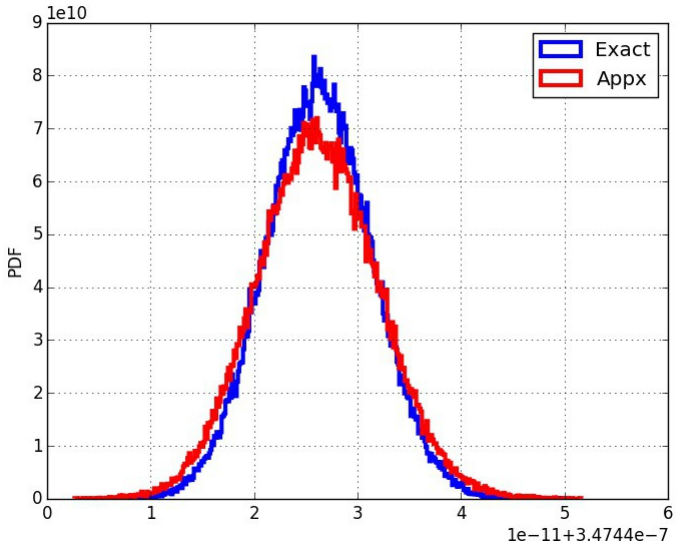

Figure 7.20 Translation perturbed DC channel response $H_{s1}^{(P)}(0)$ in straight configuration.

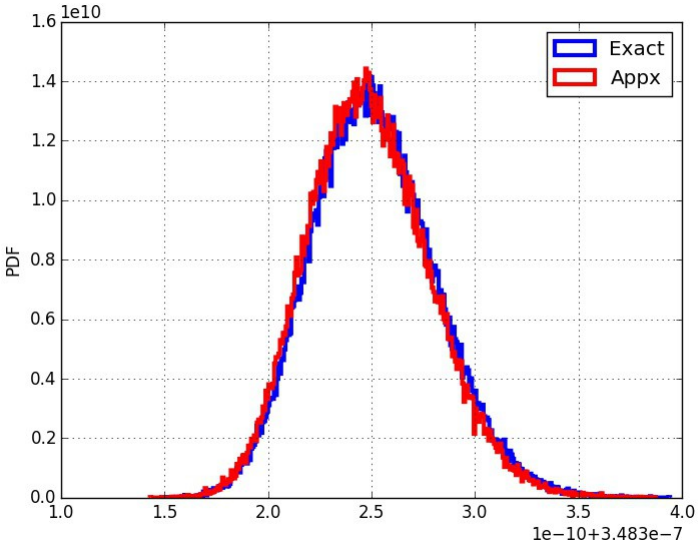

Figure 7.21 Rotation perturbed DC channel response $H_{s1}^{(P)}(0)$ in IRC configuration.

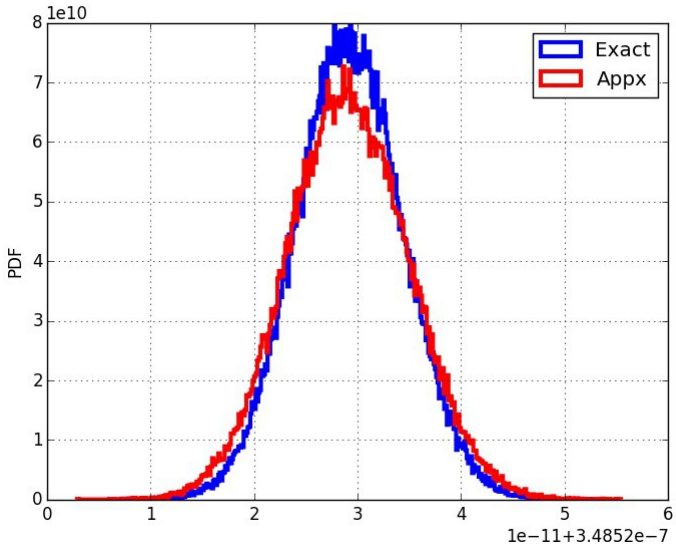

Figure 7.22 Translation perturbed DC channel response $H_{s1}^{(P)}(0)$ in IRC configuration.

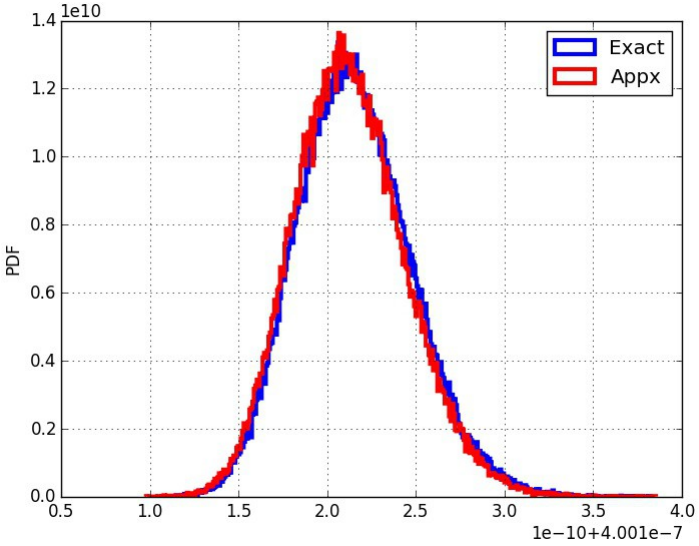

Figure 7.23 Rotation perturbed DC channel response $H_{s1}^{(P)}(0)$ in ORC configuration.

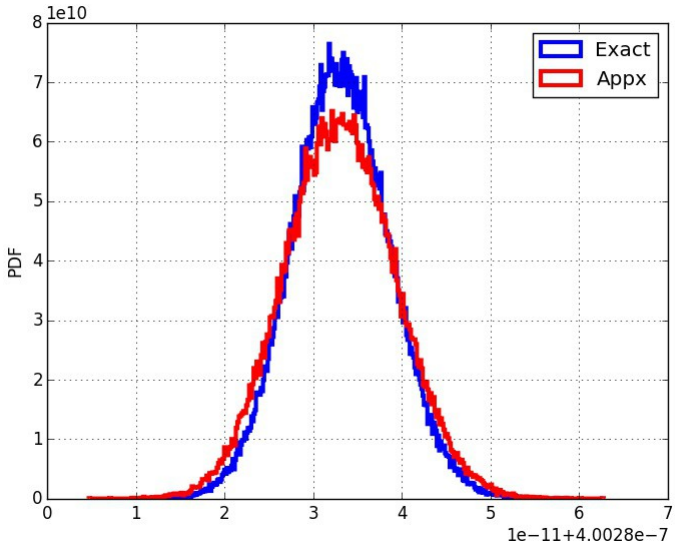

Figure 7.24 Translation perturbed DC channel response $H_{s1}^{(P)}(0)$ in ORC configuration.

From each figure set, it can be observed that the rotation perturbed exact and approximate curves show a high degree of similarity. It can therefore be implicitly assumed that the approximation of $H_{s1}^{(P)}(0)$ by equation (5.190) can confidently produce reliable results. In comparison, the results shown for the translation perturbation indicate that there is some difference between both results. However, the difference is not excessive and could be used to obtain an approximate on $H_{s1}^{(P)}(0)$ using equation (5.190). Comparing both perturbation cases, shows that the difference between the exact and approximate curves is a direct function of θ since $H_{s1}^{(P)}(0)$ is directly proportional to $I(\theta)$. This is clearly evident when comparing the rotation perturbations figures with figure 7.15, and the translation perturbation figures with figure 7.16.

Comparing the rotation perturbation of all cases, it can be observed that no clear difference between the curves can be observed. The similar observation can be found for the translation perturbed cases. Accordingly, although the relative sensor and LED positioning changes for each case, the following can be deduced. If it is required to obtain a measure of $H_{s1}^{(P)}(0)$ then it suffices to obtain a measure for any of the three road configurations, or equivalently any configuration with smaller

super-elevation angle.

The values $H_{s1}^{(P)}(0)$ shows that the mean of $H_{s1}^{(P)}(0)$ is extremely close to $H_{s1}(0)$ while the variance too, is extremely small. More precisely, in the case of the straight path, the effect of rotation perturbation on the exact $H_{s1}^{(P)}(0)$ mean and variance are respectively given as 3.47469×10^{-7} and 8.78344×10^{-22} . In comparison, the unperturbed component yields $H_{s1}(0)=3.47317\times10^{-7}$. Similarly, the translation perturbation exact mean and variance are respectively given as 3.47466×10^{-7} and 2.60870×10^{-23} . It can, therefore, be deduced that the effect of both rotation and translation perturbation on the DC channel response is extremely small, and can effectively be ignored. This statement holds true for a sensor that remains within the illumination zone in a perturbed situation. Hence, for all remaining results on the DC channel response, only $H_{s1}(0)$ will be used.

The results can now be interpreted in relation to the proposed system. Under clear night sky conditions, it can be argued that the main source of channel perturbation is induced by wind and gust. Accordingly, the influence of wind and gust is such that the transmitting luminaire will be perturbed through the luminaires translation and rotation. However, the extent of the influence of both translation and rotation perturbations will be insignificantly small on the DC channel response, to the point that such perturbations can be altogether ignored.

7.6 Channel Parameters:

In this section the two channel parameters, namely the RMS delay spread and channel capacity, are demonstrated. Specific values are going to be given in consideration to the maximum attainable bit rate applicable to the phosphor coated HB-LED.

7.6.1 RMS Channel Delay Spread:

This section will demonstrate the RMS channel delay spread for all three highway

configurations. The RMS channel delay will be obtained for the exact and approximate RMS delay implementations given respectively by equations (6.32) and (6.34). Figures 7.25, 7.26 and 7.27 are the RMS channel delays for the straight, IRC and ORC highway configurations respectively. In each figure, the RMS channel delay is obtained for each track.

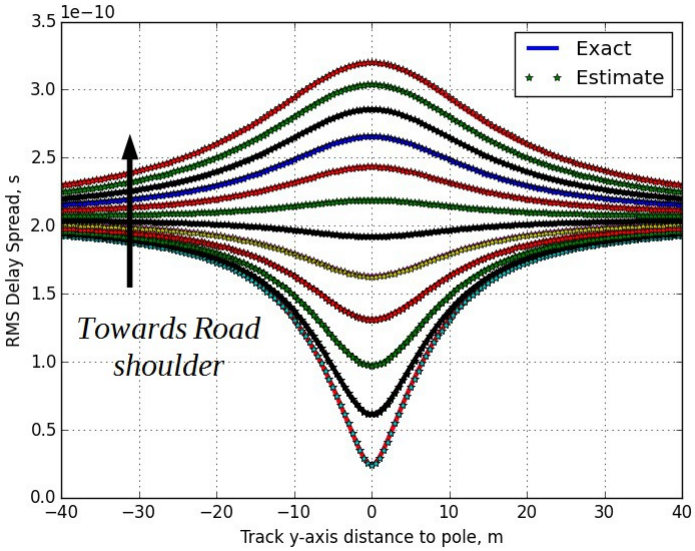

Figure 7.25 RMS channel delay for straight configuration.

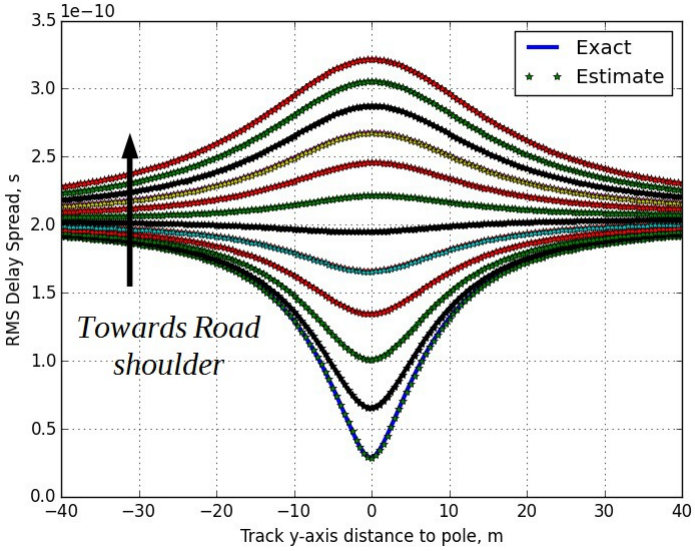

Figure 7.26 RMS channel delay for IRC configuration.

From all three figures, the first observation that can be made is the accuracy of

obtaining the RMS channel delay through equation (6.34). The implication to this result, is that the geometrical placement of LEDs within a luminaire is sufficient to obtain accurate estimates of the RMS channel delay while relying on a single center of luminaire LED $H_{s1}^{(p,-q)}(0)$

Focusing on any one of the three figures, it is clear that a sensor placed towards the inner lanes, experiences a smaller RMS channel delay compared to a sensor placed on the outer lanes. For the inner lanes, the delay decreases sharply to a minimum value as the sensor passes directly below the luminaire. The reverse then occurs as the sensor departs from beneath the luminaire. This feature can be attributed to the effect the separation distance imposes on the RMS channel delay as given in equation (6.32). On the other hand, a vehicle in the outer lanes experiences the inverse effect while traveling towards the luminaire. A maximum RMS delay spread is obtained when the sensor is aligned with the luminaire. In this condition, the effect of the DC channel response is more dominant compared to the separation distance causing the RMS delay to increase. The average RMS channel delay can therefore be obtained around the center of illuminated area over the road surface. From the three figures, this occurs at 62.5% away from the edge closer to the road center of lane 2.

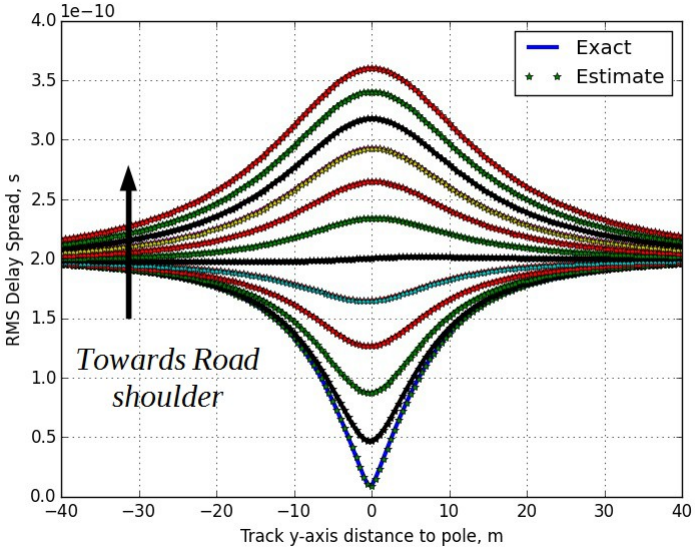

Figure 7.27 RMS channel delay for ORC configuration.

Next, the effect of the different highway configurations on the RMS channel delays

will be compared. It can be observed in the cases of the straight and IRC, that no notable difference of the RMS channel delays can be found, for all tracks. On the other hand, in the ORC configuration, it can be observed that the RMS channel delay shows greater variation for both inner and outer tracks compared to both other configurations. From this it can be observed that the track placement of a sensor traveling over an ORC highway configuration, is more sensitive to RMS channel delay compared to the other two configurations. Furthermore, in general, sensors that are placed towards the inner lane will be subjected to the greatest RMS channel variation. However, for such sensor placement, the RMS channel delay is always less than all other tracks, which if harnessed is advantageous for high speed VLC.

A measure on ISI free transmission can be obtained using the rule of $10\tau_{rms}$. By applying this rule, the average ISI transmission rates for each of the straight, IRC and ORC configurations is given as 436.7Mbps, 438.6Mbps and 432.9Mbps respectively. The results reflect upon the variation of instantaneous RMS channel delay a sensor could experience in all three road configurations. It is noteworthy to observe that in the ORC configuration, the ISI free transmission is at its lowest and will therefore be the limiting factor for high speed transmission. On the other hand, on average, the support for ISI free transmission is greatest for the IRC configuration.

To reflect upon the proposed system, it can be viewed in terms of these results the great potential of high speed VLC that can be achieved over highways by simply utilizing LED street lighting. Furthermore, in line of the integration of PLC and VLC, the probable bottleneck of high data rate transmissions, could be the PLC rather than the VLC.

7.6.2 Channel Capacity:

For the channel capacity, it is critical to observe the effect of physically perturbing the VLC link on $H_{s1}^{(P)}(0)$. As had been demonstrated in section 7.5, the effect of the perturbations is insignificant if a sensor is placed within the LED illumination zone. Under this realization, it will be assumed, as given in chapter 6, that $C_{Ave} \approx C_0$ in the case of perturbations. Hence, the channel capacity will be obtained

for the unperturbed case only, as given by equation (6.14). In the equation, it is clear that the systems BW is an important factor is determining the channel capacity. A conservative value of 5MHz for the LEDs BW has been adopted for all results herein. This choice of conservative BW is primarily due to the limited switching capability of phosphor coated types of LEDs typically used in streetlights.

Figures 7.28, 7.29 and 7.30 depict the channel capacity for a sensor traveling on all three lanes, in the straight, IRC and ORC highway configurations.

Each of the three channel capacity figures demonstrate certain common features, similar to the RMS channel delay. An increase in the capacity is evident for sensors on the inner lanes as compared to a sensor on the outer lanes. The maximum capacity for all tracks and all road configurations is centered directly beneath the luminaire. This is evidently the effect of maximum SNR influencing the outcome of the channel capacity, as indicated by equation (6.14).

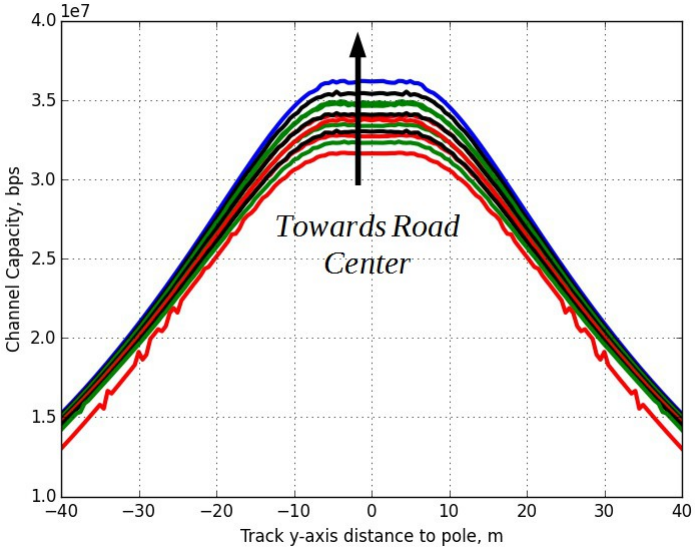

Figure 7.28 Channel capacity of straight configuration.

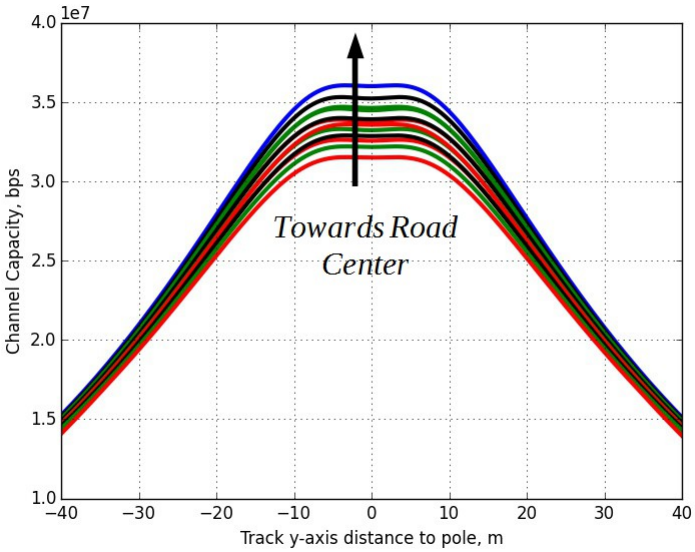

Figure 7.29 Channel capacity of IRC configuration.

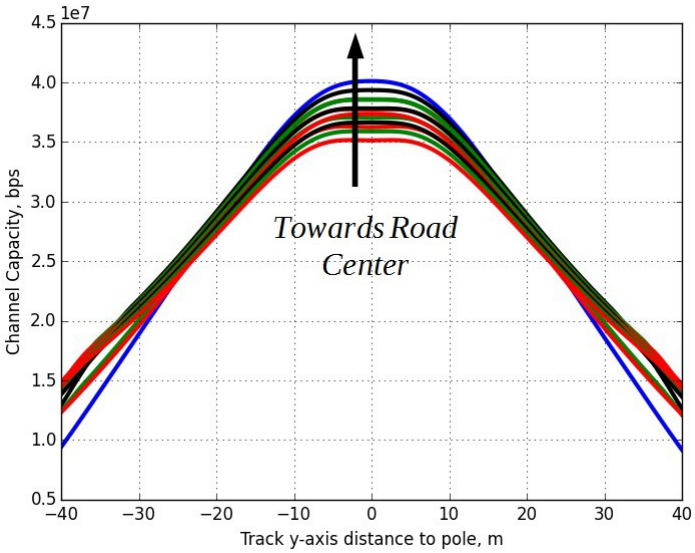

Figure 7.30 Channel capacity of ORC configuration.

Comparison of the difference in maximum channel capacity related to sensor track placement, it can be observed that for both straight and IRC configurations, the difference is approximately 4Mbps. For the ORC configuration, this figure rises slightly to approximately 6Mbps. It can be deduced from this result that a sensor traveling in the straight and IRC configurations will experience a potential capacity drop of 4Mbps between innermost and outermost lanes. While the potential capacity

drop for the ORC configuration is an extra 2Mbps from innermost to outermost lanes.

In comparing the absolute maximum channel capacities for the three road configurations, it can be observed that in the case of the straight and IRC configurations, the maximum bit rate hovers just above 36Mbps and 32Mbps for the innermost and outermost lanes. In comparison, the ORC demonstrates a maximum bit rate of 40Mbps and 34Mbps for the innermost and outermost lanes. It is clear from this that there is a clear advantage of a sensor placed within the ORC configuration compared to the other two road configurations.
These findings are equally summarized in Table 7.1 below.

Table 7.1 Maximum and minimum channel capacities under luminaire for all three road configurations.

	Straight	**IRC**	**ORC**
Maximum (Mbps)	36.0	36.0	40.0
Minimum (Mbps)	32.0	32.0	34.0

Finally, comparing these figures to the attainable ISI free transmission as indicated by figures (7.25 – 7.27) of the RMS channel delays, the results shown by the channel capacity are clearly a limiting factor. For comparison, a ratio of the maximum ISI free communication to maximum bit rate from the channel capacity is 10.97. This result signifies that a considerable drop of performance, around 11 fold, is predicted through the channel capacity.

In terms of both the channel capacity and the proposed system, the VLC end could still deliver high speed data rates, even whilst the rates are significantly lower as compared to the transmission rates reflected by the RMS channel delay. On an integration level of PLC and VLC in this case, it will be the VLC end that will suffer greatest. Hence, the bottleneck of high speed data transmissions will now be the VLC side instead of the PLC side of the system.

Chapter 8

Conclusions

8.1 Summary

This thesis is the first conducted study on the channel dedicated to I2V VLC for high speed roadways specific to clear night sky conditions, to the best of the author's knowledge. VLC integrated as a possible means to deliver ITS services has been proposed for metropolitan and urban roadways. Unlike urban roadways, high speed roads have to strictly adhere to highway specifications. Such specifications dictate the minimum turn radius of a road specific to the maximum travel velocity of vehicles. Roads that are designed with a curvature are further sloped to the interior of the curve, so as to provide vehicles with more grip. In numerous studies linked to urban roadways investigating I2V VLC have largely targeted the use of traffic light for data delivery. The lack of traffic lights on high speed roadways ultimately requires that I2V VLC is conducted otherwise. Opportunistically, VLC for such types of roads is constrained to data transmission from the streetlight poles.

To set the scene for the study, the road curvature parameter has been used. The rationale for this follows from the fact that the road curvature is directly related to the maximum permissible velocity of vehicles. Consequently, three extreme road configurations for I2V VLC has been identified and further researched. Namely, the straight, IRC and ORC road configurations. The streetlight poles in all configurations, had been setup such that the poles are placed in a road center setting. Moreover, each streetlight pole houses two luminaires that are 180^{o} apart from each other. Finally, for the receiver, the assumption has been made that it is

motorized, so that to continually assure pointing the receivers sensor towards the expected center of the closest luminaire.

Illumination using LEDs are increasingly being integrated within most man made infrastructures with lighting applications. The ability of LEDs to switch between different states has also attracted attention. Adopting an illumination and communication solution has become feasible and is gaining momentum especially with the prospect of Gbps data transmission on the horizon. One method of VLC communication, that has been recently adopted by the IEEE and has been equally taken up within this study, is known as IM/DD.

8.2 Findings

8.2.1 DC Channel Response:

This study primarily focuses on obtaining the analytical DC channel response of IM/DD system while accounting for the physical road dimensions, road curvature, road slope and directionality of the light output from the luminaires. To achieve this, unlike the undertaking in other studies, an accurate light intensity model specific to the streetlight has been included. From the analysis, it has been observed that the DC channel response is complex. This complexity can be attributed to the fact that the response is strongly influenced by three angles, a polar, an azimuthal and a sensor to LED viewing angles. On the other hand, results obtained from the simulation showed that the DC channel response is a function that increase with a Gaussian like curve, as a vehicle approaches a luminaire. The channel response is sharper and slightly greater in the ORC condition compared to the other two cases. Both other two cases show very similar results. Moreover, it can be confirmed that the DC channel response of the lanes towards the road center attains higher levels than the outer lanes. To complete on the DC channel response study, the influence of the opposite side luminaire for the same streetlight pole has been investigated. It has been observed that the particular luminaire sheds negligible light levels and could, therefore, be neglected for all further investigations.

To obtain an accurate model of the channel, requires that the DC channel response be recomputed for all points along the surface of the road. For this, obtaining the DC channel response using the direct method becomes a high complexity problem that is time consuming. The complexity is further increased knowing that streetlight luminaires are composed of multiple LEDs, each one considered in itself as a point source.

Reducing the complexity of obtaining the DC channel response has been undertaken in two different directions. First, given that the LEDs are placed in close proximity, a differential equation approach to the problem was attempted. The analytically derived equations have only increased the complexity of deriving the DC channel response. For this reason this path had been abandoned and is strongly not recommended. The second approach is the realization that the spacing between LEDs compared to the separation distance of LED and PD sensor is small. For all practical purposes, replacing the complete LED array with a single LED point source placed at the center of the array has been performed. This approach to the problem has delivered accurate results, provided that the PD sensor remains within the intended illumination zone of the transmitting luminaire. Beyond the intended zone, the proposed method becomes inaccurate as has been observed.

VLC data transmission has been demonstrated for both indoor and outdoor environments. Unlike the confined indoor environment, the light or its light source, in an outdoor environment can be influenced by numerous external factors. In the case of clear night sky, the source of light can be physically influenced by vibrations and wind of the pole structure. Furthermore, the channel could be influenced by deviations of the sensor due to the road and vehicle imperfections. By lumping all such influences into random variables affecting the luminaire, the influence of two types of perturbations on the DC channel response have been analyzed. Specifically, perturbations due to the luminaire rotation and translation.

8.2.2 Perturbation Analysis:

The perturbation analysis, has been conducted on all constituents of the DC channel response, so as to gain an insight on the outcome of each components PDF. By using small angular approximations, it has been shown that the influence of the sensor to LED viewing angle could be neglected for the analyzed system. The effect of both polar and azimuth angles influence the light intensity distribution. From the analysis and further supported by the simulations, it has been observed that for both perturbations, the azimuth angle is generally bypassed within most computations. For such reason, it is possible to ignore the azimuth angle in the case study at hand. Finally, perturbation analysis of the polar angle indicates that its outcome is Gaussian for both perturbation types, under the small angle analysis. Substitution into the intensity distribution reveals that the outcome variance of the intensity distribution can be approximated by a normal distribution. Using these results and applying it to the DC channel response has proven that the variance associated with the DC channel response is insignificant, and can be altogether neglected. This result, therefore, has been shown for all three highway configurations. Accordingly, it can be concluded that, unlike transmission of a focused light beam, the inherently wide intensity distribution of streetlight optics, makes the DC channel response insensitive to perturbations. However, the statement is true in the condition that a sensor is placed within the intended zone of luminaire illumination under all perceived perturbations.

8.2.3 Channel Capacity and RMS Channel Delay Spread:

In most channel studies, interest into the achievable bit rates is of high importance. The bit rate can be measured in two ways. In a channel that is limited by its BW and SNR, the channel capacity can be used to determine the available bit rate. The BW limitation in the streetlight LED is a direct result of the limited switching capability due to the phosphor coating on the white light HB-LEDs. On the other hand, a channel could experience multiple copies of a transmitted signal, which in turn causes ISI. For such channels, the interest surrounds the achievable bit rate for an ISI free transmission. This can be obtained from the RMS channel delay spread.

For the analyzed system, the average channel capacity and RMS channel delay spread are obtained. By acknowledging that the DC channel response variance is insignificant, therefor, it can be obtained directly using the single LED equivalency. From this, it has been observed that the channel capacity for all three road configurations is maximum for the ORC case, attaining 40Mbps. The difference between channel capacities of the IRC and the other two cases is approximately 4Mbps. Finally, it has been observed that, on average, the innermost lanes have an advantage of around 5Mbps compared to the outermost lanes.

The RMS time delay spread has been computed on the basis that the direct LOS path from each LED to sensor will experience a small amount of variation. This variation is a consequence of the applied geometry related to the LEDs positioning within the luminaire. The direct method to compute the RMS channel delay spread can be time consuming, as each LED and sensor position must be computed individually. Knowledge of the LED array geometry, in combination with the single LED equivalency DC channel response method, can alleviate this time intensive task. Both the exact and proposed method have shown exceptionally good results. Upon comparison of the RMS channel delay spread for different tracks, it has been observed that a track that travels along the center portion of the illuminated zone, will experience less fluctuations compared to the innermost and outermost lanes. Sensors situated along this track may require less channel adaptation, and hence less sophisticated hardware, to accommodate for the RMS delay variations, as compared to the tracks on either road side. Finally, in terms of the ISI free transmission, the proposed system can accommodate data rates above 430Mbps, for all three cases.

Comparing bit rate results obtained from the channel capacity and RMS delay spread, it is clear that there is a penalty of approximately 11 fold due to the BW limited channel. Therefore, it can be concluded that the channel suffers most due to the limited BW of the phosphor coating, which should be addressed if the prospect of Gbps on high speed roadways is to be achieved.

Accordingly, it can be concluded that the complete DC channel response for an I2V

VLC system proposed herein, can be obtained efficiently using the single LED model. By knowing the geometry of the LED placement an accurate measure of the RMS channel delay spread can be obtained efficiently. Furthermore, under the clear night sky condition, it has been shown that the perturbations due the relative motion of sensor and LED can be ignored, subjected to the sensor is placed within the illuminated zone. Finally, it can be claimed that the VLC channel in the high speed roadways scene, is a robust channel that can handle position variations of LED and PD sensor.

8.3 Future Work:

Exploring the field of I2V VLC for high speed roadways, to the best of the author's knowledge, has only seen its surface scratched. Many prospective future work within the field, especially that related to the VLC channel, still awaits unveiling. In direct relation to this study is exploring the channel variation in daylight and variable weather conditions. The effect of daylight optical filtering and sensor shielding from the sun, could be investigated as measures to extend the operation of the system into daylight hours. In terms of the effect of weather, rain, fog and sand in the air are all known factors that increase channel attenuation in long range FSO. For the proposed application, however, the influence of the complete weather cycle still remains an open question. Moreover, the implied channel, under clear sky conditions, has permitted the use of the LOS DC channel model. In conditions where particles are present within the air, the effect of multipath could alter the VLC channel drastically. This can be attributed to the fact that there exists numerous reflected paths rather than a single LOS path. Subsequently, the summation of all paths at the Rx will critically influence the systems performance, and therefore requires analysis to ensure sustained communications. The effect of thermal variations, known to alter the air, might not be critical to this form of communications, due to the short range. However, thermal effect could be most severe on the degradation of the transmitted light spectrum meanwhile alleviating receiver noise levels. Hence thermal variability could also become a limiting factor in the practical deployment of the envisaged system, and to effect requires proper system analysis.

Appendix

The expectation of a RV X , $\mu_X = E[X]$, with a continuous PDF, $f_x(x)$, is given by,

$$E[X] = \int_{-\infty}^{\infty} x f_x(x) dx \tag{A.1}$$

While the variance of X , σ_X^2 , is given as,

$$\sigma_X^2 = \int_{-\infty}^{\infty} (x-\mu_X)^2 f_X(x) dx \tag{A.2}$$

which can be evaluated using $\sigma_X^2 = E[X^2] - \mu_X^2$.

Expectations of RVs can be directly related to their moment generating function. Denoting the MGF of RV X as $M_X(t)$, then the nth moment of X is given by,

$$E[X^n] = M_X^n(0) \tag{A.3}$$

Using this definition for the expectation, it is simple to define the skewness and kurtosis in terms of the MGF. The skewness of X can be derived from,

$$skw_X = E[(\frac{X-\mu_X}{\sigma_X})^3] \tag{A.4}$$

By expanding the skewness parameter and substituting for the MGFs, equation 4 can be expressed as,

$$skw_X = \frac{M_X^3(0) - 3\mu_X M_X^2(0) + 2\mu_x^3}{\sigma_X^3} \tag{A.5}$$

The kurtosis of X is readily evaluated from,

$$kurt_X = E[(\frac{X-\mu_X}{\sigma_X})^4] \tag{A.6}$$

Similarly, expanding equation 6 and substituting with the MGFs, the equation can be rewritten as,

$$kurt_X = \frac{M_X^4(0) - 4\mu_X M_X^3(0) + 6\mu_X^2 M_X^2(0) - 3\mu_X^4}{\sigma_X^4} \tag{A.7}$$

References

[1] 'Fatality Analysis Reporting System', www-fars.nhtsa.dot.gov

[2] T. Komine and M. Nakagawa, “Fundamental Analysis for Visible-Light Communication System using LED Lights,” *IEEE Transactions on Consumer Electronics*, vol. 50, no. 1, pp. 100–107, Feb. 2004.

[3] J. H. Choi, S. W. Koo, and J. Y. Kim, “Influence of Optical Path Difference on Visible Light Communication Systems,” in *Proceedings of the 9th International Symposium on Communications and Information Technology (ISCIT) 2009*, Icheon, South Korea, 2009, pp. 1247–1251.

[4] J. Ding, K. Wang, and Z. Xu, “Impact of Different LED-Spacing in Arrayed LED Transmitter on VLC Channel Modeling,” in *Proceedings of the Sixth International Conference on Wireless Communications and Signal Processing (WCSP) 2014*, Hefei, China, 2014, pp. 1–6.

[5] I. Moreno, M. Avendano-Alejo, T. Saucedo-A., and A. Bugarin, “Modeling LED Street Lighting,” *Applied Optics*, vol. 53, no. 20, Jul. 2014.

[6] S. Kitano, S. Haruyama, and M. Nakagawa, “LED Road Illumination Communications System,” in *Proceedings of the 2003 IEEE 58th Vehicular Technology Conference (VTC) 2003*, Orlando, USA, 2003, vol. 5, pp. 3346–3350.

[7] P. Luo, Z. Ghassemlooy, H. Le Minh, E. Bentley, A. Burton, and X. Tang, “Fundamental Analysis of a Car to Car Visible Light Communication System,” in *Proceedings of the 9th International Symposium on Communication Systems, Networks & Digital Sign (CSNDSP) 2014*, Manchester, UK, 2014, pp. 1011–1016.

[8] J. Lord, *Beacon Lights of History, Vol VI (in 15 Volumes): Renaissance and Reformation*, vol. 15. New York, USA: Cosimo, 2009.

[9] W. O. Popoola and Z. Ghassemlooy, “BPSK Subcarrier Intensity Modulated Free-Space Optical Communications in Atmospheric Turbulence,” *Journal of Lightwave Technology*, vol. 27, no. 8, Apr. 2009.

[10] S. Singh and R. Bharti, “163m/10Gbps 4QAM-OFDM Visible Light

Communication," *International Journal of Engineering and Technical Research (IJETR)*, vol. 2, no. 6, pp. 225–228, Jun. 2014.

[11] http://www.vlcc.net

[12] http://www.ict-omega.eu

[13] http://www.ieee802.org/15/pub/TG7.html

[14] A. Borkute and A. Padole, "(Light Fidelity)-The Future Technology in Wireless Communication," *International Journal of Scientific & Engineering Research*, vol. 4, no. 12, pp. 153–161, Dec. 2013.

[15] M. S. Hossain, M. S. Islam, A. Zainul Abadin, and M. A. Hossain, "Methodology to Achieve Enhanced Data Transmission Rate using Li-Fi in VLC Technology," *International Journal of Engineering Research*, vol. 3, no. 12, pp. 803–806, Dec. 2014.

[16]http://www.ledinside.com/news/2015/7/sanan_opto_signs_lifi_partnership_agreement_with_military_affiliated_chinese_research_institute

[17] http://www.engadget.com/2014/01/11/oledcomm-li/fi-smartphone-concept

[18] F. Schill, U. R. Zimmer, and J. Trumpf, "Visible Spectrum Optical Communication and Distance Sensing for Underwater Applications," in *Proceedings of the Australasian Conference on Robotics and Automation (ACRA)*, Canberra, Australia, 2004.

[19] P. Liu, K. Kazaura, P. Dat, K. Wakamori, and M. Matsumoto, "High-Speed Image Detector Appliance in Free Space Optical Communication," *IET Image Processing*, vol. 5, no. 5, pp. 356–362, 2011.

[20] C. Medina, M. Zambrano, and K. Navarro, "LED Based Visible Light Communication: Technology, Applications and Challenges - A Survey," *International Journal of Advances in Engineering & Technology (IJAET)*, vol. 8, no. 4, pp. 482–495, Aug. 2015.

[21] T. Yamazato, I. Takai, H. Okada, T. Fujji, T. Yendo, S. Arai, M. Andoh, T. Harada, K. Yasutomi, K. Kagawa, and S. Kawahito, "Image-Sensor-Based Visible Light Communication for Automotive Applications," *IEEE Communications Magazine*, vol. 52, no. 7, pp. 88–97, Jul-2014.

[22] J. Liao, A. Mirvakili, A. Boryssenako, V. Joyner, Z. Rena, and Huang, "Integration of LED Chip within Patch Antenna Geometry for Hybrid FSO/RF Communication," *Electronics Letters*, vol. 46, no. 19, Sep. 2010.

[23] L. Ding, F. Liu, Z. Yu, and Y. Wang, “The Demonstration of Wireless Access via Visible Light Communications,” in *Proceedings of the 2013 International Conference on Wireless Communications & Signal Processing (WCSP)*, Hangzhou, 2013, pp. 1–4.

[24] E. Leitgeb, T. Plank, P. Pezzei, D. Kraus, and J. Poliak, “Integration of FSO in Local Area Networks – Combination of Optical Wireless with WLAN and DVB-T for Last Mile Internet Connections,” in *Proceedings of the 19 European Conference on Networks and Optical Communicaitons (NOC) 2014*, Milan, Italy, 2014, pp. 120–125.

[25] H. Chowdhury and M. Katz, “Data Download on Move in Indoor Hybrid (Radio-Optical) WLAN-VLC Hotspot Coverages,” in *Proceedings of the 2013 IEEE 77th Vehicular Technology Conference (VTC Spring)*, Dresden, Germany, 2013, pp. 1–5.

[26] H. Ma, L. Lampe, and S. Hranilovic, “Integration of Indoor Visible Light and Power Line Communication Systems,” in *Proceedings of the IEEE 17th International Symposium on Power Line Communications and its Applications 2013 (ISPLC 2013)*, Johannesburg, South Africa, 2013.

[27] T. Komine and M. Nakagwa, “Integrated System of White LED Visible-Light Communication and Power-Line Communication,” in *Proceedings of the 13th IEEE International Symposium on Personal, Indoor and Mobile Radio Communications, 2002*, Lisboa, Portugal, 2002, vol. 4.

[28] T. Komine and M. Nakagawa, “Integrated System of White LED Visible-Light Communication and Power-Line Communication,” *IEEE Transactions on Consumer Electronics*, vol. 49, no. 1, Feb. 2003,pp. 71-79.

[29] T. Komine, S. Haruyama, and M. Nakagawa, “Performance Evaluation of Narrowband OFDM on Integrated System of Power Line Communication and Visible Light Wireless Communication,” in *Proceedings of the 1st International Symposium on Wireless Pervasive Computing (ISWPC), 2006*, Phuket, Thailand, 2006.

[30] P. Amirshani and M. Kavehrad, “Broadband Access over Medium and Low Voltage Power-lines and use of White Light Emitting Diodes for Indoor Communications,” in *Proceedings of the IEEE 3rd Consumer Communications and Networking Conference (CCNC) 2006*, Las Vegas, USA, 2006, vol. 2.

[31] S. E. Alavi, H. Rezaie, and A. S. M. Supa'at, "Application of OFDM on Integrated System of Visible Free Space Optic with PLC," in *Proceedings of the 2010 IEEE Asia-Pacific Conference on Applied Electromagnetics (APACE 2010)*, Port Dickson, Malaysia, 2010, pp. 1–5.

[32] J. Song, W. Ding, F. Yang, H. Yang, J. Wang, X. Wang, and X. Zhang, "Indoor Hospital Communication Systems: An Integrated Solution Based оп Power Line and Visible Light Communication," in *Proceedings of the IEEE Faible Tension Faible Consommation (FTFC)*, Monaco, 2014, pp. 1–6.

[33] Hoda Rezaie, Zahra Hashemiyan, Abu Sahmah M. Supa'at, and Seyyed Ehsan Alavi, "Application of DFE on Integrated System of VFSO and Broad band Power Line Communication," in *Proceedings of the 17th Asia-Pacific Conference on Communications (APCC) 2011*, Kota Kinabalu, Malaysia, 2011, pp. 273–277.

[34] M. Miki, K. Yoshida, and M. Yoshimi, "Faster Illuminance Convergence for the Intelligent Lighting System Using Visible Light Communication," in *Proceedings of the IEEE International Conference on Systems, Man, and Cybernetics (SMC) 2012*, Seoul, South Korea, 2012, pp. 3179–3184.

[35] A. Sevincer, A. Bhattarai, M. Bilgi, M. Yuksel, and N. Pala, "LIGHTNETs: Smart LIGHTing and Mobile Optical Wireless NETworks – A Survey," *IEEE Communications Surveys & Tutorials*, vol. 15, no. 4, Fourth Quarter 2013.

[36] http://www.itsworldcongress2016.com

[37] F.-Y. Wang, "Scanning the Issue and Beyond: Transportation and Mobility Transformation for Smart Cities," *IEEE Transactions on Intelligent Transportation Systems*, vol. 16, no. 2, pp. 525–533, Apr. 2015.

[38] M. Biagi, T. Borogovac, and T. D. C. Little, "Adaptive Receiver for Indoor Visible Light Communications," *Journal of Lightwave Technology*, vol. 31, no. 23, Dec. 2013.

[39] J. P. Ding and Y. F. Ji, "Evolutionary Algorithm-Based Optimisation of the Signal-to-Noise Ratio for Indoor Visible-Light Communication Utilising White Light-Emitting Diode," *IET Optoelectronics*, vol. 6, no. 6, pp. 307–317.

[40] X. Zhang, J. Duan, Y. Fu, and A. Shi, "Theoretical Accuracy Analysis of Indoor Visible Light Communication Positioning System Based on Received Signal Strength Indicator," *Journal of Lightwave Technology*, vol. 32, no. 21, Nov. 2014.

[41] I. Moreno and U. Contreras, "Color Distribution from Multicolor LED Arrays,"

Optics Express, vol. 15, no. 6, pp. 3607–3618, Mar. 2007.

[42] M. Zhang, Y. Chen, and G. He, “Color Temperature Tunable White-Light LED Cluster with Extrahigh Color Rendering Index,” *The Scientific World Journal*, vol. 2014, p. 6, Jan. 2013.

[43] G. Stepniak, J. Siuzdak, and P. Zwierko, “Compensation of a VLC Phosphorescent White LED Nonlinearity by Means of Volterra DFE,” *IEEE Photonics Technology Letters*, vol. 25, no. 16, pp. 1597–1600, Aug. 2013.

[44]G. Pang, T. Kwan, H. Liu, and C.-H. Chan, “Optical Wireless Based on High Brightness Visible LEDs,” in *Conference Record of the 1999 IEEE Industry Applications Conference, 1999. Thirty-Fourth IAS Annual Meeting.*, Phoenix, USA, 1999, vol. 3, pp. 1693–1699.

[45] G. Pang, T. Kwan, C.-H. Chan, and H. Liu, “LED Traffic Light as a Communications Device,” in *Proceedings of the IEEE/IEEJ/JSAI International Conference on Intelligent Transportation Systems*, Tokyo, Japan, 1999, pp. 788–793.

[46] T. Komine, J. Hwan, S. Haruyama, and M. Nakagawa, “Adaptive Equalization System for Visible Light Wireless Communication Utilizing Multiple White LED Lighting Equipment,” *IEEE Transactions on Wireless Communications*, vol. 8, no. 6, Jun. 2009.

[47] K.-D. Langer, J. Vucic, C. Kottke, L. F. Del Rosal, S. Nerreter, and J. Walewski, “Advances and Prospects in High-Speed Information Broadcast using Phosphorescent White-Light LEDs,” in *Proceedings of the IEEE 11th International Conference on Transparent Optical Networks (ICTON) 2009*, Azores, Portugal, 2009, pp. 1–6.

[48] C. W. Chow, C. H. Yeh, Y. F. Liu, and Y. Liu, “Improved modulation speed of LED visible light communication system integrated to main electricity network,” *Electronics Letters*, vol. 47, no. 15, Jul. 2011.

[49] N. Lourenco, D. Terra, N. Kumar, L. N. Alves, and R. L. Aguiar, “Visible Light Communication System for Outdoor Applications,” in *Proceedings of the 8th IEEE, IET International Symposium on Communication Systems, Networks and Digital Signal Processing (CSNDSP) 2012*, Poznan, Poland, 2012, pp. 1–6.

[50] I. S., V. Nair, S. Jain, and S. Chaudhury, “Video Based Adaptive Road Traffic Signaling,” in *Proceedings of the IEEE Seventh International Conference on Distributed Smart Cameras (ICDSC) 2013*, Palm Springs, USA, 2013, pp. 1–6.

[51] F. Caicedo, C. Blazquez, and P. Miranda, “Prediction of Parking Space Availability in Real Time,” *Elsevier Expert Systems with Applications*, vol. 39, pp. 7281–7290, 2012.

[52] http://www.its.dot.gov/

[53] http://www.itsa.org/

[54] http://ertico.com/

[55] https://www.its-australia.com.au/

[56] V. Joshi, N. Rajamani, K. Takayuki, N. Prathapaneni, and L. V. Subramaniam, “Information Fusion Based Learning for Frugal State Sensing,” in *Proceedings of the Twenty-Third International Joint Conference on Artificial Intelligence (IJCAI-13)*, Beijing, China, 2013.

[57] M. Rahnema, *UMTS Network Planning, Optimization and Inter-Operation with GSM*, 1st ed. Singapore: John Wiley & Sons (Asia), Inc., 2008.

[58]T. Hara, S. Iwasaki, T. Yendo, T. Fujji, and M. Tanimoto, “A New Receiving System of Visible Light Communication for ITS,” in *Proceedings of the 2007 IEEE Intelligent Vehicles Symposium*, Istanbul, Turkey, 2007, pp. 474–479.

[59] G. Pang, “Information Technology Based on Visible LEDs for Optical Wireless Communications,” in *Proceedings of the 2004 IEEE Region 10 Conference TENCON 2004*, Chiang Mai, Thailand, 2004, vol. 2, pp. 395–398.

[60] R. D. Roberts, S. Rajagopal, and S.-K. Lim, “IEEE 802.15.7 Physical Layer Summary,” in *Proceedings of the 2011 GLOBECOM Workshops (GC Wkshps), 2011*, Houston, USA, 2011, pp. 772–776.

[61] S. Rajagopal, R. D. Roberts, and S.-K. Lim, “IEEE 802.15.7 Visible Light Communication: Modulation Schemes and Dimming Support,” *IEEE Communications Magazine*, Mar-2012.

[62] E. Monteiro and S. Hranilovic, “Design and Implementation of Color-Shift Keying for Visible Light Communications,” *Journal of Lightwave Technology*, vol. 32, no. 10, pp. 2053–2060, May 2014.

[63] E. Sarbazi and M. Uysal, “PHY Layer Performance Evaluation of the IEEE 802.15.7 Visible Light Communication Standard,” in *Proceedings of the 2nd International Workshop on Optical Wireless Communications (IWOW) 2013*, Newcastle upon Tyne, UK, 2013, pp. 35–39.

[64] H.-D. Moon and S.-Y. Jung, “Group Waveform-coded Pulse Width Position

Modulation(PWPM) for Vehicular Visible Light Communications," in *Proceedings of the IEEE 2011 International Conference on ICT Convergence (ICTC) 2011*, Seoul, South Korea, 2011, pp. 294–299.

[65] N. Fujimoto and H. Mochizuki, "614 Mbit/s OOK-Based Transmission by the Duobinary Technique using a Single Commercially Available Visible LED for High-Speed Visible Light Communications," in *Proceedings of the 38th European Conference and Exhibition on Optical Communications (ECOC) 2012*, Amsterdam, Holland, 2012, pp. 1–3.

[66] A. Belle, M. Falcitelli, M. Petracca, and P. Pagano, "Development of IEEE802.15.7 Based ITS Services Using Low Cost Embedded Systems," in *Proceedings of the 13th International Conference on ITS Telecommunications (ITST) 2013*, Tampere, Finland, 2013, pp. 419–425.

[67] Y. Yi, P. Li, C. Li, and C. Azurdia, "An Effective Scheme for Optical Doppler Shift Alleviation in Intelligent Transportation System Integrating Visible Light Communication," in *Proceedings of the 13th International Conference on Advanced Communication Technology (ICACT) 2011*, Seoul, South Korea, 2011, pp. 1253–1258.

[68] B. Tomas, H.-M. Tsai, and M. Boban, "Simulating Vehicular Visible Light Communication: Physical Radio and MAC Modeling," in *Proceedings of the 2014 IEEE Vehicular Networking Conference (VNC 2014)*, Paderborn, Germany, 2014, pp. 222–225.

[69] A. Cailean, B. Cagneau, L. Chassagne, S. Topsu, Y. Alayi, and J.-M. Blosseville, "Visible Light Communications: Application to Cooperation Between Vehicles and Road Infrastructures," in *Proceedings of the IEEE Intelligent Vehicles Symposium (IV), 2012*, Alcala de Henares, Spain, 2012, pp. 1055–1059.

[70] A. Cailean, B. Cagneau, L. Chassagne, M. Dimian, and V. Popa, "Novel Receiver Sensor for Visible Light Communications in Automotive Applications.," *IEEE Sensors Journal*, vol. 15, no. 8, pp. 4632–4639, Jun. 2015.

[71] J. Kim, S. Lee, Y. Lee, S. Hyun, M. Ju, and Y. Park, "Vehicle-to-Vehicle Visible Light Communications Using Sub-Pulse Manchester Modulation," in *Proceedings of the 2014 Sixth International Conference on Ubiquitous and Future Networks (ICUFN) 2014*, Shanghai, China, 2014, pp. 481–482.

[72] J. Liu, P. W. C. Chan, D. W. K. Ng, E. S. Lo, and S. Shimamoto, "Hybrid Visible

Light Communications in Intelligent Transportation Systems with Position Based Services," in *Proceedings of the 2012 IEEE Globecom Workshops (GC Wkshps) 2012*, Anaheim, USA, 2012, pp. 1254–1259.

[73] N. Kumar, N. Lourenco, D. Terra, L. N. Alves, and R. L. Aguiar, "Visible Light Communications in Intelligent Transportation Systems," in *2012 Intelligent Vehicles Symposium*, Alcala de Henares, Spain, 2012.

[74] N. Kumar, D. Terra, N. Lourenco, L. N. Alves, and R. L. Aguiar, "Visible Light Communication for Intelligent Transportation in Road Safety Applications," in *Proceedings of the 7th International Wireless Communications and Mobile Compting Conference (IWCMC) 2011*, Istanbul, Turkey, 2011, pp. 1513–1518.

[75] A.-M. Cailean, B. Cagneau, L. Chassagne, S. Topsu, Y. Alayli, and M. Dimian, "Visible Light Communications Cooperative Architecture for the Intelligent Transportation System," in *Proceedings of the 2013 IEEE 20th Symposium on Communications and Vehicular Technology in the Benelux (SCVT) 2013*, Namur, Belgium, 2013, pp. 1–5.

[76] A.-M. Cailean, B. Cagneau, L. Chassagne, S. Topsu, Y. Alayi, and M. Dimian, "Design and Implementation of a Visible Light Communications System for Vehicle Applications," in *Proceedings of the 21st Telecommunications Forum (TELFOR) 2013*, Belgrade, Serbia, 2013, pp. 349–352.

[77] M. Y. Abualhoul, M. Marouf, O. Shagdar, and F. Nashashibi, "Enhancing the Field of View Limitation of Visible Light Communication-based Platoon," in *Proceedings of the 2014 IEEE 6th International Symposium on Wireless Vehicular Communications (WiVeC2014)*, Vancouver, Canada, 2014, pp. 1–5.

[78] M. Y. Abualhoul, M. Marouf, O. Shagdar, and F. Nashashibi, "Platooning Control Using Visible Light Communications: A Feasibility Study," in *Proceedings of the 16th International IEEE Annual Conference on Intelligent Transportation Systems (ITSC) 2013*, The Hague, Netherlands, 2013, pp. 1535–1540.

[79] http://au.mathworks.com/products/simulink/

[80] R. Ashtari, S. Mao, and M. C. Hamilton, "A Low-Cost NLOS Ultra-Violet V2I Identification System for Vehicular Theft Recovery," in *Proceedings of the 2013 International Conference on Connected Vehicles and Expo (ICCVE)*, Las Vegas, USA, 2013, pp. 785–790.

[81] W. Zhang and M. Kavehrad, "A 2-D Indoor Localization System Based On

Visible Light LED," in *Proceedings of the IEEE Photonics Society Summer Topical Meeting Series, 2012*, Seattle, USA, 2012, pp. 80–81.

[82] H.-S. Kim, D.-R. Kim, S.-H. Yang, Y.-H. Son, and S.-K. Han, "An Indoor Visible Light Communication Positioning System Using a RF Carrier Allocation Techniqu," *Journal of Lightwave Technology*, vol. 31, no. 1, Jan. 2013.

[83] R. Roberts, P. Gopalakrishnan, and S. Rathi, "Visible Light Positioning: Automotive Use Case," in *Proceedings of the IEEE Vehicular Networking Conference (VNC) 2010*, Jersey City, USA, 2010, pp. 309–314.

[84] R. Corsini, R. Pelliccia, G. Cossu, A. M. Khalid, M. Ghibaudi, M. Petracca, P. Pagano, and E. Ciaramella, "Free Space Optical Communication in the Visible Bandwidth for V2V Safety Critical Protocols," in *Proceedings of the 8th International Conference on Wireless Communications and Mobile Computing Conference (IWCMC), 2012*, Limassol, Cyprus, 2012, pp. 1097–1102.

[85] X.-H. Lee, I. Moreno, and C.-C. Sun, "High-Performance LED Street Lighting Using Microlens Arrays," *Optics Express*, vol. 21, no. 9, May 2013.

[86] K. Wang, S. Liu, F. Chen, Z. Qin, Z. Liu, and X. Luo, "Freeform LED Lens for Rectangularly Prescribed Illumination," *Journal of Optics A: Pure and Applied Optics*, vol. 11, no. 10, pp. 1–10, Oct. 2009.

[87] http://optics.synopsys.com/lighttools/

[88] S. J. Lee, J. K. Kwon, S. Y. Jung, and Y. H. Kwon, "Simulation Modeling of Visible Light Communication Channel for Automotive Applications," in *Proceedings of the2012 15th International IEEE Conference on Intelligent Transportation Systems (ITSC)*, Anchorage, Alaska, USA, 2012, pp. 463–468.

[89] L. Cheng, L. Nong, and C. JianXin, "The Research of LED Arrays for Uniform Illumination," *Advances in Information Sciences and Service Sciences (AISS)*, vol. 4, no. 10, Jun. 2012.

[90] M. Akanegawa, Y. Tanaka, and M. Nakagawa, "Basic Study on Traffic Information System Using LED Traffic Lights," *IEEE Transactions on Intelligent Transportation Systems*, vol. 2, no. 4, pp. 197–203, Dec. 2001.

[91] R. Hu and X. Luo, "Adding an Extra Condition: A General Method to Design Double Freeform-Surface Lens for LED Uniform Illumination," *Journal of Solid State Lighting*, vol. 1, no. 3, 2014.

[92] Z. Zhenrong, H. Xiang, and L. Xu, "Freeform Surface Lens for LED Uniform

Illumination," *Applied Optics*, vol. 48, no. 35, Dec. 2009.

[93] L. Saen-chan and P. Buranasiri, "Lens Design for Illumination of LED using Non-Imaging Optics Method," *Thai Journal of Physics*, 2014.

[94] Y. Ding, X. Liu, Z. Zheng, and P. Gu, "Freeform LED Lens for Uniform Illumination," *Optics Express*, vol. 16, no. 17, Aug. 2008.

[95] A. Ashok, M. Gruteser, N. Mandayam, J. Silva, M. Varga, and K. Dana, "Challenge: Mobile Optical Networks Through Visual MIMO," in *Proceedings of the ACM Annual International Conference on Mobile Computing and Networking 2010 (MobiCom 2010)*, Chicago, USA, 2010.

[96] H. Okada, S. Misawa, T. Yamazato, T. Fujji, and T. Yendo, "Channel Information Estimation for Error Correcting Code in Road-to-Vehicle Visible Light Communication Systems," in *Proceedings of the 5th International Symposium on Wireless Vehicular Communications (WiVeC) 2013*, Dresden, Germany, 2013.

[97] I. Takai, S. Ito, K. Yasutomi, K. Kagawa, M. Andoh, and S. Kawahito, "LED and CMOS Image Sensor Based Optical Wireless Communication System for Automotive Applications," *IEEE Photonics Journal*, vol. 5, no. 5, Oct. 2013.

[98] I. Takai, T. Harada, M. Andoh, K. Yasutomi, K. Kagawa, and S. Kawahito, "Optical Vehicle-to-Vehicle Communication System Using LED Transmitter and Camera Receiver," *IEEE Photonics Journal*, vol. 6, no. 5, Oct. 2014.

[99] T. Saito, S. Haruyama, and M. Nakagawa, "A New Tracking Method using Image Sensor and Photo Diode for Visible Light Road-to-Vehicle Communication," in *Proceedings of the 10 International Conference on Advanced Communication Technology (ICACT 2008)*, Phoenix Park, Korea, 2008.

[100] S. J. Lee and S.-Y. Jung, "A SNR Analysis of the Visible Light channel Environment for Visible Light Communication," in *Proceedings of the 18th Asia Pacific Conference on Communications (APCC) 2012*, Jeju Island, Korea, 2012.

[101] http://www.dial.de/DIAL/en/dialux.html

[102] L. Grobe and K.-D. Langer, "Block-Based PAM with Frequency Domain Equalization in Visible Light Communications," in *Proceedings of the 4th IEEE Workshop on Wireless Optical Communications - (Globecom 2013), 2013*, Atlanta, USA, 2013, pp. 1070–1075.

[103] K. Lee and H. Park, "Channel Model and Modulation Schemes for Visible Light Communications," in *Proceedings of the IEEE 54th Intenational Midwest*

Symposium on Circuits and Systems (MWSCAS), 2011, Seoul, South Koreaq, 2011, pp. 1–4.

[104] J. M. Kahn and J. R. Barry, “Wireless Infrared Communications,” *Proceedings of the IEEE*, vol. 85, no. 2, pp. 265–298, Feb. 1997.

[105] S. Long, M. A. Khalighi, M. Wolf, S. Bourennane, and Z. Ghassemlooy, “Channel Characterization for Indoor Visible Light Communications,” in *Proceedings of the 3rd International Workshop in Optical Wireless Communications (IWOW), 2014*, Funchal, Portugal, 2014, pp. 75–79.

[106] M. Safari and M. Uysal, “Do We Really Need OSTBCs for Free-Space Optical Communication with Direct Detection?,” *IEEE Transactions on Wireless Communications*, vol. 7, no. 11, pp. 4445–4448, Nov. 2008.

[107] S. Rajbhandari, Z. Ghassemlooy, P. A. Haigh, T. Kanesan, and X. Tang, “Experimental Error Performance of Modulation Schemes Under a Controlled Laboratory Turbulence FSO Channel,” *Journal of Lightwave Technology*, vol. 33, no. 1, Jan. 2015.

[108] S. M. Navidpour, M. Uysal, and M. Kavehrad, “BER Performance of Free-Space Optical Transmission with Spatial Diversity,” *IEEE Transactions on Wireless Communications*, vol. 6, no. 8, Aug. 2007.

[109] L.-C. Wu and H.-M. Tsai, “Modeling Vehicle-to-Vehicle Visible Light Communication Link Duration with Empirical Data,” in *GLOBECOM 2013 Workshops (GC Wkshps) - Optical Wireless Communications 2013*, Atlanta, USA, 2013, pp. 1103–1109.

[110] Z. Cui, C. Wang, and H.-M. Tsai, “Characterizing Channel Fading in Vehicular Visible Light Communications with Video Data,” in *Proceedings of the IEEE Vehicular Networking Conference 2014 (VNC) 2014*, Paderborn, Germany, 2014, pp. 226–229.

[111] J. Ding, K. Wang, and Z. Xu, “Impact of LED Array Simplification on Indoor Visible Light Communication Channel Modeling,” in *Proceedings of the 9th International Symposium on Communication Systems, Networks & Digital Sign (CSNDSP) 2014*, Manchester, UK, 2014, pp. 1159–1164.

[112] J. Ding and Z. Xu, “Accuracy Analysis of Different Modeling Schemes in Indoor Visible Light Communications with Distributed Array Sources,” in *Proceedings of the 9th International Symposium on Communication Systems,*

Networks & Digital Sign (CSNDSP) 2014, Manchester, UK, 2014, pp. 1005–1010.

[113] T. Nagura, T. Yamazato, M. Katayama, T. Yendo, T. Fujji, and H. Okada, "Tracking an LED Array Transmitter for Visible Light Communications in the Driving Situation," in *Proceedings of the 7th International Symposium on Wireless Communication Systems (ISWCS) 2010*, York, UK, 2010, pp. 765–769.

[114] S. Iwasaki, C. Premachandra, T. Endo, T. Fujji, M. Tanimoto, and Y. Kimura, "Visible Light Road-To-Vehicle Communication using High-Speed Camera," in *Proceedings of the 2008 IEEE Intelligent Vehicles Symposium*, Eindhoven, The Netherlands, 2008.

[115] S. Arai, S. Mase, T. Yamazato, T. Endo, T. Fujji, M. Tanimoto, K. Kidono, Y. Kimura, and Y. Ninomiya, "Experiment on Hierarchical Transmission Scheme for Visible Light Communication using LED Traffic Light and High-Speed Camera," in *Proceedings of the IEEE 66th Vehicular Technology Conference 2007 (VTC-2007) Fall*, Baltimore, USA, 2007, pp. 2174–2178.

[116] S. Iwasaki, M. Wada, T. Endo, T. Fujji, and M. Tanimoto, "Basic Experiments on Paralle Wireless Optical Communication for ITS," in *Proceedings of the 2007 IEEE Intelligent Vehicles Symposium*, Istanbul, Turkey, 2007, pp. 321–326.

[117] S. J. Lee, J. K. Kwon, S.-Y. Jung, and Y.-H. Kwon, "Evaluation of Visible Light Communication Channel Delay Profiles for Automotive Applications," *EURASIP Journal on Wireless Communications and Networking*, Dec. 2012.

[118] http://www.3ds.com/products-services/catia

[119] J.-H. Yoo, R. Lee, J.-K. Oh, H.-W. Seo, J.-Y. Kim, H.-C. Kim, and S.-Y. Jung, "Demonstration of Vehicular Visible Light Communication Based on LED Headlamp," in *Proceedings of the 2013 Fifth International Conference on Ubiquitous and Future Networks (ICUFN) 2013*, Da Nang, Vietnam, 2013, pp. 465–467.

[120] S. Watada, K.-I. Hayashi, and M. Toda, "Range Finding System Using Monocular In-Vehicle Camera and LED," in *Proceedings of the International Symposium on Intelligent Signal Processing and Communication Systems (ISPACS) 2009*, Kanazawa, Japan, 2009, pp. 493–496.

[121] M. D. Higgins, R. J. Green, and M. S. Leeson, "Channel Viability of Intra-Vehicle Optical Wireless Communications," in *Proceedings of the 2nd IEEE Workshop on Optical Wireless Communications - GLOBECOM Workshops (GC*

Wkshps) 2011, Houston, USA, 2011, pp. 813–817.

[122] Mathew D. Higgins, Roger L. Green, and Mark S. Leeson, "Optical Wireless for Intravehicle Communications: A Channel Viability Analysis," *IEEE Transactions on Vehicular Technology*, vol. 61, no. 1, pp. 123–129, Jan. 2012.

[123] http://au.mathworks.com/matlabcentral/fileexchange/45355-optometrika

[124] C. W. Chow, C. H. Yeh, Y. F. Liu, and P. Y. Huang, "Background Optical Noises Circumvention in LED Optical Wireless Systems Using OFDM," *IEEE Photonics Journal*, vol. 5, no. 2, Apr. 2013.

[125] S. Verma, A. Shandilya, and A. Singh, "A Model for Reducing the Effect of Ambient Light Source in VLC System," in *Proceedings of the 2014 IEEE International Advance Computing Conference (IACC)*, Gurgaon, India, 2014.

[126] I. E. Lee, M. L. Sim, and F. W. L. Kung, "A Dual-Receiving Visible-Light Communication System under Time-Variant Non-Clear Sky Channel for Intelligent Transportation System," in *Proceedings of the 16th European Conference on Networks and Optical Communications (NOC) 2011*, Newcastle upon Tyne, UK, 2011, pp. 153–156.

[127] D.-R. Kim, S.-H. Yang, H.-S. Kim, Y.-H. Son, and S.-K. Han, "Outdoor Visible Light Communication For InterVehicle Communication Using Controller Area Network," in *Proceedings of the Fourth International Conference on Communications and Electronics (ICCE), 2012*, Hue, Vietnam, 2012, pp. 31–34.

[128] K. Cui, G. Chen, Z. Xu, and R. D. Roberts, "Experimental Characterization of Traffic Light to Vehicle VLC Link Performance," in *Proceedings of the 2nd IEEE Workshop on Optical Wireless Communications - GLOBECOM Workshopts (GC Wkshps), 2011*, Houston, USA, 2011, pp. 808–812.

[129] R. E. Bird and C. Riordan, "Simple Solar Spectral Model for Direct and Diffuse Irradiance on Horizontal and Tilted Planes at the Earth's Surface for Cloudless Atmospheres.," *Journal of Climate and Applied Meteorology*, vol. 25, Jan. 1986.

[130] A. Vavoulas, H. G. Sandalidis, and D. Varoutas, "Weather Effects on FSO Network Connectivity," *Journal of Optical Communication and Networking*, vol. 4, no. 10, Oct. 2012.

[131] H. Shaban, S. D. Abd El Aziz, A. K. AboulSeoud, and M. H. Aly, "Error Performance of Free Space Optical MIMO Systems in Weak, Moderate, and Severe

Atmospheric Turbulence Channels," in *Proceedings of the 24th Canadian Conference on Electrical and Computer Engineering (CCECE) 2011*, Niagara Falls, Canada, 2011, pp. 777–782.

[132] N. Cvijetic, S. G. Wilson, and M. Brandt-Pearce, "Performance Bounds for Free-Space Optical MIMO Systems with APD Receivers in Atmospheric Turbulence," *IEEE Journal on Selected Areas in Communications*, vol. 26, no. 3, Apr. 2008.

[133] A. J. Kshatriya, Y. B. Acharya, and A. Aggarwal, "Analysis of Free Space Optical Link in Ahmedabad Weather Conditions," in *Proceedings of the IEEE Conference on Information and Communication Technologies (ICT 2013)*, Jeju Island, Korea, 2013, pp. 272–276.

[134] N. T. Dang, H. T. T. Pham, and A. T. Pham, "Average BER Analysis of Multihop FSO Systems over Strong Turbulence and Misalignment Fading Channels," in *Proceedings of the 2nd IEEE/CIC International Conference on Communications in China (ICCC): Optical Communication Systems (OCS)*, Xi'an, China, 2013, pp. 153–157.

[135] D. A. Luong, T. C. Thang, and A. T. Pham, "Average Capacity of MIMO/FSO Systems with Equal Gain Combining over Log-Normal Channels," in *Fifth International Conference on Ubiquitous and Future Networks (ICUFN) 2013*, Da Nang, Vietnam, 2013, pp. 306–309.

[136] P. Kaur, V. K. Jain, and S. Kar, "Capacity of Free Space Optical Links with Spatial Diversity and Aperture Averaging," in *Proceedings of the 27th Biennial Symposium on Communications*, Kingston, ON, 2014, pp. 14–18.

[137] O. Fiser, V. Brazda, and L. Rejfek, "Two Ways to Consider Atmospheric Turbulences in FSO Propagation," in *Proceedings of the 24th International Conference Radioelektronika 2014*, Bratislava, 2014, pp. 1–4.

[138] G. A. Cap, H. H. Refai, and J. J. J. Sluss, "Optical Tracking and Auto-Alignment Transceiver System," *IEEE A&E Systems Magazine*, Sep. 2010.

[139] S. Qazi, "Challenges In Outdoor and Indoor Optical Wireless Communications," in *Proceedings of the 2006 International Conference on Wireless Networks*, Las Vegas, USA, 2006, pp. 448–458.

[140] W. Gappmair, S. Hranilovic, and E. Leitgeb, "Performance of PPM on Terrestrial FSO Links with Turbulence and Pointing Errors," *IEEE Communications*

Letters, vol. 14, no. 5, May 2010.

[141] P. Liu, K. Kazaura, K. Wakamori, and M. Matsumoto, “Studies on C_n^2 and its effects on free space optical communication system,” in *Proceedings of the IEEE 8th Asia-Pacific Symposium on Information and Telecommunication Technologies (APSITT) 2010*, Kuching, Malaysia, 2010, pp. 1–6.

[142] A. C. Motlagh, V. Ahmadi, Z. Ghassemlooy, and K. Abedi, “The Effect of Atmospheric Turbulence on the Performance of the Free Space Optical Communications,” in *Proceedings of the 6th International Symposium on Communication Systems, Networks and Digital Signal Processing (CNSDSP) 2008*, Graz, Austria, 2008, pp. 540–543.

[143] S. Devi and L. Govindaraju, “A Study on Wind Induced Vibration on Lighting Poles,” *International Journal of Research in Engineering and Technology (IJRET)*, vol. 3, no. 6, May 2014.

[144] C. R. Briden, “Light Poles: A Guide to their Selection, Installation and Maintenance, including the cause and effects of Pole Vibration.” Cooper Lighting, 24-Jun-2009.

[145] Lithonia Lighting, “Light Standards Effects of Vibration,” PL-150.

[146] M. Rogers, *Highway Engineering*. Oxford, UK: Blackwell Science, 2003.

[147] American Association of State Highway and Transportation Officials, *A Policy on Geometric Design of Highways and Streets*, Fourth. Washington D. C.: American Association of State Highway and Transportation Officials, 2001.

[148] Z. Ghassemlooy, W. Popoola, and S. Rajbhandari, *Optical Wireless Communications: System and Channel Modelling with MatLab*, First Edition. Boca Raton: CRC Press Taylor & Francis Group, 20120615.

[149] “Hamamatsu Si-Photodiodes.” http://www.hamamatsu.com/jp/en/product/category/3100/4001/index.html.

[150] “High Power LED Street Light SP-90.” DMX tecnologias, http://www.dmxledlights.com/docs/DMX_High_Power_LED_Streetlight_User_Manual.pdf.

[151] B. A. Jacobson, R. D. Gengelback, N. W. Medendorp Jr., L. Roberts, and J. Perry, “Optical System for Batwing Distribution,” 2009/0225543 A1.

[152] TJOI - Professional Lighting Solutions, “Expressway LED Lighting Retrofit.”

[153] T. Q. Wang, Y. A. Sekercioglu, and J. Armstrong, “Analysis of an Optical

Wireless Receiver Using a Hemispherical Lens With Application in MIMO Visible Light Communications," *Journal of Lightwave Technology*, vol. 31, no. 11, Jun. 2013.

[154] D. Zuo and C. Letchford, "Investigation of Wind-Induced Highway Lighting Pole Vibration Using Full-Scale Measurement," Texas Tech University, Research FHWA/TX-08-0-4586-5, Jun. 2008.

[155] L. A. Arioan, "The Probability Function of the Product of Two Normally Distributed Variables," *The Annals of Mathematical Statistics*, vol. 18, pp. 256–271, 1947.

[156] C. C. Craig, "On the Frequency Function of xy," *Annals of Mathematical Society*, vol. 7, pp. 1–15, 1936.

[157] A. Seijas-Macias and A. Oliveira, "An Approach to Distribution of the Product of Two Normal Variables," *Discussiones Mathematicae Probability and Statistics*, vol. 32, no. 2012, pp. 87–99, 2012.

[158] R. Ware and F. Lad, "Approximating the Distribution for Sums of Products of Normal Variables," Department of Mathematics and Statistics, University of Canterbury, New Zealand, Research Paper 2003-15, 2003.

[159] L. A.-H. Azizan, M. S. Ab-Rahman, and K. Jumiran, "Analytical Approach on SNR Performance of Visible Light Communication for Modern Lighting Layout," in *Proceedings of the 2012 International Conference on Innovation, Management and Technology Research (ICIMTR2012*, Malacca, Malaysia, 2012, pp. 332–336.

[160] D. Tsonev, S. Sinanovic, and H. Haas, "Practical MIMO Capacity for Indoor Optical Wireless Communication with White LEDs," in *Proceedings of the 77th Vehicular Technology Conference (VTC Spring) 2013*, Dresden, Germany, 2013.